DOCTORAL THESIS

Nanoemulsion-hydrogel composites: electro-kinetic dynamics, viscoelastic and swelling responses

Gbolahan Akeem Afuwape



Department of Chemical Engineering
McGill University

February 2021

A thesis submitted in partial fulfilment of the requirements for the degree of Doctor of Philosophy

© Gbolahan Akeem Afuwape, 2020

Preface

This is a manuscript-based thesis written in accordance with McGill's Guidelines for Thesis Preparation. It includes six (6) manuscripts for submission to peer-reviewed journals (chapters 3, 4, 5, 6, 7 and 8)

- G. A. Afuwape (main author): Wrote chapters 1, 2, and 9 with editorial corrections suggested by his research supervisor (R. J. Hill). The main author designed and performed experiments, data analysis, and wrote the initial drafts of chapters 3–8. Codes provided by the co-author were adapted for theoretical interpretations undertaken in chapters 3 and 4. All manuscripts are co-authored with his research supervisor. Other experimental contributions have been acknowledged in each chapters, in accordance with McGill's thesis regulations.
- R. J. Hill (co-author): Provided codes for electrokinetic modelling, and developed the theory used in chapters 6 and 7, guided by the experiments in those chapters. He supervised the research, assisted with experimental designs, revised all manuscripts, and guided data interpretation in chapters 3–8.

MCGILL UNIVERSITY

Abstract

Faculty of Engineering

Department of Chemical Engineering

Doctor of Philosophy

Nanoemulsion-hydrogel composites: electro-kinetic dynamics, viscoelastic and swelling responses

by Gbolahan Akeem Afuwape

Nanoemulsion-hydrogels have been touted as materials of choice for the localized and controlled-release of hydrophobic active pharmaceutical ingredients (APIs). The hydrogels are designed to respond to pre-defined stimuli, while the droplets serve as cargo until localized delivery is required. This thesis provides fundamental understanding of the composites using various theoretical and experimental methods. Dynamic mobility spectra of SDS-stabilized hexadecane droplets in Newtonian electrolytes and gels are obtained from electro-kinetic-sonic amplitude measurements, and interpreted with theories that capture the effect of Marangoni and viscous stresses due to surface concentration gradients and internal fluid circulation. For these interpretations, droplet surface charge was prescribed using adsorption isotherm developed from interfacial tensiometry, and effective particle diameters were furnished by the polydisperse nature of nanoemulsions. For droplets dispersed in polymer gels, the polymer contributions to the shear viscosity were obtained. These contributions depend on the oil volume fraction. The effects of encapsulated oil droplets on the micro-structure and macroscopic properties of polymers were probed using confocal microscopy, rheology, and swelling experiments. Confocal images revealed densely packed immobilized droplets, while swelling experiments showed these droplets reduced the composite swelling ratio as compared to hydrogels without oil drops. Rheological analysis suggested that the imbedded drops behave as rigid inclusions due to their interfacial tension. These insights on the electrokinetic dynamics of nanoemulsions and composites, and the influence of oil nanodroplets on hydrogel properties are vital in the design of nanoemulsion-hydrogels as carriers of APIs.

UNIVERSITÉ MCGILL

Abrégé

Faculté de génie Département de génie chimique

Docteur en Philosophie

Composites nanoémulsion-hydrogel: dynamique électro-cinétique, réponses viscoélastiques et gonflantes

par Gbolahan Akeem Afuwape

Les composites de nano-émulsions-hydrogels sont souvent vantés comme des matériaux de choix pour la libération localisée et contrôlée d'ingrédients pharmaceutiques actifs hydrophobes (IPA). Les hydrogels sont conçus pour réagir à des stimuli prédéfinis, tandis que les gouttelettes transportent les IPAs jusqu'aux sites de libération désirés. Cette thèse présente une interprétation fondamentale de ce type de composites en utilisant une combinaison de méthodes théoriques et expérimentales. La mobilité dynamique des gouttelettes de cétane stabilisées au SDS est mesurée en présence d'électrolytes et d'hydrogels. Les résultats sont ensuite interprétés en utilisant des théories capturant les effets de Marangoni et du stress visqueux dus aux gradients de concentration à la surface et de la circulation interne des fluides. Pour chaque interprétation, la charge de surface des gouttelettes a été prescrite en utilisant un isotherme d'adsorption développé à l'aide d'un tensiomètre, et le diamètre effectif des particules a été fourni par la nature polydispersée des nano-émulsions. Pour les gouttelettes dispersées dans les gels, la contribution des polymères à la viscosité de cisaillement a été obtenue. Cette contribution dépend de la fraction volumique de la phase huileuse. Les effets des gouttelettes d'huile sur la micro-structure et sur les propriétés macroscopiques des polymères ont été étudiés à l'aide de la microscopie confocal, de la rhéologie et d'expériences de gonflement des composés. La microscopie a révélé des zones à haute densité de

gouttelettes immobilisées, tandis que les expériences de gonflement ont démontré que les gouttelettes réduisent l'indice de gonflement des composites par rapport aux hydrogels sans gouttelettes. Les études rhéologiques suggérent que les gouttelettes se comportent en tant qu'inclusions rigides dues à leur tension superficielle. Ces renseignements sur la dynamique électrocinétique des nano-émulsions et des composites, et sur les influences de nano-gouttelettes d'huile sur les propriétés des hydrogels sont essentiels à la conception de composites de nano-émulsions-hydrogel pour le transport et la libération contrôlée de IPAs.

Acknowledgements

The main author wishes to acknowledge the following contributions: Dr. V. Adibnia provided training to perform electrokinetic-sonic-amplitude (ESA) and rheology measurements. D. Cannon of Colloidal dynamics was available for discussions about the ESA measurements of emulsions. Dr. C. Du provided guidance on dielectric relaxation (DR) experiments and designed the cell used to perform experiments. Mr L. Hudon performed the initial DR studies as a SURE research project in 2017; these guided subsequent DR measurements. Mr Andrew Golszatan and Ranjan Roy provided trainings in pendant drop tensiometry and dynamic light scattering methods, and answered his questions on instrument limitations. Ms. A. Djuric provided access to the Horiba particle size analyzer used in emulsion size characterization. Mr Frank Caporuscio redesigned the reverse-osmosis plant to improve water quality, and for always been resourceful. Mr Al-Amodi provided confocal microscopy training and insights on choice of fluorescent lipids to aid imaging. Mrs O. Odunola assisted with thermogravimetric experiments on composites. Mr. M. Morunov engaged in useful discussions on overcoming limitations of pendant drop measurements at lower surface tensions. Mr J. Goulet helped with abstract translation to french.

Main author gratefully acknowledges the opportunity given by co-author (**Prof. Reghan J. Hill**) to study at McGill University, guardianship, and financial support through nominations for EUL award, and contributions towards the MEDA award. He is also grateful for funding support provided by McGill Engineering faculty in terms of McGill Engineering Doctoral and Graduate Excellence Awards. He acknowledges NSERC Discovery and Research Tools and Instruments for grants towards this research.

He will also like to acknowledge the support of the past President of Nigeria (Dr. Goodluck Jonathan: 2006–2015) for the merit based scholarship via the National University Commission (NUC) and Petroleum Technology Development Fund (PTDF).

Special thanks to: Mrs T. Olusa (mum), Mr F. Olusa (stepdad), siblings (Lolade, Opeyemi and Maggi), step-siblings (Dare, Olaitan and Busola), and foster siblings (Ope and Afeez Alebiosu). To the men who coached him through, and accepted me as a brother: Mr. B. and S. Ayantuga (the maths lessons, farming, feeding guinea pigs). To the teachers who taught him, he could be anything and everything (Mr Amole (Chemistry teacher) and Mr Ogundana (Physics teacher)). To his CHG10 community (esp. Nikkidizzle), we shaped boys into champions, and that never

say die attitude got him this far. His doctoral student community (Dr. Olufayo (ETS), Dr. Akande (Duke), Dr. Adekunle (McGill), Dr. Idris (McGill), Dr. Alex (McGill), Tolu (PhD. Cand.), Ibeh (PhD. Cand.)) and those who decided M.sc. was enough (Aileme, Tomi, Dayo, Segun, Laguda, Ogunbiyi), his PhD watch ends here. To his summer soccer community, thanks for the energy sapping Saturday mornings. He would like to express immense gratitude to everyone who has contributed to the accomplishment of this degree. The names mentioned here are not exhaustive, if he has missed out due to page limitations, "thank you".

Finally, this achievement would be impossible without the support of his heart-beats, the yard people: the Afuwapes (Afunshur, Ashabi and Ruby). What is life without your love?

Contents

\mathbf{P}_{1}	refac	е																	i
\mathbf{A}	bstra	ct																	ii
\mathbf{A}	brége	5																	iv
\mathbf{A}	ckno	wledge	ements																vi
\mathbf{C}	onter	nts																	viii
Li	st of	Figur	es															:	xiii
Li	st of	Table	S																xxi
\mathbf{A}	bbre	viation	ıs															X	xiv
1	Intr	oduct	ion																1
	1.1	Motiv	ation																1
	1.2	Thesis	s objective	es															2
	1.3	Thesis	s organiza	tion	1			•											3
${f 2}$	$\operatorname{Lit}_{\epsilon}$	erature	e Review	7															5
	2.1	Nanoo	composites	s.															5
		2.1.1	Nanoem	ıulsi	ons														6
		2.1.2	Hydroge	els															7
		2.1.3	Nanoem	ıulsi	ion-h	ydro	ogel	S											8
	2.2	Electr	okinetic p	oher	ome	ena a	and	the	eor	ies									9
		2.2.1	Standard	d el	ectro	okin	etic	th	eor	ies									10
	2.3	Exper	imental m	neth	ods														13
		2.3.1	Electroa	ıcou	stic	spec	ctro	sco	ру										13
			2.3.1.1	T	heory	y of	elec	etro	aco	ous	tics	8.							13
			$2\ 3\ 1\ 2$	M	etho	dolo	voor												15

Contents ix

		2.3.2		ic relaxation spectroscopy (DRS)	
			2.3.2.1	Theory	
			2.3.2.2	Methodology	18
3	Frac	ctional	ionizat	ion of SDS micelles from dielectric relaxation	
		${ m ctrosec}$			2 9
	3.1	Prefac	ee		29
	3.2	Abstra	act		29
	3.3	Introd	luction .		30
	3.4	Theor	etical inte	erpretation	32
	3.5	Mater	ials and r	methods	35
		3.5.1	Dielectr	ic relaxation spectroscopy	35
	3.6	Result	s and dis	cussion	37
		3.6.1	Conduct	tivity isotherms and theoretical interpretation	40
		3.6.2	Conduct	tivity increment spectra and theoretical interpretation	43
	3.7	Concl	usions .		49
	3.8	Ackno	wledgeme	ent	50
	3.9	Autho	or contribu	utions	50
	3.A	Electr	okinetic s	sonic amplitude of SDS micelle solutions	54
1	Flac	at no lei e	atia inte	proportation of polystymone letipos	5 6
4	4.1				56
	4.1				56
	4.2				57
	4.4				58
	4.4	4.4.1			58
			_		59
		4.4.2		*	
	4 5	4.4.3		cussion	60
	4.5				64
				1	
	4 C	4.5.2	•		65
	4.6				68
	4.7				69
	4.8		_		70
	4.9	Autho	r contribi	utions	70
5	Die	lectric	relaxati	on spectroscopy of oil-in-water nanoemulsions	7 3
	5.1	Prefac	e		73
	5.2	Abstra	act		73
	5.3	Introd	luction .		74
	5.4	Mater	ials and r	nethods	76
		5.4.1	Nanoem	ulsion preparation	76
		5.4.2		± ±	77
		5.4.3			77
		5.4.4			77

<u>Contents</u> x

	5.5	Results and discussion	8
		5.5.1 Interfacial tension of the hexadecane-water interface in the	
		presence of SDS and NaCl	8
		5.5.2 Surfactant material balance	1
		5.5.3 Dielectric relaxation of oil-in-water emulsions 8	2
		5.5.4 Electrokinetic interpretation of nanoemulsions 8	4
	5.6	Conclusions	0
	5.7	Acknowledgements	0
	5.8	Author contributions	0
	5.A	Interpretation with O'Brien's "closed-form" expression 9	3
	5.B	Comparison of drop size characterization methods 9	4
6	-	namic mobility from highly charged oil-in-water nanoemul-	
	sion		
	6.1	Preface	
	6.2	Abstract	
	6.3	Introduction	
	6.4	Materials and methods	
		6.4.1 Nanoemulsion preparation	
		6.4.2 Electroacoustic spectroscopy	
		6.4.3 Dynamic mobility	
	6.5	Results and discussion	
		6.5.1 Nanoemulsions with SDS below the c.m.c	
		6.5.2 Nanoemulsions with SDS above the c.m.c	
	6.6	Conclusions	
	6.7	Acknowledgements	
	6.8	Author contributions	
	6.A	Fitting dynamic mobility models to measured spectra	3
7	Dyr	namic mobility of nanodrops in hydrogels 11	7
	7.1	Preface	7
	7.2	Abstract	7
	7.3	Introduction	8
	7.4	Materials and methods	9
		7.4.1 Synthesis of nanoemulsion-doped polyacrylamide hydrogel	0
		composites	
		7.4.2 Electroacoustic spectroscopy	
	→ -	7.4.3 Rheology	
	7.5	Results and discussion	
		7.5.1 Rheology	
		7.5.2 Dynamic mobility spectra	
		7.5.3 Theoretical interpretation	
	7.6	Conclusions	
	7.7	Acknowledgements	
	7.8	Author contributions	9

Contents xi

	7.A	Particle size characterization
	7.B	Dynamic mobility spectra
8	Nan	noemulsion-doped hydrogels 136
	8.1	Preface
	8.2	Abstract
	8.3	Introduction
	8.4	Materials and methods
		8.4.1 Nanoemulsions
		8.4.2 Polyacrylamide gels
		8.4.3 Nanoemulsion-hydrogel composites
		8.4.4 Confocal microscopy
		8.4.5 Rheology
		8.4.6 Swelling
		8.4.7 Thermogravimetric analysis
	8.5	Results and discussion
		8.5.1 Swelling
		8.5.2 Rheology
	8.6	Conclusions
	8.7	Acknowledgements
	8.8	Author contributions
9	Con	clusions and future work 155
	9.1	Summary of conclusions
	9.2	Contributions to knowledge
	9.3	Suggestions for future work
٨	Diol	ectric relaxation spectroscopy of polyacrylamide hydrogels 159
A		Preface
		Materials and methods
		Results
		Conclusions
	71.1	Concrasions
_	_	
В		ailed experimental protocols 164
	B.1	Electroacoustic spectroscopy
		B.1.1 Pre-experimental cleanup
		B.1.2 Post-experimental cleanup
		B.1.3 Conductivity probe calibration
		B.1.4 pH probe calibration
		B.1.5 ESA cell calibration
		B.1.6 ESA for nanoemulsions
		B.1.7 ESA for gels
	B.2	Dielectric relaxation spectroscopy

X11
AII

	Open/short compensation			
Bibliography			1	.72

List of Figures

2.1	Nanoemulsion-hydrogel hypothesized temperature induced polymerization mechanism as hypothesized by Hashemnejad et al. (2019).	
2.2	Image used with publisher's permission	9
	charged particles between the electrodes, and counterion distribution around each particle with the applied electric field E and the	
2.3	internal electric field in the double layer E' (Adibnia, 2015) A setup for a dielectric relaxation experiment using the Keysight	14
2.0	E4990A Impedance analyzer	17
3.1	In-house sample holder for dielectric spectroscopy. Sample is injected into the space between two parallel stainless steel electrodes,	
3.2	separated by an acrylic spacer: $A \approx 1.2 \text{ cm}^2$ and $h \approx 3 \text{ mm}$ Conductivity (left) and apparent dielectric constant (right) spectra	37
	of aqueous SDS solutions with SDS concentrations $c_{\infty} = 1, 3, 5, 8, 10, 15, 30, 50, 70, and 100 mM, no added salt $	38
3.3	Dielectric constant spectra of aqueous (a) SDS solutions at SDS concentrations $c_{\infty} = 3$ (blue), 8 (red) and 30 (yellow) mM, no added salt; and (b) NaCl solutions at NaCl concentrations [NaCl] = 5 (blue), 10 (red) and 30 (yellow) mM. Corrected data (open cir-	30
	cles) are compared with their uncorrected (for electrode polarization, filled circles) counterparts. The electrode-polarization model	
	fitting parameter D is provided in table 3.1	38
3.4	Dielectric constant spectra of aqueous SDS solutions with added NaCl concentrations [NaCl] = 0 (blue), 1 (red), and 5 (yellow) mM.	
	Black circles are dielectric spectra for aqueous NaCl with NaCl concentration [NaCl] = c_{∞}	39
3.5	Conductivity and dielectric constant at $f \approx 1$ MHz versus SDS	
	concentration for several added NaCl concentrations	41
3.6	Conductivity (left) and dielectric constant (right) increments of SDS micelle solutions above the c.m.c. (a) $c_{\infty} = 15$ (blue), 20 (red) and	
	30 mM (yellow). SEKM _{ac/nsa} with $\zeta = -3.42~k_BT/e$ (solid lines) and SEKM ₀ with $\zeta = -5.3~k_BT/e$ (dashed lines). (b) $c_{\infty} = 15$	
	(blue) and 20 (red) mM. SEKM _{ac/nsa} with $\zeta = -3.3 k_B T/e$ (solid);	
	SEKM ₀ with $\zeta = -5.28 \ k_B T/e$ (dashed). (c) $c_{\infty} = 15$ (blue) and 20 (red) mM. SEKM _{ac/nsa} with $\zeta = -2.85 \ k_B T/e$ (solid); SEKM ₀	
	with $\zeta = -5.1 \ k_B T/e \ (dashed)$	44

List of Figures xiv

3.7	Conductivity (left) and dielectric constant (right) increment spectra for SDS micelles (at infinite dilution) according to the SEKM. Added NaCl concentration [NaCl] = 1 mM (c.m.c. ≈ 7.97 mM,	
3.8	$\kappa a_m \approx 0.69$), and $\zeta = -5.28~k_BT/e$	45
3.9	at $f = 0.1$ MHz	47
3.10	$\kappa a_m \approx 0.72.$	49
3.11	in the range -5 –0°; these small values reflect the small particle size. ESA spectra for SDS concentrations $c_{\infty}=0,1,3,8,10,20,30,50,$ and 100 mM with NaCl concentration [NaCl] = 1 mM. Black line is the ESA for a 1 mM NaCl solution without SDS. Conductivities (from the ESA instrument) are $\sigma=0.012,0.019,0.031,0.059,0.063,0.085,0.107,0.152,$ and $0.272~S~m^{-1}$	4954
3.12	ESA magnitude and phase angle at $f=11.1$ MHz versus SDS concentration with added NaCl concentrations [NaCl] = 0 (blue), 1 (red), 10 (yellow), and 20 (violet) mM.	55
4.1	Fits of Eqn. (4.2) to dielectric constant data for KCl solutions with $I_s = 0.1$ (blue) and 1 mM (red)	60
4.2	Conductivity increments of 200 nm diameter polystyrene spheres in aqueous KCl solutions versus ϕ : $f=1$ kHz (blue) and $f=1$ MHz (red). Lines are fit to data with $\Delta \sigma = \Delta \sigma_0 (1-a\phi)$ and $\Delta \sigma = \Delta \sigma_0 (1-a\phi+b\phi^2)$ for 0.1 and 1 mM, respectively	61
4.3	Conductivity (left) and dielectric constant (right) increments of 200 nm diameter polystyrene latices in electrolyte solutions. SEKM calculations are undertaken with the manufacturer's surface charge density for each batch ($\sigma \approx -0.6$ (panel a) and -1.3 (panel b) μ C cm ⁻²) Solid lines account for added counterions and non-specific adsorption.	
4.4	Conductivity (left) and dielectric constant (right) increments of 200 nm diameter polystyrene latices (batch B with $\sigma = -1.3 \mu\text{C cm}^{-2}$) in $I_s = 1$ mM KCl electrolyte solutions with $\phi = 0.02$ (blue), 0.035 (red), 0.05 (yellow). SEKM calculations for bare spheres (lines) are undertaken with different surface charge densities: $\sigma \approx -1.3$ (blue), -1.5 (red) and -1.9 (yellow) $\mu\text{C cm}^{-2}$). Solid lines account	
	for added counterions and non-specific adsorption	64

List of Figures xv

	Conductivity (left) and dielectric constant (right) increments of 200 nm diameter polystyrene latices (batch B) in $I_s = 1$ mM KCl electrolyte solutions, with $\phi = 0.02$ (blue), 0.035 (red), 0.05 (yellow). SEKM calculations for soft spheres (lines) are undertaken with a hairy layer thickness $L = 5$ nm, fixed charge densities $N_f = 0.027$ (yellow), 26.9 (red), and 107.6 (blue) M, and Stokes segment density $N_s = 0.13$ M and radius $a_s = 0.95$ Å (Brinkman length $\ell_B \approx 2.63$ nm). Solid lines account for added counterions	4.5
. 66	and non-specific adsorption	4.0
	Hair-layer interpretation of conductivity (left) and dielectric constant (right) increments of 200 nm diameter polystyrene lattices (batch B) in $I_s = 1$ mM KCl (circles) with $\phi = 0.02$ (blue), 0.035 (red), 0.05 (yellow). SEKM calculations for soft spheres (lines) are undertaken with a hairy layer thickness $L = 5$ nm, fixed charge density $N_f = 108$ M, Stokes segment density $N_s = 13.4$ (blue), 1.34 (red), and 0.13 (yellow) M, and Stokes radius $a_s = 0.95$ Å (the corresponding Brinkman lengths are reported in table 4.3). Solid lines	4.6
. 67	account for added counterions and non-specific adsorption	
. 67	Conductivity (left) and dielectric constant (right) increments of 200 nm diameter polystyrene latices (batch B) in $I_s = 1$ mM KCl electrolyte solutions (circles), with $\phi = 0.02$ (blue), 0.035 (red), 0.05 (yellow). SEKM calculations for soft spheres (lines) are undertaken with a hairy layer thickness $L = 5$ nm, fixed charge densities $N_f = 107.6$ M and Stokes segment density $N_s = 0.13$ M, and segment radius $a_s = 9.5$ (blue), 0.95 (red) and 0.0095 (yellow) Å (the corresponding Brinkman lengths are reported in table 4.3). Solid lines account for added counterions and non-specific adsorption.	4.7
. 00		E 1
. 80	(a) Fits of Eqn. (5.1) to surface-tension data (for the hexadecane-SDS-water interface) with added NaCl concentrations $I_s = 0$ (blue), 1 (red), 5 (yellow) and 20 (violet) mM. Solid lines are fits with Γ and n as adjustable parameters for each added salt concentration. Corresponding dashed (colored) lines are fits using the averaged (over I_s) parameters in table 5.2. Black lines are the model evaluated with the parameters of Borwankar and Wasan for the hexane-SDS-water interface (no added salt). (b) Fits of Eqn. (5.1) to data (for each salt concentration) with Γ and n as fitting parameters (dashed lines, same as in (a)); and with only δ as the fitting parameter (solid lines, with prescribed $a_s = 2.42$ Å, $\Delta \epsilon = -19$). All fits undertaken with $\gamma_0 \approx 47$ mN m ⁻¹	5.1

List of Figures xvi

5.2	Surface charge density (left) and ζ -potential (right) as a function of bulk surfactant concentration c_{∞} for added NaCl concentrations	
	$I_s = 10^{-2}$ (blue), 1 (red), 5 (yellow) and 20 mM (yellow). The model has been extrapolated beyond beyond the c.m.c. for each added	
	salt concentration. These calculations undertaken with the optimal	
	two-parameter model ($\delta = 0.665$ Å, $a_s = 3.34$ Å, and $\Delta \epsilon = -18.9$)	0.0
5 9	across all ionic strengths (see table 5.3)	82
5.3	Dielectric relaxation spectra (conductivity and dielectric constant) for emulsions with oil volume fractions $\phi = 0, 0.02, 0.05, 0.1$ (black, blue, red, yellow). Bulk aqueous-phase SDS and added NaCl concentrations are c_{∞}^* and I_s . Circles are for the emulsions, and dashed	
	lines are for the subnatant	83
5.4	Calculated conductivity and dielectric constant increment spectra for emulsions with oil volume fractions $\phi = 0.02, 0.05, 0.1$ (blue, red, yellow) from nanoemulsion and subnatant spectra. Bulk aqueous-	
	phase SDS and added NaCl concentrations are c_{∞}^* and I_s	85
5.5	Conductivity and dielectric constant increments for a nanoemul-	
	sions with oil volume fraction $\phi = 0.05$ and bulk SDS concentra-	
	tion $c_{\infty,0} = 4.75$ mM. Solid lines are the SEKM for oil nanodrops	
	(modelled as rigid spheres). Dashed lines are calculations without the contributions of added counter-ions and non-specific adsorption.	
	Drop diameters d_{85}, d_{50}, d_{15} measured using sound-wave attenuation	
	are: (a) 507 (blue), 410 (red), and 326 nm (yellow); (b) 701 (blue),	
	417 (red), and 249 (yellow) nm; (c) 724 (blue), 431 (red), 257 (yellow) nm	88
5.6	Conductivity and dielectric constant increments for a nanoemul-	00
	sions with oil volume fraction $\phi=0.05$ and bulk SDS concentration $c_{\infty,0}=4.75$ mM. Solid lines are the SEKM for oil nanodrops	
	(modelled as rigid spheres). Dashed lines are calculations without	
	the contributions of added counter-ions and non-specific adsorption. Nanoemulsion droplet diameters d_{85} , d_{50} , d_{15} measured using sound-	
	wave attenuation are: (a) 507 (blue), 410 (red), and 326 nm (yel-	
	low); (b) 701 (blue), 417 (red), and 249 (yellow) nm; (c) 724 (blue),	
	431 (red), 257 (yellow) nm. Diameters are measured from sound	
	wave attenuation	89
5.7	Conductivity (left) and dielectric (right) increment spectra for na-	
	noemulsions with bulk volume fraction $\phi = 0.02$ (a), 0.05 (b) and 0.1 (c) with bulk SDS concentration $c_{\infty,0} = 5$ mM and NaCl con-	
	centrations $I_s = 0$ (blue), 1 (red) and 5 (yellow) mM. Solid lines	
	are Eqn. (5.9) with ζ -potentials from the adsorption isotherm with	
	measured d_{85} particle diameters	94

List of Figures xvii

6.1	Electrophoretic mobility, highlighting the possibility of two ζ -potentic roots for highly charged colloids. Solid lines are approximate solutions (O'Brien and Hunter, 1981) of the standard electrokinetic model (O'Brien and White, 1978) for $\kappa a = 20$ (blue), 75 (red), 150 (yellow), and 230 (violet). Dashed lines are an approximation of Henry's function for $\kappa a = 20$ (blue) and 230 (violet) (Ohshima,	
6.2	Equilibrium characteristics of the SDS-oil-water interface plotted versus the bulk surfactant concentration c_{∞} in the presence of added NaCl at concentrations $I_s = c_{-}^{\infty} = 10^{-2}$ (blue), 1, 5 and 20 (violet) mM. Data (circles) and model (lines) are from Afuwape and Hill (2020, Ch. 5) with isotherm parameters: $\Gamma = 4.89 \times 10^{-6}$ mol m ⁻² and $n = 4.83 \times 10^{-4}$ mol m ⁻³	. 98
6.3	Dynamic mobility spectra for an SDS-oil-water emulsion: $\phi=0.05$, $c_{\infty,0}=4.75$ mM, and $I_s=1$ mM (added NaCl). Lines are theoretical interpretations using O'Brien's (thin-double-layer) theory with the ζ -potential prescribed by the adsorption isotherm of Afuwape and Hill (2020, Ch. 5) ($\zeta=-8.53~k_BT/e$) (red) and according to the Acoustosizer II instrument ($\zeta=-3.84~k_BT/e$) (blue). Both calculations are undertaken with a drop diameter $2a=701$ nm, as prescribed by sound-wave attenuation, with $c_{\infty}=3.67$ mM and	
6.4	$\kappa a=78.8$ from a surfactant material balance. The same data as in figure 6.3 compared with O'Brien's theory (black dashed lines) and the fluid-sphere model of Hill and Afuwape (2020) (solid lines) with drop viscosities $\eta_i=\infty$ (rigid sphere with interfacial DS ⁻ diffusivity $D=0$, blue), $\eta_i=\infty$ (rigid sphere, $D=1.02\times 10^{-10}~{\rm m^2~s^{-1}}$, red), $\eta_i=3.45~{\rm mPa~s}$ (fluid sphere, ${\rm Ma}_c=0$ ($\beta=0$), yellow) and $\eta_i=3.45~{\rm mPa~s}$ (fluid sphere, ${\rm Ma}_c=1.20\times 10^5$, violet). Both theories (including the isotherm) are evaluated with a drop diameters $2a=701~{\rm nm}$.	
6.5	Dynamic mobility for nanoemulsions with aqueous-phase surfactant concentration $c_{\infty,0}/(1-\phi)=5$ mM, and added salt concentrations $I_s=10^{-2}$ (blue, c.m.c. ≈ 8.18 mM), 1 (red, c.m.c. ≈ 7.97 mM), and 5 mM (yellow, c.m.c. ≈ 6.85 mM). Solid lines are theoretical fits of Eqn. (6.4) using the drop diameter \hat{d} as the fitting parameter (see table 6.1). The c.m.c. for each ionic strength is estimated from conductivity measurements (Afuwape and Hill, 2020, Ch. 3)	. 107
6.6	Dynamic mobility for nanoemulsions with aqueous-phase surfactant concentration $c_{\infty,0}/(1-\phi)=13$ mM (above the c.m.c.), and added salt concentrations $I_s=10^{-2}$ (blue, c.m.c. ≈ 8.18 mM), 1 (red, c.m.c. ≈ 7.97 mM), and 5 mM (yellow, c.m.c. ≈ 6.85 mM). Solid lines are theoretical fits of Eqn. (6.4) using the drop diameter \hat{d} as the fitting parameter (see table 6.1). The c.m.c. for each ionic strength is estimated from conductivity measurements (Afuwape and Hill, 2020, Ch. 3). See figure 6.7 for an improved fit based on setting $\beta=0$. 109

List of Figures xviii

6.7	The same data as in figure 6.6, but the model is fitted without Marangoni effects (setting $\beta = 0$). This is suggested as a better approximation when above the c.m.c., based on the equilibrium interfacial surface tension being a very weak function of surfactant concentration in this regime
6.8	Fitting the fluid-sphere model of Hill and Afuwape (2020) (drop radius a as the fitting parameter) to measured dynamic-mobility spectra using (i) real and imaginary parts (blue, $2a=712$ nm), (ii) real part (red, $2a=726$ nm), and (ii) magnitude (yellow, $2a=707$ nm). Bulk surfactant concentration $c_{\infty,0}/(1-\phi)=5$ mM, added salt concentration $I_s=1$ mM, oil volume fraction $\phi=0.05$ 113
7.1	Nanoemulsion-doped hydrogel in the ESA polysphenylenesulphide (PPS) spacer of the ESA sensor (left) and attached to the ESA electrode (right)
7.2	Rheological characterization of polyacrylamide hydrogels and nanoemulsion doped hydrogels: $P_0G_4S_0$ (black), $P_2G_4S_0$ (blue), $P_5G_4S_0$ (red) and $P_{10}G_4S_0$ (yellow). (a) Storage modulus time series with $\omega=1$ rad s ⁻¹ , $\gamma=2$ % (b) Storage modulus strain sweep with $\omega=1$ rad s ⁻¹ . (c) Storage and (d) loss moduli (shear viscosity $\eta'=G''/\omega$) frequency sweeps with $\gamma=2$ %
7.3	Dynamic mobility spectra for nanoemulsions with volume fraction $\phi = 0.02$ (black), and for nanoemulsion-doped hydrogels $P_2G_4S_0$ during gelation (with time increasing from $t \sim 4.5$ (blue) to 135 (red) min at time intervals $\Delta t \sim 4.5$ min. Both samples have no added NaCl
7.4	Dynamic mobility time series ($\omega/(2\pi) = 2.1$ MHz, no added NaCl) for nanoemulsions with oil volume fraction $\phi = 0.05$ (black) and nanoemulsion-doped hydrogels: $P_5G_4S_0$ (blue), $P_5G_{5.5}S_0$ (red) and $P_5G_8S_0$ (yellow)
7.5	Conductivity spectra for polyacrylamide hydrogels with 2 (blue), 4 (red), 8 (yellow) and 16 % wt monomer (violet) and no added salt. Black line is for a solution containing ammonium persulfate and TEMED at the same concentrations used to synthesize gels 126
7.6	Conductivity of NaCl (right) and SDS (right) in solutions (red) and polyacrylamide hydrogel (4 wt%, blue) as a function of NaCl and SDS concentration, respectively. For the hydrogels, the conductivity of the gels without added NaCl and SDS has been subtracted ($\sigma_{gel} \approx 0.140 \text{ S m}^{-1}$). Lines are best fits, identifying c.m.c.s of SDS $\approx 6.15 \text{ mM}$ (polymer, blue), and $\approx 8.18 \text{ mM}$ (aqueous solution, red) with no added NaCl

List of Figures xix

7.7	Steady-state dynamic mobility magnitude (left) and phase (right) spectra of composites after polymerization. Solid lines are fits of the fluid-sphere model of Hill and Afuwape (2020) with a complex shear viscosity. Fitting parameters are in table 7.2 with prescribed parameters: $I_g = 11.2$ mM (from the final hydrogel conductivity), $\eta_o = 0.89$ mPa s, $\eta_i = 3.4$ mPa s, $T = 298$ K, $\rho_o = 997$ kg m ⁻³ , and $\rho_i = 771$ kg m ⁻³	. 128
7.8	Steady-state dynamic mobility magnitude (left) and phase (right) spectra of composites after polymerization. Solid lines are fits of the fluid-sphere model of Hill and Afuwape (2020) with a complex shear viscosity. Fitting parameters are in table 7.2 with prescribed parameters: $I_s = 11.2$ mM (from the final hydrogel conductivity), $\eta_o = 0.89$ mPa s, $\eta_i = 3.4$ mPa s, $T = 298$ K, $\rho_o = 997$ kg m ⁻³ , and $\rho_i = 771$ kg m ⁻³	134
7.9	The same as figure 7.8, but with added NaCl concentration $I_{s,0} =$. 101
7.10	4 mM: $P_2G_4S_5$ (blue), $P_5G_4S_5$ (red), and $P_{10}G_4S_5$ (yellow) The same as Figure 7.8 for samples with no added NaCl salt: $P_5G_4S_0$. 135
7.10	(blue), $P_5G_{5.5}S_0$ (red), and $P_5G_8S_0$ (yellow)	. 135
8.1	Representative gels: (A) PA gel in as-prepared state; (B) Nano-emulsion-doped gel in as-prepared state; (C) Nano-emulsion-doped gel in "dried" state (following ~ 12 hr in air)	. 142
8.2	Confocal microscopy of a nanoemulsion-hydrogel composite (a) prepared from nanoemulsion with oil volume fraction $\phi = 0.1$, aqueous phase SDS concentration $c_{\infty,0}/(1-\phi) = 5$ mM and diameter $d_{85} = 785$ nm (from sound-wave attenuation) compared with a pure AAm hydrogel (b). Both gels have a monomer concentration ≈ 4 wt % and monomer to cross-linker ratio 19:1	
8.3	Swelling-ratio time series of initially as-prepared (a) and dried (b) hydrogels and nanoemulsion-hydrogel composites. Hydrogels are from ≈ 4 wt % monomer with oil volume fractions $\phi=0$ (black), 0.08 (blue) and 0.16 (red), and aqueous-phase SDS concentration $c_{\infty,0}/(1-\phi)=13$ mM	
8.4	Gravimetric analysis of hexadecane (blue), an as-prepared nanoemuls hydrogel composite ($\phi = 0.16$, red), dried nanoemulsion-hydrogel composite ($\phi = 0.16$, yellow), and as-prepared or dried hydrogel ($\phi = 0$, violet) versus temperature	
8.5	Rheological characterization of polyacrylamide and nanoemulsion composites with 4 wt % monomer concentration and oil volume factions $\phi = 0$ (black), 0.02 (blue), 0.05 (red), 0.1 (yellow), and 0.2 (violet). (a) Storage modulus time series with $\omega = 1$ rad s ⁻¹ , $\gamma = 2\%$ (b) Storage modulus sweep with $\omega = 1$ rad s ⁻¹ . (c) Storage and (d) loss modulus frequency sweep with $\gamma = 2\%$	

List of Figures xx

8.6	(a) Steady-state storage modulus (blue) and exponent α (Eqn.(8.3), red) for cross-linked nanoemulsion composites versus oil volume fraction ϕ ($\gamma \approx 2\%$, $\omega \approx 1$ rad s ⁻¹). Error bars are the standard deviation from three samples. (b) The storage modulus scaled with the value for gels with $\phi = 0$. Solid line is a linear fit that weights residuals according to the errors: $G'/G'_0 = (4.7 \pm 1.9)\phi + (1.00 \pm 0.1)$ (Browaeys, 2020). This is compared to the Einstein viscosity formula (Einstein, 1906) (red) and its counterpart for inviscid, but penetrable spheres (Wang and Hill, 2009) (yellow, dashed line).	. 148
A.1	Conductivity (left) and dielectric constant (right) time series for polyacrylamide hydrogels (2 wt %) with added NaCl concentrations $I_s = 0$ (blue), 1 (red), 5 (yellow), 10 (violet), 20 mM (green) measured at $f = 100$ kHz	. 160
A.2	Conductivity (left) and dielectric constant (right) spectra of polyacrylamide hydrogels (2 wt %), with added NaCl concentrations I_s = 0 (blue), 1 (red), 5 (yellow), 10 (violet), 20 mM (green). Dashed lines are spectra for NaCl solutions with NaCl concentrations I_s = 1 (red), 5 (yellow), 10 (violet) mM	161
A.3	Conductivity (left) and dielectric constant (right) time series for polyacrylamide hydrogels (4 wt%) with SDS concentrations $c_{\infty} = 0$ (blue), 5 (red), 8 (yellow), 13 (violet), 20 (green) mM measured at	
A.4	f=1 MHz	
A.5		
A.6	Conductivity (left) and dielectric constant (right) time series for 2 (blue), 4 (red), 8 (yellow), and 16 (violet) wt% polyacrylamide hydrogels with no added salt	
A.7		
B.1	Conductivity (right) and dielectric constant (left) spectra of aqueous KCl solutions with ionic strength $I_s = 0.01$ (blue), 0.1 (red), 1 (yellow), and 10 (violet) mM. Dashed lines are dielectric constant spectra corrected for electrode polarization using the single-spacer technique	. 171

List of Tables

3.1	Fitting parameter D for the electrode-polarization corrections in	
	figure 3.3. At $c_{\infty} = 30$ mM, above the c.m.c., D at the c.m.c.	
	is used for the correction, thus assuming that the excess SDS (in	
	micelles) does not change the composition of the background elec-	
	trolyte contributing to D	39
3.2	Parameters extracted from the conductivity isotherms $(T = 22^{\circ}\text{C})$	
	in figure 3.5: Δ_1 and Δ_2 are slopes below and above the c.m.c.,	
	respectively. Note that λ_{Na+} is prescribed from Moroi and Yoshida	
	(1997), corrected for temperature using $\lambda_i(T) = \lambda_i^0 [1 + 0.02(T -$	
	25°C)] (SAS, 2003)	41
3.3	Parameters as input for SEKM calculations of the mobility and	
0.0	conductivity increment for SDS micelles at infinite micelle dilution,	
	i.e., at the c.m.c. These data at $T=25$ °C	42
3.4	Number of charges N (and $\alpha = N/N_{aqq}$ with $N_{aqq} = 64$ (Mo-	
0.1	roi and Yoshida, 1997)) for SDS micelles calculated according to	
	Eqn. (3.14) and the Poisson-Boltzmann equation for the accompa-	
	nying ζ -potential, each obtained by fitting either SEKM ₀ or SEKM _{ac/ns}	a
	to the post-c.m.c. slopes of the conductivity isotherms in figure 3.5	a
	and summarized in table 3.2	43
3.5	Micelle valence N and $\alpha = N_m/N_{agg}$ with $N_{agg} \approx 64$ (Moroi and	
	Yoshida, 1997)) according to the Poisson-Boltzmann equation for	
	the accompanying ζ -potential, each obtained by fitting either SEKM ₀	
	or SEKM $_{ac/nsa}$ to the conductivity increment spectra in figure 3.6	46
3.6	Micelle mobility M_m from the SEKM and α according to Eqn. (3.9)	
	with N_{agg} , a_m and λ_{DS^-} as prescribed in table 3.3	46
3.7	Scaled electrokinetic surface potential $-\zeta e/(k_B T)$ of SDS micelles	
	from the present work and past literature	48
	r r r	
4.1	Parameters as input for SEKM calculations of the mobility and	
	conductivity increment for polystyrene latex particles at infinite	
	micelle dilution, i.e., at the c.m.c. These data at $T=25~^{\circ}\text{C}$	60
4.2	Model parameters obtained from the fit of conductivity increment	
	data (plotted in figure 4.2) to $\Delta \sigma = \Delta \sigma_0 (1 - a\phi)$ and $\Delta \sigma = \Delta \sigma_0 (1 - a\phi)$	
	$a\phi + b\phi^2$)	61
4.3	Brinkman screening lengths ℓ_B from a nominal segment density N_s	
	and segment radius a_s	66

List of Tables xxii

5.1	Particle size moments from sound wave attenuation. Conductivities were measured in the instrument sample cell. The bulk aqueous-	
5.2	phase SDS concentration is denoted as c_{∞}^*	78
	eters obtained by fitting Eqn. (5.1) (equivalent to Eqn. (5.4)) to data at each added NaCl concentration with Γ and n as fitting	
5.3	parameters. Here, δ , a_s and $\Delta \epsilon$ are derived from Γ and n 8 SDS-hexadecane-NaCl solution adsorption isotherm model parame-	3C
0.0	ters obtained by fitting Eqn. (5.1) (equivalent to Eqn. (5.4)) to data at each added NaCl concentration with δ as the fitting parameter	
	(prescribed $\Delta \epsilon \approx -19$ and $a_s = 2.42$ Å). Here, Γ and n are derived from the fitted and prescribed parameters	31
5.4	C.m.c. from surface tension γ and conductivity σ (Afuwape and Hill, 2020, Chapter 3). γ and σ are the surface tension and conduc-	
. .	tivity at the c.m.c. *From Dunstan and White (1990) 8 Conductivity increment $\Delta \sigma$ for nanoemulsions are estimated as	31
5.5	$\Delta \sigma = \sigma - \sigma_{\infty}/(\sigma_{\infty}\phi)$ using the nanoemulsion conductivity σ and	
	respective subnatant conductivity σ_{∞} at $f \approx 100$ kHz. Subnatant	
	electrolyte concentrations are estimated from independent conductivity-	
	concentration plots for SDS solutions (see Afuwape and Hill (2020, Chapter 3))	34
5.6	ζ -potential and equilibrium aqueous-phase SDS concentrations were calculated from the absorption isotherm coupled to the SDS mate-	ם כל
	rial balance (Eqns. (5.2) and (5.3) with Eqn. (6.8)) with particle	
	diameters d_{15} (top), d_{50} , d_{85} (bottom) obtained from sound wave	~ -
5.7	attenuation	37
0.1	tion of measurements from the Horiba laser scattering particle size	
	analyzer. Data courtesy of Aleksandra Djuric, Materials Engineer-	
	ing Laboratory, Rm 2410, M.H. Wong Building, McGill University 9	95
6.1	Drop diameter moments from sound wave attenuation, and effective	
	drop diameter \hat{d} from the theoretical fits of Eqns. (6.4)–(6.6) to measure data and a will be larger and a will be in the control of the	
	sured dynamic mobility (with SDS material balance and equilibrium isotherm). Aqueous phase SDS concentration $c_{\infty,0}/(1-\phi) = 5$ mM. 10)6
6.2	Drop size moments from sound wave attenuation, and effective drop	
	diameter \hat{d} from the theoretical fits of Eqns. (6.4)–(6.6) to measured	
	dynamic mobility data with SDS material balance and equilibrium isotherm). Bulk aqueous-phase SDS concentration $c_{\infty}^* (\equiv c_{\infty,0}/(1-$	
	ϕ) = 13 mM. Note that $(-\zeta e/kT) = (-\zeta e/kT)_{\beta=0}$	10
7.1	Nanoemulsion-doped polyacrylamide hydrogel compositions and steady-	
	state storage moduli G' , as furnished by Eqn. (7.1) from bulk rheology, 12	

List of Tables xxiii

7.2	Parameters for the fluid-sphere model of Hill and Afuwape (2020)	
	with a complex shear viscosity $\eta^*(\omega)$ (see Eqn. (7.2)). Data and	
	the model are plotted in figure 7.7. The accompanying aqueous	
	phase SDS concentration c_{∞} and ζ -potential, are furnished by the	
	isotherm and SDS material balance	. 127
7.3	Sound-wave-attenuation diameters for nanoemulsions $(c_{AAm} = 0)$	
	and nanoemulsion-hydrogels at varying monomer concentrations	. 133
8.1	Model parameters according to fits of Eqn. (8.2) to swelling time series for initially as-prepared (top) and dried (bottom) nanoemulsion-	
	hydrogel composites (figure 8.3). The mesh size $\xi = (k_B T/G_{\infty}')^{1/3}$,	
	and the characteristic length L calculated for dried samples from	
	their mass, accounting for the change in oil volume fraction, e.g.,	
	$L_d^3 = m_d/[\phi_d\rho_o + (1-\phi_d)\rho_w].$. 144

Abbreviations

SEKM Standard ElectroKinetic Model

CMC Critical Micelle Concentration

SDS Sodium Dodecyl Sulfate

In memory of the late Adekunle Afuwape and late Dr. Adekunle Alebiosu

Chapter 1

Introduction

1.1 Motivation

The practical uses of nanoemulsions are limited because of Ostwald ripening, amongst other thermodynamic limitations, like coalescence and contact ripening (Helgeson, 2016). However, the incorporation of lipophilic entities in food (Xianquan et al., 2005, McClements and Rao, 2011), pharmaceutical (Rehman et al., 2014) and biomedical materials (Jaiswal et al., 2014, Hashemnejad et al., 2019) necessitates ongoing research into techniques for overcoming these challenges. Recently, success has been achieved by encapsulating oil droplets in polymer networks to form nanoemulsion-hydrogels, with materials tailored for specific applications (Hashemnejad et al., 2019, Gupta et al., 2016, Gutièrrez et al., 2008, Jaiswal et al., 2014, An et al., 2012, Shao et al., 2016, Delmas et al., 2011).

Despite a surge in developing nanoemulsion-hydrogel composites, basic understanding of (i) the colloidal behaviour of nanoemulsions (ii) nanodroplet-hydrogel interactions, (iii) composite uniqueness in comparison with nanoparticle-hydrogels, and (iv) effective property changes during encapsulation (pre-gel to sol-gel transition) are lacking. Here, the goal is to understand the dynamics of surfactant stabilized oil-droplets in aqueous salt solutions, and polymer networks, and offer theoretical interpretations of observed dynamics over wide parameter space. Electroacoustic and dielectric relaxation spectroscopies are used as non-invasive techniques to probe the composite dynamics. These techniques maintain the unique

advantage of being applicable to both opaque and transparent samples. Rheological analysis and swelling experiments are used to study contributions of oil droplets to hydrogel microstructure and macroscopic properties.

1.2 Thesis objectives

This work seeks to build foundational understanding of SDS-stabilized oil droplet dynamics in aqueous solutions and polymers, which is integral in developing nanoemulsion-hydrogels for specific applications. These composites are generating interest as advanced nano-materials for use in the controlled and localized delivery of lipophilic molecules. The objectives pursued in the following chapters include:

- To probe the colloidal dynamics of polystyrene beads, account for the contribution of added counter-ions and non-specific adsorption to suspension conductivity, and offer insights to the potential causes for disparity between the electro-kinetic and titratable charges.
- To elucidate colloidal dynamics of highly charged micelles using standard electrokinetic models, and obtain insights on the "perceived" degree of ionization.
- To unify interfacial thermodynamics and electro-kinetics for the study of oil-in water-emulsions in a bid to improve theoretical interpretation.
- Experimentally test the theory of Hill and Afuwape (2020) to interpret the electroacoustic spectra of SDS-stabilized hexadecane-in-water nanoemulsions in a bid to advance present electrokinetic models.
- Experimentally test the theory by Hill and Afuwape (2020) modified as proposed by Wang and Hill (2009) to interpret the dynamics of oil droplets embedded in uncharged viscoelastic networks, and ascertain how polymers affect droplet mobility.
- To ascertain the extent to which hydrogel bulk properties change with the presence of oil droplets in the heterogeneous structure.

1.3 Thesis organization

A review of the literature on nanoemulsions, hydrogels and nanoemulsion-hydrogels is provided in Chapter 2. Background theories for interpreting experimental techniques (electroacoustic, dielectric relaxation spectroscopies), and descriptions of the experimental methods are also included.

Chapters 3–8 are manuscripts to be submitted to peer-reviewed journals. Additional materials on the detailed experimental protocols, and data analysis are provided as appendices. Chapters 3 and 4 present studies of the electrokinetic responses of SDS and polystyrene latex beads solutions. The potential contribution of added counter-ions and their non-specific adsorption are highlighted. Chapters 5 and 6 address the dynamics of surfactant-stabilized-oil-in-water nanoemulsions. The possibility of highly charged surfaces was explored, and tested using electroacoustic and dielectric-relaxation spectroscopies. In Chapter 7, an electroacoustic study of nanoemulsion-hydrogel composites is undertaken. Oil droplets were encapsulated in uncharged polymer networks, and composite properties were probed to ascertain how oil inclusions modify properties of viscoelastic networks. Chapter 8 documents a physical study of nanoemulsion-hydrogels. Bulk rheology, confocal microscopy, thermogravimetric analysis and swelling experiments were used to investigate the composites, and ascertain how oil inclusions affect hydrogels. A summary of the findings, limitations, and original contributions to knowledge are provided in Chapter 9.

Bibliography

- H. Z. An, M. E. Helgeson, and P. S. Doyle. Nanoemulsion composite microgels for orthogonal encapsulation and release. *Adv. Mater.*, 24(28, SI):3838–3844, 2012.
- T. Delmas, H. Piraux, A. Couffin, I. Texier, F. Vinet, P. Poulin, M. Cates, and J. Bibette. How to prepare and stabilize very small nanoemulsions. *Langmuir*, 27(5):1683–1692, 2011.
- A. Gupta, H. B. Eral, T. A. Hatton, and P. S. Doyle. Nanoemulsions: formation, properties and applications. *Soft Matter*, 12:2826–2841, 2016.

- J. Gutièrrez, C. Gonzélez, A. Maestro, I. Solé, C. Pey, and J. Nolla. Nano-emulsions: New applications and optimization of their preparation. *Curr. Opin. Colloid Interface Sci.*, 13(4):245–251, 2008.
- S. M. Hashemnejad, A. Z. M. Badruddoza, B. Zarket, C. Ricardo Castaneda, and P. S. Doyle. Thermoresponsive nanoemulsion-based gel synthesized through a low-energy process. *Nat. Commun.*, 10(1):2749, 2019.
- M. E. Helgeson. Colloidal behavior of nanoemulsions: Interactions, structure, and rheology. Curr. Opin. Colloid Interface Sci., 25:39 50, 2016.
- R. J. Hill and G. A. Afuwape. Dynamic mobility of surfactant stabilized nanodroplets: unifying equilibrium thermodynamics, electro-kinetics and Marangoni effects. *J. Fluid Mech.*, 895(A14), 2020.
- M. Jaiswal, R. Dudhe, and P. K. Sharma. Nanoemulsion: an advanced mode of drug delivery system. *Biotech.*, 5(2):123–127, 2014.
- D. J. McClements and J. Rao. Food-grade nanoemulsions: formulation, fabrication, properties, performance, biological fate, and potential toxicity. *Crit. Rev. Food Sci. Nutr.*, 51(4):285–330, 2011.
- K. Rehman, M. Amin, and M. Zulfakar. Development and physical characterization of polymer-fish oil bigel (hydrogel/oleogel) system as a transdermal drug delivery vehicle. *J. Oleo Sci.*, 63(10):961–970, 2014.
- M. Shao, Z. Hussain, H. E. Thu, S. Khan, H. Katas, T. A. Ahmed, M. Tripathy, J. Leng, H.-L. Qin, and S. N. A. Bukhari. Drug nanocarrier, the future of atopic diseases: Advanced drug delivery systems and smart management of disease. Colloid Surf. B, 147:475–491, 2016.
- M. Wang and R. J. Hill. Dynamic electric-field-induced response of charged spherical colloids in uncharged hydrogels. *J. Fluid Mech.*, 640:357–400, 2009.
- S. Xianquan, J. Shi, Y. Kakuda, and J. Yueming. Stability of lycopene during food processing and storage. *J. Med. Food*, 8(4):413–422, 2005.

Chapter 2

Literature Review

2.1 Nanocomposites

Technological advancements in engineering have brought to focus the use of nanomaterials for practical applications in various fields, such as food (Kim et al., 2001, Sala et al., 2007, Chojnicka et al., 2009, Lei et al., 2017), cosmetics (Gilbert et al., 2013, Lupi et al., 2015), biomedicine (Mitragotri et al., 2015, Sharma et al., 2015, Yang et al., 2015) etc. Nanomaterials are of special interest because they exhibit unique nanoscale properties (e.g., optical, magnetic, electrical, etc.), which are distinctly different from their bulk counterparts. These materials are described to possess a characteristic dimension in the range 1–100 nm (Commission, 2012), but the exact size range can differ with materials, and a characteristic dimension may not result in nanoscale properties (Nature, 2019). Examples of nanomaterials are nanoparticles, nanoemulsions, nanotubes, dendrimers, quantum dots, fullerenes etc. (Hamidi et al., 2008, Katime et al., 2012, Dannert et al., 2019).

Despite wide interests in nanomaterials and their remarkable properties, the nanoscale size is difficult to maintain in most applications. Aggregation, flocculation, and Ostwald ripening are some of the processes that limit nanomaterial use. The incorporation of nanomaterials into hydrogels has been proposed to overcome these disadvantages for some applications (Alexander, 2001, Hamidi et al., 2008). Hydrogels made from natural (e.g., DNA, chitosan, alginate, etc.), and synthetic (e.g. PEG, hyaluronic acid, etc.) can be used as carriers for nanoparticles, biomolecules, and drugs in cancer treatment (Ta et al., 2008, Chao et al., 2020), bone reconstruction (Wang et al., 2017, Chung et al., 2007), and other related drug-delivery

applications (Wei et al., 2009, An et al., 2012, Thoniyot et al., 2015, Shao et al., 2016). For nanoparticles, the polymer network limits particle aggregation by providing steric repulsion, and inhibits the degradation of their encapsulated content (Dannert et al., 2019). Composite contents can be delivered to target sites using stimuli responsive polymers (SRPs), e.g., the swelling of composites have been used as a release pathway (Barbucci, 2010), while structural collapse due to hydrolyzed bonds in their target environment has been exploited for controlled delivery (Nazli et al., 2014).

2.1.1 Nanoemulsions

Nanoemulsions are two-phase systems in which a dispersed phase (typically droplets with characteristic sizes between 20–500 nm) coexists with a continuous phase, in the presence of surface-active agents, to provide stability (Tadros et al., 2004, Solans et al., 2005, Leong et al., 2009, Gupta et al., 2016). Nanoemulsions were initially developed to aid the production of latex nanoparticles via the miniemulsion polymerization method where monomer (e.g., styrene) is dispersed in aqueous surfactant solutions(e.g., SDS) above the critical micelle concentration, with hydrocarbon oil or alcohol (e.g., hexadecane) added as a co-stabilizer, and the mixture subjected to high-energy emulsification, preceded by high temperature polymerization, and subsequent sonication to break up the gel (Asua, 2002).

Nanoemulsions, also referred to as mini-emulsions, are kinetically stable systems for which stability can be achieved at low surfactant concentrations, unlike their microemulsion counterparts that are thermodynamically stable (Tadros et al., 2004, Bouchemal et al., 2004). Most emulsions are either oil-in-water, water-in-oil or bicontinuous. The ability of oil-in-water nanoemulsions to transport hydrophobic substances through a continuous aqueous phase makes them beneficial for topical applications. The nanosize provides high surface area, and facilitates greater absorption and bioavailability for drug-delivery applications (Jaiswal et al., 2014, Shao et al., 2016). For example, nanoemulsions have been used to solubilize and protect lipophilic drugs from hydrolysis and oxidation, while emulsion-hydrogel composites (with the oil phase as hydrocarbons) have demonstrated high stability: retaining the oil phase for months. The composite properties depend on the composition and method of preparation (Solans et al., 2005, Gutièrrez et al., 2008).

Nanoemulsions are prepared either by high- or low-energy methods. High-energy methods make use of devices capable of supplying mechanical energy to break up macroscopic oil phases, which are simultaneously stabilized by surfactants. These are high-cost processes, but the benefits of such a controlled approach have found use in food, pharmaceuticals and agricultural industries. Examples of high-energy methods are sonication, homogenization, microfluidization *etc.* Low-energy methods require minimal to no energy input. These methods exploit thermodynamics to induce a phase change, *e.g.*, spontaneous emulsification, phase-inversion emulsification, *etc.* (Abismal et al., 1999, Delmas et al., 2011, Gupta et al., 2016).

In the last decade, different researchers have studied and claimed the great potential for nanoemulsions in numerous applications, but very few direct applications have been realized. A major limitation for the application of nanoemulsions is the stability. Emulsifiers can act as stabilizers, but the nanoscale size of the dispersed droplets makes them susceptible to Ostwald ripening (Lifshitz, 1961, Taylor, 1995). The droplet small size favours solubility; thus they preferentially dissolve to form larger droplets over time. It is necessary to maintain stability for drug delivery or transdermal applications, until the target action is required. Hydrogels have been proposed as dependable support systems for such applications (Bouchemal et al., 2004, Komarova et al., 2013).

2.1.2 Hydrogels

Hydrogels are polymeric networks with nano- and micro-pores that are capable of imbibing large amounts of fluid. They are often hydrated networks capable of conformational change, and possessing physical properties similar to living tissues (Hamidi et al., 2008). Hydrogels are made from synthetic materials such as polyethylene-oxide (PEO), polyvinyl-alcohol(PVA), polyacrylamide, polyacrylic acid etc., or naturally derived materials, e.g., agarose, alginate, chitosan, collagen etc. (Barbucci, 2010). The presence of chemical or physical crosslinks (tie-points, junctions and entanglements) preserves their physical integrity and ensures their insolubility in aqueous phases (Peppas et al., 2000).

Hydrogels have extensive use as stimulus responsive polymers (SRPs) due to

network interconnectivity, which aids their potential use as free-standing materials or thin films on a support. This is because the network integrity is preserved by crosslinks, and provides flexibility to ensure visible changes to peculiar stimuli (Tjong et al., 2012). For example, polymeric water-saturated networks with molecular-scale porosity are used in molecular separation with poly(N-isopropylacrylamide-co-butylmethacrylate) used to design a thermosensitive molecular membrane for size separation of organic compounds (Feil et al., 1991); aramid-nanofibre-hydrogel composite membranes have been used to achieve high solvent recovery of methane, acetone and formaldehyde (Li et al., 2019); pluronics polymers have served as carriers of bioactive molecules in drug delivery applications due to their ability to modulate release of active cargo (Hashemnejad et al., 2019). Other uses include scaffolds in tissue engineering, because of their ability to support cell proliferation and migration to permit oxygen and nutrient transport, while mimicking native extracellular matrix (Barbucci, 2010, Spicer, 2020); for wound dressing to keep the wound moist and supply bioactive ingredients (Pal et al., 2007, Koehler et al., 2018); and in the design of lab-on-chip devices that require molecular diffusive membranes or other controlled cellular microenvironments required in microfluidic applications (Chung et al., 2012, Annabi et al., 2013).

2.1.3 Nanoemulsion-hydrogels

The low viscosity and potential loss of stability due to Ostwald ripening of nanoemulsion present limitations for practical applications (Taylor, 1995, Jiao and Burgess, 2003, Mou et al., 2008). Embedding nano-droplets in hydrogels may yet be a creative way to overcome these limitations, and possibly develop a new class of advanced material feasible for use in cosmetics, pharmaceutical industries and food engineering. In pharmaceuticals, the need to encapsulate drugs in emulsions, coupled with the knowledge that hydrogels can provide mechanical support, and be used to induce release in target environment has made nanoemulsion-hydrogel composites an emerging class of biomaterials (Grazia-Cascone et al., 2002, Gulsen and Chauhan, 2005, Chen et al., 2007). Ongoing research into the discovery and design of stimuli responsive polymers necessitates the need to understand how a desired collapse or response of a polymer network can be exploited to release embedded nanodroplets, or transport lipophilic drugs (or active biological agents) in drug-delivery applications. The polymer network modulates the release of the

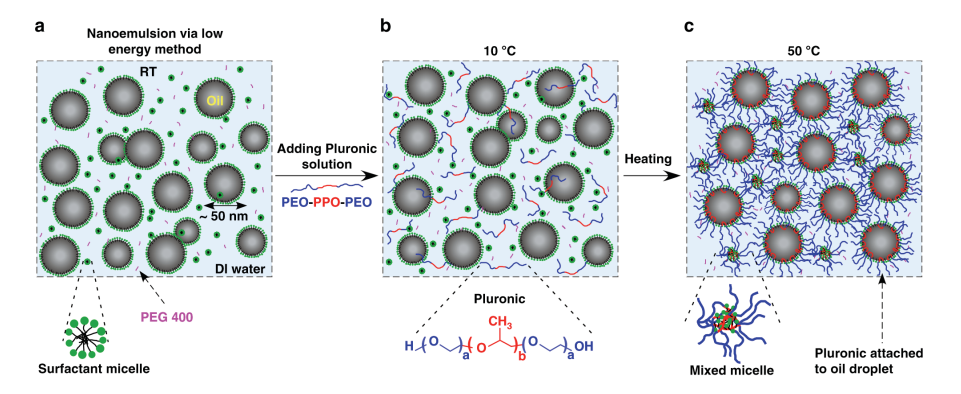


FIGURE 2.1: Nanoemulsion-hydrogel hypothesized temperature induced polymerization mechanism as hypothesized by Hashemnejad et al. (2019). Image used with publisher's permission.

nanodroplets by responding to a predefined environmental stimulus. For example, oil-filled hydrogels have been touted as the ideal material suited for encapsulating and transporting hydrophobic entities. They are formed by trapping oil phase in a continuous polymer matrix. The immiscibility of oil and aqueous phase is overcome by emulsifiers. Emulsifiers alter the droplet size distribution, and provide an opportunity to modify the composites to suit specific design objectives e.g., the controlled release of ibuprofen has been reported using thermoreponsive nanoemulsion-based hydrogels (Hashemnejad et al., 2019). The hypothesis that stimulus-induced collapse can be used for localized delivery was investigated by Komarova et al. (2013) on cryogels, with encouraging results for further studies and applications.

2.2 Electrokinetic phenomena and theories

Electrokinetic phenomena describe dynamics due to tangential fluid motion along a charged surface, e.g., electrophoresis, electro-osmosis, streaming, and sedimentation potentials, etc. These phenomena have been used in colloidal science to understand electrical double layers, electrostatic forces, colloidal aggregation, and stability, etc. (Delgado et al., 2007, Wall, 2010), and have been exploited for: DNA and protein separation (Electrophoresis) (Aaij and Borst, 1972, Johnson and Grossman, 1977), design of pumps capable of generating constant and pulse-free flows (Electro-osmosis) (Wang et al., 2009), characterization of particulate matter from natural waters (Beckett et al., 1992), etc.

The equilibrium electric double layer of a charged surface contains a spatial distribution of ions due to fixed charge bound to the surface, their counterions from the charging process, and oftentimes added ions from the bulk. The electrical double layer refers to the uncharged space between the surface and the closely packed counterions (Stern layer) and the region of ions beyond (diffuse layer), with elaborate models dividing the Stern layer into inner and outer Helmholtz layers (Lyklema, 1995). The surface charge density (or its potential) can be measured by applying tangential flow along a charged surface using an applied external electric field or mechanical force, and the potential at the plane of slip with respect to the bulk solution is referred to as the ζ -potential. Ambiguities exist as to exact location of this plane, as the boundary between the hydrodynamically mobile and immobile fluid is not distinct, hence, in practice, ζ -potential is often observed to be lower in magnitude than the surface potential ψ . Researchers have established that ζ -potential is attributed to the nature of a surface, the charge, and nature and concentration of electrolyte solution, but it is not a directly measurable property. It is often furnished by converting other measurable electrokinetic quantities (e.g., electrophoretic mobility, electrokinetic sonic amplitude, etc.) using developed standard electrokinetic theories (Hunter, 1962, 1981, Delgado et al., 2007).

2.2.1 Standard electrokinetic theories

Smoluchowski's theory was the pioneering attempt to relate electroosmotic slip velocity to ζ -potential, and it is valid for particles where the curvature radius largely exceeds the Debye length ($\kappa a \gg 1$), followed by Henry and Lapworth (1931) theory for arbitrary κa values to a lower limit ($\kappa a \ll 1$) provided the electrophoretic motion does not deform the double layer (Stigter and Mysels, 1955). Double-layer-relaxation effects where included in the Overbeek (1943) theory and simplification for symmetric electrolytes followed (Booth and Mott, 1950). For more comprehensive parameter space encountered in practical application, Wiersema et al. (1966) developed a numerical solution for systems with two ionic species, but solutions were lacking for systems with high ζ -potentials (O'Brien and White, 1978). Models for arbitrary values of κa and ζ -potentials were developed independently to predict the electrophoretic mobility (O'Brien and White, 1978) and electrical conductivity (Saville, 1979) of colloidal particles. These models have been adapted for interpreting dynamic mobility of colloidal particles (Zukoski and

Saville, 1985, Mangelsdorf and White, 1992, Ohshima, 1997), electrokinetics of soft particles (Ohshima, 2013), electrophoresis of fluid droplets (Baygents and Saville, 1991, Djerdjev et al., 2003b, Hill and Afuwape, 2020), dielectric responses of colloidal particles (O'brien, 1981, DeLacey and White, 1981, Dunstan and White, 1992, Mangelsdorf and White, 1997), electrokinetics of micelles (Dunstan and White, 1990), polymer-coated nanoparticles (Hill et al., 2003a,c,b), nanoparticle-doped hydrogels (Wang and Hill, 2009, Bhosale et al., 2011, Adibnia and Hill, 2014).

Model solutions are developed from equilibrium perturbations when a steady or oscillatory electric field is applied to a spherical colloidal particle (the assumption of infinite dilution) in an electrolyte solution. To obtain these model solutions, authors apply different boundary conditions, but the electrokinetic equations to be solved are often the same. The control volume at a given time t, is described to have an electrostatic potential $\psi(\mathbf{r},t)$, with the number densities $n_j(\mathbf{r},t)$ and drift velocities $\mathbf{v}_j(\mathbf{r},t)$ of each ionic species j=1,2...N, with the fluid velocity $\mathbf{u}(\mathbf{r},t)$ and pressure $p(\mathbf{r},t)$ of the medium at every point \mathbf{r} . These terms are related by Poisson, ion-conservation, fluid mass and momentum equations, and an equation for the sum of viscous, electrostatic and thermodynamic forces, which act on ions (DeLacey and White, 1981, Mangelsdorf and White, 1992):

$$\varepsilon_s \varepsilon_0 \nabla^2 \psi(\mathbf{r}) = -\rho(\mathbf{r}, t)$$
 (2.1)

with the charge density ρ defined as

$$\rho(\mathbf{r}) = \sum_{j=1}^{N} z_j e n_j(r, t), \qquad (2.2)$$

$$\nabla \cdot n_j \mathbf{v}_j = -\frac{\partial n_j}{\partial t} \quad (j = 1, 2 \dots N), \tag{2.3}$$

$$\nabla \cdot \mathbf{u}(\mathbf{r}) = 0, \tag{2.4}$$

$$\eta \nabla^2 \mathbf{u} - \nabla p = \rho \nabla \psi + \rho_s \frac{\partial \mathbf{u}}{\partial t}, \qquad (2.5)$$

$$-\lambda_j(\mathbf{v}_j - \mathbf{u}) - z_j e \nabla \psi - k_B T \nabla \ln n_j = 0, \qquad (2.6)$$

where $\varepsilon_s \varepsilon_0$, z, ρ_s and $\lambda_j = N_A e^2 |z_j|/\Lambda_j$, n_j , and \mathbf{v}_j are the dielectric permittivity of the solvent, ion valence, solvent density, drag coefficient, bulk ion number density and velocity of ionic species respectively with Λ_j the limiting ionic conductance.

These equations are the foundation for most electrokinetic theories, and have been extended to bare particles (DeLacey and White, 1981, O'Brien and White, 1978, Mangelsdorf and White, 1992), charged and neutral polymer coated particles (Hill et al., 2003a,b, Ohshima, 2013), and drops (considered as rigid particles (Booth, 1951).

Numerical solutions used in Chapters 3–5 are standard electrokinetic solutions from the MPEK package (Mobility and Polarizability of a spherical polymer-coated colloidal particle from solutions of the governing Electro-Kinetic transport equations), or its derivatives developed by Hill et al. (2003a,b,c). The far field solution yields real and imaginary parts of the polarizability, which can be related to experimentally measurable terms, such as conductivity and dielectric constant increments. The far-field decay of the perturbed electrostatic potential takes the form

$$\psi' \approx -\mathbf{E}' \cdot \mathbf{r}' + D'\mathbf{E}' \cdot \hat{\mathbf{r}}/r'^2 \text{ as } r' \to \infty ,$$
 (2.7)

with scaled electrostatic potential $\psi' = \psi e/k_B T$, radial distance $r' = \kappa r$, electric field strength $\mathbf{E}' = \mathbf{E}e/(\kappa k_B T)$ and polarizability $D' = D\kappa^3$. According to Hill et al. (2003c), the dimensionless polarizability is defined as $\mathscr{P} = D'/(\kappa a)^3$, where the conductivity increment becomes

$$\Delta \sigma = \frac{\sigma_e - 1}{\phi} = 3[\Re(\mathscr{P}) + \hat{\omega}\Im(\mathscr{P})] , \qquad (2.8)$$

and dielectric constant increment as

$$\Delta \varepsilon = \frac{\varepsilon_e - 1}{\phi} = 3[\Re(\mathscr{P}) - \hat{\omega}^{-1}\Im(\mathscr{P})]$$
 (2.9)

with $\hat{\omega} = \omega \varepsilon_s \varepsilon_0 / \sigma_\infty$, where σ_∞ is the background conductivity, $\varepsilon_s \varepsilon_0$ is the dielectric permittivity of the solvent, and ω is the angular frequency of the electric field, σ_e and ε_e are the effective conductivity and dielectric constant scaled with σ_∞ and ε_s , respectively (Hill et al., 2003a,b,c).

The (dimensionless) dynamic mobility can be obtained from a force balance on a particle under oscillatory electric field, giving

$$\frac{V}{E} = \frac{3C^E}{3C^U - (\kappa a)^3 (\rho_p/\rho - 1)},\tag{2.10}$$

where C^U and C^E are scalar coefficients obtained by solving the ordinary differential equations when the particle is fixed at origin (V=0) and (i) a fluid velocity \mathbf{U} is prescribed at $r'=\infty$ in the absence of an electric field, and (ii) an electric field \mathbf{E} is applied in the absence of a far-field flow.

2.3 Experimental methods

2.3.1 Electroacoustic spectroscopy

2.3.1.1 Theory of electroacoustics

Sound propagation through aqueous electrolytes generates an alternating electric field, because the fluctuating pressure induces ion motion. The resulting change in electric potential is known as the ultrasonic vibration potential (Debye, 1933). A similar relationship has been observed for colloids. An alternating electric field applied across a colloidal suspension produces sound pressure per unit applied field, otherwise known as the Electrokinetic Sonic Amplitude (ESA). These electroacoustic effects can be related to electrokinetic phenomena in colloidal suspensions (O'Brien, 1988, O'Brien et al., 1995, Hunter and O'Brien, 1997).

Commercial instruments such as the Colloidal Dynamics AcoustoSizer (frequency range 0.3–11 MHz) and AcoustoSizer II (frequency range 1–18 MHz) are used to measure the ESA. The high frequencies achievable by these instruments enable simultaneous measurement of particle size and zeta potential. The lower frequency measurement can be used to approximate the DC electrophoretic mobility often measured using electrophoretic light scattering technique (Hunter, 2004).

The ESA is proportional to the complex dynamic mobility (μ_d) of the particles, from which particle properties such as size and ζ -potential, are furnished. The relationship

$$ESA = A(\omega)\phi \frac{\rho_p - \rho}{\rho} \mu_d \left(\frac{Z_s Z_r}{Z_s + Z_r} \right)$$
 (2.11)

is valid for dilute colloidal dispersions, with $A(\omega)$ a complex-valued instrument factor, Z_s and Z_r are the acoustic impedances of the glass rod and suspension, ϕ is the volume fraction, ρ_p , and ρ are the density of the dispersed and bulk phase, respectively. The complex-valued dynamic mobility with thin double layer

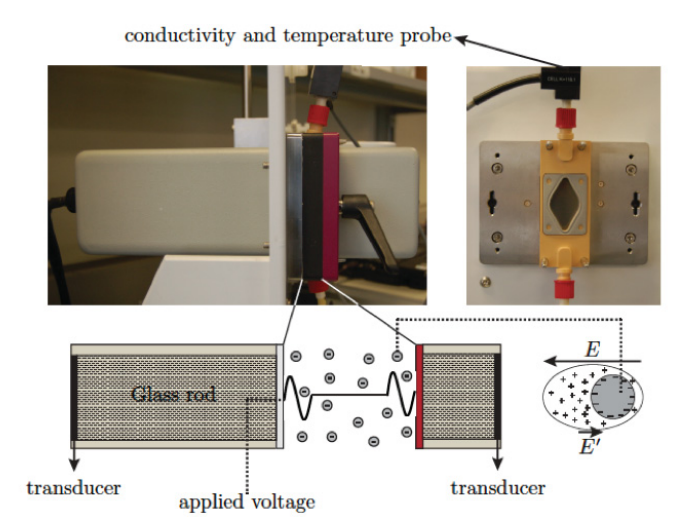


FIGURE 2.2: ESA cell of the AcoustoSizer II. The schematic shows negatively charged particles between the electrodes, and counterion distribution around each particle with the applied electric field E and the internal electric field in the double layer E' (Adibnia, 2015).

approximation $(\kappa a \gg 1)$ is

$$\mu_d = \frac{2\epsilon \zeta}{3\eta} G(\omega a^2 / \nu) [1 + f(\lambda, \omega')], \qquad (2.12)$$

where $G(\omega a^2/\nu)$ is a complex inertia factor that depends on particle size, and $1 + f(\lambda, \omega')$ relates to the tangential electric field at the particle surface. The Dukhin number $\lambda = K_s/(K_\infty a)$ relates the surface conductance behind the double layer to the bulk conductivity of the suspension. The surface conductivity contributions are due to diffuse-layer charges outside the shear plane, and the charges in the stagnant layer. Most theories do not account for the stagnant-layer conduction due to immobile absorbed charge species, hence not used in calculating the Dukhin parameter (O'Brien et al., 1995, Hunter and O'Brien, 1997, Djerdjev et al., 2003a). For a two-species symmetric electrolyte, with tangential current carried by ions above the shear plane,

$$\lambda = \frac{2}{\kappa a} \left[\cosh \left(\frac{ze\zeta}{2kT} - 1 \right) \right] \left[1 + \frac{2\epsilon(kT)^2}{z^2 \eta De^2} \right], \tag{2.13}$$

where κa is the ratio of particle radius to double layer thickness, z is the coion valence, and D is the ion diffusivity (Bikerman, 1940). Additional surface

conductivity to account for the immobile surface conductance (K^i) is

$$\lambda = \lambda^i + \lambda^d = \frac{K^i}{K_{\infty}a} + \frac{K^d}{K_{\infty}a},\tag{2.14}$$

where K_{∞} is the bulk conductivity, K^d is the diffuse-layer conductance, and a is the particle radius. A reported advantage of electroacoustics over DC electrophoretic mobility for obtaining electrokinetic parameters is the ability to resolve the two-roots ζ -potential problem encountered with highly charged colloidal systems such as nanoemulsions (Hunter, 2004).

2.3.1.2 Methodology

The ESA is a conductivity dependent function. A standard conductivity solution is pumped through the ESA cell to estimate the cell constant. Pre-calibration to obtain the instrument calibration factor is performed with an electrolyte solution capable of producing a strong ESA signal. The Acoustosizer II uses a solution of potassium α -dodecatungstosilicate (KSiW). The instrument calibration is expressed

$$\frac{ESA}{S_a - S_e} = B\gamma = B\sum_{j} \phi_j(\Delta \rho_j/\rho)M_j, \qquad (2.15)$$

where B is the calibration constant. The parameters S_a and S_e are the Fourier transforms of the reference sound wave of air and electrolyte in the cell, respectively. $\gamma = -3.02 \times 10^{-9} K_{\infty}$ for KSiW solutions (O'Brien et al., 1995). Detailed experimental protocols are outlined in Appendix B. Results obtained are processed in the software using Eqn. (2.11) to obtain the dynamic mobility. Acoustic attenuation is available for obtaining the particle-size distribution for samples with $\Delta \rho \leq 0.5 \text{ g cm}^{-3}$ (hexadecane-water $\sim 0.23 \text{ g cm}^{-3}$).

2.3.2 Dielectric relaxation spectroscopy (DRS)

2.3.2.1 Theory

Dielectric relaxation spectroscopy is a versatile and non-invasive technique for probing the structural, electrical, and other dynamic properties of heterogeneous materials. Dielectric dispersions exist as γ -, δ - and α - dispersions. The γ -dispersions reflect the frequency dependence of background solutions on a molecular level, and

are related to the polar nature of the molecules. They manifest in the gigahertz to tetrahertz range; thus, these are not considered in electrokinetic studies. The δ -dispersions are direct consequences of the Maxwell-Wagner-O'Konski (MWO) relaxation (*i.e.*, build up and depletion of charged species). These dispersions capture the frequency dependence of the charge dipoles, despite the frequency independent properties of the particle and electrolyte. The α -dispersions are attributed to the background electrolyte asymmetry, and manifest as a large increase in dielectric permittivity at low frequencies (Grosse and Delgado, 2010, Bordi et al., 2004).

Quantities such as particle size, shape, aggregation tendency, equilibrium surface potential, charges and ion diffusion coefficients are implicit in the frequency spectra obtained from an applied electric field. The frequency dependent conductivity and permittivity spectra also reflect double-layer ionic processes if interpreted with the relevant theories (Asami, 2002, DeLacey and White, 1981, Hollingsworth and Saville, 2004).

Pioneering studies for relating experimentally measured conductivity, dielectric spectra to the dipole strength of colloidal particles in aqueous solutions was undertaken by DeLacey and White (1981). The far-field solutions of the perturbed electrostatic potential of a colloidal particle were expressed in the form of the complex-valued dipole coefficients. The dipole strength furnishes the extent of charge polarization around colloidal particles, which is related to the experimentally measured complex conductivity of a colloidal suspension. The dipole coefficient for a particle in an aqueous electrolyte solution can be calculated, but an approximate formula valid at megahertz frequencies is

$$C_0 = \frac{i\omega\varepsilon_s\varepsilon_0 - i\omega\varepsilon_p\varepsilon_0 + 2K_s/a - K_\infty}{-2i\omega\varepsilon_s\varepsilon_0 - i\omega\varepsilon_p\varepsilon_0 + 2K_s/a + 2K_\infty},$$
(2.16)

where K_s , K_{∞} , $\varepsilon_0 \varepsilon_s$, $\varepsilon_0 \varepsilon_p$, a, and ω are the surface conductivity, bulk conductivity, solvent and particle permittivity, particle radius, and frequency, respectively (O'Brien, 1988). The effective dielectric constant increment can be expressed as (DeLacey and White, 1981)

$$\Delta \varepsilon'(\omega) = \frac{3\varepsilon_0}{a^3} \left[C_0'(\omega) - \frac{K^{\infty}}{\omega \varepsilon_0} C_0'' \right], \tag{2.17}$$

and the effective conductivity increment as

$$\Delta K_e(\omega) = \Delta K(\omega) + \omega \Delta \varepsilon''(\omega) = \frac{3\varepsilon_0}{a^3} \left[K^{\infty} C_0'(\omega) + \omega \varepsilon_0 C_0'' \right]. \tag{2.18}$$

Experimental studies in this thesis were undertaken using a Keysight Impedance analyzer (frequency range 20 Hz–10 MHz) following the model of Hollingsworth and Saville (2003), and corrections for electrode polarization are achieved using the single-spacer technique by Beltramo and Furst (2012a). The total admittance of a colloidal suspension is expressed as

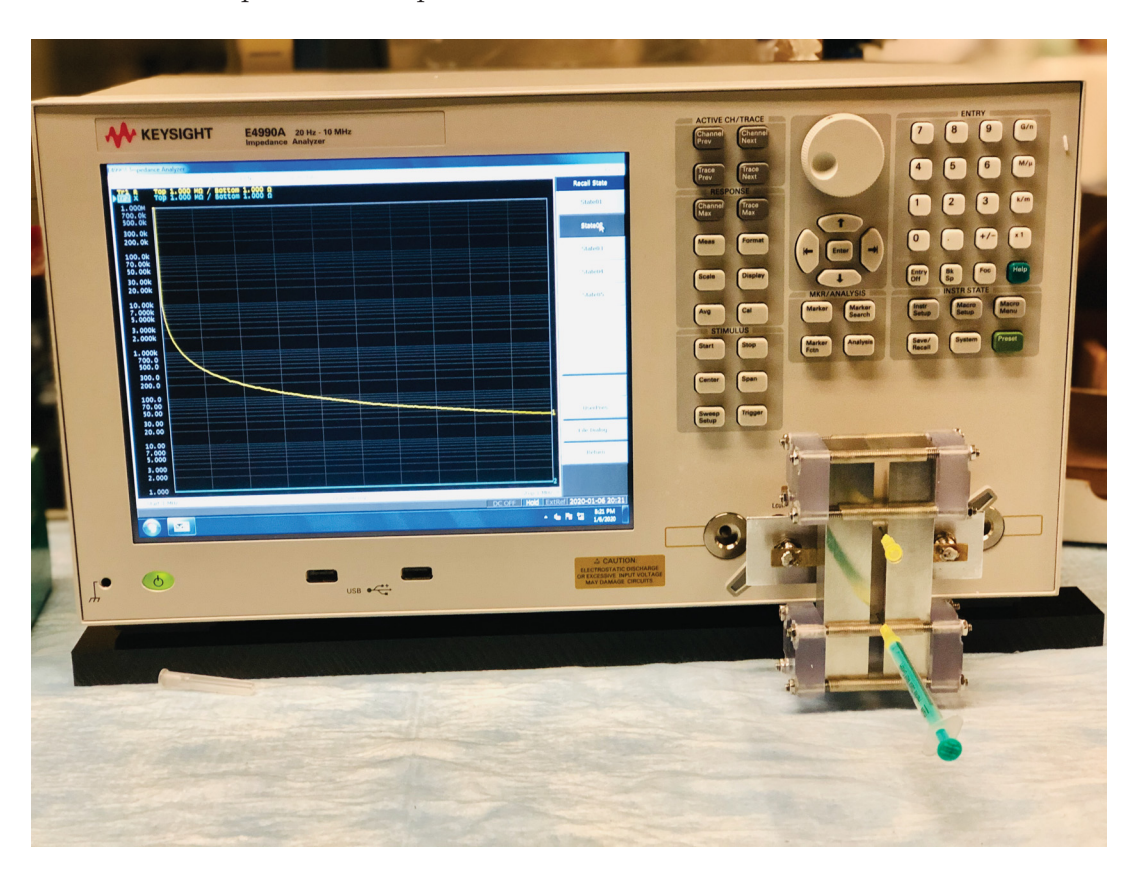


FIGURE 2.3: A setup for a dielectric relaxation experiment using the Keysight E4990A Impedance analyzer.

$$Y^*(\omega) = \frac{A}{2h} \left[\sigma(\omega) + i\omega \varepsilon_0 \varepsilon'_{app}(\omega) \right], \tag{2.19}$$

where the complex conductivity $\sigma(\omega)$ ($\equiv \sigma_{\infty} - \omega \varepsilon_0 \varepsilon''(\omega)$), ε'_{app} is the apparent dielectric constant, σ_{∞} background electrolyte conductivity, ε'' the dielectric loss, ε_{∞} the dielectric constant of the background electrolyte, and A/2h is the cell constant (A is the electrode area and 2h is the spacer gap). A limitation of dielectric

relaxation experiments is the presence of electrode polarization effects, which occur at low frequencies ($f \sim 1$ MHz depending on the ionic strength of background electrolyte). A theoretical approach for correcting electrode polarization was developed by Hollingsworth and Saville (2003). They expressed the admittance of a colloidal suspension as a function of the sample conductivity and dielectric permittivity:

$$Y^*(\omega) = \frac{A}{2h} \left[\sigma_{\infty} \frac{\beta^2 (\omega/\kappa^2 D)^2}{1 + \beta^2 (\omega/\kappa^2 D)^2} + i\omega \varepsilon_0 \varepsilon_{\infty} \beta \frac{1 + \beta(\omega/\kappa^2 D)^2}{1 + \beta^2 (\omega/\kappa^2 D)^2} \right], \tag{2.20}$$

where $\beta = \kappa h$ with κ^{-1} the Debye length and h the spacer half thickness. In the low frequency range, and large electrode separation, $\beta^2(\omega/(\kappa^2 D))^2 \gg 1$,

$$\frac{\varepsilon_{app}'}{\varepsilon_{\infty}} \approx 1 + \frac{\kappa^4 D^2}{\kappa h \omega^2} \tag{2.21}$$

$$\frac{\sigma'_{app}}{\sigma_{\infty}} \approx 1 - \frac{\kappa^4 D^2}{\kappa^2 h^2 \omega^2} \tag{2.22}$$

The single spacer technique of Beltramo and Furst (2012a) estimates value of D from the fit of the imaginary part background electrolyte's dielectric spectra to Eqn. (2.20), and corrected dielectric constant spectrum is calculated from

$$\varepsilon'(\omega) = \frac{\varepsilon'_{app}(\omega)}{1 + \frac{\kappa^3 D^2}{\omega^2 h}}.$$
 (2.23)

After correcting for electrode polarization, conductivity and permittivity increments of a colloidal suspension are obtained from the spectra as

$$\Delta\sigma(\omega) = \frac{\sigma(\omega)/\sigma_{\infty} - 1}{\phi} \tag{2.24}$$

and

$$\Delta \varepsilon'(\omega) = \frac{\varepsilon'(\omega)/\varepsilon_{\infty} - 1}{\phi} \tag{2.25}$$

2.3.2.2 Methodology

Samples are loaded between electrodes with an acrylic spacer using a syringe, as shown in figure 2.3. Electrical residuals in the test fixture are measured to account for systematic errors. Open-compensation measurements are performed by placing an acrylic spacer between both electrodes to account for stray admittances, and

short compensation measurements account for the residual impedance by placing electrodes in direct contact. Open and short measurements are used to compensate for errors in sample-impedance data using Eqn. (2.26). The sample impedance Z^* is converted to conductivity and dielectric permittivity with Eqn. (2.19). Note that

$$Z^* = \frac{Z_m - Z_s}{1 - (Z_m - Z_s)Y_o},\tag{2.26}$$

where Z_m is the measured impedance, Z_s is the residual impedance, and Y_o is the stray admittance (Beltramo and Furst, 2012b, Hollingsworth and Saville, 2003).

Bibliography

- C. Aaij and P. Borst. The gel electrophoresis of dna. *Biochim. Biophys. Acta, Nucleic Acids Protein Synth.*, 269(2):192 200, 1972.
- B. Abismal, J. Canselier, A. Wilhelm, H. Delmas, and C. Gourdon. Emulsification by ultrasound: drop size distribution and stability. *Ultrason. Sonochem.*, 6(1–2): 75–83, 1999.
- V. Adibnia. Electroacoustic and rheological characterization of hydrogel nanocomposites. PhD thesis, McGill University, 2015.
- V. Adibnia and R. J. Hill. Electroacoustic spectroscopy of nanoparticle-doped hydrogels. *Macromolecules*, 47(22):8064–8071, 2014.
- C. Alexander. Synthetic polymer systems in drug delivery. Expert Opin. Emerg. Drugs, 6(2):345–363, 2001.
- H. Z. An, M. E. Helgeson, and P. S. Doyle. Nanoemulsion composite microgels for orthogonal encapsulation and release. *Adv. Mater.*, 24(28, SI):3838–3844, 2012.
- N. Annabi, S. Selimović, J. P. Acevedo Cox, J. Ribas, M. Afshar Bakooshli, D. Heintze, A. S. Weiss, D. Cropek, A. Khademhosseini, and A. Khademhosseini. Hydrogel-coated microfluidic channels for cardiomyocyte culture. *Lab Chip*, 13(18):3569—3577, 2013.
- K. Asami. Characterization of heterogeneous systems by dielectric spectroscopy. *Prog. Polym. Sci.*, 27(8):1617–1659, 2002.

- J. M. Asua. Miniemulsion polymerization. *Prog. Polym. Sci.*, 27(7):1283 1346, 2002.
- R. Barbucci. *Hydrogels: Biological properties and applications*. Springer Science & Business Media, 2010.
- J. C. Baygents and D. A. Saville. Electrophoresis of drops and bubbles. *J. Chem. Soc.*, Faraday Trans., 87:1883–1898, 1991.
- R. Beckett, G. Nicholson, D. M. Hotchin, and B. T. Hart. The use of sedimentation field-flow fractionation to study suspended particulate matter. *Hydrobiologia*, 235(1):697–710, 1992.
- P. Beltramo and E. Furst. A simple, single-measurement methodology to account for electrode polarization in the dielectric spectra of colloidal dispersions. *Chem. Lett.*, 41(10):1116–1118, 2012a.
- P. J. Beltramo and E. M. Furst. Transition from dilute to concentrated electrokinetic behavior in the dielectric spectra of a colloidal suspension. *Langmuir*, 28 (29):10703–10712, 2012b.
- P. Bhosale, J. Chun, and J. Berg. Electroacoustics of particles dispersed in polymer gel. *Langmuir*, 27(12):7376–7379, 2011.
- J. J. Bikerman. Electrokinetic equations and surface conductance. a survey of the diffuse double layer theory of colloidal solutions. *Trans. Faraday Soc.*, 35: 154–160, 1940.
- F. Booth. The cataphoresis of spherical fluid droplets in electrolytes. *J. Chem. Phys.*, 19(11):1331–1336, 1951.
- F. Booth and N. F. Mott. The cataphoresis of spherical, solid non-conducting particles in a symmetrical electrolyte. *Proc. R. Soc. London, Ser. A*, 203(1075): 514–533, 1950.
- F. Bordi, C. Cametti, and R. H. Colby. Dielectric spectroscopy and conductivity of polyelectrolyte solutions. *J. Phys.: Condens. Matter*, 16(49):R1423, 2004.
- K. Bouchemal, S. Briançon, E. Perrier, and H. Fessi. Nano-emulsion formulation using spontaneous emulsification: solvent, oil and surfactant optimisation. *Int.* J. Pharm., 280(1–2):241–251, 2004.

- Y. Chao, Q. Chen, and Z. Liu. Smart injectable hydrogels for cancer immunotherapy. *Adv. Funct. Mater.*, 30(2):1902785, 2020.
- H. Chen, D. Mou, D. Du, X. Chang, D. Zhu, J. Liu, H. Xu, and X. Yang. Hydrogel-thickened microemulsion for topical administration of drug molecule at an extremely low concentration. *Int. J. Pharm.*, 341(1–2):78–84, 2007.
- A. Chojnicka, G. Sala, C. G. de Kruif, and F. van de Velde. The interactions between oil droplets and gel matrix affect the lubrication properties of sheared emulsion-filled gels. *Food Hydrocoll.*, 23(3):1038–1046, 2009.
- B. G. Chung, K.-H. Lee, A. Khademhosseini, and S.-H. Lee. Microfluidic fabrication of microengineered hydrogels and their application in tissue engineering. *Lab Chip*, 12:45–59, 2012.
- Y.-I. Chung, K.-M. Ahn, S.-H. Jeon, S.-Y. Lee, J.-H. Lee, and G. Tae. Enhanced bone regeneration with bmp-2 loaded functional nanoparticle—hydrogel complex. J. Controlled Release, 121(1):91 – 99, 2007.
- E. Commission. Types and uses of nanomaterials, including safety aspects accompanying the communication from the commission to the european parliament, the council and the european economic and social committee on the second regulatory review on nanomaterials. Technical Report 572 Final, European Commission, 2012.
- C. Dannert, B. T. Stokke, and R. S. Dias. Nanoparticle-hydrogel composites: From molecular interactions to macroscopic behavior. *Polymers*, 11(2):275, 02 2019.
- P. Debye. A method for the determination of the mass of electrolytic ions. *J. Chem. Phys.*, 1(1):13–16, 1933.
- E. H. B. DeLacey and L. R. White. Dielectric response and conductivity of dilute suspensions of colloidal particles. *J. Chem. Soc.*, Faraday Trans. 2, 77:2007–2039, 1981.
- A. Delgado, F. González-Caballero, R. Hunter, L. Koopal, and J. Lyklema. Measurement and interpretation of electrokinetic phenomena. J. Colloid Interface Sci., 309(2):194 224, 2007.

- T. Delmas, H. Piraux, A. Couffin, I. Texier, F. Vinet, P. Poulin, M. Cates, and J. Bibette. How to prepare and stabilize very small nanoemulsions. *Langmuir*, 27(5):1683–1692, 2011.
- A. M. Djerdjev, J. K. Beattie, and R. J. Hunter. Stagnant layer conduction in surfactant-stabilized hexadecane emulsion systems measured by electroacoustics. *Aust. J. Chem.*, 56(10):1081–1089, 2003a.
- A. M. Djerdjev, J. K. Beattie, and R. J. Hunter. An electroacoustic and high-frequency dielectric response study of stagnant layer conduction in emulsion systems. *J. Colloid Interface Sci.*, 265(1):56–64, 2003b.
- D. E. Dunstan and L. R. White. An electrokinetic study of micellar solutions. *J. Colloid Interface Sci.*, 134(1):147 151, 1990.
- D. E. Dunstan and L. R. White. The dielectric response of dilute polystyrene latex dispersions. J. Colloid Interface Sci., 152(2):308 313, 1992.
- H. Feil, Y. H. Bae, J. Feijen, and S. W. Kim. Molecular separation by thermosensitive hydrogel membranes. *J. Membr. Sci.*, 64(3):283 294, 1991.
- L. Gilbert, C. Picard, G. Savary, and M. Grisel. Rheological and textural characterization of cosmetic emulsions containing natural and synthetic polymers: Relationships between both data. *Colloids Surf.*, A, 421:150–163, 2013.
- M. Grazia-Cascone, Z. Zhu, F. Borselli, and L. Lazzeri. Poly(vinyl alcohol) hydrogels as hydrophilic matrices for the release of lipophilic drugs loaded in plga nanoparticles. *J. Mater. Sci. Mater. Med.*, 13(1):29–32, 2002.
- C. Grosse and A. Delgado. Dielectric dispersion in aqueous colloidal systems. Curr. Opin. Colloid Interface Sci., 15(3):145 – 159, 2010.
- D. Gulsen and A. Chauhan. Dispersion of microemulsion drops in {HEMA} hydrogel: a potential ophthalmic drug delivery vehicle. *Int. J. Pharm.*, 292(1–2): 95–117, 2005.
- A. Gupta, H. B. Eral, T. A. Hatton, and P. S. Doyle. Nanoemulsions: formation, properties and applications. *Soft Matter*, 12:2826–2841, 2016.
- J. Gutièrrez, C. Gonzélez, A. Maestro, I. Solé, C. Pey, and J. Nolla. Nano-emulsions: New applications and optimization of their preparation. *Curr. Opin. Colloid Interface Sci.*, 13(4):245–251, 2008.

- M. Hamidi, A. Azadi, and P. Rafiei. Hydrogel nanoparticles in drug delivery. *Adv. Drug Deliv. Rev.*, 60(15):1638–1649, 2008.
- S. M. Hashemnejad, A. Z. M. Badruddoza, B. Zarket, C. Ricardo Castaneda, and P. S. Doyle. Thermoresponsive nanoemulsion-based gel synthesized through a low-energy process. *Nat. Commun.*, 10(1):2749, 2019.
- D. C. Henry and A. Lapworth. The cataphoresis of suspended particles. part i. *Proc. R. Soc. London, Ser. A*, 133(821):106–129, 1931.
- R. J. Hill and G. A. Afuwape. Dynamic mobility of surfactant stabilized nanodroplets: unifying equilibrium thermodynamics, electro-kinetics and Marangoni effects. *J. Fluid Mech.*, 895(A14), 2020.
- R. J. Hill, D. Saville, and W. Russel. Polarizability and complex conductivity of dilute suspensions of spherical colloidal particles with charged (polyelectrolyte) coatings. J. Colloid Interface Sci., 263(2):478 497, 2003a.
- R. J. Hill, D. Saville, and W. Russel. Electrophoresis of spherical polymer-coated colloidal particles. *J. Colloid Interface Sci.*, 258(1):56 74, 2003b.
- R. J. Hill, D. A. Saville, and W. B. Russel. High-frequency dielectric relaxation of spherical colloidal particles. *Phys. Chem. Chem. Phys.*, 5:911–915, 2003c.
- A. Hollingsworth and D. Saville. A broad frequency range dielectric spectrometer for colloidal suspensions: cell design, calibration, and validation. *J. Colloid Interface Sci.*, 257(1):65 – 76, 2003.
- A. D. Hollingsworth and D. A. Saville. Dielectric spectroscopy and electrophoretic mobility measurements interpreted with the standard electrokinetic model. *J. Colloid Interface Sci.*, 272(1):235 245, 2004.
- R. J. Hunter. The calculation of ζ -potential from mobility measurements. J. Phys. Chem., 66(7):1367–1368, 1962.
- R. J. Hunter. Zeta Potential in Colloid Science. Academic Press, 1981. ISBN 978-0-12-361961-7.
- R. J. Hunter. More reliable zeta potentials using electroacoustics. In *Surface and Colloid Science*, pages 1–10, Berlin, Heidelberg, 2004. Springer Berlin Heidelberg.

- R. J. Hunter and R. W. O'Brien. Electroacoustic characterization of colloids with unusual particle properties. *Colloids Surf.*, A, 126(2):123 128, 1997.
- M. Jaiswal, R. Dudhe, and P. K. Sharma. Nanoemulsion: an advanced mode of drug delivery system. *Biotech.*, 5(2):123–127, 2014.
- J. Jiao and D. J. Burgess. Ostwald ripening of water-in-hydrocarbon emulsions. J. Colloid Interface Sci., 264(2):509–516, 2003.
- P. H. Johnson and L. I. Grossman. Electrophoresis of dna in agarose gels. optimizing separations of conformational isomers of double- and single-stranded dnas. *Biochemistry*, 16(19):4217–4225, 1977.
- I. Katime, L. Guerrero, and E. Mendizabal. Size matters: Smart copolymeric nanohydrogels: Synthesis and applications. *Front. Biosci. Elite*, 4 E(4):1314–1334, 2012.
- K. Kim, J. Renkema, and T. Van Vliet. Rheological properties of soybean protein isolate gels containing emulsion droplets. *Food Hydrocoll.*, 15(3):295–302, 2001.
- J. Koehler, F. P. Brandl, and A. M. Goepferich. Hydrogel wound dressings for bioactive treatment of acute and chronic wounds. *Eur. Polym. J.*, 100:1 11, 2018.
- G. Komarova, S. Starodubtsev, V. Lozinsky, I. Nasimova, and A. Khokhlov. Intelligent gels and cryogels with embedded emulsions of various oils. *J. Appl. Polym. Sci.*, 127(4):2703 2709, 2013.
- L. Lei, Y. Zhang, L. He, S. Wu, B. Li, and Y. Li. Fabrication of nanoemulsion-filled alginate hydrogel to control the digestion behavior of hydrophobic nobiletin. LWT-Food Sci. Technol., 82:260–267, 2017.
- T. Leong, T. Wooster, S. Kentish, and M. Ashokkumar. Minimising oil droplet size using ultrasonic emulsification. *Ultrason. Sonochem.*, 16(6):721–727, 2009.
- Y. Li, E. Wong, A. Volodine, C. Van Haesendonck, K. Zhang, and B. Van der Bruggen. Nanofibrous hydrogel composite membranes with ultrafast transport performance for molecular separation in organic solvents. J. Mater. Chem. A, 7:19269–19279, 2019.
- I. Lifshitz. The kinetics of precipitation from supersaturated solid solutions. *J. Phys. Chem. Solids*, 19:35–50, 1961.

- F. Lupi, L. Gentile, D. Gabriele, S. Mazzulla, N. Baldino, and B. de Cindio. Olive oil and hyperthermal water bigels for cosmetic uses. J. Colloid Interface Sci., 459:70–78, 2015.
- J. Lyklema. Fundamentals of Interface and Colloid Science, volume 2. Elservier Academic press, 1995.
- C. S. Mangelsdorf and L. R. White. Electrophoretic mobility of a spherical colloidal particle in an oscillating electric field. J. Chem. Soc., Faraday Trans., 88:3567– 3581, 1992.
- S. C. Mangelsdorf and L. R. White. Dielectric response of a dilute suspension of spherical colloidal particles to an oscillating electric field. *J. Chem. Soc.*, Faraday Trans., 93:3145–3154, 1997.
- S. Mitragotri, D. G. Anderson, X. Chen, E. K. Chow, D. Ho, A. V. Kabanov, J. M. Karp, K. Kataoka, C. A. Mirkin, S. H. Petrosko, J. Shi, M. M. Stevens, S. Sun, S. Teoh, S. S. Venkatraman, Y. Xia, S. Wang, Z. Gu, and C. Xu. Accelerating the translation of nanomaterials in biomedicine. ACS Nano, 9(7):6644–6654, 2015.
- D. Mou, H. Chen, D. Du, C. Mao, J. Wan, H. Xu, and X. Yang. Hydrogel-thickened nanoemulsion system for topical delivery of lipophilic drugs. *Int. J. Pharm.*, 353(1):270 276, 2008.
- Nature. Nanomaterials definition matters. Nat. Nanotechnol., 14(3):193–193, 2019.
- C. Nazli, G. S. Demirer, Y. Yar, H. Y. Acar, and S. Kizilel. Targeted delivery of doxorubicin into tumor cells via mmp-sensitive peg hydrogel-coated magnetic iron oxide nanoparticles (mionps). *Colloids Surf.*, B, 122:674 – 683, 2014.
- R. O'brien. The electrical conductivity of a dilute suspension of charged particles.

 J. Colloid Interface Sci., 81(1):234 248, 1981.
- R. W. O'Brien. Electro-acoustic effects in a dilute suspension of spherical particles. J. Fluid Mech., 190:71–86, 1988.
- R. W. O'Brien and L. R. White. Electrophoretic mobility of a spherical colloidal particle. *J. Chem. Soc.*, Faraday Trans. 2, 74:1607–1626, 1978.

- R. W. O'Brien, D. W. Cannon, and W. N. Rowlands. Electroacoustic determination of particle size and zeta potential. *J. Colloid Interface Sci.*, 173(2):406–418, 1995.
- H. Ohshima. Dynamic electrophoretic mobility of spherical colloidal particles in concentrated suspensions. J. Colloid Interface Sci., 195(1):137 148, 1997.
- H. Ohshima. Electrokinetic phenomena of soft particles. Curr. Opin. Colloid Interface Sci., 18(2):73 – 82, 2013. ISSN 1359-0294.
- J. Overbeek. Theorie der electrophorese. Kolloid B, 1(54):287–364, 1943.
- K. Pal, A. K. Banthia, and D. K. Majumdar. Biomedical evaluation of polyvinyl alcohol–gelatin esterified hydrogel for wound dressing. J. Mater. Sci. - Mater. Med., 18(9):1889–1894, 2007.
- N. Peppas, P. Bures, W. Leobandung, and H. Ichikawa. Hydrogels in pharmaceutical formulations. *Eur. J. Pharm. Biopharm.*, 50(1):27–46, 2000.
- G. Sala, F. van de Velde, M. Cohen Stuart, and G. van Aken. Oil droplet release from emulsion-filled gels in relation to sensory perception. *Food Hydrocoll.*, 21 (5–6):977–985, 2007.
- D. A. Saville. Electrical conductivity of suspensions of charged particles in ionic solutions. *J. Colloid Interface Sci.*, 71(3):477 490, 1979.
- M. Shao, Z. Hussain, H. E. Thu, S. Khan, H. Katas, T. A. Ahmed, M. Tripathy, J. Leng, H.-L. Qin, and S. N. A. Bukhari. Drug nanocarrier, the future of atopic diseases: Advanced drug delivery systems and smart management of disease. Colloid Surf. B, 147:475–491, 2016.
- S. Sharma, A. Verma, B. V. Teja, G. Pandey, N. Mittapelly, R. Trivedi, and P. Mishra. An insight into functionalized calcium based inorganic nanomaterials in biomedicine: Trends and transitions. *Colloids Surf.*, B, 133:120 – 139, 2015.
- C. Solans, P. Izquierdo, J. Nolla, N. Azemar, and M. Garcia-Celma. Nano-emulsions. *Curr. Opin. Colloid Interface Sci.*, 10(3–4):102–110, 2005.
- C. D. Spicer. Hydrogel scaffolds for tissue engineering: the importance of polymer choice. *Polym. Chem.*, 11:184–219, 2020.

- D. Stigter and K. J. Mysels. Tracer electrophoresis. ii. the mobility of the micelle of sodium lauryl sulfate and its interpretation in terms of zeta potential and charge. J. Phys. Chem., 59(1):45–51, 1955.
- H. T. Ta, C. R. Dass, and D. E. Dunstan. Injectable chitosan hydrogels for localised cancer therapy. *J. Controlled Release*, 126(3):205 216, 2008.
- T. Tadros, P. Izquierdob, J. Esquenab, and C. Solansb. Formation and stability of nano-emulsions. *Adv. Colloid Interface Sci.*, 108–109:303–318, 2004.
- P. Taylor. Ostwald ripening in emulsions. *Colloids Surf.*, A, 99(2–3):175–185, 1995.
- P. Thoniyot, M. J. Tan, A. A. Karim, D. J. Young, and X. J. Loh. Nanoparticle—hydrogel composites: Concept, design, and applications of these promising, multi-functional materials. *Adv. Sci.*, 2(1-2):1400010, 2015.
- V. Tjong, J. Zhang, A. Chilkoti, and S. Zauscher. Stimulus-Responsive Polymers as Intelligent Coatings for Biosensors: Architectures, Response Mechanisms, and Applications, pages 1–30. John Wiley & Sons, Inc., 2012.
- S. Wall. The history of electrokinetic phenomena. Curr. Opin. Colloid Interface Sci., 15(3):119 124, 2010.
- M. Wang and R. J. Hill. Dynamic electric-field-induced response of charged spherical colloids in uncharged hydrogels. *J. Fluid Mech.*, 640:357–400, 2009.
- X. Wang, C. Cheng, S. Wang, and S. Liu. Electroosmotic pumps and their applications in microfluidic systems. *Microfluid Nanofluidics*, 6(2):145, Feb 2009. ISSN 1613-4982 (Print); 1613-4982 (Linking).
- Y. Wang, D. W. Malcolm, and D. S. Benoit. Controlled and sustained delivery of sirna/nps from hydrogels expedites bone fracture healing. *Biomaterials*, 139: 127 138, 2017.
- L. Wei, C. Cai, J. Lin, and T. Chen. Dual-drug delivery system based on hydrogel/micelle composites. *Biomaterials*, 30(13):2606 2613, 2009.
- P. Wiersema, A. Loeb, and J. Overbeek. Calculation of the electrophoretic mobility of a spherical colloid particle. *J. Colloid Interface Sci.*, 22(1):78 99, 1966.
- X. Yang, M. Yang, B. Pang, M. Vara, and Y. Xia. Gold nanomaterials at work in biomedicine. *Chem. Rev.*, 115(19):10410–10488, 2015.

C. F. Zukoski and D. A. Saville. An experimental test of electrokinetic theory using measurements of electrophoretic mobility and electrical conductivity. J. Colloid Interface Sci., 107(2):322-333, 1985.

Chapter 3

Fractional ionization of SDS micelles from dielectric relaxation spectroscopy

3.1 Preface

Electrophoretic mobility and conductometric titration are accepted methods for probing the electrical charge of SDS micelle solutions, but theoretical interpretations of these data, to obtain the surface charge density and ζ -potential, have produced diverse results. Here, an experimental study of aqueous SDS micelle solutions is undertaken, using the standard electrokinetic model to interpret the dielectric relaxation spectra. The influence of added salt on the electrical properties and micelle dissociation is investigated, and the theoretical interpretation accounts for the contributions of added counter-ions and non-specific adsorption on the conductivity.

3.2 Abstract

Dielectric relaxation spectra of aqueous sodium dodecyl sulphate (SDS) solutions containing micelles are measured and interpreted using a variety of definitions of their fractional ionization. Here, particular attention is given to interpretations based on the standard electrokinetic model, accounting for added counterions and

non-specific adsorption. These are found to have a significant influence on the resulting ζ -potential and the accompanying micelle charge. Thus, the degree of ionization, as adopted in the closed-association model of micellization, may be more a consequence of approximations in past electrokinetic interpretations of conductivity and electrophoretic mobility data. Whereas the fractional degree of ionization for SDS micelles has been widely reported ~ 0.3 , we find the fractional degree of ionization for SDS to be closer to one, consistent with SDS being a strong electrolyte. This interpretation provides new insights on SDS micelle thermodynamics, and may help to better understand the charging of other highly charged, self-assembled polyelectrolytes.

3.3 Introduction

The onset of micelle formation changes physical properties (e.g., surface tension, osmotic pressure, conductivity, etc.) of surfactant solutions (Rosen, 1989). The micelle shape and structure is hypothesized to change with the surfactant concentration. At low concentrations in aqueous solution, micelles are thought to have a spherical core of hydrophobic tails with a corona of hydrophilic heads. Ellipsoidal micelles are common at higher concentrations.

For ionic surfactants, such as sodium dodecyl sulphate (SDS) and cetrimonium bromide, the hydrophilic head is considered to form part of a Stern layer with partially bound counter-ions. The combination of the core and Stern layer presents what is termed a kinetic micelle, modelled as a colloidal sphere with an electrical double layer (Stigter, 1967, Tanford, 1972). Various methodologies have been devised to ascertain the degree of micelle ionization (α), aggregation number (N_{agg}), critical micelle concentration (c.m.c.), and micellization constant (K_n) (the rate constant of surfactant molecule in micelle formation). These methods usually involve a single or combination of experiments (e.g., static light scattering, photochemistry, conductivity, electrophoretic mobility, etc.) (Stigter, 1967, Moroi and Yoshida, 1997, Patist et al., 2001).

The c.m.c. can be identified by a distinct change in the slope of the conductivity versus surfactant concentration plot, and the degree of dissociation and micelle molar conductivity have been estimated from the change in slope of the conductivity isotherm. In principle, the surface charge density and ζ -potential can be

obtained from conductivity measurements (Moroi and Yoshida, 1997, Us'yarov, 2007)

Electrokinetic theories for colloidal dispersions have been extended to SDS micelle solutions to infer micelle properties. However, such studies are limited by the need for independent measurements of the aggregation number and radius (Dunstan and White, 1990). The application of electrokinetic theory to infer the ζ -potential has not provided consistent results from the electrophoretic mobility (Stigter and Mysels, 1955), because the ζ -potential depends on assumptions in the particular theory of choice. Perturbations in the concentration of small ions were unaccounted for in the early literature (Stigter, 1967, Hunter, 1962) that seems to have shaped present understanding of micelle charge. However, the availability of more complete electrokinetic models has been proposed to address these inconsistencies (Saville, 1983).

For SDS micelles in water, an electrokinetic interpretation of the conductivity, as described theoretically by Saville (1983), furnished a ζ -potential $\approx -6.4 \, k_B T/e$ (Dunstan and White, 1990) with no added salt. This is significantly larger in magnitude than the value $\approx -3.92 \, k_B T/e$ (mobility converted to ζ -potential using the theory of Booth (1951)) reported from early tracer-electrophoresis without added salt (Stigter and Mysels, 1955), but somewhat closer to the value $-5.7 \, k_B T/e$ ascertained using spectroscopic probes (Hartland et al., 1987). These disparities motivate further attempts to understand the charge.

Recent technological advances provide new opportunities to study micelle electrokinetic over a wide frequency range (kHz to GHz). Dielectric relaxation has been widely used for investigating the electrical double layer of colloidal suspensions, such as micelles (Lanzi et al., 2009, Khademi and Barz, 2019), latex beads (Zukoski and Saville, 1985, Rosen and Saville, 1991, Dunstan and White, 1992, Gittings and Saville, 1995, Hollingsworth and Saville, 2004, Beltramo and Furst, 2012b), and silica nanoparticles (Zhao and He, 2006).

Dynamic exchange of surfactants between the bulk solution and micelles, as influencing the association and dissociation rate constants for micelle formation, can be neglected at frequencies above 1 kHz (Aleiner and Us'yarov, 2010). This is because micelle formation and dissolution times have been calculated from first-order reaction constants, measured using a pressure-jump technique (Patist et al., 2001, Aleiner and Us'yarov, 2010). This involves the pressurization of surfactants at high

concentration, followed by a return to atmospheric pressure, producing an exponential decay of electrical conductivity with time constants spanning milliseconds to minutes (Oh and Shah, 1993).

At the high frequencies that can be probed with DRS, it is possible to resolve the various dipole relaxation processes, such as water orientation, ion pairing, and dipole polarization (due to ions) around charged micelles (Lanzi et al., 2009). Also, the addition of salt to micelle solutions has been shown to reduce the amplitude and time constant of micelle relaxation, attributed to the surface charge interaction (surface conductivity) in the double layer (Khademi and Barz, 2019). An understanding of micelle physicochemical properties, such as the surface charge, provides a basis for understanding other self-assembled molecular structures (e.g., nanoemulsions, vesicles and proteins) with similarly charged interfaces.

In this study, theoretical predictions of the particle electrophoretic mobility and dispersion conductivity are undertaken using the standard electrokinetic model (DeLacey and White, 1981, Mangelsdorf and White, 1997), which is solved numerically according to the MPEK package (Hill et al., 2003b,a,c), which furnishes a calculation of the contributions of added counterions and non-specific adsorption to the conductivity. Micelles in aqueous electrolytes are modelled as rigid spheres with a hydrophobic, uncharged interior and a charged interface. Micelle radius and aggregation number are sourced from independent literature. Conductivity measurements are used to determine other parameters, such as surfactant and counterion molar conductivities, required as input for the standard electrokinetic model. Impedance spectra are resolved into conductivity and apparent permittivity spectra, from which the c.m.c. and degree of micelle ionization α above the c.m.c. are estimated using customary and new interpretations.

3.4 Theoretical interpretation

SDS is widely considered to be a strong electrolyte, suggesting that the degree of micelle ionization $\alpha=1$. However, α has been widely reported $\ll 1$: 0.287 (Stigter and Mysels, 1955), 0.19 (Us'yarov, 2007), 0.181 (Lanzi et al., 2009), 0.28 (Shanks and Franses, 1992), 0.26–0.27 (Moroi and Yoshida, 1997). In electrokinetic literature, α has been considered the fraction of counterions that reside beyond the shear plane, so that a fraction $1-\alpha$ are associated with the micelle (Stigter, 1967).

On the other hand, the chemistry literature considers α as an integral part of an ionization reaction (Marcolongo and Mirenda, 2011), termed the closed-association model of micellization. Here we set out several ways of interpreting or defining α .

According to Kohlraush's law, for an electrolyte of N ionic species at low concentration, the conductivity can be expressed (Castellan, 1982)

$$\sigma = \sum_{i}^{N} n_i \lambda_i, \tag{3.1}$$

where n_i are the ion number densities, and the limiting molar conductivities

$$\lambda_i = \frac{(z_i e)^2 D_i}{k_B T},\tag{3.2}$$

where D_i are the ion diffusion coefficients with $z_i e$ the charge and $k_B T$ the thermal energy.

For a completely dissociated anionic surfactant solution below the c.m.c. (in the presence of an added salt),

$$\sigma = n_s \lambda_s + n_c \lambda_c + n_+ \lambda_+ + n_- \lambda_- + \sum_{j=1}^{\infty} n_j \lambda_j, \quad (n_s = n_c < \text{c.m.c.})$$
 (3.3)

where subscripts +, - denote the principal added salt cation and anion, the sum over j denotes other ions in the aqueous phase (e.g., due to dissolved carbon dioxide) and s, c denote the surfactant (valence z) and its counter-ion (valence -z). Thus, the change in conductivity with respect to the surfactant concentration is

$$\frac{\partial \sigma}{\partial n_c} = \lambda_s + \lambda_c, \quad (n_s = n_c < \text{c.m.c.}).$$
 (3.4)

With knowledge of the limiting conductivities of the ions, the limiting conductivity of the surfactant counter ion λ_c can be determined.

Above the c.m.c., assuming the surfactant is present as micelles with aggregation number N_{agg} and surfactant monomers,

$$\sigma = n_{cmc}(\lambda_s + \lambda_c) + n_m(\lambda_m + \alpha N_{agg}\lambda_c) + n_+\lambda_+ + n_-\lambda_- + \sum_j n_j\lambda_j, \quad (n_s > \text{c.m.c.})$$
(3.5)

where the micelle number density

$$n_m = \frac{n_s - n_{cmc}}{N_{aqq}} \tag{3.6}$$

with n_{cmc} the surfactant number density at the c.m.c.

The degree of ionization α can therefore be ascertained from the change in the slope of the conductivity with respect to surfactant concentration (Moroi and Yoshida, 1997):

$$\frac{\partial \sigma}{\partial n_s} = \frac{\lambda_m}{N_{aaa}} + \alpha \lambda_c. \quad (n_s > \text{c.m.c.})$$
(3.7)

However,

$$\lambda_m = -\alpha N_{agg} e M_m [\zeta e/(k_B T), \kappa a_m], \qquad (3.8)$$

where $-\alpha N_{agg}e$ is the micelle charge, and $M_m[\zeta e/(k_BT), \kappa a_m]$ is its electrophoretic mobility $(\zeta e/(k_BT))$ is the ζ -potential scaled with $k_BT/e \approx 25$ mV, and κa_m is the micelle radius a_m scaled with the Debye length κ^{-1}), which also depends on the charge. Thus, for example, according to the Hückel theory (Russel et al., 1989),

$$M_m[|\zeta|e/(k_BT) \ll 1, \kappa a_m \ll 1] \approx -\frac{\alpha N_{agg}e}{6\pi \eta a_m}$$
 (3.9)

where $a_m = k_B T/(D_m 6\pi \eta)$ is the micelle radius (η is the electrolyte shear viscosity). Accordingly, the Hückel mobility furnishes

$$\lambda_m \approx \frac{(\alpha N_{agg} e)^2}{6\pi \eta a_m} \tag{3.10}$$

so

$$\frac{\partial \sigma}{\partial n_s} = \frac{N_{agg}(\alpha e)^2}{6\pi \eta a_m} + \alpha \lambda_c. \quad (n_s > \text{c.m.c.})$$
(3.11)

Since the Hückel mobility is an approximation (valid for low ζ -potential and $\kappa a_m \ll 1$), Eqn. (3.9) defines α as an effective degree of ionization, whereas if $M_m[\zeta e/(k_BT), \kappa a_m]$ is measured or calculated independently from an exact electrokinetic theory, then

$$\frac{\partial \sigma}{\partial n_s} = -\alpha e M_m [\zeta e/(k_B T), \kappa a_m] + \alpha \lambda_c, \quad (n_s > \text{c.m.c.})$$
 (3.12)

where α must be considered an actual degree of ionization.

Finally, according to electrokinetic theory for the conductivity of dilute colloidal dispersions (Saville, 1983), we may write

$$\sigma = \left[n_{cmc}(\lambda_s + \lambda_c) + n_+ \lambda_+ + n_- \lambda_- + \dots \right] \left[1 + \Delta \sigma_m n_m \frac{4\pi a_m^3}{3} \right] \quad (n_s > \text{c.m.c.}), \quad (3.13)$$

where $\Delta \sigma_m[\zeta e/(k_B T), \kappa a_m, ...]$ is the micelle conductivity increment. This may be compared directly to conductivity increment spectra, but we also have

$$\frac{\partial \sigma}{\partial n_s} = n_{cmc} (\lambda_s + \lambda_c) \Delta \sigma_m \frac{4\pi a_m^3}{3N_{agg}}. \quad (n_s > \text{c.m.c.})$$
 (3.14)

Thus, one may fit the SEKM to the slope of the conductivity isotherm, e.g., by varying ζ with prescribed κa_m and N_{agg} , and then calculate the accompanying α from the surface charge $-\alpha N_{agg}e$, as furnished by the Poisson-Boltzmann equation. Yet another approach would be prescribe the surface charge density $N_{agg}/(4\pi a_m^2)$ in the SEKM, and adjust a_m , for example, to fit the predicted slope from Eqn. (3.14) to the measured value.

3.5 Materials and methods

Solutions of sodium dodecyl sulphate (SDS) (98.5 % pure from Sigma Aldrich) were prepared by dissolving prescribed masses in reverse osmosis (RO) water (Type 1, $\sigma \approx 5.6~\mu \mathrm{S~m^{-1}}$, $\Omega \approx 18$ MOhm cm), stirred for ≈ 1 min using a vortex mixer. Various ionic strengths were obtained by pre-dissolving NaCl (Sigma Aldrich) in RO water. All materials were used as provided by the manufacturer.

3.5.1 Dielectric relaxation spectroscopy

Dielectric relaxation spectra (20 Hz–10 MHz) were measured using an impedance analyzer (Keysight E4990A) and an in-house sample cell based on the design of Beltramo (2013). Cell calibration and correction for test fixture residuals were undertaken using open/short compensation (Hollingsworth and Saville, 2003). Corrections for electrode polarization were undertaken using the single-spacer approach (Beltramo and Furst, 2012a). Background and sample measurements were achieved using a syringe to pump samples into a parallel electrode configuration with acrylic spacer and stainless steel electrodes, as shown in figure 3.1.

According to Hollingsworth and Saville (2003), the sample admittance ("raw" measurement) may be expressed as

$$Y_{tot}^* = \frac{A}{2h} \left[\sigma(\omega) + i\omega \varepsilon_0 \varepsilon_{app}'(\omega) \right], \qquad (3.15)$$

where $\sigma(\omega) \equiv \sigma_{\infty} - \omega \varepsilon_0 \varepsilon''(\omega)$ is the complex conductivity (σ_{∞} is the conductivity, ε_0 is the vacuum permittivity, and $\varepsilon''(\omega)$ is the dielectric loss), ε'_{app} is the apparent dielectric constant, and A/(2h) the cell constant with A the electrode area in contact with the sample and 2h the spacer thickness.

The apparent dielectric constant has been expressed as (Hollingsworth and Saville, 2003)

$$\varepsilon_{app}'(\omega) = \varepsilon_{\infty} \beta \frac{1 + \beta(\omega/\kappa^2 D)^2}{1 + \beta^2(\omega/\kappa^2 D)^2},$$
(3.16)

where ε_{∞} is the solvent dielectric constant, $\beta = \kappa h$ is the scaled electrode separation, κ is the reciprocal Debye length, D is the mean ion diffusion coefficient, and $\omega = 2\pi f$ is the angular frequency. To correct for the effects of electrode polarization, Eqn. (3.16) is fit to measured ε'_{app} with D as the fitting parameter.

For low frequencies and large electrode separation $\beta^2(\omega/\kappa^2D)^2 \gg 1$ (e.g., frequency f=1 kHz for an electrolyte with ionic strength 10 mM, spacer separation $h \sim 3$ mm and $D \sim 10^{-9}$ m² s⁻¹ gives $\beta^2(\omega/\kappa^2D)^2 \sim 370$), which simplifies Eqn. (3.16) to (Hollingsworth and Saville, 2003)

$$\varepsilon'_{app}(\omega) = \varepsilon_{\infty} \left(1 + \frac{\kappa^3 D^2}{\omega^2 h} \right).$$
 (3.17)

The dielectric constant of the sample—corrected for electropolarization—was calculated as (Beltramo and Furst, 2012a)

$$\varepsilon'(\omega) = \frac{\varepsilon'_{app}(\omega)}{1 + \frac{\kappa^3 D^2}{\omega^2 h}}.$$
(3.18)

The conductivity and dielectric constant increments for SDS micelle solutions were calculated from the spectra as

$$\Delta\sigma(\omega) = \frac{\sigma(\omega)/\sigma_{\infty} - 1}{\phi} \tag{3.19}$$

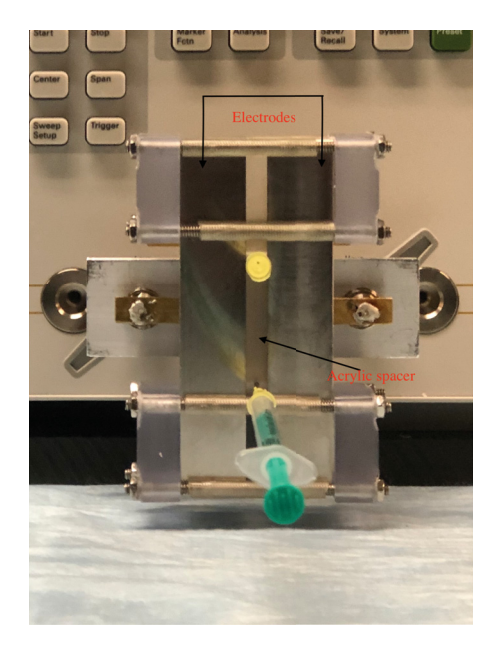


FIGURE 3.1: In-house sample holder for dielectric spectroscopy. Sample is injected into the space between two parallel stainless steel electrodes, separated by an acrylic spacer: $A \approx 1.2 \text{ cm}^2$ and $h \approx 3 \text{ mm}$.

and

$$\Delta \varepsilon(\omega) = \frac{\varepsilon'(\omega)/\varepsilon_{\infty} - 1}{\phi},\tag{3.20}$$

where $\phi = (4/3)\pi a_m^3 (n_s - n_{cmc})/N_{agg}$ is the micelle volume fraction, and ε_{∞} and σ_{∞} are the electrolyte dielectric constant and conductivity. Note that we will assume that the volumetric radius equals the hydrodynamic radius.

3.6 Results and discussion

Figure 3.2 shows the dielectric spectra of SDS solutions without added salt, at SDS concentrations from below to well above the c.m.c. SDS solution conductivity increases with frequency, reaching a plateau at $\approx 10^4$ Hz where the values are very close to those reported by off-the-shelf DC-conductivity probes (Us'yarov, 2007, Aleiner and Us'yarov, 2010). The apparent dielectric constant decreases with frequency, reaching a high-frequency plateau. As highlighted above, the dielectric constant at low frequencies is dominated by dynamic process at the electrode-sample interface that are not representative of the bulk.

Accordingly, measuring the dielectric constant of colloidal suspensions is plagued by electrode polarization (Hollingsworth and Saville, 2003, Beltramo and Furst,

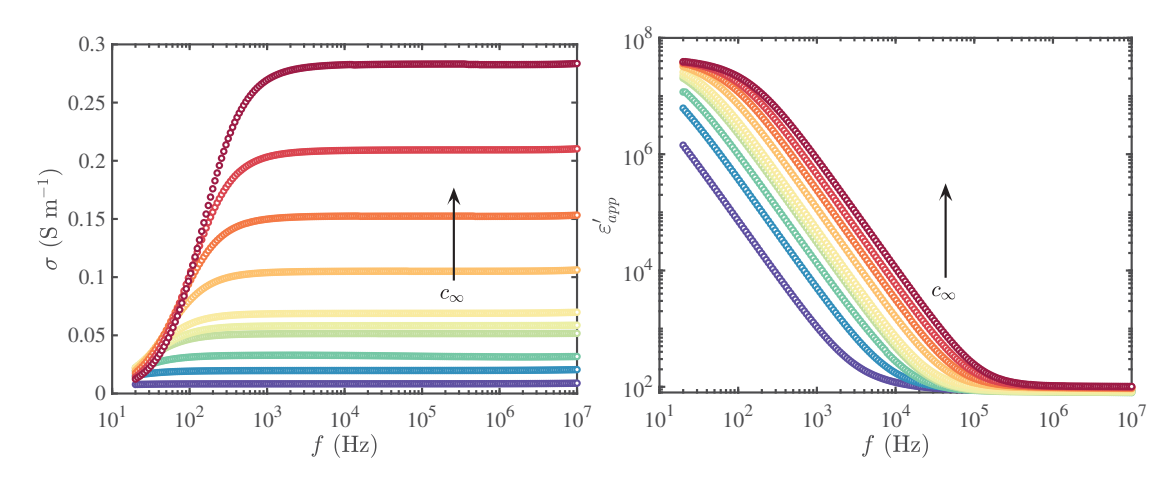


FIGURE 3.2: Conductivity (left) and apparent dielectric constant (right) spectra of aqueous SDS solutions with SDS concentrations $c_{\infty} = 1, 3, 5, 8, 10, 15, 30, 50, 70,$ and 100 mM, no added salt.

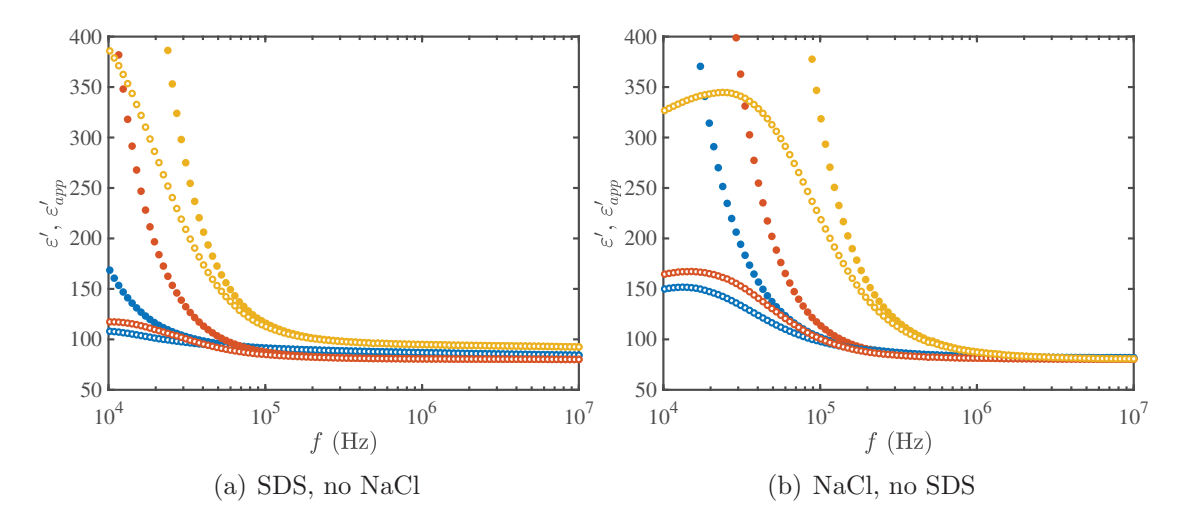


FIGURE 3.3: Dielectric constant spectra of aqueous (a) SDS solutions at SDS concentrations $c_{\infty} = 3$ (blue), 8 (red) and 30 (yellow) mM, no added salt; and (b) NaCl solutions at NaCl concentrations [NaCl] = 5 (blue), 10 (red) and 30 (yellow) mM. Corrected data (open circles) are compared with their uncorrected (for electrode polarization, filled circles) counterparts. The electrode-polarization model fitting parameter D is provided in table 3.1.

2012a), so electrode polarization corrections using the single-spacer technique are shown in figure 3.3 (and accompanying table 3.1) for representative SDS concentrations well below, close to, and well above the c.m.c.

Figure 3.4 shows uncorrected dielectric constant spectra in a narrower range of frequencies. These highlight the subtle way in which the polarization of SDS solutions differ from their pure NaCl counterparts.

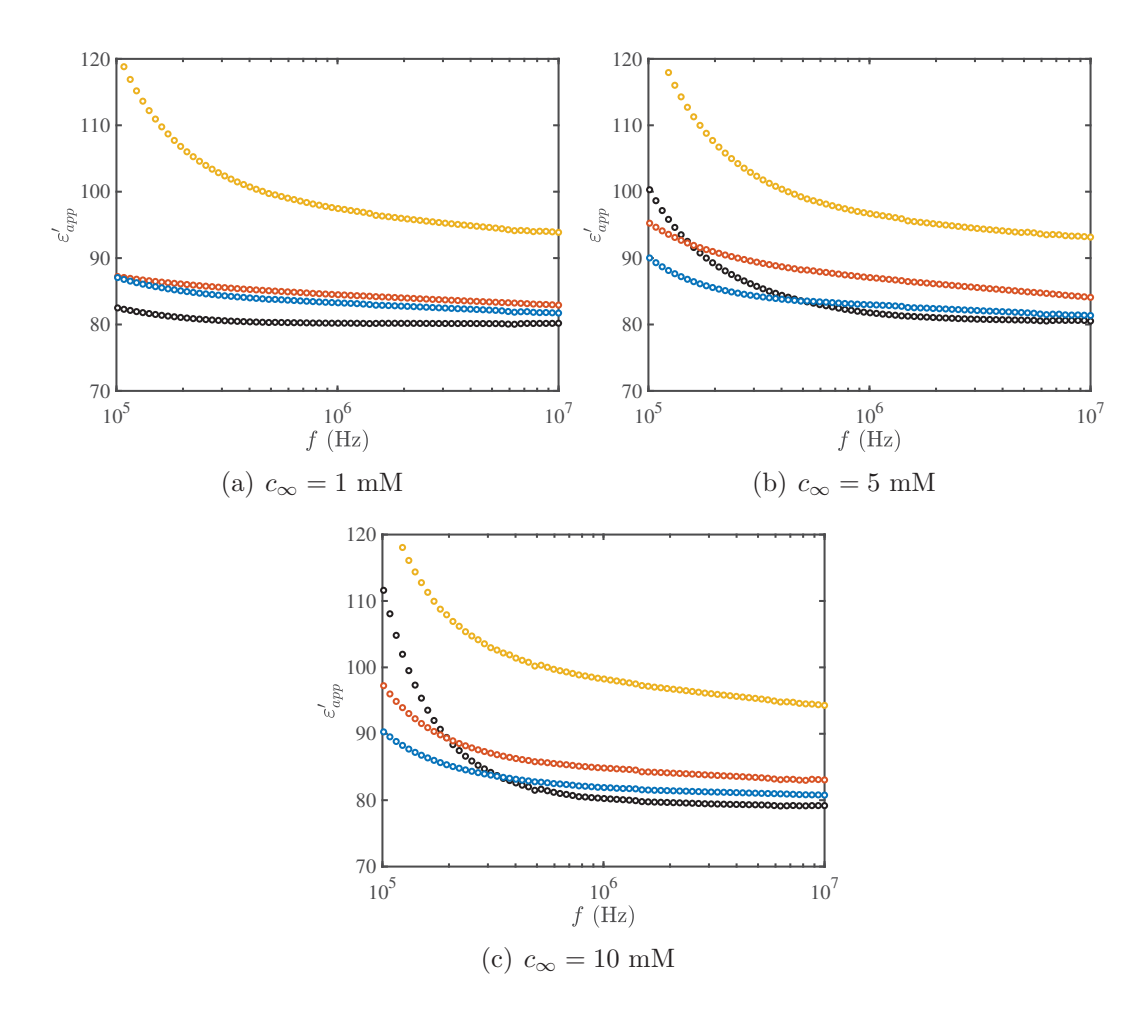


FIGURE 3.4: Dielectric constant spectra of aqueous SDS solutions with added NaCl concentrations [NaCl] = 0 (blue), 1 (red), and 5 (yellow) mM. Black circles are dielectric spectra for aqueous NaCl with NaCl concentration [NaCl] = c_{∞} .

Table 3.1: Fitting parameter D for the electrode-polarization corrections in figure 3.3. At $c_{\infty} = 30$ mM, above the c.m.c., D at the c.m.c. is used for the correction, thus assuming that the excess SDS (in micelles) does not change the composition of the background electrolyte contributing to D.

4.
4 .
$^{-1})$
$^{-1})$

3.6.1 Conductivity isotherms and theoretical interpretation

Conductivities and dielectric constants from the measured spectra at 1 MHz are plotted versus the SDS concentration in figure 3.5. According to Eqn. (3.18), the contribution of electrode polarization is negligible $\gtrsim 1$ MHz, so $\varepsilon'_{app}(\omega) \equiv \varepsilon'(\omega)$, since $\kappa^3 D^2/\omega^2 h \ll 1$. It is generally considered that above 1 kHz there is insufficient time for surfactant to exchange between the electrolyte and micelles (Aleiner and Us'yarov, 2010). The c.m.c. is identified as a distinct change in the slope of the conductivity with respect to SDS concentration at each electrolyte (salt) concentration. The c.m.c.s identified using this technique are within 2% of those reported by Us'yarov (2007) and Dunstan and White (1990).

Unlike NaCl solutions, an increase in the dielectric constant with electrolyte concentration (at high frequencies $\gtrsim 1$ MHz, see figure 3.3(b)) is evident for SDS solutions below the c.m.c. This clearly cannot be attributed to micelles, suggesting a polarization of DS⁻ that reflects dynamics of the charged head with respect to the uncharged tail. This relaxation seems to have gone unnoticed in previous studies (Lanzi et al., 2009, Khademi and Barz, 2019).

The limiting molar conductivity of DS⁻ at each NaCl solution is reported in table 3.2. The decrease with NaCl concentration is surprising given the low (\sim mM) ion concentrations, but similar variations have been reported by others (Moroi and Yoshida, 1997). Note that molar conductivities (25°C) for Na⁺ (at similar dilute concentrations) have been reported 49.27, 48.93 and 47.55 S cm² equiv⁻¹; whereas for DS⁻, molar conductivities are sensitive to concentration: 21.11, 20.84 and 20.02 S cm² equiv⁻¹ at SDS bulk concentrations 0.5, 1.05 and 4.99 mM, respectively (Moroi and Yoshida, 1997). These suggest much stronger, significant ionic interactions, even at \sim mM SDS concentrations.

The parameters required as input for the SEKM are drawn from literature and the foregoing dielectric-relaxation spectra, as summarized in table 3.3. Note that all SEKM calculations were undertaken with fixed concentration of $[HCO_3^-] = [H_3O^+] = 3.2 \ \mu\text{M}$, corresponding to a pH ≈ 5.6 . The core micelle density has been reported 802 kg m⁻³ (Stigter, 1967), and limiting molar conductivities at T = 25°C for Na⁺ and Cl⁻ are 50.1 and 76.3 S cm² equiv⁻¹, respectively (Moroi and Yoshida, 1997).

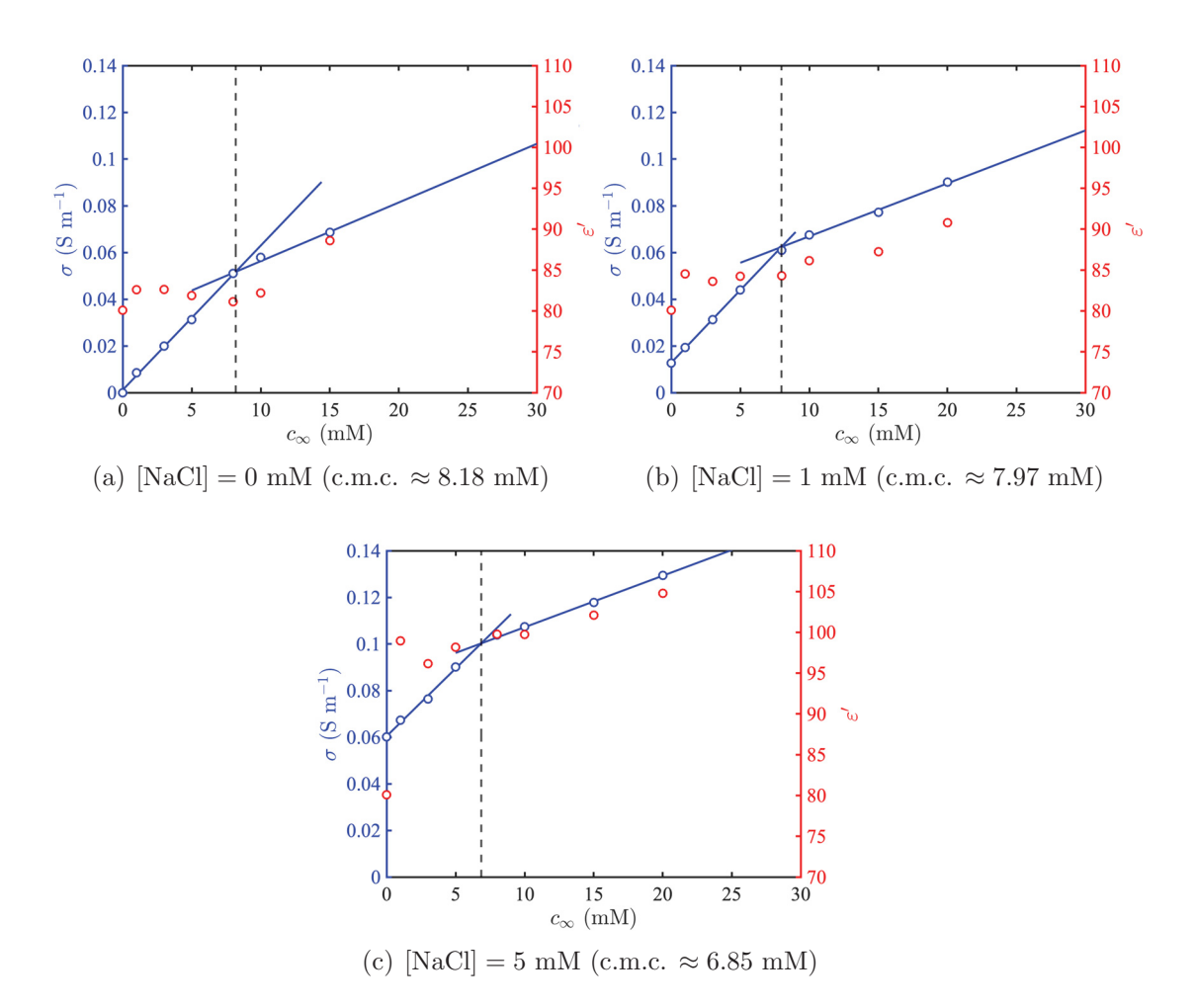


FIGURE 3.5: Conductivity and dielectric constant at $f \approx 1$ MHz versus SDS concentration for several added NaCl concentrations.

TABLE 3.2: Parameters extracted from the conductivity isotherms $(T=22^{\circ}\text{C})$ in figure 3.5: Δ_1 and Δ_2 are slopes below and above the c.m.c., respectively. Note that λ_{Na+} is prescribed from Moroi and Yoshida (1997), corrected for temperature using $\lambda_i(T) = \lambda_i^0[1 + 0.02(T - 25^{\circ}\text{C})]$ (SAS, 2003).

$\overline{I_s}$	Δ_1	Δ_2	c.m.c.	λ_{Na+}	λ_{DS-}
(mM)	$(S cm^2 equiv^{-1})$	$(S cm^2 equiv^{-1})$	(mM)	$(S cm^2 equiv^{-1})$	$(S cm^2 equiv^{-1})$
0	61.8	25.1	8.18	47.1	14.7
1	62.1	22.6	7.97	47.1	15.0
5	58.1	22.1	6.85	47.1	11.0

Table 3.3: Parameters as input for SEKM calculations of the mobility and conductivity increment for SDS micelles at infinite micelle dilution, i.e., at the c.m.c. These data at $T=25~{\rm ^{\circ}C}$.

Parameter	Value	Units	Source
a_m	2.23	nm	Dunstan and White (1990)
N_{agg}	64		Moroi and Yoshida (1997)
c.m.c	6.85 – 8.18	mM	Measured
[NaCl]	0.01 - 5	mM	Measured
$[\mathrm{HCO}_3^-] = [\mathrm{H}_3\mathrm{O}^+]$	3.2	$\mu\mathrm{M}$	Beltramo and Furst (2012a)
λ_{s^-}	14.46	${\rm S~cm^2~equiv^{-1}}$	Estimated from table 3.2
λ_{Na}	50.1	${\rm S~cm^2~equiv^{-1}}$	Moroi and Yoshida (1997)
λ_{Cl}	76.31	${\rm S~cm^2~equiv^{-1}}$	Moroi and Yoshida (1997)
$\lambda_{H_3O^+}$	349.65	${\rm S~cm^2~equiv^{-1}}$	Beltramo and Furst (2012a)
$\lambda_{HCO_3^-}$	44.5	$S cm^2 equiv^{-1}$	Beltramo and Furst (2012a)
$arepsilon_m$	2		
$arepsilon_{\infty}$	78.54		Beltramo and Furst (2012a)
$ ho_m$	802	${\rm kg~m^{-3}}$	Stigter (1967)
$ ho_{\infty}$	997	${\rm kg~m^{-3}}$	Beltramo and Furst (2012a)

The micelle radius $a_m = 2.23$ nm adopted herein is from the electrokinetic study of micelle solutions by Dunstan and White (1990). This value is close to $a_m = 2.18$ nm predicted by an equation relating the aggregation number N_{agg} to the micelle volume (Tanford, 1972). Values in the range $a_m = 2.25-2.57$ nm have been reported from small angle neutron scattering by Payne et al. (1987) and from 2.42-2.68 nm by (Hayter and Penfold, 1983).

According to the conductivity isotherm, Eqn. (3.11) furnishes an apparent degree of ionization $\alpha \approx 0.49$ with $N_{agg} = 64$, $a_m = 2.23$ nm, $\lambda_{Na+} = 47.09$ S cm² equiv⁻¹, and (averaged over variations in salt concentration) $\Delta_2 = 23.38$ S cm² equiv⁻¹. On the other hand, when the standard electrokinetic model (SEKM) of Hill et al. (2003a,b,c) is used to calculate the mobility $|M_m|(\zeta = -5.3k_BT/e, \kappa a_m \approx 0.66) \approx 4.38 \times 10^{-8}$ m² V⁻¹ s⁻¹ (at 0.1 MHz), Eqn. (3.12) furnishes $\alpha \approx 0.16$. Details of this calculation are provided below, where we also address in detail how the SEKM is applied directly to the conductivity spectra.

Table 3.4 shows the micelle conductivity increment extracted from the conductivity isotherms, according to Eqn. (3.14). Fitting the SEKM to these data (adjusting ζ with prescribed a_m and N_{agg}) furnishes the accompanying ζ -potentials and micelle charge -Ne. The fractional degree of ionization emerging from SEKM₀ are physically unrealizable ($\alpha \gg 1$), but SEKM_{ac/nsa} furnishes values that are similar to those obtained from solving Eqn. (3.11).

Table 3.4: Number of charges N (and $\alpha = N/N_{agg}$ with $N_{agg} = 64$ (Moroi and Yoshida, 1997)) for SDS micelles calculated according to Eqn. (3.14) and the Poisson-Boltzmann equation for the accompanying ζ -potential, each obtained by fitting either SEKM₀ or SEKM_{ac/nsa} to the post-c.m.c. slopes of the conductivity isotherms in figure 3.5 and summarized in table 3.2.

[NaCl]	κa_m	$\Delta \sigma_m$	$-\zeta e/(k_BT)$	$N(\alpha_0)$	$-\zeta e/(k_BT)$	$N (\alpha_{ac/nsa})$
(mM)	-	-	$(SEKM_0)$	$(SEKM_0)$	$(SEKM_{ac/nsa})$	$(SEKM_{ac/nsa})$
0.01	0.66	114	12.20	963 (>> 1)	4.85	35 (0.55)
1	0.69	105	7.53	101 (> 1)	4.31	29(0.45)
5	0.79	127	8.93	178 (> 1)	4.58	30 (0.46)

To test how sensitive α is to the choice of a_m (and N_{agg}), we varied a_m in the range 2.13–2.63 nm, maintaining $N_{agg}=64$. The values of α in table 3.4 with $a_m=2.23$ nm are practically independent of a_m . However, if we prescribe the surface charge density as $-N_{agg}/(4\pi a_m^2)$, adopting a_m as a fitting parameter (maintaining $N_{agg}=64$), then $\alpha=1$, giving $a_m\approx 2.37$, 2.35 and 2.38 nm with mobilities 4.48, 4.51, and 4.48×10^{-8} m² V⁻¹ s⁻¹ (SEKM₀) and $a_m\approx 2.79$, 2.78 and 2.97 nm with mobilities 4.26, 4.26, and 4.16×10^{-8} m² V⁻¹ s⁻¹ (SEKM_{ac/nsa}) for [NaCl] = 0.01, 1 and 5 mM, respectively. These larger micelle radii, which arise from the SEKM with fully ionized DS micelles ($\alpha=1$), suggest a more dynamic and diffuse micelle structure than demanded by the foregoing $a_m=2.23$ nm.

3.6.2 Conductivity increment spectra and theoretical interpretation

Figure 3.6 compares the measured conductivity and dielectric constant increments with predictions of the SEKM Hill et al. (2003a,b,c) at various NaCl concentrations (with SDS, HCO_3^- , H_3O^+). Above the c.m.c., the electrolyte is prescribed to comprise Na⁺ and DS⁻ at the c.m.c. concentration, plus the added salt with concentration [NaCl]. Note that the dissolved CO_2 concentration ([HCO_3^-] = $[H_3O^+] = 3.2~\mu M$) was assumed constant with a negligible impact on the c.m.c. ζ -potentials are estimated from a fit of the SEKM to the conductivity increment. SEKM_{ac/nsa} are calculations that account for the contribution of added counterions (a.c.) and non-specific adsorption (n.s.a.) to the conductivity increment, whereas SEKM₀ are calculations without the a.c. and n.s.a. (see table 3.7). Note that a.c. and n.s.a. contribute a frequency independent constant to the conductivity increment at each added NaCl concentration.

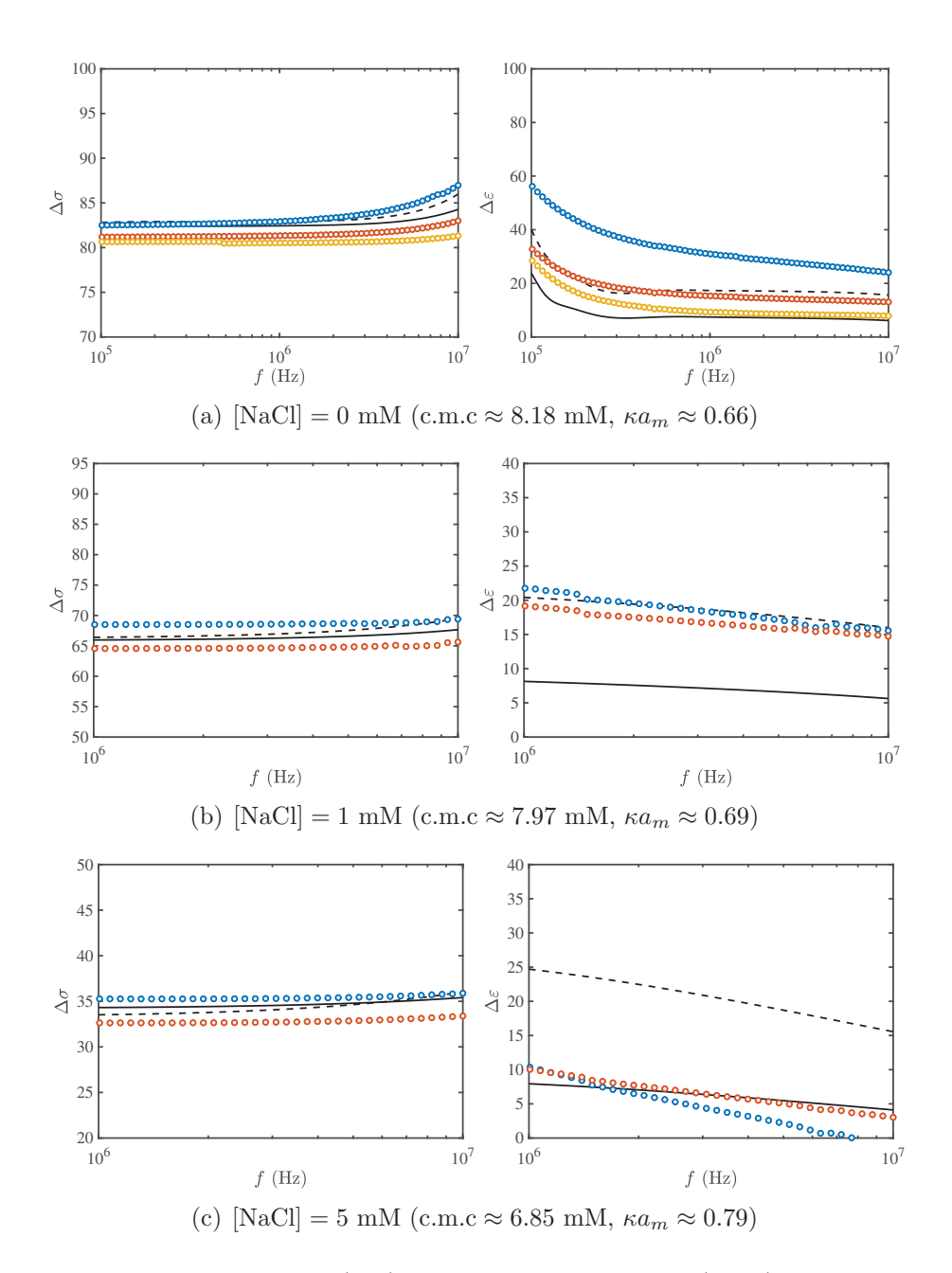


FIGURE 3.6: Conductivity (left) and dielectric constant (right) increments of SDS micelle solutions above the c.m.c. (a) $c_{\infty}=15$ (blue), 20 (red) and 30 mM (yellow). SEKM_{ac/nsa} with $\zeta=-3.42~k_BT/e$ (solid lines) and SEKM₀ with $\zeta=-5.3~k_BT/e$ (dashed lines). (b) $c_{\infty}=15$ (blue) and 20 (red) mM. SEKM_{ac/nsa} with $\zeta=-3.3~k_BT/e$ (solid); SEKM₀ with $\zeta=-5.28~k_BT/e$ (dashed). (c) $c_{\infty}=15$ (blue) and 20 (red) mM. SEKM_{ac/nsa} with $\zeta=-2.85~k_BT/e$ (solid); SEKM₀ with $\zeta=-5.1~k_BT/e$ (dashed).

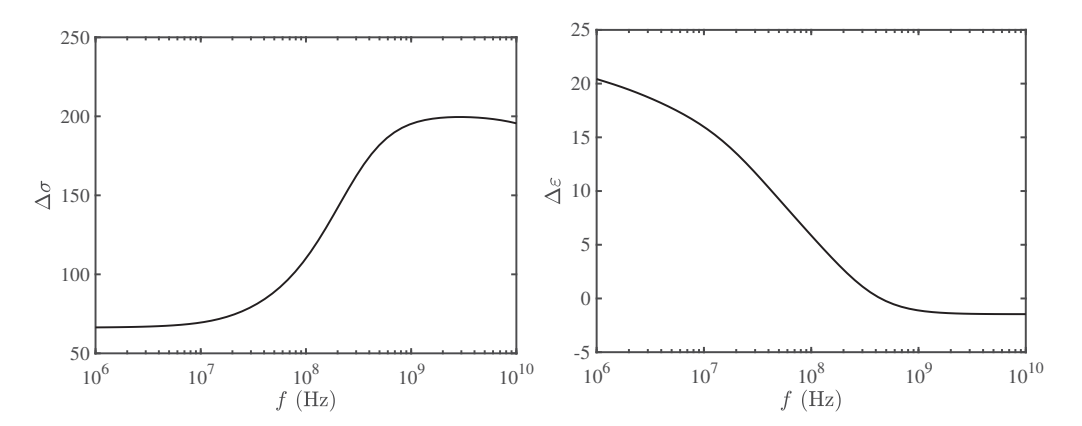


FIGURE 3.7: Conductivity (left) and dielectric constant (right) increment spectra for SDS micelles (at infinite dilution) according to the SEKM. Added NaCl concentration [NaCl] = 1 mM (c.m.c. ≈ 7.97 mM, $\kappa a_m \approx 0.69$), and $\zeta = -5.28$ k_BT/e .

For such small, highly charged spheres ($\kappa a \lesssim 1$, $|\zeta e/(k_B T)| \gtrsim 2$), the calculated dielectric relaxation spectra exhibit spurious numerical artifacts (manifesting as large frequency oscillations) at frequencies $f \lesssim 1$ MHz (depending on the grid resolution and position of the far-field boundary condition). Figure 3.6 shows calculations (with experimental data) only over the experimental range for which the calculations are robust. Figure 3.7 shows representative spectra from 1 MHz to well beyond the experimentally accessible range, thus highlighting the general form.

 ζ -potentials estimated from electrophoretic mobility, conductivity, and surface pK_a measurements in the literature are summarized in table 3.7. The mobilities of Stigter and Mysels (1955) have been converted by Stigter (1967) and Dunstan and White (1990) to ζ -potentials using various electrokinetic theories (table 3.7). According to Stigter (1967), the asymptotic series of Booth (1951) furnishes $-3.92k_BT/e$, and the method of Hunter (1962) furnishes $-5.3k_BT/e$; whereas, according to Dunstan and White (1990), the SEKM of O'Brien and White (1978) furnishes $-5.6k_BT/e$, close to spectroscopic surface potential measurements by Hartland et al. (1987).

Variations in the ζ -potential from measured electrophoretic mobilities have been ascribed to the inability of the theories to adequately capture the interaction of ionic species in the double layer and bulk (Stigter, 1967). The conversion of measured conductivity to ζ -potential by Dunstan and White (1990) yielded higher values than from the electrophoretic mobility (at low added NaCl concentration). This was ascribed to the presence of ionic impurities in SDS, the effects of which

TABLE 3.5: Micelle valence N and $\alpha = N_m/N_{agg}$ with $N_{agg} \approx 64$ (Moroi and Yoshida, 1997)) according to the Poisson-Boltzmann equation for the accompanying ζ -potential, each obtained by fitting either SEKM₀ or SEKM_{ac/nsa} to the conductivity increment spectra in figure 3.6.

[NaCl]	κa_m	$-\zeta e/(k_BT)$	$N(\alpha_0)$	$-\zeta e/(k_BT)$	$N (\alpha_{ac/nsa})$
(mM)	-	$(SEKM_0)$	$(SEKM_0)$	$(SEKM_{ac/nsa})$	$(SEKM_{ac/nsa})$
0.01	0.66	5.30	41 (0.64)	3.42	20 (0.31)
1	0.69	5.28	43(0.67)	3.30	20(0.31)
5	0.79	5.10	44(0.69)	2.85	18 (0.28)

TABLE 3.6: Micelle mobility M_m from the SEKM and α according to Eqn. (3.9) with N_{agg} , a_m and λ_{DS^-} as prescribed in table 3.3.

[NaCl]	$-M_m[\zeta e/(k_BT), \kappa a_m]_0$	α_0	$-M_m[\zeta e/(k_BT), \kappa a_m]_{ac/nsa}$	$\alpha_{ac/nsa}$
(mM)	$(10^{-8} \text{ m}^2 \text{ V}^{-1} \text{ s}^{-1})$		$(10^{-8} \text{ m}^2 \text{ V}^{-1} \text{ s}^{-1})$	
0.01	4.38	0.160	3.65	0.133
1	4.40	0.161	3.55	0.129
5	4.39	0.160	3.27	0.119

are concealed at higher electrolyte concentrations. At higher NaCl concentration, Dunstan and White (1990) reported ζ -potentials less than from the spectroscopic surface potential measurements of Hartland et al. (1987), attributing difference to the location of the slipping plane as which electrokinetic ζ -potentials apply (Dunstan and White, 1990).

Here, theoretical conductivity increment spectra were fit to measured spectra by adjusting the ζ -potential, with bulk SDS concentration set equal to the c.m.c. at each added salt concentration, and other parameters as prescribed in table 3.3. Without accounting for added counterions and non-specific adsorption (SEKM₀), the ζ -potential agrees (within experimental errors) with values obtained from the spectroscopic surface potential measurements of Hartland et al. (1987), whereas SEKM_{ac/nsa} furnishes a much lower ζ -potential. Dynamic mobility spectra (calculated from the SEKM) are shown in figure 3.10 (and table 3.6) for both ζ -potentials. The higher mobilities calculated in this work agree with those measured from tracer electrophoresis of SDS solutions (Stigter and Mysels, 1955).

The apparent degrees of ionization calculated from the SEKM, using Eqn. (3.9) with $N_{agg} \approx 64$, are also consistent with values inferred by experiments: $\alpha \approx 0.160$ (from SEKM₀), $\alpha \approx 0.126$ (and SEKM_{ac/nsa}) (see table 3.6). However, calculating the degree of ionization as $\alpha = N/N_{agg}$, where N is the number of surface charges from the Poisson-Boltzmann equation, furnishes considerably larger $\alpha \approx 0.667$

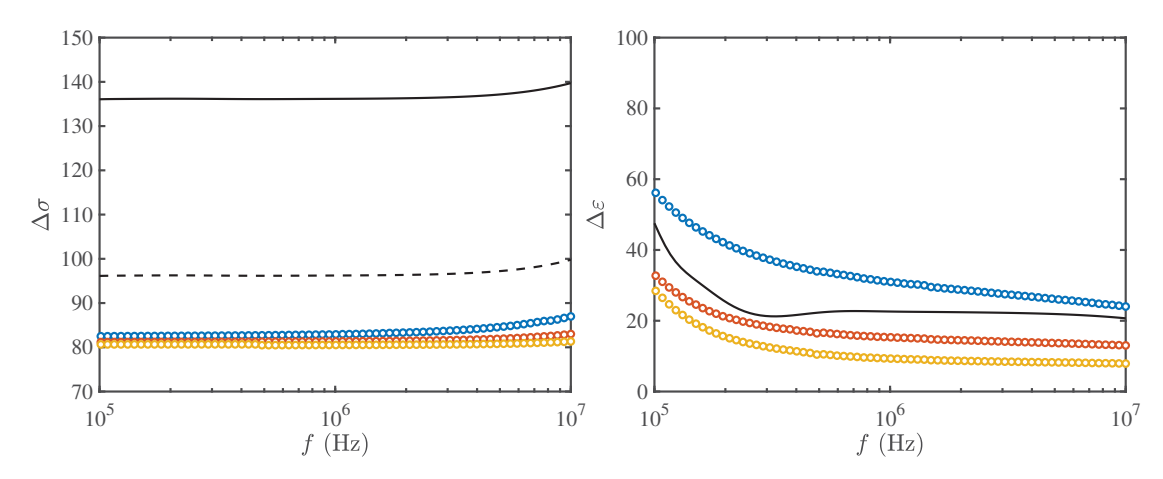


FIGURE 3.8: Conductivity (left) and dielectric constant (right) increments of SDS micelle solutions above the c.m.c. (c.m.c ≈ 8.18 mM, $\kappa a_m \approx 0.66$) with $c_{\infty} = 15$ (blue), 20 (red) and 30 mM (yellow) with no added salt. Solid lines are SEKM_{ac/nsa}, and dashed line is SEKM₀, both with $\zeta = -6.56~k_BT/e$, corresponding to a micelle charge $-N_{agg}e$ with dynamic mobility magnitude $|M_m| = 4.6 \times 10^{-8}~\text{m}^2~\text{V}^{-1}~\text{s}^{-1}$ at f = 0.1~MHz.

(from SEKM₀) and $\alpha \approx 0.302$ (and SEKM_{ac/nsa}). Thus, the lower values of α seem to reflect the shortcomings of the Hückel mobility, suggesting that non-linear electrostatics and, possibly, dynamic electrokinetic influences (polarization and relaxation) are ultimately responsible for the low apparent degrees of ionization reported in the literature. To test this hypothesis, we performed SEKM calculations with $\alpha = 1$, giving the results shown in figure 3.8 with no added salt. The resulting ζ -potential is $-6.56~k_BT/e$ with $\alpha \approx 0.17$ according to Eqn. (3.9).

Note that, with a prescribed $N_{agg} = 64$, the surface charge density, and hence the ζ -potential and conductivity increment, are sensitive to the prescribed micelle radius a_m . As shown in figure 3.9, increasing a_m from 2.23 nm to 2.43 nm brings the conductivity increment according to SEKM₀ into excellent agreement with the data. While an even larger increase could bring SEKM_{ac/nsa} into closer correspondence, it is not clear whether such an adjustment is reasonable. This requires more comprehensive experimental data on N_{agg} and a_m . In the absence of such data, it seems that, for SEKM_{ac/nsa} to bear closer correspondence to data, micelles must be considered much more dynamic, diffuse structures, rather than the compact, spherical bodies that they are customarily assumed to be.

TABLE 3.7: Scaled electrokinetic surface potential $-\zeta e/(k_BT)$ of SDS micelles from the present work and past literature.

	I_s	Present work (SEKM _{ac/nsa})	Present work (SEKM ₀)	Stigter and Mysels (1955)
Theory \rightarrow	(mM)	Hill et al. $(2003b,a,c)$	Hill et al. $(2003b,a,c)$	Booth (1951)
	0	3.42	5.3	3.92
	П	3.30	5.28	
	ರ	2.85	5.1	
	I_s	Stigter and Mysels (1955)	Stigter and Mysels (1955)	
Theory \rightarrow	(mM)	Hunter (1962)	O'Brien and White (1978)	
	0	5.3	5.6	
	\vdash		5.4	
	ರ		5.2	
	I_s	Dunstan and White (1990)	Hartland et al. (1987)	
Theory \rightarrow	(mM)	Saville (1983)		
		& Dunstan and White (1990)		
	0	6.4	5.7	
	\vdash	5.8	5.6	
	ಬ	5.1	4.73	

 $\overline{\text{SEKM}_{ac/nsa}}$ and $\overline{\text{SEKM}}_0$ are the $\overline{\text{SEKM}}$ without and including the contributions of added counter-ion and nonspecific adsorption.

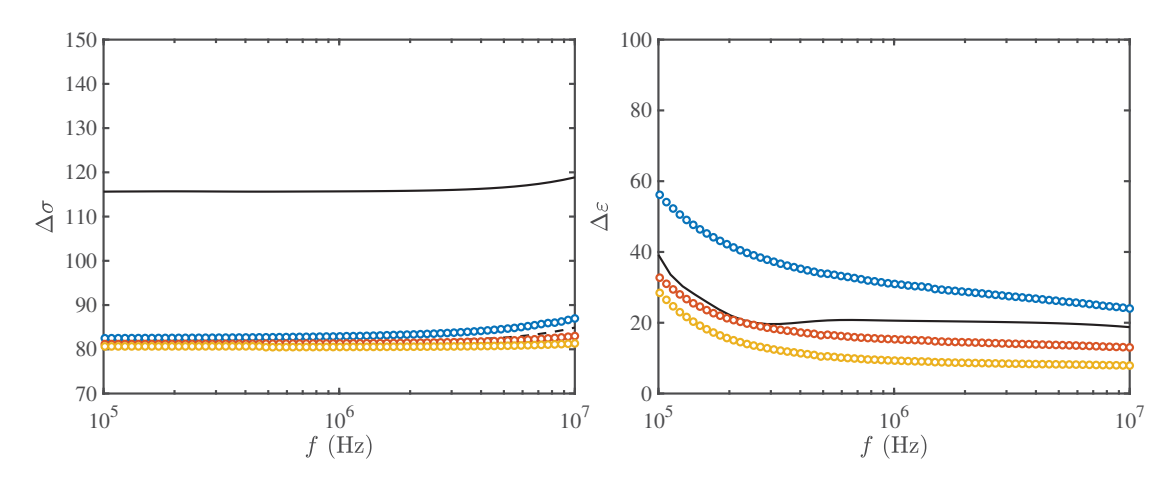


FIGURE 3.9: Same as figure 3.8, but with slightly larger $a_m = 2.43$ nm, giving $\kappa a_m \approx 0.72$.

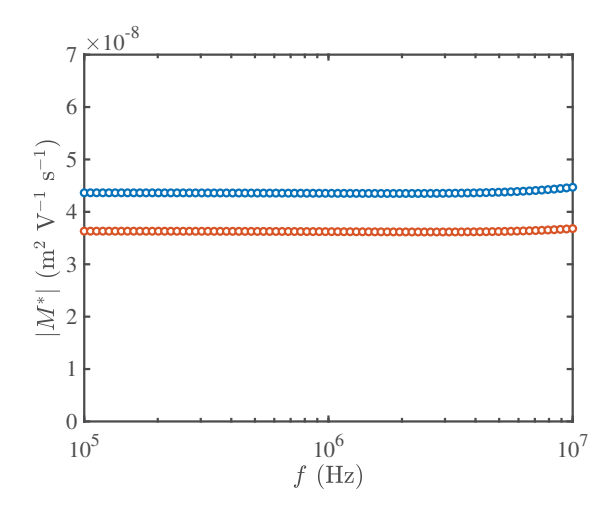


FIGURE 3.10: Dynamic mobility (according to the SEKM) of SDS micelles with no added salt for $\zeta = -5.2k_BT/e$ (blue) and $-3.4k_BT/e$ (red) with $\kappa a \approx 0.69$ obtained by fitting the SEKM to conductivity spectra, not accounting for (blue) and accounting for (red) for added counterions and non-specific adsorption. Phase angles (not shown) are in the range $-5-0^{\circ}$; these small values reflect the small particle size.

3.7 Conclusions

Dielectric relaxation spectroscopy has been used to measure the frequency-dependent conductivity of SDS micelle solutions. The conductivity of the surfactant solutions at different concentrations was used to determine the c.m.c. as a function of added NaCl concentration from the change in slope of the conductivity isotherm. The c.m.c. of SDS decreased with increasing NaCl concentration, consistent with previous literature (Dunstan and White, 1990, Moroi and Yoshida, 1997). The standard electrokinetic model was then adopted to interpret conductivity and dielectric constant spectra, using the ζ -potential as the fitting parameter. Two

different ζ -potentials were reported by accounting for (SEKM_{ac/nsa}) and neglecting (SEKM₀) the contribution of added counter-ions and non-specific adsorption. SEKM₀ furnished ζ -potentials in good agreement with independent experiments and interpretations in the literature that do not account for added counterions and non-specific adsorption. However, our application of SEKM_{ac/nsa} furnished a much lower ζ -potential, also furnishing an apparent charge for SDS micelles that is lower than previously thought. The actual degree of ionization estimated from the number of surface charges according to the Poisson-Boltzmann equation is larger than estimated from micelle mobility. Thus, our findings suggest that α should not be considered an actual degree of ionization, as suggested by the closed-association model, but rather a consequence of non-linear electrostatics, i.e., counterion condensation, arising from the high surface charge density.

3.8 Acknowledgement

This work was supported by NSERC Discovery and Research Tools and Instruments grants to R.J.H. G.A. was supported by a PRESSID/PTDF scholarship (Nigeria). Dr. C. Du is acknowledged for designing and constructing the dielectric spectrometer sample holder.

3.9 Author contributions

G.A. and R.J.H. designed the experiments. G.A. performed the experiments, analyzed the data, and conducted the SEKM calculations. G.A. and R.J.H. interpreted the data and wrote the paper.

Bibliography

- G. S. Aleiner and O. G. Us'yarov. Conductivity of micellar solutions of ionic surfactants and surface conductivity of micelles. *Colloid J.*, 72(5):588–594, 2010.
- P. Beltramo and E. Furst. A simple, single-measurement methodology to account for electrode polarization in the dielectric spectra of colloidal dispersions. *Chem. Lett.*, 41(10):1116–1118, 2012a.

- P. J. Beltramo. *Polarization and self-assembly of colloidal suspensions*. PhD thesis, University of Delaware, 2013.
- P. J. Beltramo and E. M. Furst. Transition from dilute to concentrated electrokinetic behavior in the dielectric spectra of a colloidal suspension. *Langmuir*, 28 (29):10703–10712, 2012b.
- F. Booth. The cataphoresis of spherical fluid droplets in electrolytes. *J. Chem. Phys.*, 19(11):1331–1336, 1951.
- G. Castellan. *Physical Chemistry*. The Benjamin/Cummings Publishing Co, 1982.
- E. H. B. DeLacey and L. R. White. Dielectric response and conductivity of dilute suspensions of colloidal particles. *J. Chem. Soc.*, Faraday Trans. 2, 77:2007–2039, 1981.
- D. E. Dunstan and L. R. White. An electrokinetic study of micellar solutions. *J. Colloid Interface Sci.*, 134(1):147 151, 1990.
- D. E. Dunstan and L. R. White. The dielectric response of dilute polystyrene latex dispersions. J. Colloid Interface Sci., 152(2):308 313, 1992.
- M. R. Gittings and D. A. Saville. Electrophoretic mobility and dielectric response measurements on electrokinetically ideal polystyrene latex particles. *Langmuir*, 11(3):798–800, 1995.
- G. V. Hartland, F. Grieser, and L. R. White. Surface potential measurements in pentanol–sodium dodecyl sulphate micelles. *J. Chem. Soc.*, Faraday Trans. 1, 83:591–613, 1987.
- J. B. Hayter and J. Penfold. Determination of micelle structure and charge by neutron small-angle scattering. *Colloid Polym. Sci.*, 261(12):1022–1030, 1983.
- R. J. Hill, D. Saville, and W. Russel. Polarizability and complex conductivity of dilute suspensions of spherical colloidal particles with charged (polyelectrolyte) coatings. J. Colloid Interface Sci., 263(2):478 – 497, 2003a.
- R. J. Hill, D. Saville, and W. Russel. Electrophoresis of spherical polymer-coated colloidal particles. *J. Colloid Interface Sci.*, 258(1):56 74, 2003b.
- R. J. Hill, D. A. Saville, and W. B. Russel. High-frequency dielectric relaxation of spherical colloidal particles. *Phys. Chem. Chem. Phys.*, 5:911–915, 2003c.

- A. Hollingsworth and D. Saville. A broad frequency range dielectric spectrometer for colloidal suspensions: cell design, calibration, and validation. *J. Colloid Interface Sci.*, 257(1):65 – 76, 2003.
- A. D. Hollingsworth and D. A. Saville. Dielectric spectroscopy and electrophoretic mobility measurements interpreted with the standard electrokinetic model. J. Colloid Interface Sci., 272(1):235 – 245, 2004.
- R. J. Hunter. The calculation of ζ -potential from mobility measurements. J. Phys. Chem., 66(7):1367–1368, 1962.
- M. Khademi and D. P. J. Barz. Dielectric relaxation spectroscopy of aqueous micellar electrolyte solutions: A novel application to infer dukhin number and zeta potential of a micelle. *Electrophoresis*, 40(5):710–719, 2019.
- L. Lanzi, M. Carlà, L. Lanzi, and C. M. Gambi. A new insight on the dynamics of sodium dodecyl sulfate aqueous micellar solutions by dielectric spectroscopy. J. Colloid Interface Sci., 330(1):156 – 162, 2009.
- S. C. Mangelsdorf and L. R. White. Dielectric response of a dilute suspension of spherical colloidal particles to an oscillating electric field. *J. Chem. Soc.*, Faraday Trans., 93:3145–3154, 1997.
- J. P. Marcolongo and M. Mirenda. Thermodynamics of sodium dodecyl sulfate (sds) micellization: An undergraduate laboratory experiment. J. Chem. Educ., 88(5):629–633, 2011.
- Y. Moroi and N. Yoshida. A new approach to micellization parameters: Its application to sodium dodecyl sulfate micelle. *Langmuir*, 13(15):3909–3912, 1997.
- R. W. O'Brien and L. R. White. Electrophoretic mobility of a spherical colloidal particle. *J. Chem. Soc.*, Faraday Trans. 2, 74:1607–1626, 1978.
- S. G. Oh and D. O. Shah. The effect of micellar lifetime on the rate of solubilization and detergency in sodium dodecyl sulfate solutions. *J. Am. Oil Chem. Soc.*, 70 (7):673–678, 1993.
- A. Patist, S. Oh, R. Leung, and D. Shah. Kinetics of micellization: its significance to technological processes. *Colloids Surf.*, A, 176(1):3 16, 2001.
- K. A. Payne, L. J. Magid, and D. F. Evans. Structural changes in anionic micelles induced by counterion complexation with a macrocyclic ligand: A neutron

- scattering study. In H. Hoffmann, editor, New Trends in Colloid Science, pages 10–17, Darmstadt, 1987. Steinkopff.
- L. A. Rosen and D. A. Saville. Dielectric spectroscopy of colloidal dispersions: Comparisons between experiment and theory. *Langmuir*, 7(1):36–42, 1991.
- M. J. Rosen. Surfactants and interfacial phenomena, volume 27. John Wiley & Sons, Inc., 2 edition, 1989.
- W. B. Russel, D. A. Saville, and W. R. Schowalter. *Colloidal Dispersions*. Cambridge University Press, Cambridge, UK, 1989.
- R. A. SAS. Conductivity: Theory and Practice. Radiometer analytical SAS, 2003.
- D. A. Saville. The electrical conductivity of suspensions of charged particles in ionic solutions: the roles of added counterions and nonspecific adsorption. J. Colloid Interface Sci., 91(1):34 50, 1983.
- P. C. Shanks and E. I. Franses. Estimation of micellization parameters of aqueous sodium dodecyl sulfate from conductivity data. *J. Phys. Chem.*, 96(4):1794–1805, 1992.
- D. Stigter. On density, hydration, shape, and charge of micelles of sodium dodecyl sulfate and dodecyl ammonium chloride. *J. Colloid Interface Sci.*, 23(3):379 388, 1967.
- D. Stigter and K. J. Mysels. Tracer electrophoresis. ii. the mobility of the micelle of sodium lauryl sulfate and its interpretation in terms of zeta potential and charge. J. Phys. Chem., 59(1):45–51, 1955.
- C. Tanford. Micelle shape and size. J. Phys. Chem., 76(21):3020–3024, 1972.
- O. G. Us'yarov. The electrical double layer of micelles in ionic surfactant solutions in the presence of a background electrolyte: 1. diluted micellar solutions of sodium dodecyl sulfate. *Colloid J.*, 69(1):95–102, 2007.
- K. Zhao and K. He. Dielectric relaxation of suspensions of nanoscale particles surrounded by a thick electric double layer. *Phys. Rev. B*, 74(20):205319, 2006.
- C. F. Zukoski and D. A. Saville. An experimental test of electrokinetic theory using measurements of electrophoretic mobility and electrical conductivity. J. Colloid Interface Sci., 107(2):322 333, 1985.

3.A Electrokinetic sonic amplitude of SDS micelle solutions

Electrokinetic sonic amplitude (ESA) measurements on surfactant solutions were undertaken in the frequency range 1–20 MHz, as shown in figures 3.11 and 3.12. Present formulas do not permit the conversion of ESA spectra to dynamic mobility, because they are limited to colloidal dispersions for which a thin-double-layer approximation is necessary ($\kappa a \gg 1$); otherwise computations are necessary. However, the DC conductivity reported by the ESA instrument can still be useful for identifying micelle formation. These data are provided in the caption of figure 3.11.

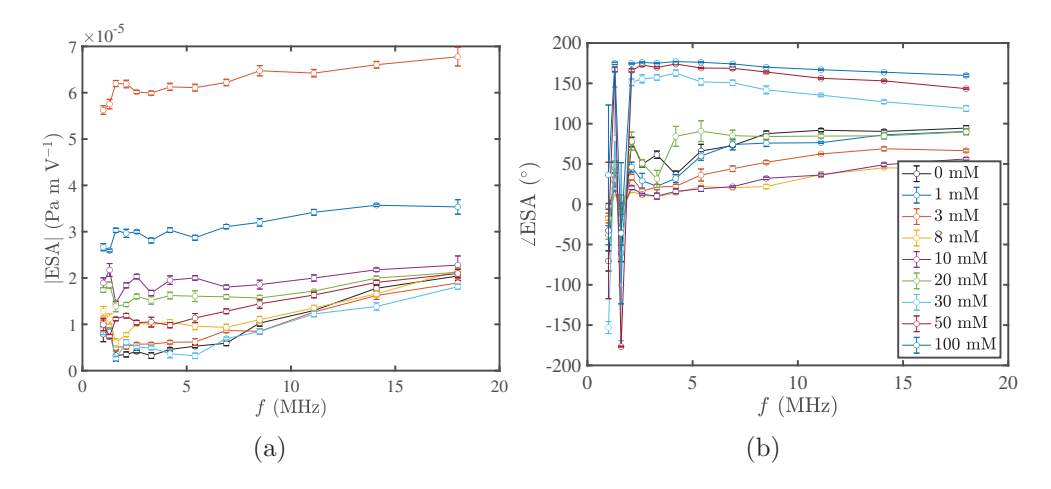


FIGURE 3.11: ESA spectra for SDS concentrations $c_{\infty} = 0$, 1, 3, 8, 10, 20, 30, 50, and 100 mM with NaCl concentration [NaCl] = 1 mM. Black line is the ESA for a 1 mM NaCl solution without SDS. Conductivities (from the ESA instrument) are $\sigma = 0.012$, 0.019, 0.031, 0.059, 0.063, 0.085, 0.107, 0.152, and 0.272 S m⁻¹.

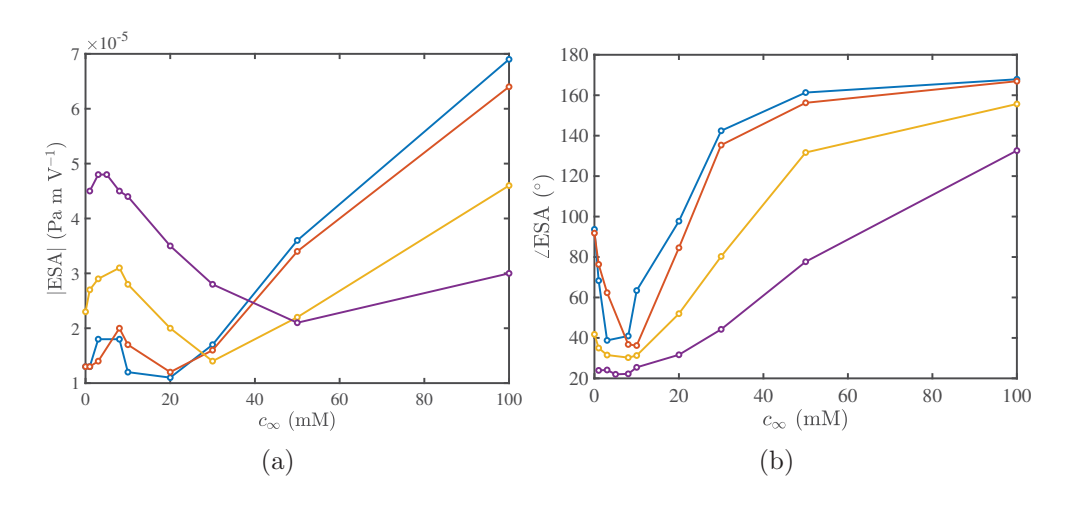


FIGURE 3.12: ESA magnitude and phase angle at f=11.1 MHz versus SDS concentration with added NaCl concentrations [NaCl] = 0 (blue), 1 (red), 10 (yellow), and 20 (violet) mM.

Chapter 4

Electrokinetic interpretation of polystyrene latices

4.1 Preface

A lack of consensus between experimental and theoretical studies of colloidal dispersions is often attributed to limitations of the standard electro-kinetic model to account for all contributions to colloidal dynamics. However, the presence of hairy layers, and sample preparation protocols for experiments may also introduce artifacts. Here, dielectric relaxation spectroscopy is used to probe polystyrene latices in electrolyte solutions. Particular attention is given to the potential contributions of added counterions and non-specific adsorption, which have not been adequately considered in previous literature, and the potential presence of hairy layers.

4.2 Abstract

Dielectric relaxation spectroscopy is used to characterize polystyrene latex dispersions. The conductivity and dielectric constant increments are theoretically interpreted using standard-electrokinetic models for bare and soft spheres, using the manufacturer's titratable charge as a basis. However, modelling the latices as bare spheres with immobile surface charge, using the manufacturer's titratable surface charge density and size under-predicted the measured increments, even when

accounting for added counterions and non-specific adsorption. The standard electrokinetic model under-predicts conductivity increment spectra. Increasing the charge density, e.g., to account for deswelling—as suggested by comparing DLS and TEM sizes—brought the theory closer to experiments, but also increased the slope of the conductivity increment with respect to frequency. We then adopted a soft-sphere model for a hairy polyelectrolyte surface, adjusting its charge density, thickness and permeability. Fitting the measured conductivity increment required the charge on the hairy layer to be \approx 5-fold higher than prescribed by the titratable charge.

4.3 Introduction

Electric-field induced double-layer polarization provides valuable insights on the electrical and structural properties of colloidal dispersions such as electrokinetic charge, particle size, degree and tendency for self-assembly etc. (Saville, 1983, Rosen and Saville, 1991, Gittings and Saville, 1995, Hill et al., 2003b, Beltramo and Furst, 2012b). Experimental studies in relevant frequency ranges are possible using dielectric relaxation and electroacoustic spectroscopies. Theoretical models to interpret these experiments have been proposed over the last two decades (Saville, 1979, DeLacey and White, 1981, Saville, 1983, Mangelsdorf and White, 1992, 1997), but the limitations of these models for "non ideal" colloidal latices are often attributed to the effects of added counterions, non-specific adsorption, and the possibility of other transport processes behind the shear plane. Non-ideal latices are defined as those for which complementary measurements of the same property disagree (Saville, 1983, Shubin et al., 1993, Hunter, 2004).

The contribution of added counterions to colloidal dispersion conductivity refers the change in ion density in both the electrical double layer and the bulk electrolyte due to surface charge of colloidal latices, while the subsequent redistribution of the ion cloud because of the attraction of counter- and repulsion of co-ions is termed non-specific adsorption (Loeb et al., 1961, Saville, 1979). The extent to which both terms contribute to the conductivity of colloidal suspensions is not well understood e.g. the influence of the volume occupied by uncharged latices, and change in co-ion concentration in the electrical double layer to conductivity have been stated as insignificant (Stigter, 1979) and significant (Saville, 1983). Accurately accounting for their contribution when comparing experiments and theoretical predictions

requires an understanding of the behaviour of model colloidal spheres in electrolyte solutions (Rosen and Saville, 1991, Gittings and Saville, 1995, Hollingsworth and Saville, 2004)

Here, dielectric relaxation spectra of polystyrene latices in potassium chloride solutions were interpreted using the standard electrokinetic model of Hill et al. (2003a,b) as solved by the MPEK package for bare spheres. The contributions of added counterions and non-specific adsorption due to particle surface charge were duly accounted for, and the SEKM-furnished electrokinetic charge was compared to the manufacturer's titratable charge. The possibility of charge-carrying hairy layers on latices was also probed.

4.4 Materials and methods

Dispersions of polystyrene spheres were prepared from 8 w/v% sulfate latex bead suspensions (TEM diameter $\approx 210 \pm 0.006$ nm, batch A: Lot #1850680 ($\sigma = 0.6~\mu\text{C cm}^{-2}$), batch B: Lot # 638478 ($\sigma = 1.3~\mu\text{C cm}^{-2}$), Life Technologies Inc.). Electrolyte solutions were prepared from KCl powder (Sigma-Aldrich Canada Co.). All materials, except the latices, were used as provided by the manufacturer.

4.4.1 Dispersion preparation and cleaning protocol

To obtain the required volume fractions, concentrated latex dispersions were diluted to 1 w/v % with the background salt solution, and washed using a centrifugation-decantation procedure (Beltramo and Furst, 2012b). Dilute suspensions were centrifuged at 17,000 g for 45 minutes, decanted and re-dispersed using the desired background salt solution. The conductivity of the supernatant was measured using a conductivity probe after each step till it became approximately equal (6% deviation on average) to the background salt conductivity (after 4–5 repeats). The subnatant was re-dispersed in 1 ml of background salt solution to form a concentrated suspension, and 200 μ l of the concentrated suspension was measured, weighed, and dried in an oven at $T=60^{\circ}\mathrm{C}$ to estimate the new concentration of the suspension. Different volume fractions were obtained by diluting the final redispersed suspension with a prescribed volume of background electrolyte. Samples

were sonicated for 10 min in a water-bath sonicator, and sample impedance was measured using an impedance analyzer with a parallel electrode configuration.

4.4.2 Dielectric relaxation spectra measurements

Dielectric spectroscopy was undertaken as detailed by Afuwape and Hill (2020, Ch. 3). The instrument comprises an in-house sample cell with parallel stainless steel electrodes and an acrylic spacer, which is connected to a Keysight E4990A impedance analyzer. Corrections for electrode polarization were undertaken using the single-spacer approach (Beltramo and Furst, 2012a). Following Hollingsworth and Saville (2003), the sample admittance ("raw" measurement) is expressed as

$$Y_{tot}^* = \frac{A}{2h} \left[\sigma(\omega) + i\omega \varepsilon_0 \varepsilon_{app}'(\omega) \right], \tag{4.1}$$

where $\sigma(\omega) \equiv \sigma_{\infty} - \omega \varepsilon_0 \varepsilon''(\omega)$ is the complex conductivity (σ_{∞} is the conductivity, ε_0 is the vacuum permittivity, $\varepsilon''(\omega)$ is the dielectric loss, and $\omega = 2\pi f$ is the angular frequency), ε'_{app} is the apparent dielectric constant, and A/(2h) the cell constant with A the electrode area in contact with the sample and 2h the spacer thickness. Moreover, the apparent dielectric constant

$$\varepsilon_{app}'(\omega) = \varepsilon_{\infty} \beta \frac{1 + \beta(\omega/\kappa^2 D)^2}{1 + \beta^2(\omega/\kappa^2 D)^2},$$
(4.2)

where ε_{∞} is the solvent dielectric constant, $\beta = \kappa h$ is the scaled electrode separation, κ is the reciprocal Debye length, and D is the mean ion diffusion coefficient. To correct for the effects of electrode polarization, Eqn. (4.2) was fit to measured ε'_{app} with D the fitting parameter. Such fits are demonstrated in figure 4.1 for 0.1 and 1 mM KCl solutions, furnishing $D \approx 3.11 \times 10^{-9}$ and 2.54×10^{-9} m² s⁻¹, respectively. Note that the contribution of electrode polarization to "raw" conductivity measurements is negligible (see Eqn. (4.3)) (Hollingsworth and Saville, 2003).

$$\sigma_{app}(\omega) = \sigma_{\infty} \frac{\beta^2 (\omega/\kappa^2 D)^2}{1 + \beta^2 (\omega/\kappa^2 D)^2}.$$
 (4.3)

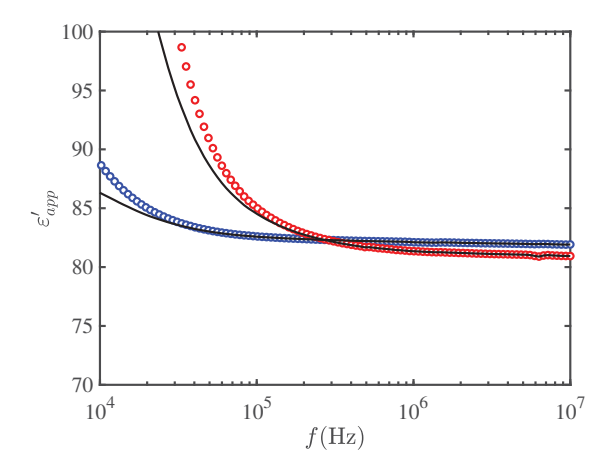


FIGURE 4.1: Fits of Eqn. (4.2) to dielectric constant data for KCl solutions with $I_s = 0.1$ (blue) and 1 mM (red).

Table 4.1: Parameters as input for SEKM calculations of the mobility and conductivity increment for polystyrene latex particles at infinite micelle dilution, i.e., at the c.m.c. These data at $T=25~^{\circ}\mathrm{C}$.

Parameter	Value	Units	Source
2a	200	nm	Life Technologies Inc.
[KCl]	0.1 - 1	mM	Measured
$[HCO_3^-] = [H_3O^+]$	3.2	$\mu\mathrm{M}$	Beltramo and Furst (2012b)
λ_{K^+}	73.48	${\rm S~cm^2~equiv^{-1}}$	Beltramo and Furst (2012b)
λ_{Cl^-}	76.31	${\rm S~cm^2~equiv^{-1}}$	Beltramo and Furst (2012b)
$\lambda_{H_3O^+}$	349.65	${\rm S~cm^2~equiv^{-1}}$	Beltramo and Furst (2012b)
$\lambda_{HCO_3^-}$	44.5	$S cm^2 equiv^{-1}$	Beltramo and Furst (2012b)
$arepsilon_m$	2.6		
$arepsilon_{\infty}$	78.54		
$ ho_m$	1055	$ m kg~m^{-3}$ $ m kg~m^{-3}$	Beltramo and Furst (2012b)
$ ho_{\infty}$	997	${\rm kg~m^{-3}}$	Beltramo and Furst (2012b)

4.4.3 SEKM calculations

The MPEK package was used to perform SEKM calculations (Hill et al., 2003b). This is based on the model of Hill et al. (2003a) for spherical colloids with an impenetrable core and a soft corona that has nominal polymer coating thickness L, segment density N_s , hydrodynamic segment size a_s , and fixed-charge density N_f . Calculations for bare spheres are undertaken by setting the hydrodynamic polymer segment size and charge density to zero. Similarly to Beltramo (2013), the concentration of dissolved carbonate ions (with hydronium to respect bulk electroneutrality) was set to 3.2 μ M.

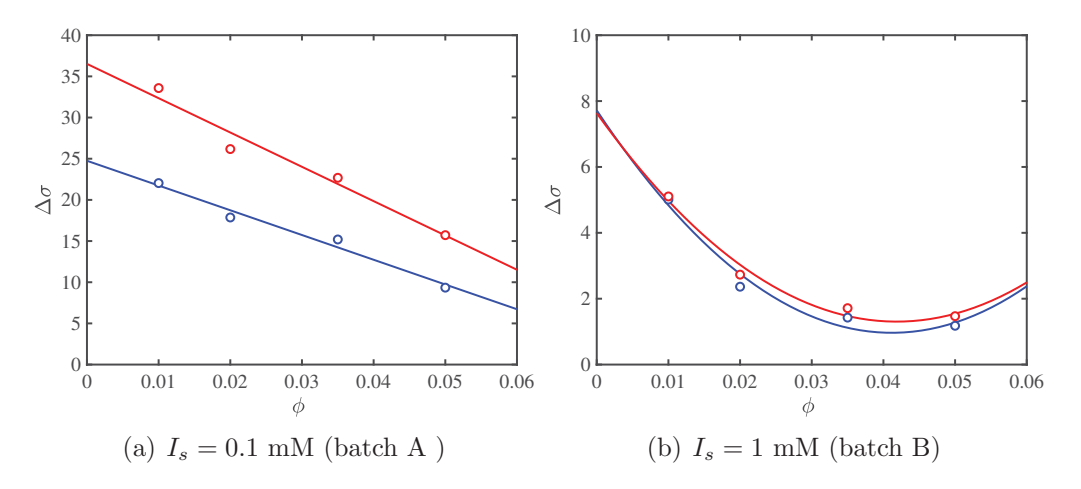


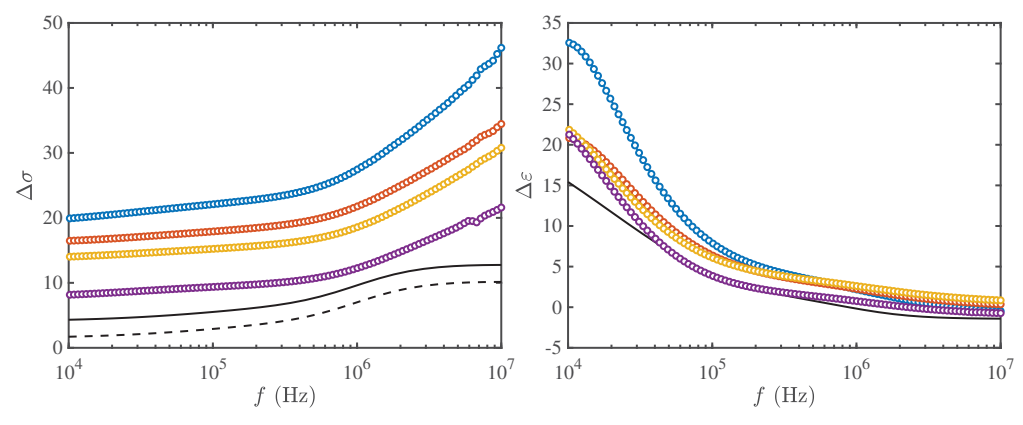
FIGURE 4.2: Conductivity increments of 200 nm diameter polystyrene spheres in aqueous KCl solutions versus ϕ : f=1 kHz (blue) and f=1 MHz (red). Lines are fit to data with $\Delta \sigma = \Delta \sigma_0 (1-a\phi)$ and $\Delta \sigma = \Delta \sigma_0 (1-a\phi+b\phi^2)$ for 0.1 and 1 mM, respectively.

Table 4.2: Model parameters obtained from the fit of conductivity increment data (plotted in figure 4.2) to $\Delta \sigma = \Delta \sigma_0 (1 - a\phi)$ and $\Delta \sigma = \Delta \sigma_0 (1 - a\phi + b\phi^2)$.

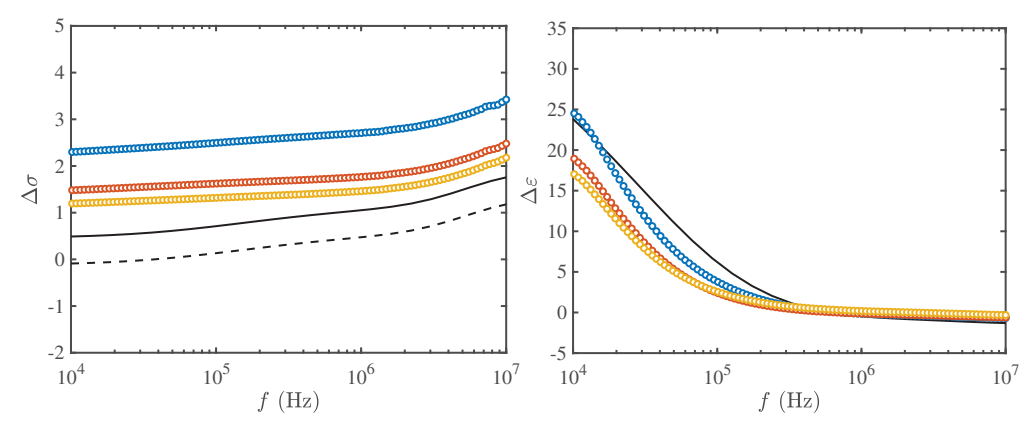
$\overline{I_s}$	f	$\Delta \sigma_0$	a	b
(mM)	(MHz)	-	-	-
0.1	0.001	24.75	12.14	_
0.1	1	36.52	11.41	-
1	0.001	7.72	42.49	516
1	1	7.63	39.63	473

4.5 Results and discussion

Figure 4.2 shows how the conductivity increment depends on volume fraction. These are shown at at f=1 kHz and 1 MHz to identify differences at low and high frequency. For 0.1 mM KCl solutions, there is a monotonic decrease in the increment with ϕ as resulting from excluded-volume and diffuse double-layer interactions. For latices in 1 mM KCl solutions, non-linear variations were observed. The transition from linear to non-linear (quadratic) dependence of conductivity increment on volume fraction when increasing salt concentration is similar to that reported by Zukoski and Saville (1985), who could not attribute the change to ionic impurities or flaws in the cleaning protocol. It is not clear why the implied interactions are stronger at the higher ionic strength (see table 4.2 for fitting parameters), but it should be noted that the latices with higher ionic strength also bear a higher surface charge.



(a) $I_s = 0.1$ mM KCl, with $\phi = 0.01$ (blue), 0.02 (red), 0.035 (yellow), 0.05 (violet), and $\sigma = -0.6~\mu\text{C cm}^{-2}$ (batch A)



(b) $I_s=1$ mM KCl, with $\phi=0.02$ (blue), 0.035 (red), 0.05 (yellow), and $\sigma=-1.3~\mu{\rm C~cm^{-2}}$ (batch B)

FIGURE 4.3: Conductivity (left) and dielectric constant (right) increments of 200 nm diameter polystyrene latices in electrolyte solutions. SEKM calculations are undertaken with the manufacturer's surface charge density for each batch ($\sigma \approx -0.6$ (panel a) and -1.3 (panel b) $\mu \rm C \ cm^{-2}$). Solid lines account for added counterions and non-specific adsorption.

Conductivity and dielectric increment spectra for 200 nm diameter polystyrene spheres in 0.1 and 1 mM KCl are shown in figure 4.3. Here, the theoretical calculations are undertaken for bare spheres using the the manufacturer's reported titratable surface charge densities: $\sigma \approx 0.6~\mu\text{C}~\text{cm}^{-2}$ for 0.1 mM KCl concentration and 1.3 $\mu\text{C}~\text{cm}^{-2}$ for 1 mM KCl concentration. The SEKM is for for infinite dilution. The increase in conductivity increment with frequency is a consequence of the imaginary part of dipole moment enhancing the macroscopic current density. The dielectric constant spectra quantify the polarizable charge relaxation. This diminishes at high frequencies due to the diffuse-layer polarization becoming weak compared to the dielectric polarization (Rosen and Saville, 1991, Hill et al., 2003a).

The offset between theory and data in figure 4.3 (dashed lines) is consistent with

that of Beltramo and Furst (2012b) for polystyrene latices in 0.01–1 mM KCl electrolytes. They performed SEKM calculations to determine the conductivity increment to subtract from their data, furnishing a corrected conductivity increment that agreed with the SEKM calculations without added counterions (a.c.) and non-specific adsorption (n.s.a.). Note that a frequency-independent correction was calculated from the SEKM using the mole-fraction averaged a.c. and n.s.a. conductivity increments for K^+ and H_3O^+ as the counterion. Nevertheless, for calculations undertaken here, K^+ was assumed to be the only counterion, since we expect the cleaning protocol to result in the exchange of surface H_3O^+ counterions with K^+ . This approximation is justified by noting that the mole-fraction weighted contribution of dissolved CO_2 to a.c and n.s.a of polystyrene lattices in a 1 mM KCl background electrolyte is $\approx 5\%$ (Beltramo and Furst, 2012b, SI).

Adopting conventions of Hill et al. (2003a), the effective conductivity may be expressed as

$$\sigma_e = \sigma_{\infty} \left[1 + \phi(\Delta \sigma + \Delta \sigma') + \mathcal{O}(\phi^2) \right], \tag{4.4}$$

where σ_{∞} is the electrolyte conductivity, $\Delta \sigma$ is the frequency-dependent conductivity increment, $\Delta \sigma'$ is the frequency-dependent conductivity increment due to added counterions and non-specific adsorption, and ϕ is the particle volume fraction.

The added counter-ion contribution arises from the change in ion densities in the bulk due to the surface-charge dissociation. The average number density of added counter-ion is $n_1^c = -Qn_p/(z_1^c e)$, with $n_p = 4\pi a^3/(3\phi)$ and σ the number of counterions per unit surface area, with Q the charge per particle, and a the particle radius. These additional mobile ions, which are distributed in the bulk, result in a redistribution of ionic species to maintain bulk electro-neutrality. According to Hill et al. (2003a), this non-specific adsorption process alters the bulk electrolyte concentration by an amount

$$\delta n_j^{\infty} = n_p n_j^{\infty} \kappa^{-3} \int_{\kappa a}^{\infty} [1 - \exp(-z_j \psi^0)] 4\pi r^2 dr, \qquad (4.5)$$

and total conductivity increment due to added counterions and non-specific adsorption is

$$\Delta \sigma' = \frac{\sum_{j=1}^{N} (n_j^c / \phi + \delta n_j^{\infty} / \phi) z_j^2 D_j}{\sum_{j=1}^{N} n_j^{\infty} z_j^2 D_j}.$$
 (4.6)

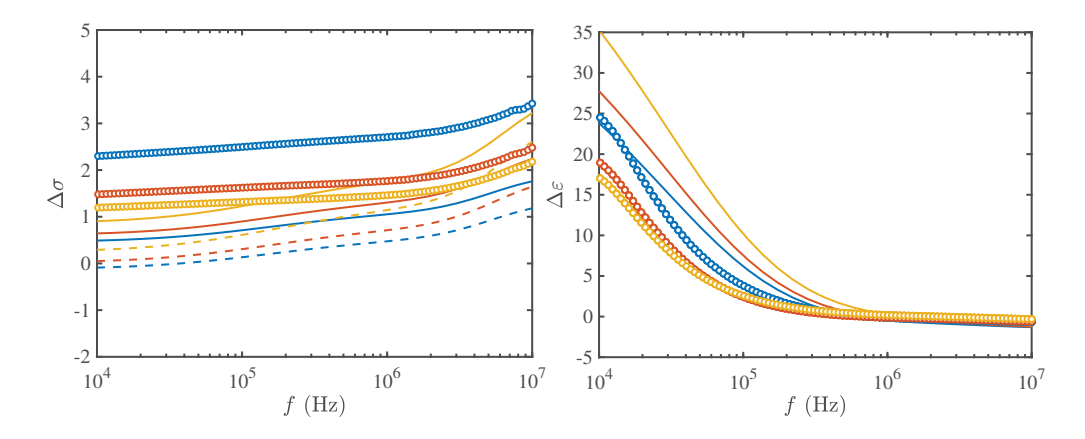


FIGURE 4.4: Conductivity (left) and dielectric constant (right) increments of 200 nm diameter polystyrene latices (batch B with $\sigma = -1.3~\mu\text{C cm}^{-2}$) in $I_s = 1~\text{mM}$ KCl electrolyte solutions with $\phi = 0.02$ (blue), 0.035 (red), 0.05 (yellow). SEKM calculations for bare spheres (lines) are undertaken with different surface charge densities: $\sigma \approx -1.3$ (blue), -1.5 (red) and -1.9 (yellow) $\mu\text{C cm}^{-2}$). Solid lines account for added counterions and non-specific adsorption.

4.5.1 Bare-sphere SEKM interpretation

The solid lines in figure 4.3 account for these contributions to the conductivity increment with K⁺ as the counterion, but there are still ostensible disparities. Note that the best-fit surface charge reported by Beltramo and Furst (2012b) ($\sigma = -1.6 \,\mu\text{C cm}^{-2}$) was higher than the manufacturer's reported titratable charge ($\sigma = -1.3 \,\mu\text{C cm}^{-2}$) for 200 nm lattices in 1 mM KCl aqueous solution, after subtracting a frequency-independent value from their data. The difference can be attributed to charge behind the slipping plane, i.e., within then Stern layer. Their dynamic light scattering (DLS) revealed a slightly smaller particle size as compared to the manufacturer's size by TEM (Beltramo, 2013). This suggests that the latices in aqueous solution may bear a higher surface charge density than inferred by the manufacturer's titratable charge.

In figure 4.4, the surface charge was increased for polystyrene latex in 1 mM KCl solutions, to account for a possible increase in the surface charge density due to deswelling in an aqueous medium (as compared to the vacuum in which TEM size is determined). Comparing the theoretical calculations in figures 4.3(b) and 4.4 shows that increasing the surface charge density does not shift the increment spectra uniformly with respect to frequency, thus prohibiting a satisfactory fit.

4.5.2 Hairy-layer interpretation

The possibility of polystyrene latices having hairy layers is widely reported (van der Put and Bijsterbosch, 1983, Rosen and Saville, 1991, Gittings and Saville, 1995, Seebergh and Berg, 1995). Beltramo and Furst (2012b) perform SEKM calculations invoking charged and uncharged hairy layers with a bare surface bearing a prescribed surface charge. A hairy layer produced subtle changes in the dielectric spectra. For charged layers, an arbitrary nominal charge density was added to the bare sphere to probe the effect on the double layer dynamics in comparison with an equivalent bare particle.

Here, we modelled the lattices as hairy spheres according to the soft-sphere model of Hill et al. (2003a), assuming instead that all the charge resides on the hairy layer. These calculations were undertaken with a step-like segment density $n_s = 0.5N_s \operatorname{erfc}[(r-L)/\delta]$ using $\delta = 0.1L$.

The nominal fixed ion density was prescribed using the manufacturer's titratable charge as $N_f = \sigma/(ezL)$ (assuming $L \ll a$). For example, for $\sigma = 1.3~\mu\text{C cm}^{-2}$ with L = 5 nm gives $N_f \approx 0.026$ M. Note that polymer coatings for polystyrene latices have been reported $\sim 3-7$ nm thick (Seebergh and Berg, 1995). The values of N_s and a_s prescribe the coating hydrodynamic permeability via the nominal Brinkman screening length

$$\ell_B = 1/\sqrt{n_s 6\pi a_s F_s} = a_s/\sqrt{9\phi_s F_s/2}$$
 (4.7)

where the segment volume fraction $\phi_s = n_s 4\pi a_s^3/3$ and the drag coefficient $F_s > 1$ increases with ϕ_s (Hill et al., 2003a).

Note that electroosmotic and hydrodynamic flow in the layer increases when increasing ℓ_B with respect to L (Hill et al., 2003a). To have a coating with nominal Brinkman screening length comparable to values obtainable from electrophoretic mobility measurements, N_s and a_s were first selected to establish $\ell_B(N_s, a_s) \sim L$; e.g., with $N_s = 0.33$ M and $a_s = 1$ Å, we find $\ell_B \approx 1.7$ nm. Table 4.3 reports the various Brinkman screening lengths calculated from Eqn. (4.7).

In figure 4.5, for polystyrene latices (batch B) in 1 mM KCl solution, the fixed charge was varied (at constant coating thickness L) from 27 mM to 108 M, an \approx 5-fold increase in the fixed charge—with respect to the manufacturer's titratable

TABLE 4.3: Brinkman screening lengths ℓ_B from a nominal segment density N_s and segment radius a_s .

$\overline{N_s}$	a_s	ℓ_B
(M)	(Å)	(nm)
0.134	9.5	0.83
0.134	0.95	2.63
0.134	0.0095	26.8
13.40	0.95	0.26
1.34	0.95	0.82
0.13	0.95	2.63

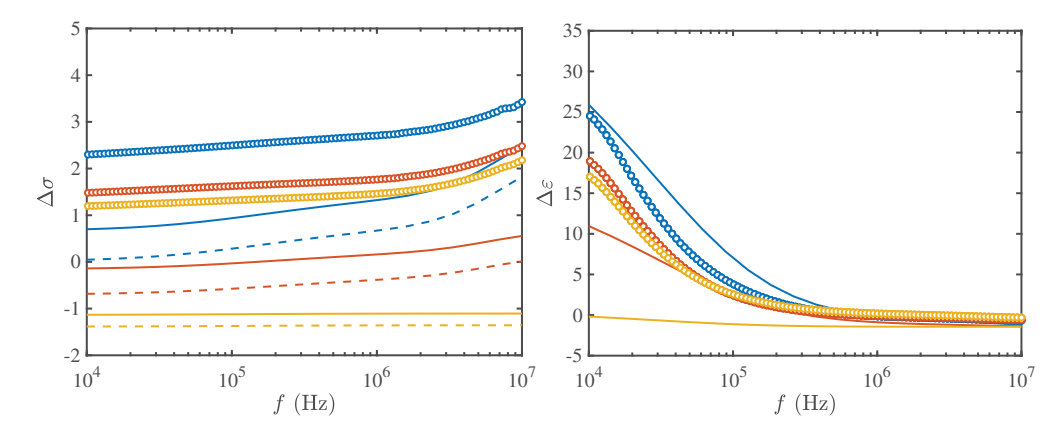


FIGURE 4.5: Conductivity (left) and dielectric constant (right) increments of 200 nm diameter polystyrene latices (batch B) in $I_s = 1$ mM KCl electrolyte solutions, with $\phi = 0.02$ (blue), 0.035 (red), 0.05 (yellow). SEKM calculations for soft spheres (lines) are undertaken with a hairy layer thickness L = 5 nm, fixed charge densities $N_f = 0.027$ (yellow), 26.9 (red), and 107.6 (blue) M, and Stokes segment density $N_s = 0.13$ M and radius $a_s = 0.95$ Å (Brinkman length $\ell_B \approx 2.63$ nm). Solid lines account for added counterions and non-specific adsorption.

charge—achieves the best correspondence with lower frequency deviations still apparent. However, it is difficult to justify such a high charge.

To explore the effect of coating segment density on the conductivity increment spectra, N_s is varied at a constant segment size in figure 4.6. This does not improve the model fit. Note that conductivity and dielectric constant increments increased with decreasing N_s . This is because there is a significant contribution to the polarization from electroosmotic flow in the hairy layers when increasing the permeability. Thus, a similar effect comes from decreasing a_s (see figure 4.7).

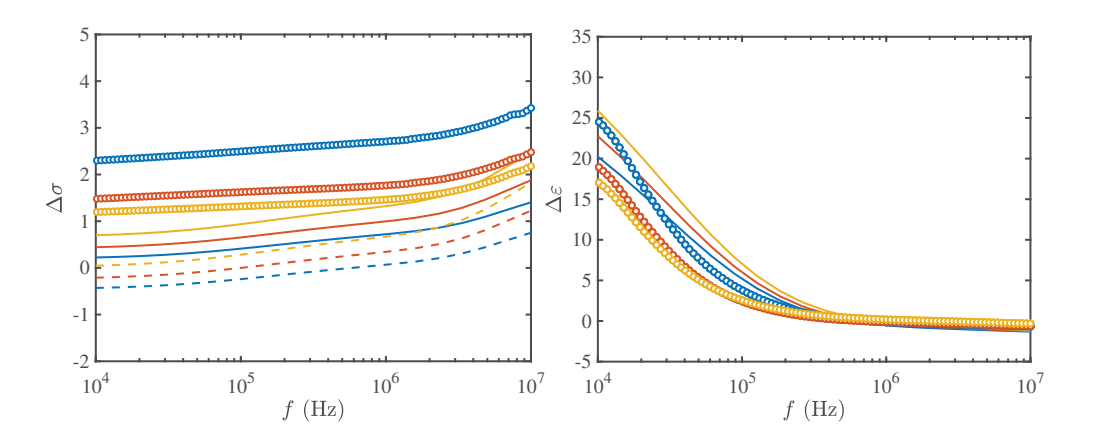


FIGURE 4.6: Hair-layer interpretation of conductivity (left) and dielectric constant (right) increments of 200 nm diameter polystyrene lattices (batch B) in $I_s = 1$ mM KCl (circles) with $\phi = 0.02$ (blue), 0.035 (red), 0.05 (yellow). SEKM calculations for soft spheres (lines) are undertaken with a hairy layer thickness L = 5 nm, fixed charge density $N_f = 108$ M, Stokes segment density $N_s = 13.4$ (blue), 1.34 (red), and 0.13 (yellow) M, and Stokes radius $a_s = 0.95$ Å (the corresponding Brinkman lengths are reported in table 4.3). Solid lines account for added counterions and non-specific adsorption.

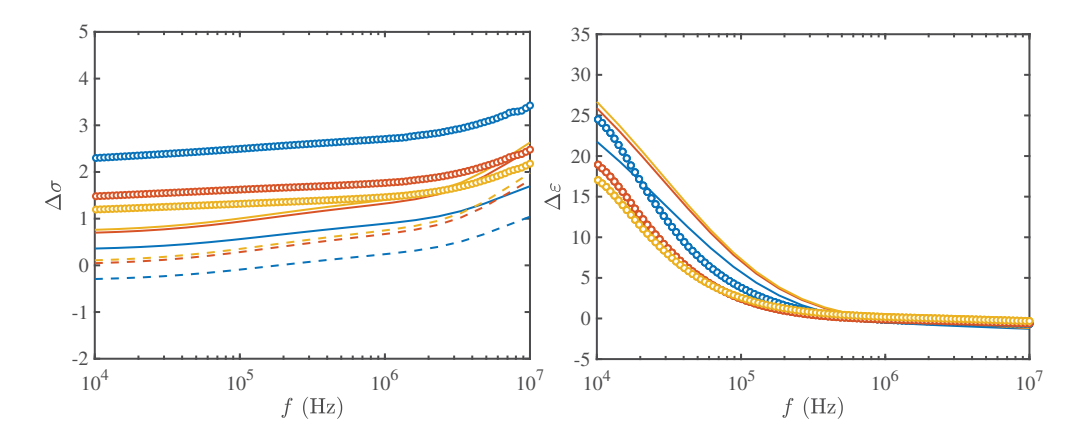


FIGURE 4.7: Conductivity (left) and dielectric constant (right) increments of 200 nm diameter polystyrene latices (batch B) in $I_s = 1$ mM KCl electrolyte solutions (circles), with $\phi = 0.02$ (blue), 0.035 (red), 0.05 (yellow). SEKM calculations for soft spheres (lines) are undertaken with a hairy layer thickness L = 5 nm, fixed charge densities $N_f = 107.6$ M and Stokes segment density $N_s = 0.13$ M, and segment radius $a_s = 9.5$ (blue), 0.95 (red) and 0.0095 (yellow) Å (the corresponding Brinkman lengths are reported in table 4.3). Solid lines account for added counterions and non-specific adsorption.

4.6 Counterion identity

Surface-bound sulphate groups infer that the added counterions of the as procured latices are H_3O^+ . However, centrifugation and re-dispersion with prescribed background KCl concentration dilutes H_3O^+ so the post-cleaning bulk electrolyte concentration is set by the added KCl with concentration $[K^+]_0 = [Cl^-]_0$. The average counterion concentration

$$[X^{+}]_{0} = -\sigma 4\pi a^{2} \phi / (4\pi e a^{3}/3) = -3\sigma \phi / (ea), \tag{4.8}$$

where σ is the (titratable) surface charge density, and ϕ is the particle volume fraction. SEKM calculations require an electroneutral bulk, therefore, in an electrolyte with only KCl, the bulk ion concentrations must satisfy

$$[K^{+}]_{0} = [Cl^{-}]_{0}.$$
 (4.9)

If we introduce H_3O^+ ions to the bulk (from the surface charging), then the bulk ion concentrations (neglecting any OH^-) must satisfy

$$[K^{+}]_{\infty} + [H_{3}O^{+}]_{\infty} = [Cl^{-}]_{\infty}$$
 (4.10)

with $[Cl^-]_{\infty} = [Cl^-]_0$.

If we now invoke the ansatz

$$[H_3O^+]_{\infty} \approx [X^+]_0 + O(\phi^2),$$
 (4.11)

then Eqns. (4.8)-(4.11) give

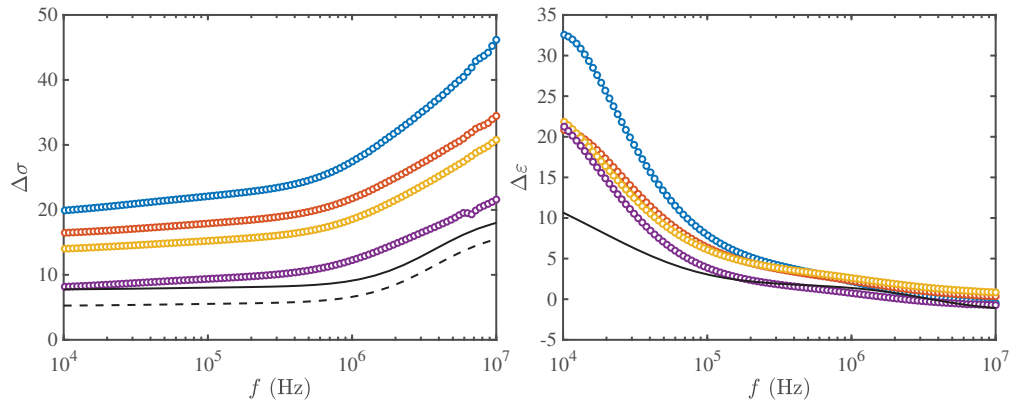
$$[H_3O^+]_{\infty} \approx \frac{1}{1/(-3\sigma\phi/ea) + 1/[K^+]_0} + O(\phi^2),$$
 (4.12)

and

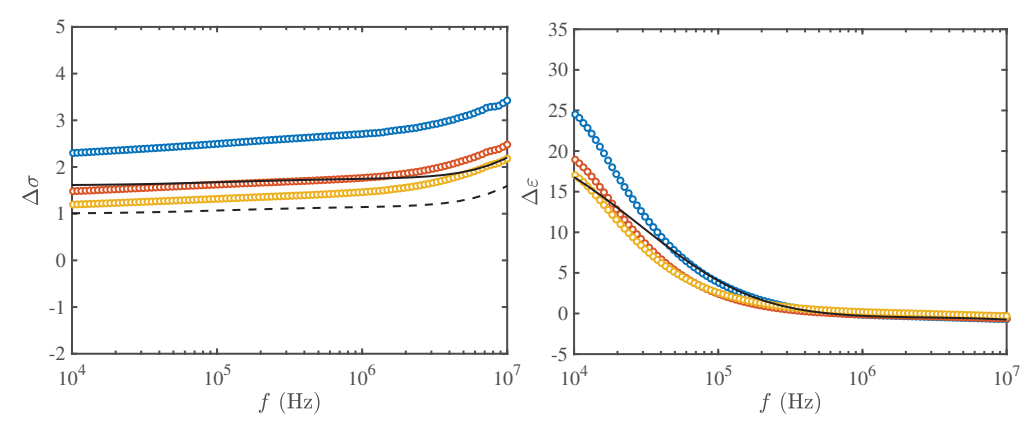
$$[K^{+}]_{\infty} \approx \frac{[K^{+}]_{0}}{1 + (-3\sigma\phi/ea)/[K^{+}]_{0}} + O(\phi^{2}),$$
 (4.13)

Note that pH should be measured to assess the H₃O⁺ concentration.

Figure 4.8 compares experiments to the SEKM with the bulk concentrations of K^+ and H_3O^+ according to Eqns. (4.12) and (4.13) with $\phi = 0.03$, and with H_3O^+ as the counterion in the SEKM calculations. This provides better correspondence,



(a) $I_s=0.1$ mM KCl, with $\phi=0.01$ (blue), 0.02 (red), 0.035 (yellow), 0.05 (violet), and $\sigma=-0.6~\mu\mathrm{C~cm^{-2}}$ (batch A)



(b) $I_s=1$ mM KCl, with $\phi=0.02$ (blue), 0.035 (red), 0.05 (yellow), and $\sigma=-1.3~\mu{\rm C~cm^{-2}}$ (batch B)

FIGURE 4.8: Conductivity (left) and dielectric constant (right) increments of 200 nm diameter polystyrene latices in electrolyte solutions. SEKM calculations are undertaken with the manufacturer's surface charge density for each batch ($\sigma \approx -0.6$ (panel a) and -1.3 (panel b) μ C cm⁻²) with $\phi = 0.03$. Bulk ion concentrations are calculated according to Eqns. (4.12) and (4.13), with H₃O⁺ as counterion, and solid lines account for added counterions and non-specific adsorption.

and accounts for added counterions and non-specific adsorption at the higher added salt concentration ($I_s = 1 \text{ mM}$) with $\sigma = 1.3 \mu\text{C cm}^{-2}$. However, at the lower KCl concentration (0.1 mM), quantitative agreement could not be achieved.

4.7 Conclusions

Dielectric relaxation spectroscopy was used to probe polystyrene latices in aqueous KCl solutions of varying KCl and latex concentration. Standard electrokinetic model was used to interpret dielectric relaxation spectra, using the electrokinetic surface charge as a fitting parameter with which to compare with the manufacturer's titratable charge. Unlike past studies of similar dispersions (Beltramo and Furst, 2012b), where the contribution of added counterions and non-specific adsorption to the conductivity was calculated as a mole-fraction weighted average, the counterion in this study was assumed to be potassium. Further, we considered the the possibility of deswelling on the surface charge density. Quantitative correspondence could not be achieved without adopting an unreasonably large electrokinetic charge, even when accounting for uncertainties in the surface area. The possibility of polyelectrolyte hairy layers enhancing the polarization was also explored, but this required the hairy-layer charge to be \approx 5-fold higher than the titratable charge. Much closer correspondence could be achieved by adopting a counterion mobility for $\rm H_3O^+$, even though the cleaning protocol suggests an exchange of $\rm H_3O^+$ for $\rm K^+$. From an electrokinetic and surface-charge perspective, polystyrene latices are not ideal behaving model colloids.

4.8 Acknowledgements

This work was supported by NSERC Discovery and Research Tools and Instruments grants to R.J.H. G.A. was supported by a PRESSID/PTDF scholarship (Nigeria). Dr. C. Du is acknowledged for designing and constructing the dielectric spectrometer sample holder.

4.9 Author contributions

G.A. and R.J.H. designed the experiments. G.A. performed the experiments, analyzed the data, and conducted the SEKM calculations. G.A. and R.J.H. interpreted the data and wrote the paper.

Bibliography

G. A. Afuwape and R. J. Hill. Nanoemulsion-hydrogel composites: Electro-kinetic dynamics, viscoelastic and swelling responses. PhD thesis, McGill University, 2020.

- P. Beltramo and E. Furst. A simple, single-measurement methodology to account for electrode polarization in the dielectric spectra of colloidal dispersions. *Chem. Lett.*, 41(10):1116–1118, 2012a.
- P. J. Beltramo. *Polarization and self-assembly of colloidal suspensions*. PhD thesis, University of Delaware, 2013.
- P. J. Beltramo and E. M. Furst. Transition from dilute to concentrated electrokinetic behavior in the dielectric spectra of a colloidal suspension. *Langmuir*, 28 (29):10703–10712, 2012b.
- E. H. B. DeLacey and L. R. White. Dielectric response and conductivity of dilute suspensions of colloidal particles. *J. Chem. Soc.*, Faraday Trans. 2, 77:2007–2039, 1981.
- M. R. Gittings and D. A. Saville. Electrophoretic mobility and dielectric response measurements on electrokinetically ideal polystyrene latex particles. *Langmuir*, 11(3):798–800, 1995.
- R. J. Hill, D. Saville, and W. Russel. Polarizability and complex conductivity of dilute suspensions of spherical colloidal particles with charged (polyelectrolyte) coatings. *J. Colloid Interface Sci.*, 263(2):478 497, 2003a.
- R. J. Hill, D. Saville, and W. Russel. Electrophoresis of spherical polymer-coated colloidal particles. *J. Colloid Interface Sci.*, 258(1):56 74, 2003b.
- A. Hollingsworth and D. Saville. A broad frequency range dielectric spectrometer for colloidal suspensions: cell design, calibration, and validation. J. Colloid Interface Sci., 257(1):65 – 76, 2003.
- A. D. Hollingsworth and D. A. Saville. Dielectric spectroscopy and electrophoretic mobility measurements interpreted with the standard electrokinetic model. *J. Colloid Interface Sci.*, 272(1):235 245, 2004.
- R. J. Hunter. More reliable zeta potentials using electroacoustics. In *Surface and Colloid Science*, pages 1–10, Berlin, Heidelberg, 2004. Springer Berlin Heidelberg.
- A. L. Loeb, J. T. G. Overbeek, P. H. Wiersema, and C. V. King. The electrical double layer around a spherical colloid particle. *J. Electrochem. Soc.*, 108(12): 269C, 1961.

- C. S. Mangelsdorf and L. R. White. Electrophoretic mobility of a spherical colloidal particle in an oscillating electric field. J. Chem. Soc., Faraday Trans., 88:3567– 3581, 1992.
- S. C. Mangelsdorf and L. R. White. Dielectric response of a dilute suspension of spherical colloidal particles to an oscillating electric field. *J. Chem. Soc.*, Faraday Trans., 93:3145–3154, 1997.
- L. A. Rosen and D. A. Saville. Dielectric spectroscopy of colloidal dispersions: Comparisons between experiment and theory. *Langmuir*, 7(1):36–42, 1991.
- D. A. Saville. Electrical conductivity of suspensions of charged particles in ionic solutions. *J. Colloid Interface Sci.*, 71(3):477 490, 1979.
- D. A. Saville. The electrical conductivity of suspensions of charged particles in ionic solutions: the roles of added counterions and nonspecific adsorption. *J. Colloid Interface Sci.*, 91(1):34 50, 1983.
- J. E. Seebergh and J. C. Berg. Evidence of a hairy layer at the surface of polystyrene latex particles. *Colloids Surf.*, A, 100:139 153, 1995.
- V. E. Shubin, R. J. Hunter, and R. W. O'Brien. Electroacoustic and dielectric study of surface conduction. *J. Colloid Interface Sci.*, 159(1):174 183, 1993.
- D. Stigter. Theory of conductance of colloidal electrolytes in univalent salt solutions. J. Phys. Chem., 83(12):1663–1670, 1979.
- A. G. van der Put and B. H. Bijsterbosch. Electrokinetic measurements on concentrated polystyrene dispersions and their theoretical interpretation. *J. Colloid Interface Sci.*, 92(2):499 507, 1983.
- C. F. Zukoski and D. A. Saville. An experimental test of electrokinetic theory using measurements of electrophoretic mobility and electrical conductivity. J. Colloid Interface Sci., 107(2):322 – 333, 1985.

Chapter 5

Dielectric relaxation spectroscopy of oil-in-water nanoemulsions

5.1 Preface

Attempts to interpret the conductivity of surfactant stabilized drops using the standard electrokinetic model have been inconclusive, perhaps due to the high surface charge and inner electrical double layer dynamics. Here, an attempt to unify interfacial thermodynamics and electro-kinetics is undertaken for SDS-stabilized hexadecane nanodrops in salt solutions. Pendant-drop tensiometry is used to quantify surfactant adsorption at macroscopic oil-water interfaces, and the frequency-dependent conductivity of oil-in-water nanoemulsions is measured using dielectric relaxation spectroscopy. Dielectric relaxation spectra are interpreted using the standard electrokinetic model, as calculated by the standard electrokinetic model, according to the MPEK package (Hill et al., 2003a,c), but with the adsorption isotherm to prescribe the surface charge.

5.2 Abstract

Dielectric relaxation spectra of sodium dodecyl sulphate (SDS) stabilized hexadecane nanodroplets in NaCl solutions were measured and theoretically interpreted using the standard electrokinetic model. Adsorption isotherm parameters were derived from pendant-drop surface-tension data. This adsorption isotherm, which is distinguished from literature isotherms—because it accounts for the surface charge and changing NaCl concentration—was applied to prescribe the interfacial and background surfactant concentrations in nanoemulsions (below their respective c.m.c.s). Comparing nanoemulsion conductivity and dielectric increment spectra to the electrokinetic theory identified the apparent particle polarizability as being dominated by larger droplets, since the conductivity-averaged drop size was considerably larger than the volume-average size furnished by acoustic attenuation.

5.3 Introduction

Dielectric spectroscopy provides a non-invasive measurement of frequency-dependent electrical responses (capacitance, impedance, conductivity, etc.) of heterogeneous systems. Polarization of a dispersed phase is induced by the application of an oscillatory electric field, and the resulting complex conductivity may be theoretically interpreted to ascertain the particle ζ -potential and/or particle size. These are important, because they play a vital role in controlling emulsion stability (Hill and Cooper, 1992, Asami, 2002, Grosse and Delgado, 2010).

Dielectric spectra results are often interpreted in terms of relaxation times. For emulsions, the relaxation times of importance include those of molecular dipoles ($\sim 10^{-9}$ s), charge transport across or around the dispersed particles ($\sim 10^{-6}$ s), charge separation across the oil-surfactant interface ($\sim 10^{3}$ s) and bulk macroscopic sample (10 s) (Hill and Cooper, 1992).

Electrokinetic theories for rigid-particle dispersions have been widely applied to dispersed fluids (Barchini and Saville, 1996, Nespolo et al., 2001, Djerdjev et al., 2003), justified by (i) similarities in their rheology (Mason et al., 1996, Mason, 1999, Chanamai and McClements, 2000) and (ii) the presence of surface-active impurities suppressing internal circulation (Hollingshead et al., 1965). However, Booth (1951), who accounted for internal electric-field-induced circulation in drops, identified that rigid-particle electrokinetics might not capture the electrokinetics of fluid particles. While there may be cases where fluid drops do behave as rigid spheres, others have identified differences arising from the Maxwell, Marangoni, viscous stresses (Baygents and Saville, 1991).

The electrical study of heterogeneous systems is based on electrokinetic models advancing on Maxwell's theory for the effective conductivity of composites. Analytic forms of the Maxwell model and its derivatives tend to produce small errors for particles where the thin-double-layer approximation is reasonable, but substantial deviations are observed when particle radius and double-layer thickness are comparable (Grosse and Delgado, 2010). This has motivated numerical solutions of the standard electrokinetic model to account for shortcomings of the analytical approximations (Saville, 1979, DeLacey and White, 1981, Mangelsdorf and White, 1992). Electrokinetic studies of colloidal dispersions often indicate the inherent roughness of the particle surface as a reason for the difference between experiments and theory (Rosen and Saville, 1991). However, attempts to reconcile anomalous behaviour have been attempted by synthesizing emulsions with surface charges derived from the dissociation of a surfactant, which provides electro-steric stabilization. The electrokinetic charge density and ζ -potential can be estimated from knowledge of the emulsion conductivity using the standard electrokinetic model. However, a consistent interpretation of the electrokinetic anomalies observed for highly charged particles is elusive. Reasonings of ion adsorption, surface roughness (Barchini and Saville, 1996), and stagnant-layer conduction (Djerdjev et al., 2003) have been proposed. A lack of consistency between electrophoretic mobility and conductivity has also been reported due to the large counter-ion density for such highly charged drops (Barchini and Saville, 1996).

DeLacey and White (1981) provided a rigorous theoretical basis for obtaining non-measurable electrokinetic parameters from the induced dipole and its effect on the conductivity of a colloidal dispersion. For highly charged drops, the surface charge density can be ascertained from an interfacial adsorption isotherm that incorporates the electrostatic contribution to the interfacial free energy using Guoy-Chapman theory (Hill and Afuwape, 2020). Incorporating the drop and interfacial dynamics has produced encouraging interpretations of the dynamic electrophoretic mobility. Here, we examine the degree to which the theory might be applied to interpret dielectric relaxation spectra of such nanoemulsions, albeit without considering the drop and interfacial dynamics. Previous attempts to apply a closed-form expression for the dipole strength (O'Brien, 1988) to interpret the electrical conductivity and dielectric responses did not produce conclusive results. It has been suggested that this is because that theory is valid only for thin double layers $\kappa a \gg 1$ and high frequencies $\omega a^2/D \gg 1$ (Mangelsdorf and White, 1997).

The present work is divided into three parts: (i) an adsorption model for an oil-water interface is developed, and used to compute the ζ -potential from Gouy-Chapman theory; (ii) dielectric relaxation spectra of SDS-stabilized hexadecane nanoemulsions are measured; and (iii) interpretations of the dielectric relaxation spectra are undertaken using the standard electrokinetic model and the adsorption isotherm according to the surfactant and added NaCl concentrations.

5.4 Materials and methods

Oil-in-water nanoemulsions were prepared with hexadecane (99 %, Sigma-Aldrich Canada), sodium dodecyl sulphate (SDS) (98.5 %, Sigma-Aldrich Canada), and reverse-osmosis (RO) water (Type 1, $\sigma \approx 5.6~\mu \mathrm{S~m^{-1}}$, $\Omega \approx 18~\mathrm{MOhm~cm}$). Different ionic strengths were obtained by pre-dissolving prescribed mass of NaCl (Sigma Aldrich) and SDS in RO water. Interfacial tension measurements were performed with the aid of Kel-F-Hub needle (21 gauge, Point style 3, Hamilton) and Luer lock syringe (500 $\mu \mathrm{L}$ Model 1750 TLL, Hamilton) setup in an Optical Contact-Angle-Goniometer (DataPhysics Instruments). All materials were used as provided by the manufacturer.

5.4.1 Nanoemulsion preparation

For samples with added salt, prescribed masses of NaCl were added to known volume of reverse-osmosis (RO) water to make stock solutions of known salt concentrations I_s . Surfactant solutions were prepared with a prescribed mass of SDS added to a known volume of pure RO water or stock solution, and stirred in a vortex mixer for 1 min to ensure dissolution giving an aqueous-phase SDS concentration. A prescribed volume of oil was added to the solution to obtain a coarse emulsion of known volume fraction ϕ . High-energy emulsification was undertaken using a probe sonicator (QSonica Q500 model) at 20 kHz (2 runs, 15 minutes each, separated by \sim 2 min). Sonication is widely used to produce nanoemulsions, but the procedure is not standardized, as the sonication time depends on the power intensity. By trail and error, the sample temperature could be maintained less than \sim 35°C for each 15 min run.

5.4.2 Interfacial tension measurement

Interfacial tension was measured using pendant-drop tensiometry. A prescribed mass of NaCl was added to known volume of RO water, and stirred with a vortex mixer for ~ 1 min to obtain a stock salt solution of known ionic strength. A prescribed mass of SDS was added to a known volume of the stock solution and further diluted to obtain solutions with various concentrations of surfactant and added salt. Solution was loaded into a syringe, and 1.5 mL of the oil dispensed into a glass cuvette. From the syringe, a prescribed volume of the surfactant solution was placed into contact with the oil, forming a pendant drop, and an image captured using the SCA20 software (DataPhysics Instruments). The interfacial surface tension was determined from a fit of an axisymmetric pendant-drop, minimizing gravitational and interfacial energy. This was undertaken using the Opendrop software (Berry et al., 2015), which takes a pendant-drop image, needle diameter, drop and continuous phase densities as input parameters.

5.4.3 Particle size measurement

The particle size distribution moments were obtained from sound-wave attenuation (Acoustosizer II, Colloidal Dynamics LLC) following calibration, as detailed in the instrument manual. 20 mL of nanoemulsion was pumped through the ESA flow cell during the measurements. Dispersed and continuous phases were selected from the ESA software library (densities and thermal properties are predefined), and the weight fraction of the oil phase was input. The particle size option was preselected to perform a lognormal fit. Size determination by sound-wave attenuation is recommend by the instrument manufacturer as best for heterogeneous samples with density contrast $|\Delta \rho| \approx 0.5$ g mL⁻¹, because it takes into account thermal properties of both phases. The instrument's transducer records the attenuation spectrum, and the software reports a best-fit log-normal size distribution with its moments.

5.4.4 Dielectric relaxation spectra measurement

Details of this instrument and interpretation of its data are provided elsewhere (Afuwape and Hill, 2020, Ch. 3).

$c_{\infty}^* \; (\mathrm{mM})$	$I_s \text{ (mM)}$	ϕ	$d_{15} \; (\mu {\rm m})$	$d_{50} \; (\mu {\rm m})$	$d_{85} \; (\mu {\rm m})$	$\sigma (\mathrm{S m^{-1}})$
5	0	0.02	0.338	0.437	0.543	0.0294
5	0	0.05	0.326	0.41	0.507	0.0232
5	0	0.1	0.476	0.625	0.785	0.0209
5	1	0.02	0.282	0.473	0.794	0.0376
5	1	0.05	0.249	0.417	0.701	0.0352
5	1	0.1	0.363	1.153	2.273	0.0316
5	5	0.02	0.257	0.431	0.723	0.0829
5	5	0.05	0.257	0.431	0.724	0.0764
5	5	0.1	0.353	0.528	2.201	0.0720

Table 5.1: Particle size moments from sound wave attenuation. Conductivities were measured in the instrument sample cell. The bulk aqueous-phase SDS concentration is denoted as c_{∞}^* .

5.5 Results and discussion

Experiments were conducted with added NaCl concentrations $I_s \leq 5$ mM to avoid micelles, assuming that the c.m.c. is independent of the drop size (diameters $\approx 200\text{--}1000 \text{ nm}$). Particle size and bulk conductivity are reported in table 5.1. Narrower size distributions (as inferred by d_{85}/d_{15}) are evident for oil volume fractions $\phi = 0.02$ and 0.05, but samples with $\phi = 0.1$ have a notably large d_{85} . At each bulk surfactant concentration, the bulk conductivity decreases with the oil volume fraction, possibly due to the increasing interfacial surface area for surfactant adsorption, and the low conductivity of oil with respect to water.

5.5.1 Interfacial tension of the hexadecane-water interface in the presence of SDS and NaCl

Following Hill and Afuwape (2020), the surface tension is related to the surfactant (SDS) and added salt (NaCl) concentrations (c_{∞} for SDS, and $I_s = c_{-}^{\infty}$ for Cl⁻) by

$$\gamma(c_{\infty}, c_{-}^{\infty}) = \gamma(0, 0) - k_B T \int_0^{c_{\infty}} \frac{\hat{\Gamma}}{c_{\infty}} dc_{\infty}$$

$$-4k_B T \int_0^{c_{\infty}} \left\{ \cosh\left[\zeta e/(2k_B T)\right] - 1 \right\} \sqrt{\frac{k_B T \epsilon_o \epsilon_0}{2(c_{\infty} + c_{-}^{\infty})e^2}} dc_{\infty}, \tag{5.1}$$

where $\gamma(0,0)$ is the surface tension of the oil-water interface with no surfactant or added salt. The adsorption isotherm is

$$\hat{\Gamma} = \frac{c_{\infty} \Gamma}{e^{ze\zeta/(k_B T)} n + c_{\infty}},\tag{5.2}$$

where the surface charge density (Gouy-Chapman formula (Russel et al., 1989))

$$\hat{\Gamma}ze = 2\sqrt{2k_B T \epsilon_o \epsilon_0 (c_-^{\infty} + c_{\infty})} \sinh[|z|e\zeta/(2k_B T)]$$
(5.3)

and (model parameters)

$$\Gamma = 1/(\pi a_s^2)$$
 and $n = e^{\Delta \epsilon}/(\pi a_s^2 \delta)$.

Solving these equations was demonstrated to be equivalent to the closed-form solution of Borwankar and Wasan (1988):

$$\gamma(c_{\infty}, c_{-}^{\infty}) = \gamma(0, 0) - k_{B}T\Gamma \left[\ln \left(1 - \frac{\hat{\Gamma}}{\Gamma} \right) - \frac{4k_{B}T\sqrt{2\epsilon_{o}\epsilon_{0}kT(c_{\infty} + c_{-}^{\infty})}}{e} \right] \left[\cosh \left(\frac{ze\zeta}{2k_{B}T} \right) - 1 \right]$$

$$(5.4)$$

for which Γ and n are fitting parameters.

Non-linear least-squares fits of Eqn. (5.1) to data are reported in table 5.2. The surface excess Γ decreases with increasing added salt concentration I_s , which indicates that electrostatic screening reduces the electrostatic penalty for SD⁻ adsorption. Alternatively, Eqn. (5.1) can be evaluated as a one-parameter model by prescribing values for the free energy change to transfer a hydrocarbon chain of similar length from the bulk to the oil-water interface, $\Delta \epsilon \approx -19$ (Persson et al., 2003), and $a_s = 2.42$ Å (solution radius of an SO₄²⁻ ion to represent the DS⁻ polar head group in water (Marcus, 1988). Fitted values of δ using this approach are reported in table 5.3.

To establish an optimal set of parameters that might be independent of I_s , figure 5.1(a) shows the model evaluated with the averaged (over I_s) fitting parameters from table 5.2: $\delta = 0.665$ Å, $a_s = 3.34$ Å and $\Delta \epsilon = -18.9$. Note that (Hill and Afuwape, 2020) previously suggested $\delta = 0.225a_s \approx 0.54$ Å, having prescribed $a_s = 2.42$ Å, and $\Delta \epsilon = -19$, and Borwankar and Wasan reported

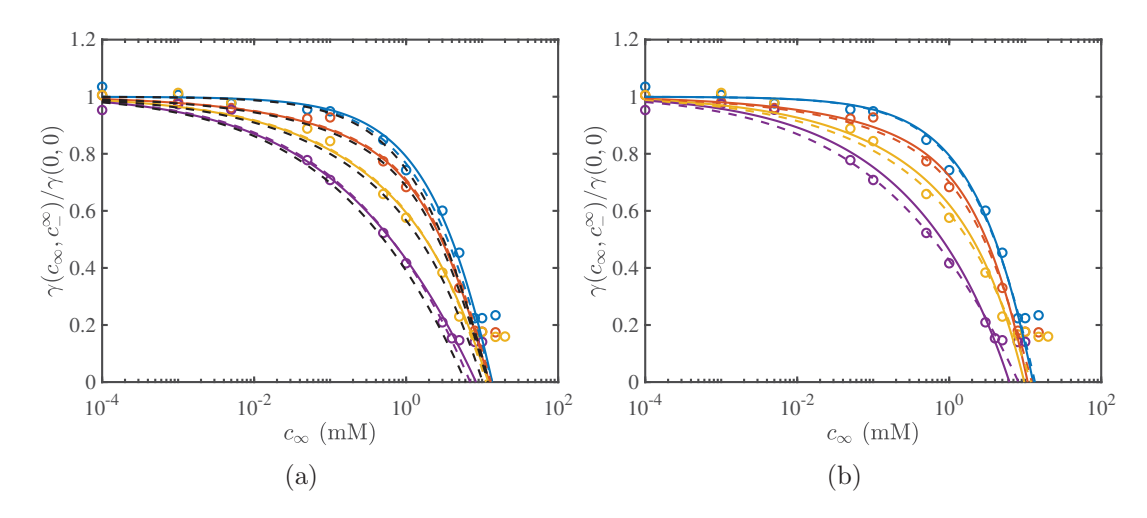


FIGURE 5.1: (a) Fits of Eqn. (5.1) to surface-tension data (for the hexadecane-SDS-water interface) with added NaCl concentrations $I_s=0$ (blue), 1 (red), 5 (yellow) and 20 (violet) mM. Solid lines are fits with Γ and n as adjustable parameters for each added salt concentration. Corresponding dashed (colored) lines are fits using the averaged (over I_s) parameters in table 5.2. Black lines are the model evaluated with the parameters of Borwankar and Wasan for the hexane-SDS-water interface (no added salt). (b) Fits of Eqn. (5.1) to data (for each salt concentration) with Γ and n as fitting parameters (dashed lines, same as in (a)); and with only δ as the fitting parameter (solid lines, with prescribed $a_s=2.42$ Å, $\Delta\epsilon=-19$). All fits undertaken with $\gamma_0\approx 47$ mN m⁻¹.

TABLE 5.2: SDS-hexadecane-NaCl solution adsorption isotherm model parameters obtained by fitting Eqn. (5.1) (equivalent to Eqn. (5.4)) to data at each added NaCl concentration with Γ and n as fitting parameters. Here, δ , a_s and $\Delta\epsilon$ are derived from Γ and n.

I_s	Γ	n	δ	a_s	$-\Delta\epsilon$
(mM)	$(10^{-6} \text{ mol m}^{-2})$	$(10^{-4} \text{ mol m}^{-3})$	(Å)	(Å)	
0	6.499	8.606	0.559	2.852	18.721
1	4.814	4.037	0.663	3.314	19.008
5	4.228	3.523	0.705	3.536	18.953
20	3.930	3.144	0.732	3.667	18.956

 $\Gamma=4.45\times 10^{-6}~{\rm mol~m^{-2}}$ and $n=3.13\times 10^{-4}~{\rm mol~m^{-3}}$ for the heptane-SDS-water interface (without added NaCl). Our analysis here suggests optimal values for hexadecane-SDS-NaCl solutions: $\Gamma=4.89\times 10^{-6}~{\rm mol~m^{-2}}$ and $n=4.83\times 10^{-4}~{\rm mol~m^{-3}}$. Note that these are equivalent to $\delta=0.105~{\rm \AA}$ and $\Delta\epsilon=-19$ when prescribing $a_s=2.42~{\rm \AA}$, or $\delta=0.567~{\rm \AA}$ and $a_s=3.28~{\rm \AA}$ when prescribing $\Delta\epsilon=-19$.

Table 5.4 reports the c.m.c.s obtained from interfacial tension and conductivity measurements. There is no standardized method of determining c.m.c.s from

Table 5.3: SDS-hexadecane-NaCl solution adsorption isotherm model parameters obtained by fitting Eqn. (5.1) (equivalent to Eqn. (5.4)) to data at each added NaCl concentration with δ as the fitting parameter (prescribed $\Delta\epsilon \approx -19$ and $a_s = 2.42$ Å). Here, Γ and n are derived from the fitted and prescribed parameters.

$\overline{I_s}$	δ	Γ	n
(mM)	(Å)	$(10^{-6} \text{ mol m}^{-2})$	$(10^{-4} \text{ mol m}^{-3})$
0	0.386	9.026	1.309
1	0.489	9.026	1.034
5	0.436	9.026	1.159
20	0.392	9.026	1.290

TABLE 5.4: C.m.c. from surface tension γ and conductivity σ (Afuwape and Hill, 2020, Chapter 3). γ and σ are the surface tension and conductivity at the c.m.c. *From Dunstan and White (1990).

$\overline{I_s}$	γ	c.m.c. (from γ)	σ	c.m.c. (from σ)	c.m.c. (from σ)*
(mM)	$(mN m^{-1})$	(mM)	$(S m^{-1})$	(mM)	(mM)
0	10.5	8	0.052	8.18	8.31
1	8.5	7.2	0.061	7.95	7.7
5	7.8	6.5	0.105	6.85	6.72
20	6.6	3.8	-	_	_

such isotherms, so we identified the intersection of the closest surface tension measurement to the isotherm, to the right of the isotherm.

Figure 5.2 shows the accompanying ζ -potential and surface charge density $\sigma^0 = \hat{\Gamma}ze$ from the model, as furnished by Eqns. (5.2) and (5.3). The plot has been extrapolated to surfactant concentrations well above the c.m.c. Note that adding NaCl increases the surface charge density while decreasing the ζ -potential, whereas, for a surface with a fixed surface charge density, the surface potential would more conventionally decrease with increasing salt concentration.

5.5.2 Surfactant material balance

Surfactant adsorption at the oil-water interface in a nanoemulsion necessitates a material balance to estimate the final bulk surfactant in the electrolyte because sonication creates a large surface area, depleting the total surfactant concentration in the aqueous phase. Assuming a monodisperse emulsion with drop radius a, the equilibrium surfactant concentration can be estimated by combining the adsorption isotherm Eqn. (5.2) with a material balance on the oil-water interface to

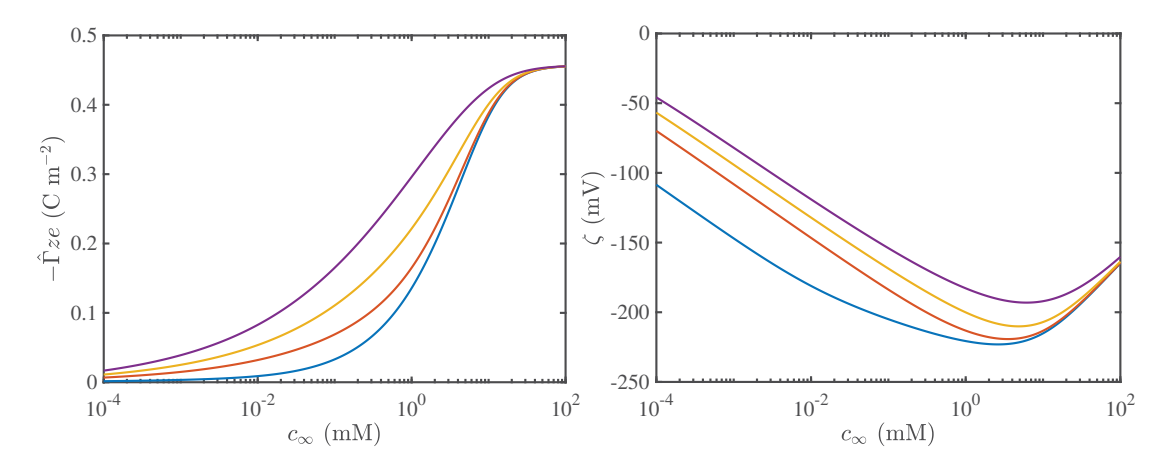


FIGURE 5.2: Surface charge density (left) and ζ -potential (right) as a function of bulk surfactant concentration c_{∞} for added NaCl concentrations $I_s=10^{-2}$ (blue), 1 (red), 5 (yellow) and 20 mM (yellow). The model has been extrapolated beyond beyond the c.m.c. for each added salt concentration. These calculations undertaken with the optimal two-parameter model ($\delta=0.665$ Å, $a_s=3.34$ Å, and $\Delta\epsilon=-18.9$) across all ionic strengths (see table 5.3).

relate the total bulk surfactant concentration $c_{\infty,0}$ ($\equiv c_{\infty}^*(1-\phi)$) to the equilibrium aqueous-phase concentration c_{∞} :

$$c_{\infty,0} = \frac{3\phi\hat{\Gamma}(c_{\infty}, I_s)}{a} + c_{\infty}(1 - \phi). \tag{5.5}$$

5.5.3 Dielectric relaxation of oil-in-water emulsions

Conductivity σ and apparent dielectric constant ε'_{app} spectra for nanoemulsions with various oil volume fractions ϕ and concentrations of added salt I_s are shown in figure 5.3. Electrode polarization manifests below $f \sim 100$ Hz for conductivity, and below $f \sim 0.1$ MHz for the dielectric constant with aqueous phase surfactant concentration $c^*_{\infty} = 5$ mM. Note that $c_{\infty,0} = c^*_{\infty}(1-\phi)$, where $c_{\infty,0}$ is the total bulk surfactant concentration and ϕ is the dispersed phase volume fraction. Increasing the oil volume fraction decreases the conductivity because of the increased surface area for surfactant adsorption, and the oil phase is non-conducting. Spectra (post-emulsification) for the background electrolyte were also measured after being separated from the emulsion by centrifugation. Nanoemulsion in a centrifuge tube was centrifuged at 700g for 1 hr before the subnanant was carefully siphoned into a syringe for dielectric relaxation spectroscopy.

Conductivity increments and nanoemulsion and background (subnatant) conductivities are summarized in table 5.5. The background electrolyte concentration for

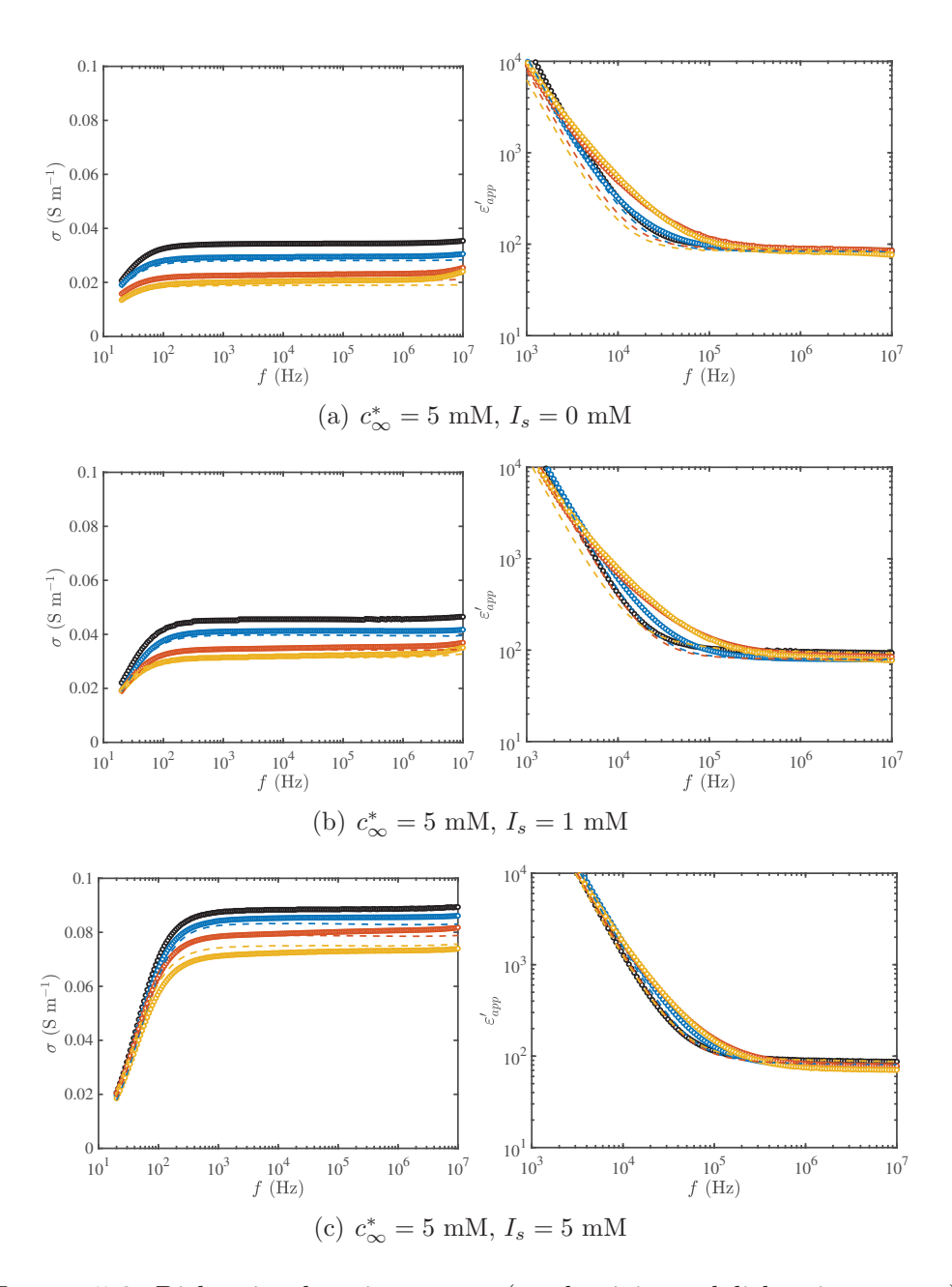


FIGURE 5.3: Dielectric relaxation spectra (conductivity and dielectric constant) for emulsions with oil volume fractions $\phi=0,\,0.02,\,0.05,\,0.1$ (black, blue, red, yellow). Bulk aqueous-phase SDS and added NaCl concentrations are c_{∞}^* and I_s . Circles are for the emulsions, and dashed lines are for the subnatant.

TABLE 5.5: Conductivity increment $\Delta \sigma$ for nanoemulsions are estimated as $\Delta \sigma = \sigma - \sigma_{\infty}/(\sigma_{\infty}\phi)$ using the nanoemulsion conductivity σ and respective subnatant conductivity σ_{∞} at $f \approx 100$ kHz. Subnatant electrolyte concentrations are estimated from independent conductivity-concentration plots for SDS solutions (see Afuwape and Hill (2020, Chapter 3)).

$\overline{I_s}$	ϕ	d_{50}	σ	σ_{∞}	$\Delta \sigma$	c_{∞}			
(mM)	_	$(\mu \mathrm{m})$	$(S m^{-1})$	$(S m^{-1})$	-	(mM)			
0	0		0.034						
0	0.02	0.437	0.030	0.028	2.575	4.355			
0	0.05	0.410	0.023	0.021	2.194	3.163			
0	0.1	0.625	0.021	0.019	0.981	2.862			
1	0		0.046						
1	0.02	0.473	0.041	0.040	2.405	4.310			
1	0.05	0.417	0.035	0.034	0.161	3.445			
1	0.1	1.153	0.032	0.031	0.236	2.989			
5	0		0.089						
5	0.02	0.431	0.086	0.083	1.824	3.896			
5	0.05	0.431	0.080	0.079	0.374	3.145			
5	0.1	0.528	0.073	0.075	-0.278	2.508			
$\Delta \sigma = f(\sigma, \sigma_{eo}, \phi) \text{ and } c_{eo} = f(c_{eo}, \sigma, \sigma_{eo})$									

 $\Delta \sigma = f(\sigma, \sigma_{\infty}, \phi) \text{ and } c_{\infty} = f(c_{\infty,0}, \sigma, \sigma_{\infty})$

each sample was estimated from its conductivity using the conductivity versus SDS concentration, as reported by Afuwape and Hill (2020, Chapter 3).

Figure 5.4 shows the conductivity and dielectric constant increment spectra for nanoemulsions. The increments are calculated as detailed in section 5.4.4. The low-frequency humps in the dielectric constant spectra are artifacts due to electrode polarization corrections, and the frequencies at which these occur depend on the ionic strength of the background solution (Beltramo and Furst, 2012). The decrease in conductivity increment with volume fraction reflects the change in SDS concentration with oil volume fraction (oil-water interfacial area).

5.5.4 Electrokinetic interpretation of nanoemulsions

The standard electrokinetic model, as calculated by Hill et al. (2003b,a,c), defines a far-field solution that yields real and imaginary parts of the polarizability, which are related to the experimentally measurable conductivity and dielectric constant increments. The far-field decay of the perturbed electrostatic potential has the form

$$\psi' \approx -E' \cdot r' + D'E' \cdot \hat{r}/r'^2 \text{ as } r' \to \infty$$
 (5.6)

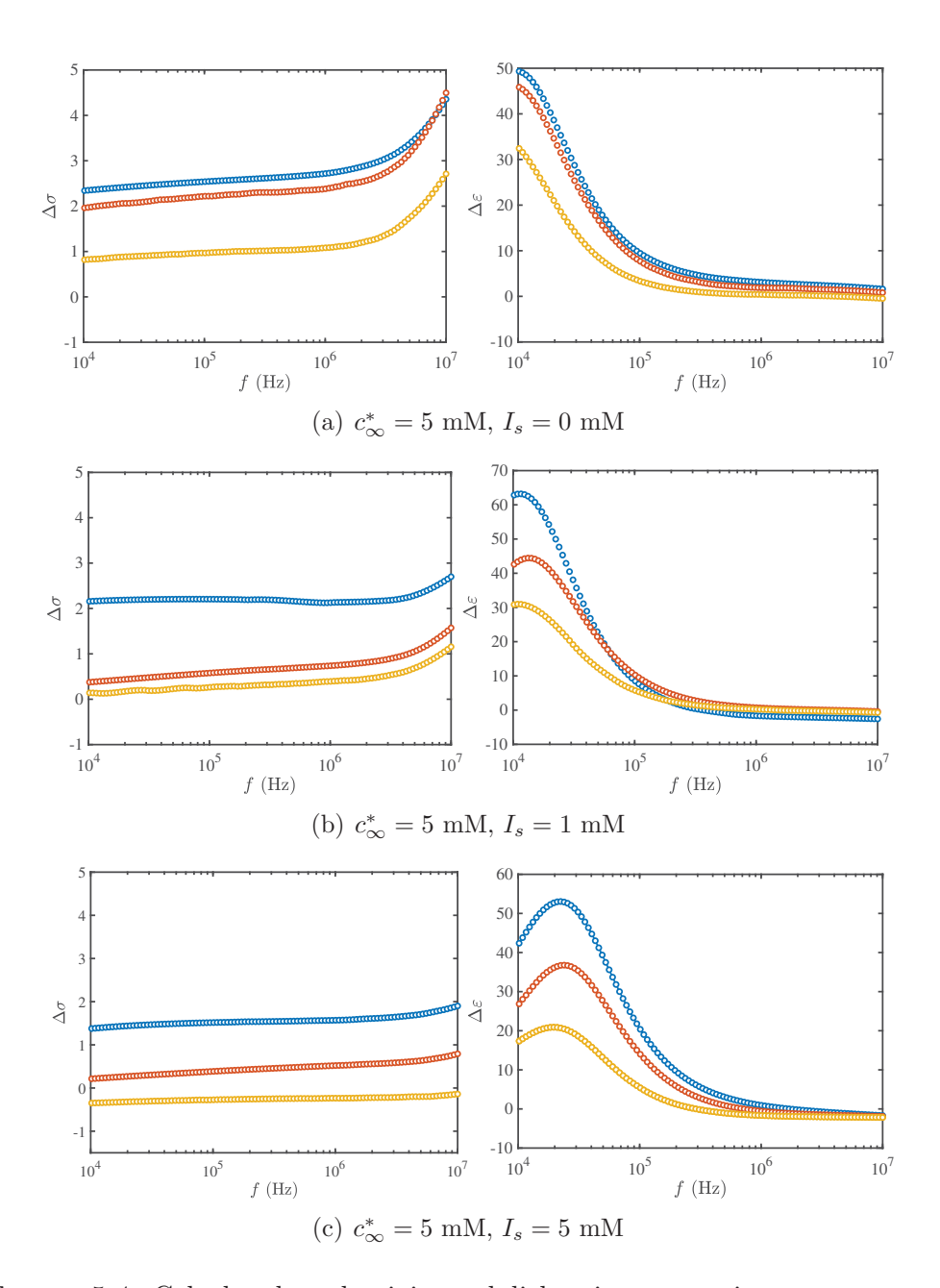


FIGURE 5.4: Calculated conductivity and dielectric constant increment spectra for emulsions with oil volume fractions $\phi=0.02,\,0.05,\,0.1$ (blue, red, yellow) from nanoemulsion and subnatant spectra. Bulk aqueous-phase SDS and added NaCl concentrations are c_{∞}^* and I_s .

with scaled electrostatic potential $\psi' = \psi e/k_B T$, radial distance $r' = \kappa r$, electric field strength $E' = Ee/(\kappa k_B T)$, polarizability $D' = D\kappa^3$, and the dimensionless polarizability $\mathscr{P} = D'/(\kappa a)^3 = D/a^3$. The conductivity increment is calculated as

$$\Delta \sigma = \frac{\sigma_e - 1}{\phi} = 3[\Re(\mathscr{P}) + \hat{\omega}\Im(\mathscr{P})], \tag{5.7}$$

and the dielectric constant increment as

$$\Delta \varepsilon = \frac{\varepsilon_e - 1}{\phi} = 3[\Re(\mathscr{P}) - \hat{\omega}^{-1}\Im(\mathscr{P})]$$
 (5.8)

with $\hat{\omega} = \omega \varepsilon_s \varepsilon_0 / \sigma_{\infty}$. Note that σ_{∞} is the background conductivity, $\varepsilon_s \varepsilon_0$ is the dielectric permittivity of the solvent, ω is the angular frequency, and σ_e and ε_e are the effective conductivity and dielectric constant scaled with σ_{∞} and ε_s , respectively (Hill et al., 2003b,a,c). For non-conducting fluid spheres, a closed-form expression for the polarizability is

$$D' = \frac{i\omega\varepsilon_s\varepsilon_0 - i\omega\varepsilon_p\varepsilon_0 + 2K_s/a - K_\infty + F'}{-2i\omega\varepsilon_s\varepsilon_0 - i\omega\varepsilon_p\varepsilon_0 + 2K_s/a + 2K_\infty + F'},$$
(5.9)

where

$$F' = \frac{2(ze)^2 \Gamma Di\omega a^2 / (2D)}{ak_B T(i\omega a^2 / (2D) - 1)}.$$
 (5.10)

The surface conductivity with respect to the bulk conductivity and particle radius (together furnishing the Dukhin number) is

$$\frac{K_s}{K_{\infty}a} = \frac{2}{\kappa a} \left[\cosh\left(\frac{ze\zeta}{2kT}\right) - 1 \right] \left(1 + \frac{2\varepsilon_0\varepsilon_s(kT)^2}{z^2\eta De^2} \right),\tag{5.11}$$

where K_{∞} , $\varepsilon_0 \varepsilon_s$, $\varepsilon_0 \varepsilon_p$, a, ω , D, and η are the bulk conductivity, solvent and particle permittivity, particle radius, frequency, counterion diffusivity, and solvent viscosity respectively. Equation (5.9) is the same as obtained by O'Brien (1988) with an additional F' term, which arises from diffusion and electro-migration of the mobile surface charge, valid at high frequencies for droplets with thin double layers and high surface charge (Hill and Afuwape, 2020).

Approximating nanodrops as rigid spheres, the SEKM was solved according to Hill et al. (2003b,c) with the ζ -potential and background surfactant concentration prescribed according to the adsorption isotherm and material balance (as reported in table 5.6), and the particle diameter as a single adjustable model parameter with which to fit to experiments. These theoretical calculations are presented in

TABLE 5.6: ζ -potential and equilibrium aqueous-phase SDS concentrations were calculated from the absorption isotherm coupled to the SDS material balance (Eqns. (5.2) and (5.3) with Eqn. (6.8)) with particle diameters d_{15} (top), d_{50} , d_{85} (bottom) obtained from sound wave attenuation.

$\overline{\phi}$	I_s	d_{15}, d_{50}, d_{85}	$-\zeta e/k_BT$	c_{∞}
-	(mM)	$(\mu \mathrm{m})$	-	(mM)
0.02	0	0.338	8.654	4.046
	0	0.436	8.647	4.266
	0	0.543	8.641	4.419
	1	0.282	8.530	3.806
	1	0.473	8.524	4.294
	1	0.794	8.517	4.608
	5	0.257	8.157	3.529
	5	0.431	8.171	4.125
	5	0.723	8.175	4.507
0.05	0	0.326	8.680	2.858
	0	0.410	8.675	3.234
	0	0.507	8.668	3.550
	1	0.249	8.509	2.449
	1	0.417	8.529	3.160
	1	0.701	8.529	3.905
	5	0.257	8.058	2.151
	5	0.431	8.130	2.959
	5	0.724	8.165	3.796

figures 5.5 for NaCl concentrations $I_s = 0$, 1, 5 mM. Drop diameters are measured from sound-wave attenuation, d_{15} , d_{50} and d_{85} , with oil volume fraction $\phi = 0.05$ and bulk surfactant concentration $c_{\infty,0} = 4.75$ mM. The best fit is achieved with d_{85} , suggesting that the polarization is dominated by the larger drops. Here we have drawn on the additive nature of electric-field-induced dynamics in polydisperse colloidal suspensions (Jiménez et al., 2007).

At lower frequencies ($f \lesssim 0.1$ MHz), the SEKM provides a better fit to the uncorrected dielectric increment spectra than to the electrode-polarization corrected data (see figures 5.5 and 5.6), which suggests electrode polarization might be negligible, since surfactant molecules have greater affinity for the oil phase.

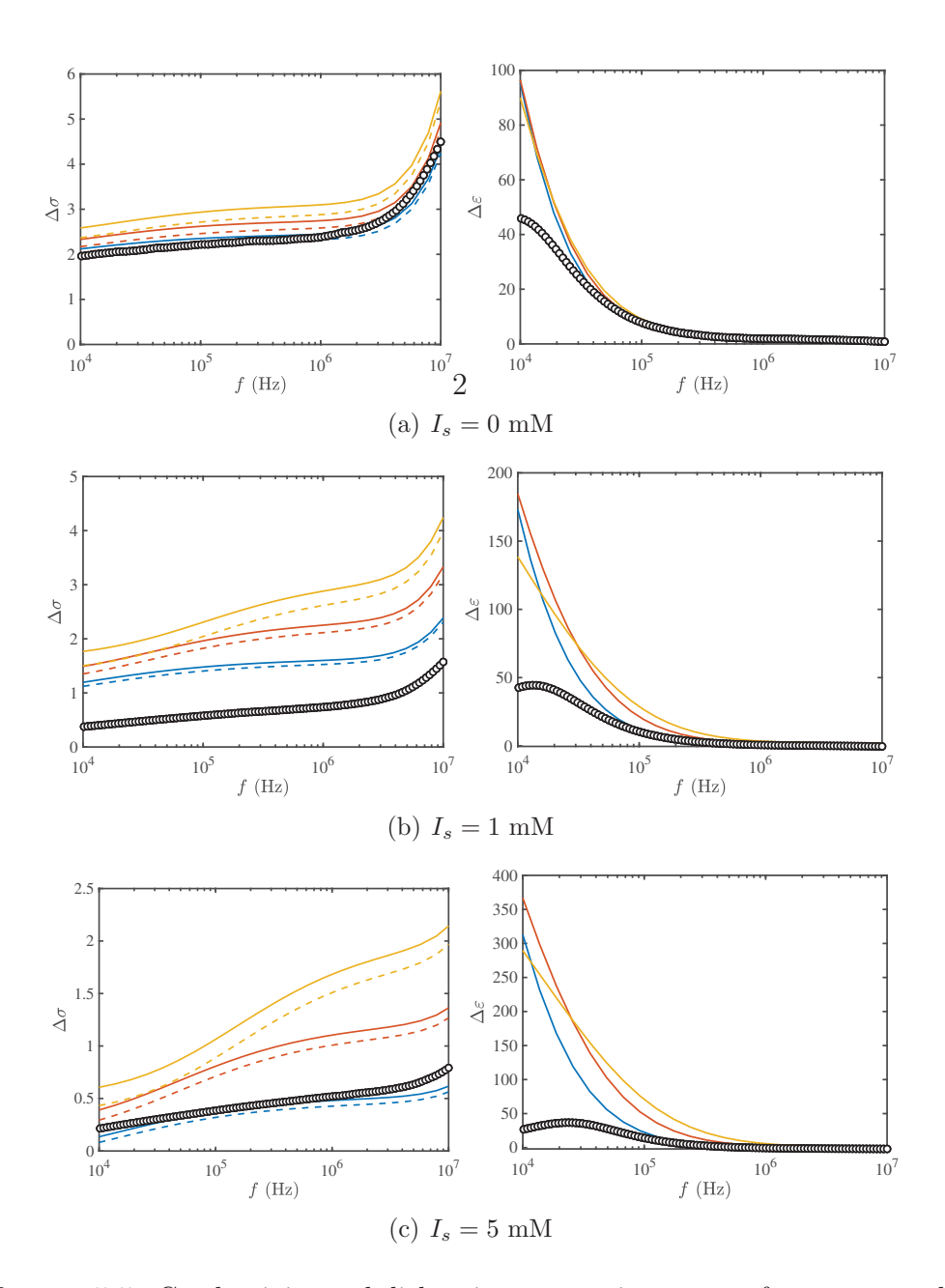


FIGURE 5.5: Conductivity and dielectric constant increments for a nanoemulsions with oil volume fraction $\phi = 0.05$ and bulk SDS concentration $c_{\infty,0} = 4.75$ mM. Solid lines are the SEKM for oil nanodrops (modelled as rigid spheres). Dashed lines are calculations without the contributions of added counter-ions and non-specific adsorption. Drop diameters d_{85} , d_{50} , d_{15} measured using soundwave attenuation are: (a) 507 (blue), 410 (red), and 326 nm (yellow); (b) 701 (blue), 417 (red), and 249 (yellow) nm; (c) 724 (blue), 431 (red), 257 (yellow) nm.

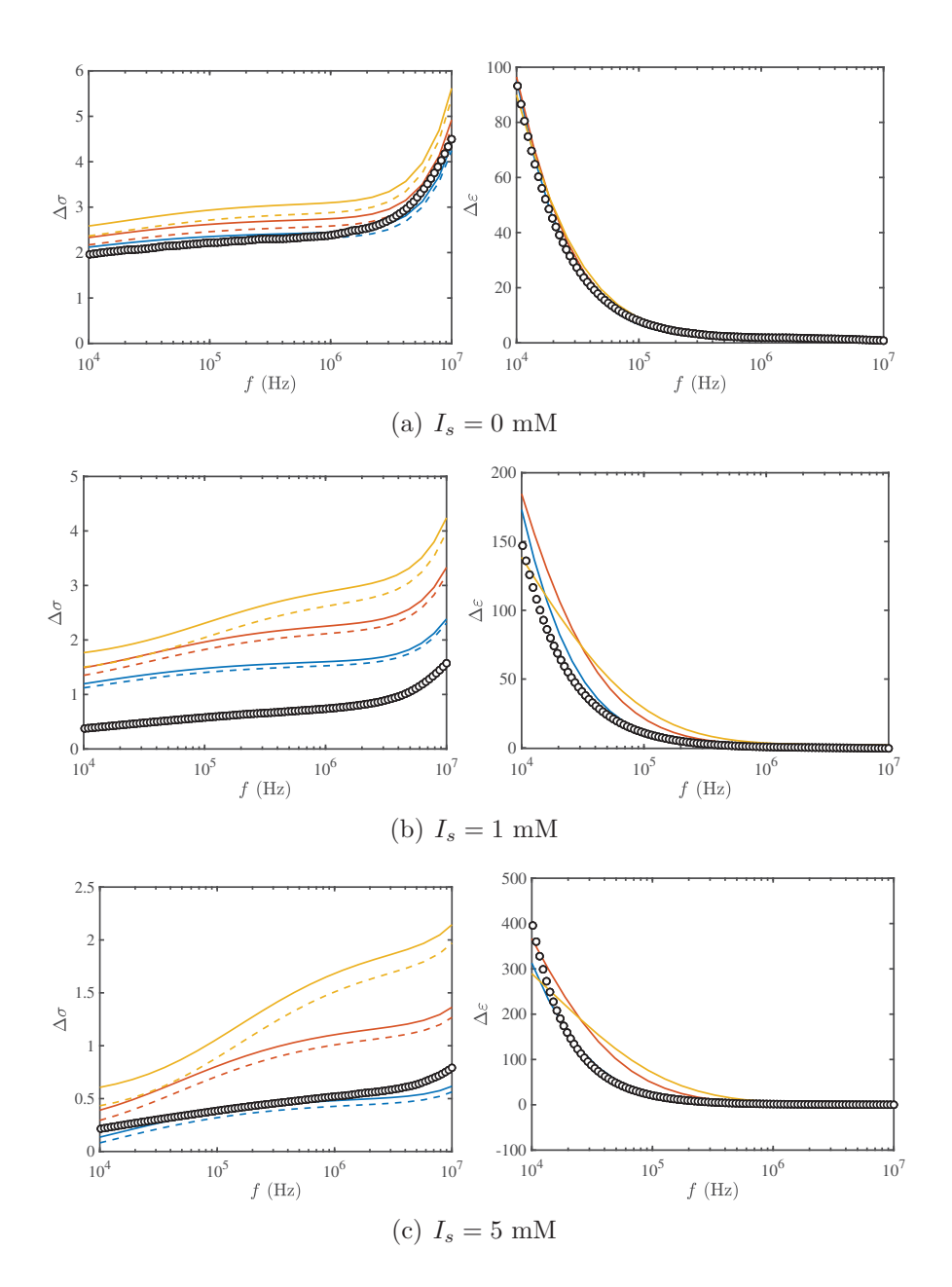


FIGURE 5.6: Conductivity and dielectric constant increments for a nanoemulsions with oil volume fraction $\phi=0.05$ and bulk SDS concentration $c_{\infty,0}=4.75$ mM. Solid lines are the SEKM for oil nanodrops (modelled as rigid spheres). Dashed lines are calculations without the contributions of added counterions and non-specific adsorption. Nanoemulsion droplet diameters d_{85}, d_{50}, d_{15} measured using sound-wave attenuation are: (a) 507 (blue), 410 (red), and 326 nm (yellow); (b) 701 (blue), 417 (red), and 249 (yellow) nm; (c) 724 (blue), 431 (red), 257 (yellow) nm. Diameters are measured from sound wave attenuation.

5.6 Conclusions

An electrokinetic study of highly charged SDS-stabilized hexadecane drops in water was undertaken, and results interpreted with the standard electrokinetic model, calculated according to Hill et al. (2003a,c). Previously, electrophoretic mobility and conductivity measurements were used by Barchini and Saville (1996) to infer ζ -potentials according to the SEKM solution of Saville (1983). In this study, ζ -potentials were prescribed from an adsorption isotherm and material balance, and the model used to infer the drop size. Particle size distributions for nanoemulsions were measured using sound wave attenuation, furnishing moments. Conductivity and dielectric constant spectra were measured using dielectric relaxation spectroscopy. A comparison of experimental and theoretical increment spectra highlights the effect of nanoemulsion polydispersity, since the prescription of a larger drops size provides a better representation of measured spectra.

5.7 Acknowledgements

This work was supported by NSERC Discovery and Research Tools and Instruments grants to R.J.H. G.A. was supported by a PRESSID/PTDF scholarship (Nigeria). Dr. C. Du is acknowledged for designing and constructing the dielectric spectrometer sample holder.

5.8 Author contributions

G.A. and R.J.H. designed the experiments. G.A. performed the experiments, analyzed the data, and conducted the SEKM calculations. G.A. and R.J.H. interpreted the data and wrote the paper.

Bibliography

G. A. Afuwape and R. J. Hill. Nanoemulsion-hydrogel composites: Electro-kinetic dynamics, viscoelastic and swelling responses. PhD thesis, McGill University, 2020.

- K. Asami. Characterization of heterogeneous systems by dielectric spectroscopy. *Prog. Polym. Sci.*, 27(8):1617–1659, 2002.
- R. Barchini and D. A. Saville. Electrokinetic properties of surfactant-stabilized oil droplets. *Langmuir*, 12(6):1442–1445, 1996.
- J. C. Baygents and D. A. Saville. Electrophoresis of drops and bubbles. *J. Chem. Soc.*, Faraday Trans., 87:1883–1898, 1991.
- P. Beltramo and E. Furst. A simple, single-measurement methodology to account for electrode polarization in the dielectric spectra of colloidal dispersions. *Chem. Lett.*, 41(10):1116–1118, 2012.
- J. D. Berry, M. J. Neeson, R. R. Dagastine, D. Y. Chan, and R. F. Tabor. Measurement of surface and interfacial tension using pendant drop tensiometry. *J. Colloid Interface Sci.*, 454:226 237, 2015.
- F. Booth. The cataphoresis of spherical fluid droplets in electrolytes. *J. Chem. Phys.*, 19(11):1331–1336, 1951.
- R. Borwankar and D. Wasan. Equilibrium and dynamics of adsorption of surfactants at fluid-fluid interfaces. *Chem. Eng. Sci.*, 43(6):1323 1337, 1988.
- R. Chanamai and D. J. McClements. Dependence of creaming and rheology of monodisperse oil-in-water emulsions on droplet size and concentration. *Colloids* Surf., A, 172(1):79 – 86, 2000.
- E. H. B. DeLacey and L. R. White. Dielectric response and conductivity of dilute suspensions of colloidal particles. J. Chem. Soc., Faraday Trans. 2, 77:2007– 2039, 1981.
- A. M. Djerdjev, J. K. Beattie, and R. J. Hunter. An electroacoustic and high-frequency dielectric response study of stagnant layer conduction in emulsion systems. *J. Colloid Interface Sci.*, 265(1):56–64, 2003.
- D. E. Dunstan and L. R. White. An electrokinetic study of micellar solutions. *J. Colloid Interface Sci.*, 134(1):147 151, 1990.
- C. Grosse and A. Delgado. Dielectric dispersion in aqueous colloidal systems. Curr. Opin. Colloid Interface Sci., 15(3):145 – 159, 2010.

- R. J. Hill and G. A. Afuwape. Dynamic mobility of surfactant stabilized nanodroplets: unifying equilibrium thermodynamics, electro-kinetics and Marangoni effects. *J. Fluid Mech.*, 895(A14), 2020.
- R. J. Hill, D. Saville, and W. Russel. Polarizability and complex conductivity of dilute suspensions of spherical colloidal particles with charged (polyelectrolyte) coatings. J. Colloid Interface Sci., 263(2):478 – 497, 2003a.
- R. J. Hill, D. Saville, and W. Russel. Electrophoresis of spherical polymer-coated colloidal particles. *J. Colloid Interface Sci.*, 258(1):56 74, 2003b.
- R. J. Hill, D. A. Saville, and W. B. Russel. High-frequency dielectric relaxation of spherical colloidal particles. *Phys. Chem. Chem. Phys.*, 5:911–915, 2003c.
- R. M. Hill and J. Cooper. Characterization of water-in-oil emulsions by means of dielectric spectroscopy. *J. Mater. Sci.*, 27(17):4818–4827, 1992.
- S. Hollingshead, G. A. Johnson, and B. A. Pethica. Electrophoretic properties of an octadecanol dispersion. *Trans. Faraday Soc.*, 61:577–582, 1965.
- M. Jiménez, F. Arroyo, A. Delgado, F. Mantegazza, T. Bellini, and R. Rica. Electrokinetics in extremely bimodal suspensions. *J. Colloid Interface Sci.*, 309 (2):296 – 302, 2007. Elkin 06, International Electrokinetics Conference, June 25-29, Nancy, France.
- C. S. Mangelsdorf and L. R. White. Electrophoretic mobility of a spherical colloidal particle in an oscillating electric field. J. Chem. Soc., Faraday Trans., 88:3567– 3581, 1992.
- S. C. Mangelsdorf and L. R. White. Dielectric response of a dilute suspension of spherical colloidal particles to an oscillating electric field. *J. Chem. Soc.*, Faraday Trans., 93:3145–3154, 1997.
- Y. Marcus. Ionic radii in aqueous solutions. Chem. Rev., 88(8):1475–1498, 1988.
- T. Mason. New fundamental concepts in emulsion rheology. Curr. Opin. Colloid Interface Sci., 4:231–238, 1999.
- T. G. Mason, J. Bibette, and D. A. Weitz. Yielding and flow of monodisperse emulsions. *J. Colloid Interface Sci.*, 179(2):439 448, 1996.

- S. A. Nespolo, M. A. Bevan, D. Y. C. Chan, F. Grieser, and G. W. Stevens. Hydrodynamic and electrokinetic properties of decane droplets in aqueous sodium dodecyl sulfate solutions. *Langmuir*, 17(23):7210–7218, 2001.
- R. W. O'Brien. Electro-acoustic effects in a dilute suspension of spherical particles. J. Fluid Mech., 190:71–86, 1988.
- C. Persson, A. Jonsson, M. Bergström, and J. C. Eriksson. Testing the gouy-chapman theory by means of surface tension measurements for sds-nacl-h2o mixtures. *J. Colloid Interface Sci.*, 267(1):151 154, 2003.
- L. A. Rosen and D. A. Saville. Dielectric spectroscopy of colloidal dispersions: Comparisons between experiment and theory. *Langmuir*, 7(1):36–42, 1991.
- W. B. Russel, D. A. Saville, and W. R. Schowalter. *Colloidal Dispersions*. Cambridge University Press, Cambridge, UK, 1989.
- D. A. Saville. Electrical conductivity of suspensions of charged particles in ionic solutions. *J. Colloid Interface Sci.*, 71(3):477 490, 1979.
- D. A. Saville. The electrical conductivity of suspensions of charged particles in ionic solutions: the roles of added counterions and nonspecific adsorption. *J. Colloid Interface Sci.*, 91(1):34 50, 1983.

5.A Interpretation with O'Brien's "closed-form" expression

The increment spectra are plotted with increments calculated from the polarizability (Eqn. (5.12)) with ζ -potentials and bulk concentration (c_{∞}) estimated from the adsorption isotherm and material balance for measured particle size d_{85} of different nanoemulsions.

$$D' = \frac{i\omega\varepsilon_s\varepsilon_0 - i\omega\varepsilon_p\varepsilon_0 + 2K_s/a - K_\infty}{-2i\omega\varepsilon_s\varepsilon_0 - i\omega\varepsilon_p\varepsilon_0 + 2K_s/a + 2K_\infty},$$
(5.12)

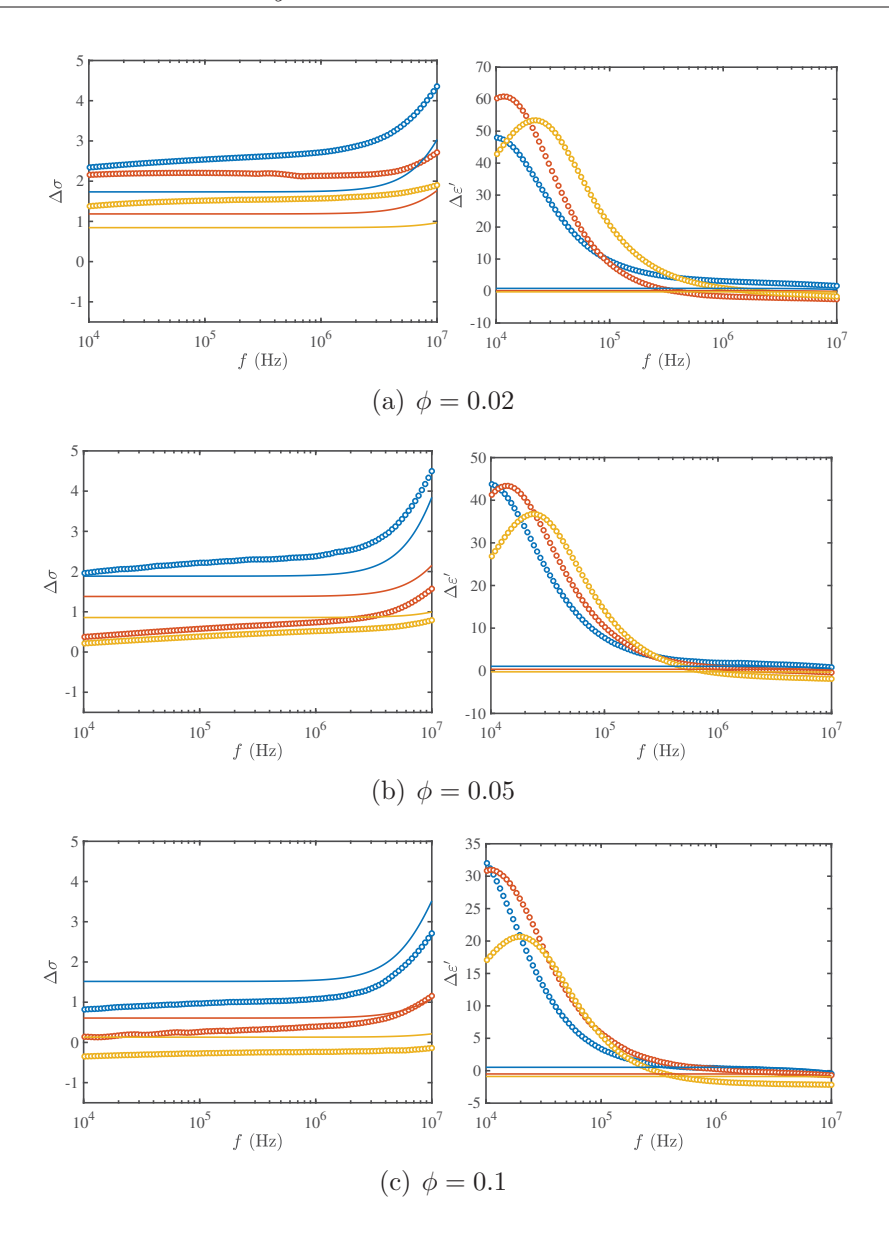


FIGURE 5.7: Conductivity (left) and dielectric (right) increment spectra for nanoemulsions with bulk volume fraction $\phi=0.02$ (a), 0.05 (b) and 0.1 (c) with bulk SDS concentration $c_{\infty,0}=5$ mM and NaCl concentrations $I_s=0$ (blue), 1 (red) and 5 (yellow) mM. Solid lines are Eqn. (5.9) with ζ -potentials from the adsorption isotherm with measured d_{85} particle diameters.

5.B Comparison of drop size characterization methods

To check particle sizes obtained from the sound-wave attenuation of the Acoustosizer II, dynamic light scattering (DLS, Horiba laser scattering particle size analyzer, Model LA-920) was used to ascertain particle size. Nanoemulsion was placed dropwise into the particle size analyzer containing pure RO water or SDS until

TABLE 5.7: Drop size distribution. Errors in d_v and d_n are the standard deviation of measurements from the Horiba laser scattering particle size analyzer. Data courtesy of Aleksandra Djuric, Materials Engineering Laboratory, Rm 2410, M.H. Wong Building, McGill University.

$c_{\infty} \; (\mathrm{mM})$	$d_{15} \; (\mu {\rm m})$	$d_{50} \; (\mu {\rm m})$	$d_{85} \; (\mu {\rm m})$	$d_v \; (\mu \mathrm{m})$	$d_n \; (\mu \mathrm{m})$
5	0.326	0.410	0.507	0.699 ± 0.238	0.450 ± 0.190
10	0.218	0.309	0.437	0.401 ± 0.114	0.324 ± 0.103
15	0.337	0.373	0.414	0.402 ± 0.106	0.318 ± 0.099
20	0.288	0.319	0.354	0.348 ± 0.110	0.218 ± 0.101

the degree of laser obstruction was ~ 15 –20% to achieve satisfactory laser scattering (as determined my the instrument software). This dilutes the nanoemulsion, whereas the Acoustosizer II enables in-situ sizing. The diameters from soundwave attenuation, which are mass-based averages, and the volume- and number-averaged diameters from DLS are summarized in table 5.7.

Chapter 6

Dynamic mobility from highly charged oil-in-water nanoemulsions

6.1 Preface

Electroacoustic spectroscopy is widely accepted for resolving the two root ζ -potential per mobility challenge when interpreting the mobility of highly charged colloidal particles. However, present electroacoustic theories to interpret the dynamic mobility spectra of fluid-behaving nanoparticulates, such as nanoemulsion oil drops in water, are incomplete, and so their accuracy cannot be known. According to a new theory that seeks to capture these dynamics (Hill and Afuwape, 2020), the high frequency mobility of nanodrops charged by the adsorption of an anionic surfactant reflects interfacial fluidity at the megahertz frequencies adopted in electroacoustic diagnostic instruments. This motivates the present electroacoustic study of oil-in-water nanoemulsions. In this chapter, measured dynamic mobility spectra are interpreted using the theory, thus establishing an electrokinetic drop size, which varies with the emulsion composition.

Abstract 6.2

Dynamic mobility spectra of sodium dodecyl sulphate (SDS)-stabilized hexadecane nanodrops in aqueous NaCl electrolytes are measured using the electro-kineticsonic amplitude, and interpreted using a recently proposed theory for highly charged drops with thin double layers. This interpretation shows that emulsion drops exhibit fluid-like dynamics at megahertz frequencies, whereas such drops have conventionally been assumed to behave as rigid spheres due to the interfacial freezing effects arising from interfacial Maxwell and Marangoni forces. Our results lend support to a view of SDS-decorated emulsion drops—in the ~ 100 – 1000 nm range—as being very highly charged, in a colloidal regime for which the standard electrokinetic model predicts two ζ -potentials for a single steady electrophoretic mobility. Whereas electrophoretic mobility measurements undertaken with light-scattering electrophoresis are conventionally converted to a ζ -potential using the Smoluchowski formula, the present experiments and theoretical interpretation suggest that the Smoluchowski ζ -potential with the Guoy-Chapman model erroneously predict the surface charge density, perhaps explaining why—despite decades of research—it has been so challenging to reach a consensus on how to resolve electro-kinetic and thermodynamic studies of SDS-decorated oil-water interfaces.

Introduction 6.3

Electrokinetic theories for rigid-particle dispersions have been widely applied to dispersed fluids (Barchini and Saville, 1996, Djerdjev et al., 2003b), justified by (i) similarities in their rheology (Mason et al., 1996, Mason, 1999, Chanamai and McClements, 2000) and (ii) surface-active impurities suppressing internal circulation (Hollingshead et al., 1965). Booth (1951), who first accounted for the electricfield-induced internal circulation in drops, identified distinct differences between the electrokinetics of fluid spheres and their rigid counterparts. Booth accounted for interfacial Maxwell (electrical) forces, but not the role of interfacial-tension gradients, which manifest as Marangoni stresses. Others have later shown that Marangoni stresses can play significant role in the interfacial fluid dynamics (Baygents and Saville, 1991).

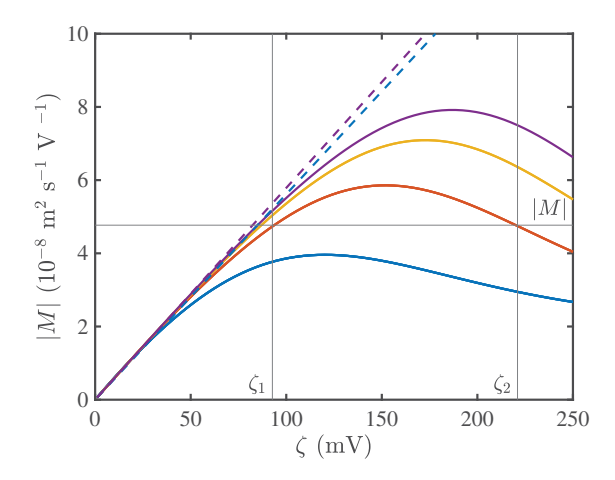


FIGURE 6.1: Electrophoretic mobility, highlighting the possibility of two ζ potential roots for highly charged colloids. Solid lines are approximate solutions (O'Brien and Hunter, 1981) of the standard electrokinetic model (O'Brien and White, 1978) for $\kappa a = 20$ (blue), 75 (red), 150 (yellow), and 230 (violet). Dashed lines are an approximation of Henry's function for $\kappa a = 20$ (blue) and 230 (violet) (Ohshima, 1994).

A wholly consistent interpretation of the anomalous electrokinetics of highly charged particles has been elusive. Reasoning along the lines of ion adsorption, surface roughness (van der Put and Bijsterbosch, 1983, Gittings and Saville, 1995) and stagnant layer conduction (Djerdjev et al., 2003b,a, Hunter, 2004) have been proposed. Ambiguity is compounded by a two valued ζ -potential for the electrophoretic mobility (O'Brien and White, 1978), as illustrated in figure 6.1. Whereas light-scattering electrophoresis conventionally furnishs ζ -potentials based on the lower value, this is controversial, and profoundly influences the physical interpretation (Hill, 2020). Some electrokinetic interpretations have favoured the lower value based on the accumulation of counterion charge in a Stern layer (Djerdjev et al., 2003a,b). Other studies, drawing on novel spectroscopic methods, have attempted to justify the lower charge on nanodrops as a consequence of interfacial charge interactions and small size (de Aguiar et al., 2010, Zdrali et al., 2017, 2019), and others have rejected the upper ζ -potential from the standard electrokinetic model, claiming such values to be unphysical (Yang et al., 2017).

Electroacoustic determination of the dynamic mobility (at megahertz frequencies) has been touted as capable of distinguishing the upper and lower ζ -potentials. Because it does not rely on light-scattering, it can be applied to dilute and concentrated colloidal dispersions (Barchini and Saville, 1996, Hunter, 2004), and is therefore well suited to studying emulsions.

The electrokinetic surface charge (furnished by the mobility) is less than the titratable charge, since the mobility reflects fluid dynamics beyond the Stern layer, whereas dispersion conductivity reflects charge transport inside and outside the Stern layer (van der Put and Bijsterbosch, 1983, Djerdjev et al., 2003b). This difference can be used to identify a Stern layer bearing mobile charge beneath the slipping plane (Mangelsdorf and White, 1990, Shubin et al., 1993, Lyklema, 1995, Mangelsdorf and White, 1998).

Stagnant layer conduction (SLC) has been adopted to explain why electrokinetic models for interpreting the dynamic mobility of colloidal dispersions might not furnish reliable ζ -potentials for highly charged drops. Simultaneous characterization of the electrical double layer using electroacoustic and dielectric relaxation spectroscopies have been used to identify SLC (Djerdjev et al., 2003a, Hunter, 2004).

In emulsions, the effect of SLC on the dynamic mobility necessitates an inner Dukhin number for theoretical dynamic mobility predictions (for rigid spheres) to match experimental results. A mobility pre-factor that captures the surface conductances, obtained from dielectric relaxation and electroacoustic spectroscopies, is often used, but this limits the use of electroacoustic spectroscopy for characterizing highly charged interfaces, such as emulsion drops (Djerdjev et al., 2003b).

Jiménez et al. (2007) examined the electrical double layer of polystyrene latex in NaCl solutions by measuring the electrophoretic mobility and dielectric relaxation, asserting that a significant contribution to the "surface" (comprising the Stern and diffuse layers) conductivity may be attributed to a stagnant layer. However, the counterion diffusion coefficients in the stagnant layer were higher than the bulk solution, making this difficult to justify from a physical perspective, since interfacial binding and crowding (e.g., steric hinderance) should hinder the surface mobility.

Fluid particles possess additional dynamics, such as internal flow driven by hydrodynamic, Maxwell and Marangoni interfacial stresses, but the Maxwell and Marangoni stresses can make their dynamics similar to rigid spheres, under steady electrophoresis (Ohshima et al., 1984, Baygents and Saville, 1991). Nevertheless, Hill and Afuwape (2020) recently proposed a theory for the dynamic mobility of highly charged surfactant-stabilized nanodroplets. At the megahertz frequencies at which these measurements are undertaken, they demonstrated distinct departures of the dynamic mobility from their rigid-sphere counterparts.

In this study, we apply the fluid-sphere theory of Hill and Afuwape (2020) to interpret dynamic mobility spectra of sodium dodecyl sulphate (SDS)-stabilized hexadecane nanodrops in aqueous NaCl electrolytes, systematically varying the SDS, oil and NaCl concentrations. According to their prescription, the surface charge density, interfacial tension, and Marangoni parameter, are calculated from an adsorption isotherm and a material balance on the SDS that accounts for the experimentally prescribed oil volume fraction. In this manner, the drop size, rather than the size and ζ -potential, becomes the single electrokinetic fitting parameter.

6.4 Materials and methods

Oil-in-water nanoemulsions were prepared with hexadecane (99 %, Sigma-Aldrich Canada), sodium dodecyl sulphate (SDS) (98.5 %, Sigma-Aldrich Canada), and reverse-osmosis (RO) water (Type 1, $\sigma \approx 5.6 \ \mu \text{S m}^{-1}$, $\Omega \approx 18 \ \text{MOhm cm}$). All materials were used as provided by the manufacturer.

6.4.1 Nanoemulsion preparation

For samples with added salt, prescribed masses of NaCl were added to known volume of reverse-osmosis (RO) water to make stock solutions of known salt concentrations. Surfactant solutions were prepared with a prescribed mass of SDS added to a known volume of pure RO water or stock solution, and stirred in a vortex mixer for 1 min to ensure dissolution. A prescribed volume of oil was added to the solution to obtain a coarse emulsion of known volume fraction ϕ . High-energy emulsification was undertaken using a probe sonicator (QSonica Q500 model) at 20 kHz (2 runs, 15 minutes each, separated by \sim 2 min). Sonication is widely used to produce nanoemulsions, but the procedure is not standardized, as the sonication time depends on the power intensity. By trail and error, the sample temperature could be maintained less than \sim 35°C for each 15 min run.

6.4.2 Electroacoustic spectroscopy

Dynamic mobility was obtained from the electrokinetic-sonic-amplitude (ESA) using an AcoustoSizer II (Colloidal Dynamics LLC) instrument. Following calibration, as detailed in the instrument's manual, 20 mL of nanoemulsion was pumped continuously through the flow cell during ESA measurements. Dispersed and continuous phases were selected from the software library (densities and thermal properties are predefined), and the weight fraction of the oil phase specified. The particle sizing option was selected to perform lognormal fitting.

The ESA is related to the dynamic mobility M by

$$ESA = A(\omega)\phi \frac{\Delta \rho}{\rho} M\left(\frac{z_s z_r}{z_s + z_r}\right)$$
(6.1)

where $A(\omega)$ a complex-valued instrument factor, and z_s and z_r are the acoustic impedances of the glass rod and dispersion (predefined with the instrument software). Moreover, ϕ is the dispersed-phase volume fraction, and $\Delta \rho = \rho_p - \rho_d$ is the dispersed- and continuous-phase density difference.

6.4.3 Dynamic mobility

For rigid spheres, in the thin-double-layer approximation ($\kappa a \gg 1$), O'Brien (1988) has shown that the complex-valued dynamic mobility

$$M = \frac{2\varepsilon\zeta}{3\eta} [1 + f(\lambda, \omega')] G(\omega a^2/\nu), \tag{6.2}$$

where $G(\omega a^2/\nu)$ is a complex-valued inertia factor (depending on the particle size and solvent kinematic viscosity ν), $\omega' = \omega \varepsilon_0 \varepsilon_o / K_\infty$, and $1 + f(\lambda, \omega')$ corrects the tangential electric field at the particle surface for surface conduction according to the surface conductivity, as captured by the (dimensionless) Dukhin number, λ . For symmetric z-z electrolytes,

$$\lambda = \frac{2}{\kappa a} \left[\cosh\left(\frac{ze\zeta}{2kT}\right) - 1 \right] \left(1 + \frac{2\varepsilon_0 \varepsilon_o(kT)^2}{z^2 \eta D e^2} \right), \tag{6.3}$$

where D the ion diffusivity (Bikerman, 1933, 1940). Below, we adopt a formula derived by O'Brien (1988) for asymmetric electrolytes, restricted to high ζ -potential.

According to Hill and Afuwape (2020), the dynamic mobility of drops at megahertz frequencies was evaluated as

$$M = \frac{V}{E} = \frac{-3c_3^E a^{-3}}{-3c_3^U a^{-3} + \rho_i/\rho_o - 1},$$
(6.4)

where (dimensionless)

$$c_{3}^{X}a^{-3} = \frac{-U}{2X} - \left[\frac{\frac{3U}{X} + \left[\frac{\eta_{i}}{\eta_{o}} \frac{T_{i}(\Omega_{i}a^{2})}{V_{i}(\Omega_{i}a^{2})} - Ma_{c} \frac{2D}{i\omega a^{2}} \right] \left[\frac{3U}{2X} + M_{s}(E/X - \hat{d}_{\psi}a^{-3}) \right]}{3 - (i - 1)\sqrt{\Omega_{o}/2}a + \frac{\eta_{i}}{\eta_{i}} \frac{T_{i}(\Omega_{i}a^{2})}{V_{i}(\Omega_{i}a^{2})} - Ma_{c} \frac{2D}{i\omega a^{2}}} \right] \frac{(\sqrt[4]{-1}\sqrt{\Omega_{o}}a + i)}{\Omega_{o}a^{2}}$$
(6.5)

and (dimensionless)

$$\hat{d}_{\psi}^{E}a^{-3} = \frac{i\omega\varepsilon_{o}\varepsilon_{0} - i\omega\varepsilon_{i}\varepsilon_{0} + 2K_{s}/a - K_{\infty} + \frac{2(ze)^{2}c^{0}Di\Omega_{D}}{ak_{B}T(i\Omega_{D} - 1)}}{2i\omega\varepsilon_{o}\varepsilon_{0} - i\omega\varepsilon_{i}\varepsilon_{0} + 2K_{s}/a + 2K_{\infty} + \frac{2(ze)^{2}c^{0}Di\Omega_{D}}{ak_{B}T(i\Omega_{D} - 1)}}.$$
(6.6)

Here, subscripts i and o denote the drop (inner) and aqueous (outer) phases with ρ , η , ε , a, ω the density, shear viscosity, dielectric permittivity, drop radius and angular frequency. Moreover, $\Omega = \omega \rho/\eta$, $\Omega_D = \omega a^2/(2D)$, $\mathrm{Ma}_c = \gamma^0 \beta c^0 a/(\eta_o D)$ is the concentration Marangoni number, K_s and K_∞ are the diffuse layer ("surface") and bulk conductivities, and $M_s = \zeta \varepsilon_o \varepsilon_0/\eta_o$ is the Smoluchowski interfacial-slip mobility. Anticipating high interfacial charge densities, we calculated the surface conductivity K_s from

$$\frac{K_s}{K_{\infty}a} = \lambda \approx \frac{n_1^{\infty} z_1^2 D_1 \sqrt{2}}{\sum_{j=1}^N z_j^2 n_j^{\infty} D_j} \left(1 + \frac{3m_1}{z_1^2} \right) \frac{e^{-ez_1 \zeta/(2k_B T)}}{\kappa a},\tag{6.7}$$

which is valid for $e^{-ez_1\zeta/(2k_BT)} \gg 1$ (O'Brien, 1988). Here, subscript 1 identifies the counterion with highest charge, and $m_1 = 2\varepsilon_0\varepsilon_o(k_BT)^2/(3\eta e^2D_1)$; n_j^{∞} , D_j and z_j are the bulk ion concentrations, ion diffusion coefficients, and valences.

6.5 Results and discussion

Following Hill and Afuwape (2020), surfactant adsorption at the oil-water interface in a nanoemulsion requires a material balance to know the equilibrium partitioning of SDS between the aqueous phase and oil-water interface. Given a bulk SDS concentration $c_{\infty,0}$ with added salt concentration (in the aqueous phase) c_{-}^{∞} , oil volume fraction ϕ with (area) average drop radius a, and an equilibrium isotherm

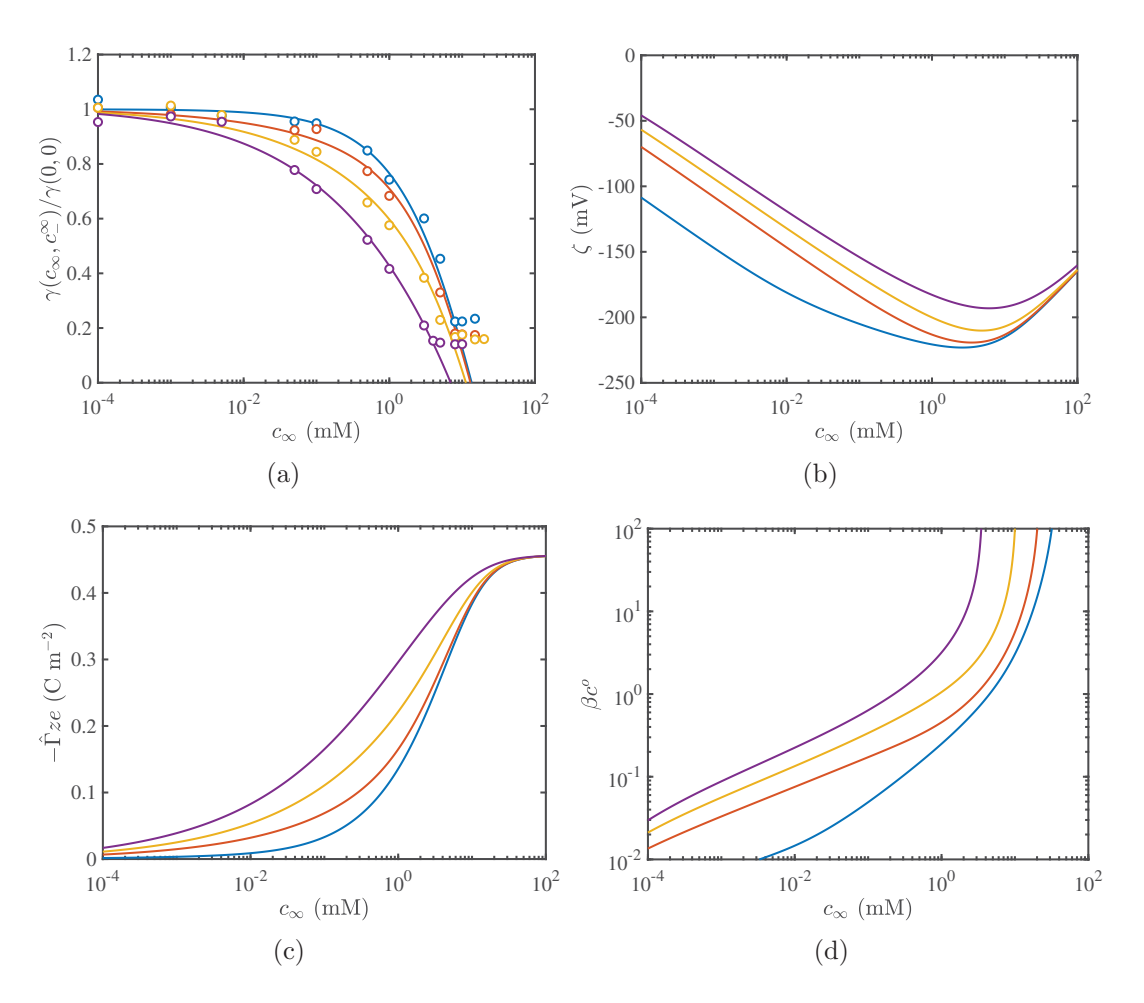


FIGURE 6.2: Equilibrium characteristics of the SDS-oil-water interface plotted versus the bulk surfactant concentration c_{∞} in the presence of added NaCl at concentrations $I_s=c_{-}^{\infty}=10^{-2}$ (blue), 1, 5 and 20 (violet) mM. Data (circles) and model (lines) are from Afuwape and Hill (2020, Ch. 5) with isotherm parameters: $\Gamma=4.89\times10^{-6}$ mol m⁻² and $n=4.83\times10^{-4}$ mol m⁻³.

 $\hat{\Gamma}(c_{\infty}, c_{-}^{\infty})$, the material balance on the SDS furnishes the aqueous SDS concentration c_{∞} by solving

$$c_{\infty,0} = \frac{3\phi\hat{\Gamma}(c_{\infty}, c_{-}^{\infty})}{a} + c_{\infty}(1 - \phi).$$
 (6.8)

The isotherm with optimized model parameters from Afuwape and Hill (2020, Ch. 5) furnishes the interfacial surface charge density $\sigma = ez\hat{\Gamma}(c_{\infty}, c_{-}^{\infty})$ (z = -1 for DS⁻), ζ -potential, and the surface tension gradient with respect to the DS⁻ surface concentration:

$$\gamma^0 \beta = -\left. \frac{\partial \gamma}{\partial c} \right|_{c^0} > 0, \tag{6.9}$$

as presented in figure 6.2.

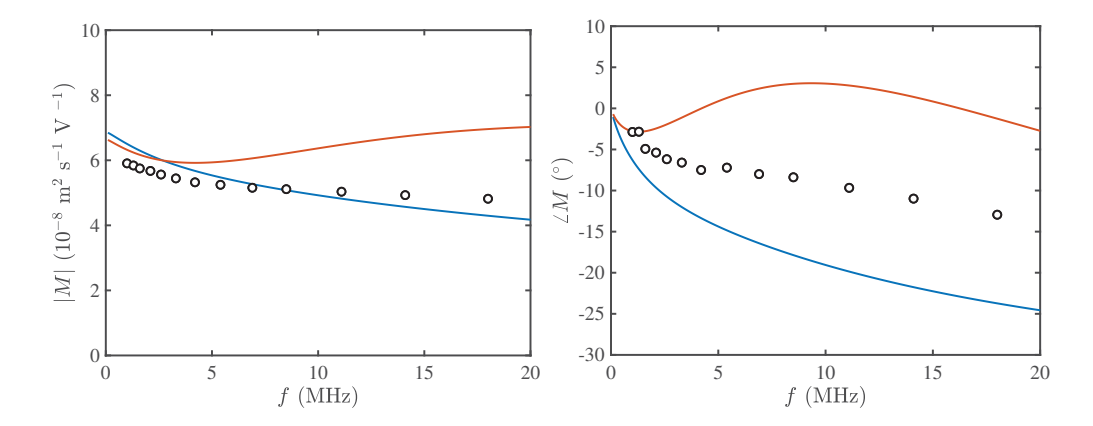


FIGURE 6.3: Dynamic mobility spectra for an SDS-oil-water emulsion: $\phi = 0.05$, $c_{\infty,0} = 4.75$ mM, and $I_s = 1$ mM (added NaCl). Lines are theoretical interpretations using O'Brien's (thin-double-layer) theory with the ζ -potential prescribed by the adsorption isotherm of Afuwape and Hill (2020, Ch. 5) ($\zeta = -8.53 \ k_B T/e$) (red) and according to the Acoustosizer II instrument ($\zeta = -3.84 \ k_B T/e$) (blue). Both calculations are undertaken with a drop diameter 2a = 701 nm, as prescribed by sound-wave attenuation, with $c_{\infty} = 3.67$ mM and $\kappa a = 78.8$ from a surfactant material balance.

6.5.1 Nanoemulsions with SDS below the c.m.c.

Dynamic mobility spectra reflect double-layer dynamics and particle inertia, and can be used determine the surface charge density (or ζ -potential) and particle size. Inertia manifests as a monotonic decrease in the mobility magnitude with increasing frequency, as shown in figure 6.3. The dynamic mobility magnitude at lower frequencies furnishes a reasonable approximation of the steady electrophoretic mobility. The phase angle depends on particle size, and increases as particle inertia causes the dynamics to increasingly lag the electric field with increasing frequency (O'Brien et al., 1995).

Figure 6.3 shows O'Brien's rigid-sphere theory (Eqn.(6.2)) evaluated using ζ -potentials from the adsorption isotherm (red) and as furnished by the Acoustosizer II fitting algorithm (blue) for an SDS-stabilized hexadecane-water nanoemulsion. Departures are significant at higher frequencies, possibly due to internal fluid and interfacial drop dynamics. Similar results were reported by Djerdjev et al. (2003b), who adopted a mobility pre-factor to model a dynamic Stern layer, which improved the model fit.

Figure 6.4 compares O'Brien's theory (O'Brien, 1988, O'Brien et al., 1995) (black, dashed lines) and the fluid-sphere theory of Hill and Afuwape (2020) (violet). This demonstrates that, at higher frequencies, Marangoni stresses influence the

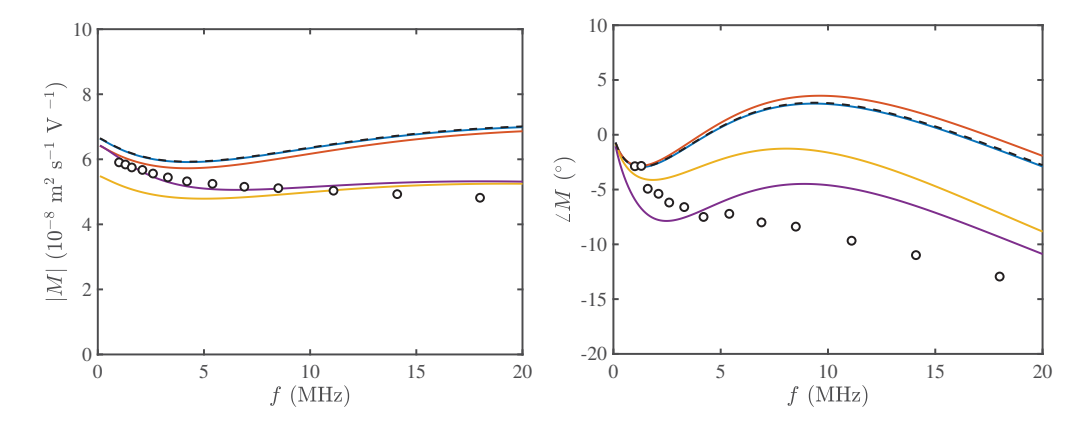


FIGURE 6.4: The same data as in figure 6.3 compared with O'Brien's theory (black dashed lines) and the fluid-sphere model of Hill and Afuwape (2020) (solid lines) with drop viscosities $\eta_i = \infty$ (rigid sphere with interfacial DS⁻ diffusivity D = 0, blue), $\eta_i = \infty$ (rigid sphere, $D = 1.02 \times 10^{-10}$ m² s⁻¹, red), $\eta_i = 3.45$ mPa s (fluid sphere, Ma_c = 0 (β = 0), yellow) and $\eta_i = 3.45$ mPa s (fluid sphere, Ma_c = 1.20 × 10⁵, violet). Both theories (including the isotherm) are evaluated with a drop diameters 2a = 701 nm.

drop dynamics. Note that the fluid-sphere theory is demonstrated to reproduce O'Brien's rigid-sphere theory when the drop viscosity is prescribed a sufficiently large value (blue) for the drop viscosity.

Prescribing a large drop viscosity to mimic a rigid particle, but maintaining a finite surface mobility (interfacial DS⁻ diffusivity $D=1.02\times 10^{-10}~\rm m^2~s^{-1}$ as prescribed by Hill and Afuwape (2020)) produced spectra that are similar to those of rigid particles according to the theory of O'Brien (1988), albeit with subtle quantitative differences (red). The DS⁻ interfacial mobility should depend on a physically motivated assessment of how the drop viscosity hinders the interfacial dynamics with respect to the electrolyte (in which the DS⁻ diffusivity $D=3.81\times 10^{-10}~\rm m^2~s^{-1}$). Note that the dynamic Stern layers adopted in previous literature have required significantly larger interfacial mobilities ($D=3.86\times 10^{-9}~\rm m^2~s^{-1}$ (Jiménez et al., 2007) and $D=8.22\times 10^{-10}~\rm m^2~s^{-1}$ (Djerdjev et al., 2003b)) to bring rigid-sphere theory into correspondence with experiments. In contrast to the model examined in this work, the interfacial mobilities are high due to the Stern layer conduction being attributed to a significant quantify of adsorbed counterions, such as Na⁺.

Figure 6.5 shows the dynamic mobility of nanoemulsions with aqueous-phase surfactant concentration $c_{\infty}^* \equiv c_{\infty,0}/(1-\phi) = 5$ mM (below the c.m.c.) for various added NaCl concentrations I_s and hexadecane volume fractions ϕ . The data are interpreted using the fluid-sphere theory of Hill and Afuwape (2020) with the

TABLE 6.1: Drop diameter moments from sound wave attenuation, and effective drop diameter \hat{d} from the theoretical fits of Eqns. (6.4)–(6.6) to measured dynamic mobility (with SDS material balance and equilibrium isotherm). Aqueous phase SDS concentration $c_{\infty,0}/(1-\phi)=5$ mM.

$\overline{I_s}$	ϕ	d_{15}	d_{50}	d_{85}	\hat{d}	$-\zeta e/k_BT$	$\lambda = K_s/(K_{\infty}a)$
(mM)	-	$(\mu \mathrm{m})$	$(\mu \mathrm{m})$	$(\mu \mathrm{m})$	$(\mu \mathrm{m})$	-	-
0	0.02	0.338	0.437	0.543	0.812	8.64	1.43
0	0.05	0.326	0.41	0.507	0.730	8.66	1.76
0	0.1	0.476	0.625	0.785	1.074	8.66	1.28
1	0.02	0.282	0.473	0.794	0.770	8.52	1.29
1	0.05	0.249	0.417	0.701	0.728	8.53	1.48
1	0.1	0.363	0.530	2.273	1.232	8.53	0.90
5	0.02	0.257	0.431	0.723	0.668	8.18	0.95
5	0.05	0.257	0.431	0.724	0.682	8.16	0.97
5	0.1	0.353	0.528	2.201	1.069	8.16	0.63

isotherm of Afuwape and Hill (2020, Ch. 3), using a drop diameter \hat{d} as the only fitting parameter (for each I_s and ϕ , as listed in table 6.1). Note that least-squares fitting was applied to the real and imaginary parts of the dynamic mobility spectra, and then plotted here as the magnitude and phase spectra.

At the lowest ionic strength (blue), the phase angle exhibits a characteristic maximum at $f \sim 5$ MHz, shifting to higher frequency with an increase in ionic strength. The mobility magnitude at low ionic strength also exhibits non-monotonic frequency dependence, particularly at low ionic strength and low oil volume fraction. Hill and Afuwape (2020) identified the transition from rigid- to fluid-interfacial dynamics occurring when their dimensionless frequency $\Omega_o a^2 \sim \text{Ma}_c D/\nu_o$, corresponding to ~ 1 MHz. The mobility fitting parameter \hat{d} varies from ≈ 780 to 1300 nm, depending on the emulsion composition (table 6.1). Note that d_{15} spans the range ≈ 260 to 480 nm with d_{85} in the range ≈ 500 to 2300 nm. Thus, the electrokinetic diameters are toward the large-end of the distributions furnished by sound-wave attenuation.

6.5.2 Nanoemulsions with SDS above the c.m.c.

Increasing the surfactant concentration has been reported to narrow the drop size distribution, and reduce the median diameter (Kong et al., 2001, 2002). However, micelles form at concentrations above the c.m.c. (Stigter and Mysels, 1955, Takata et al., 2009, Afuwape and Hill, 2020, Ch. 3). While we can measure the dynamic

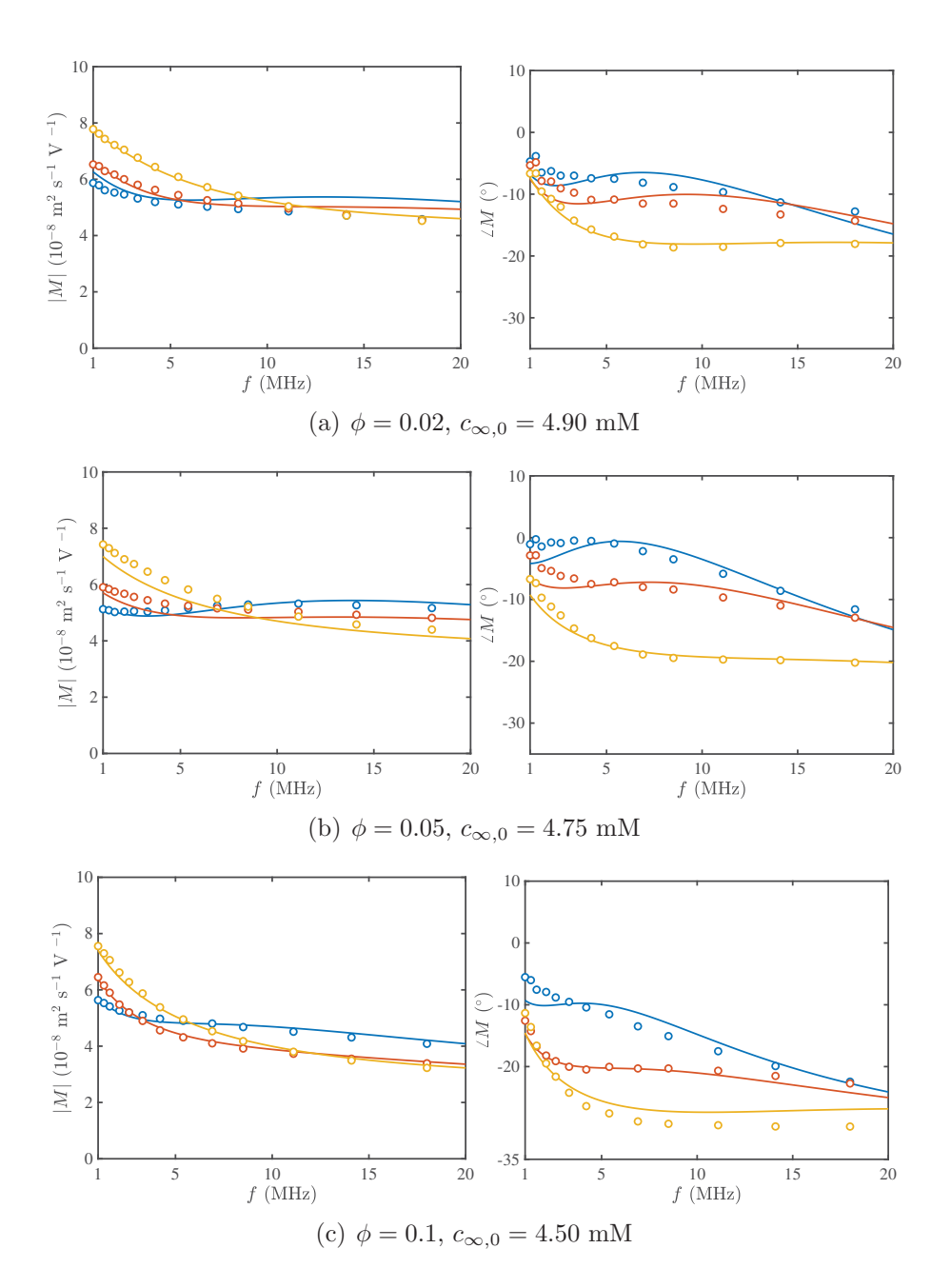


FIGURE 6.5: Dynamic mobility for nanoemulsions with aqueous-phase surfactant concentration $c_{\infty,0}/(1-\phi)=5$ mM, and added salt concentrations $I_s=10^{-2}$ (blue, c.m.c. ≈ 8.18 mM), 1 (red, c.m.c. ≈ 7.97 mM), and 5 mM (yellow, c.m.c. ≈ 6.85 mM). Solid lines are theoretical fits of Eqn. (6.4) using the drop diameter \hat{d} as the fitting parameter (see table 6.1). The c.m.c. for each ionic strength is estimated from conductivity measurements (Afuwape and Hill, 2020, Ch. 3)

.

mobility of such samples, the electrokinetic model requires separate material balance and equilibrium adsorption parameters below and above c.m.c. It is not clear how to prescribe these when above the c.m.c. At SDS concentrations above the c.m.c., we prescribed the equilibrium interfacial parameters γ_{cmc}^0 , β_{cmc} and c_{cmc}^0 to their values at the c.m.c. with the ionic strength of the background electrolyte

$$I \approx I_s + \text{c.m.c.},$$
 (6.10)

and the concentration Marangoni number

$$Ma_{c.m.c} = \frac{\gamma_{cmc}^0 \ \beta_{cmc} \ c_{cmc}^0 a}{\eta_o D}, \tag{6.11}$$

where I_s is the added salt concentration, $N_{agg} \approx 64$ is the micelle aggregation number, and c.m.c. is the critical micelle concentration. Note that added salt decreases the c.m.c., thus increasing the micelle concentration at a given SDS concentration $c_{\infty} > \text{c.m.c.}$ Moreover, Eqn. (6.10) neglects the contribution of micelles and their counterions to the ionic strength of the background electrolyte.

Dynamic mobility data were again interpreted using the fluid-sphere theory to furnish effective drop diameters \hat{d} . With this prescription, the goodness of fit decreased with increasing ionic strength, possibly because of the increasing contribution of micelles to the ESA signal or the manner in which they change the ionic composition of the background electrolyte. Note that the ESA magnitude for micelle solutions is $\sim 10^{-5}$ Pa m V⁻¹ when $c_{\infty} \approx 10$ –50 mM as compared to emulsions for which the ESA is $\sim 10^{-3}$ Pa m V⁻¹ when $\phi \approx 0.02$ –0.05.

Figure 6.6 shows the dynamic mobility of nanoemulsions with a bulk aqueousphase SDS concentration $c_{\infty,0}/(1-\phi)=13$ mM (above the c.m.c.) for various I_s and ϕ with the corresponding drop diameters listed in table 6.2. The mobility spectra are ostensibly less sensitive to the frequency, with comparable low-frequency magnitude to the data $c_{\infty,0}/(1-\phi)=5$ mM (below the c.m.c.). Although the model provides a reasonable fit to the mobility magnitude, the phase angle departs at high ϕ .

Values of \hat{d} above the c.m.c. are considerably smaller, now varying from ≈ 372 to 708 nm, depending on the emulsion composition (table 6.2). Similarly, d_{15} spans the range ≈ 250 to 380 nm with d_{85} in the range ≈ 400 to 730 nm. Thus, the

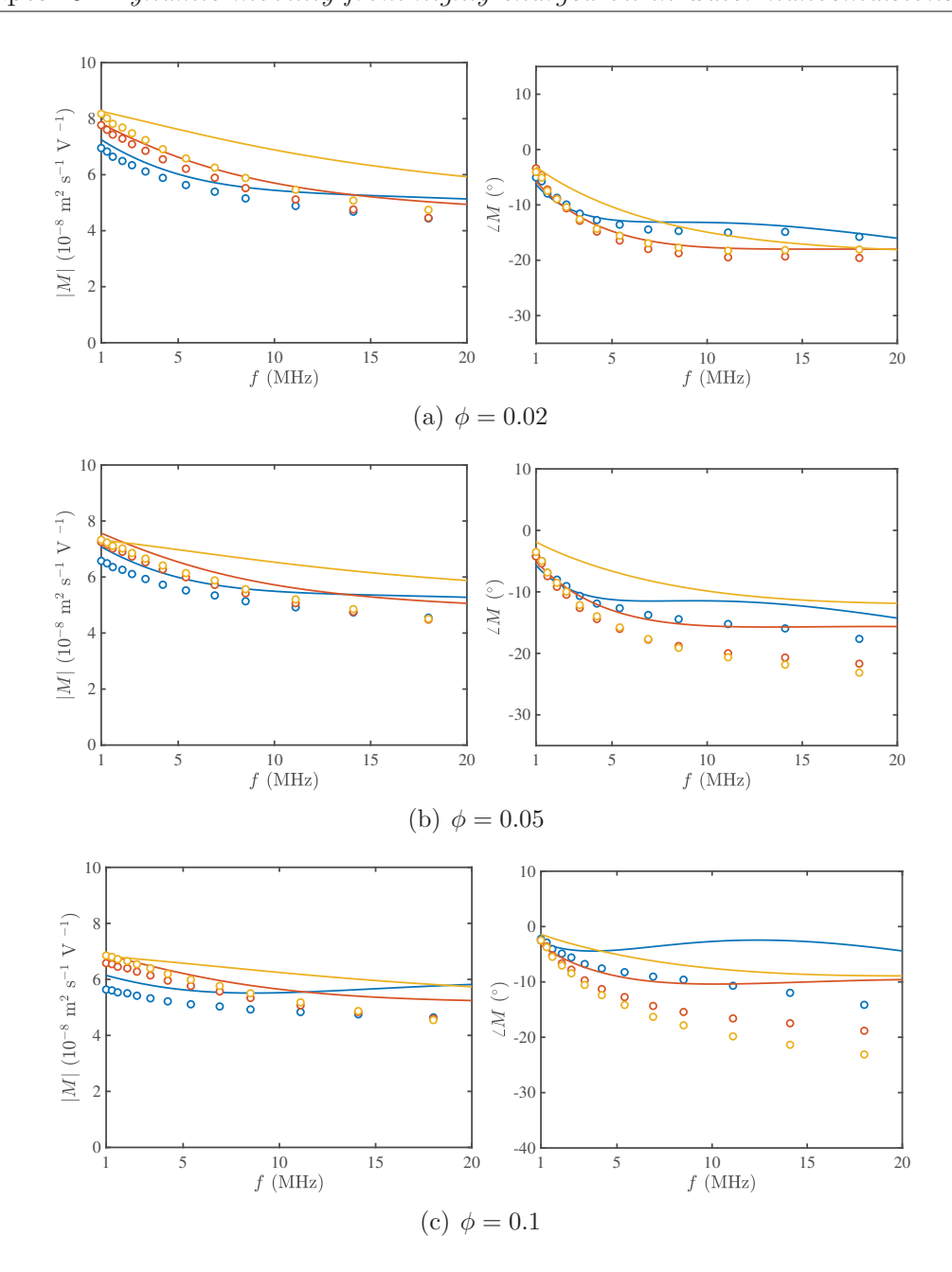


FIGURE 6.6: Dynamic mobility for nanoemulsions with aqueous-phase surfactant concentration $c_{\infty,0}/(1-\phi)=13$ mM (above the c.m.c.), and added salt concentrations $I_s=10^{-2}$ (blue, c.m.c. ≈ 8.18 mM), 1 (red, c.m.c. ≈ 7.97 mM), and 5 mM (yellow, c.m.c. ≈ 6.85 mM). Solid lines are theoretical fits of Eqn. (6.4) using the drop diameter \hat{d} as the fitting parameter (see table 6.1). The c.m.c. for each ionic strength is estimated from conductivity measurements (Afuwape and Hill, 2020, Ch. 3). See figure 6.7 for an improved fit based on setting $\beta=0$.

smaller electrokinetic diameters are again toward the large-end of the distributions furnished by sound-wave attenuation, and (consistent with the sound-wave-attenuation sizes) ostensibly smaller than when below the c.m.c.

Above the c.m.c., the foregoing estimate of β_{cmc} may be grossly overestimated,

Table 6.2: Drop size moments from sound wave attenuation, and effective drop diameter \hat{d} from the theoretical fits of Eqns. (6.4)–(6.6) to measured dynamic mobility data with SDS material balance and equilibrium isotherm). Bulk aqueous-phase SDS concentration $c_{\infty}^* (\equiv c_{\infty,0}/(1-\phi)) = 13$ mM. Note that $(-\zeta e/kT) = (-\zeta e/kT)_{\beta=0}$.

I_s	ϕ	d_{15}	d_{50}	d_{85}	\hat{d}	$(-\zeta e/kT)$	$\hat{d}_{\beta=0}$	λ	$\lambda_{\beta=0}$
(mM)	-	$(\mu \mathrm{m})$	$(\mu \mathrm{m})$	$(\mu \mathrm{m})$	$(\mu \mathrm{m})$	-	$(\mu \mathrm{m})$	-	-
0	0.02	0.377	0.418	0.464	0.708	8.47	0.846	1.12	0.94
0	0.05	0.357	0.396	0.439	0.671	8.47	0.817	1.18	0.97
0	0.1	0.334	0.375	0.420	0.506	8.47	0.671	1.57	1.18
5	0.02	0.332	0.409	0.503	0.592	8.15	0.736	0.94	0.76
5	0.05	0.315	0.388	0.477	0.547	8.15	0.717	1.02	0.78
5	0.1	0.323	0.359	0.398	0.448	8.15	0.608	1.25	0.92
20	0.02	0.275	0.359	0.446	0.372	7.48	0.560	0.75	0.50
20	0.05	0.246	0.308	0.476	0.283	7.48	0.512	1.03	0.54
20	0.1	0.283	0.348	0.429	0.246	7.48	0.394	1.13	0.71

since in this regime the surface tension is a very weak function of c_{∞} . To test this hypothesis, we fitted the model to these data with $\beta=0$, i.e., without the Marangoni effects. The results are shown in figure 6.7 with the fitted $\hat{d}_{\beta=0}$ in table 6.2. Noteworthy is a significant improvement in the fitting, especially for samples with the higher NaCl concentration (lower c.m.c.). The difference between $\hat{d}_{\beta=0}$ and \hat{d} demonstrates the significance of the Marangoni parameter for surfactant-stabilized drops at these frequencies.

6.6 Conclusions

The theory of Hill and Afuwape (2020) for fluid spheres with mobile surface charge has been used to interpret dynamic mobility measurements from hexadecane-in-water nanoemulsions with varying oil volume fraction (0.02, 0.05, and 0.1) and added salt concentration (0, 1, and 5 mM). Surface charge density (and ζ -potential), and other pertinent interfacial characteristics, were prescribed from the isotherm for SDS at the oil-water interface. The theory captured the megahertz-frequency dynamics of the mobility for emulsion drops, ascribed to Marangoni stresses and internal fluid circulation. For each emulsion, an effective drop diameter was fit.

This approach departs from previous theoretical interpretations, which have adopted a rigid-sphere dynamic mobility with a dynamic Stern layer comprising adsorbed

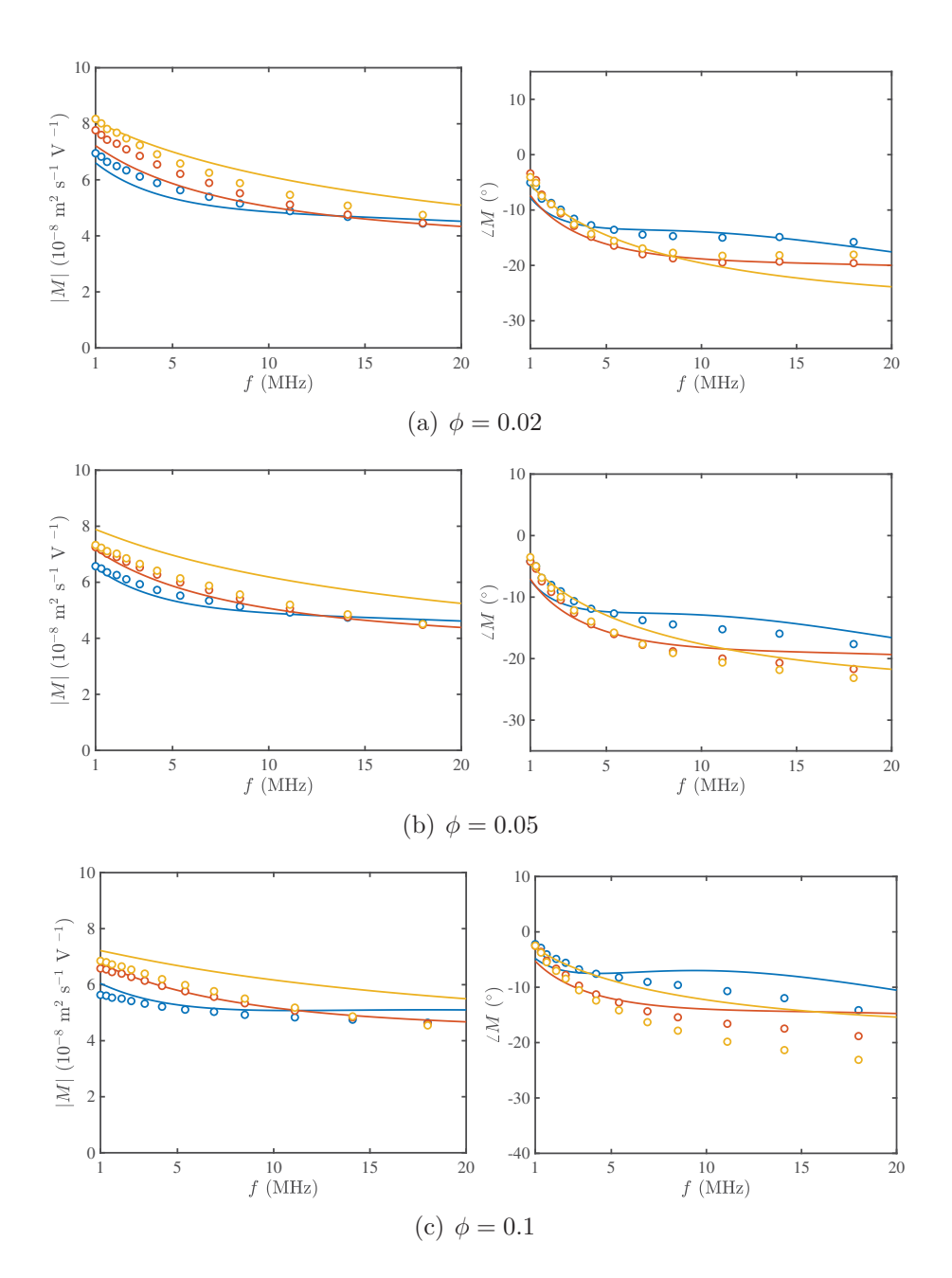


FIGURE 6.7: The same data as in figure 6.6, but the model is fitted without Marangoni effects (setting $\beta=0$). This is suggested as a better approximation when above the c.m.c., based on the equilibrium interfacial surface tension being a very weak function of surfactant concentration in this regime.

counterions. Our interpretation does not require a Stern layer, since the surfactant charge, which is assumed to reside at the "slipping plane" is intrinsically mobile.

The manner in which the "electrokinetic" drop diameter varied with emulsion composition highlights challenges arising from polydispersity. On one hand, the surfactant material balance hinges on an area-averaged drop size, whereas the dynamic mobility reflects a volume-averaged size. Future analysis might therefore benefit from attempts to model the polydispersity, for example using the lognormal drop-size distributions furnished by sound-wave attenuation.

Below the critical micelle concentration, the fluid-sphere theory produced superior fits than rigid-sphere theory, without any arbitrary prescriptions of surface conductance parameters (namely Stern-layer charge density and mobility). Above the c.m.c., equilibrium isotherm parameters were prescribed values at the c.m.c. These challenged the theory when increasing the added salt concentration, possibly a consequence of an increasing concentration of micelles modifying the background electrolyte. Nevertheless, a significant improvement was obtained by neglecting the Marangoni stresses in this regime; this is motivated by the empirical observation that the interfacial tension above the c.m.c. is a notably weak function of surfactant concentration.

6.7 Acknowledgements

This work was supported by NSERC Discovery and Research Tools and Instruments grants to R.J.H. G.A. was supported by a PRESSID/PTDF scholarship (Nigeria).

6.8 Author contributions

G.A. and R.J.H. designed the experiments. G.A. performed the experiments and analyzed the data. G.A. and R.J.H. interpreted the data and wrote the paper.

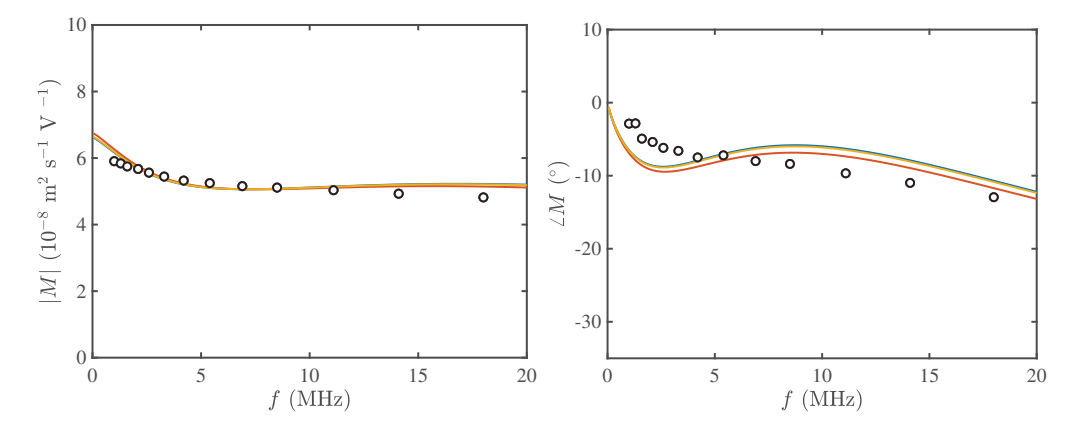


FIGURE 6.8: Fitting the fluid-sphere model of Hill and Afuwape (2020) (drop radius a as the fitting parameter) to measured dynamic-mobility spectra using (i) real and imaginary parts (blue, 2a=712 nm), (ii) real part (red, 2a=726 nm), and (ii) magnitude (yellow, 2a=707 nm). Bulk surfactant concentration $c_{\infty,0}/(1-\phi)=5$ mM, added salt concentration $I_s=1$ mM, oil volume fraction $\phi=0.05$.

6.A Fitting dynamic mobility models to measured spectra

Dynamic mobility is a complex-valued quantity for which the in- (real) and out-of-phase (imaginary) components of the particle velocity are measured respect to the applied electric field. Fitting model spectra to measured data can be undertaken in different ways, furnishing different fitting parameters, as demonstrated here. Figure 6.8 shows least-squares fits based on fitting the fluid-sphere model to (i) the real and imaginary parts of the dynamic mobility $(2a \approx 712 \text{ nm})$; (ii) only the real part of the dynamic mobility $(2a \approx 726 \text{ nm})$, and (iii) only the magnitude of the dynamic mobility $(2a \approx 707 \text{ nm})$. This shows that fitting to the real and imaginary parts furnishes a smaller size. For this example, sound-wave attenuation furnishes $\hat{d}_{85} = 701 \text{ nm}$, favouring method (i), which we have adopted throughout the main text.

Bibliography

G. A. Afuwape and R. J. Hill. Nanoemulsion-hydrogel composites: Electro-kinetic dynamics, viscoelastic and swelling responses. PhD thesis, McGill University, 2020.

- R. Barchini and D. A. Saville. Electrokinetic properties of surfactant-stabilized oil droplets. *Langmuir*, 12(6):1442–1445, 1996.
- J. C. Baygents and D. A. Saville. Electrophoresis of drops and bubbles. *J. Chem. Soc.*, Faraday Trans., 87:1883–1898, 1991.
- J. J. Bikerman. Ionentheorie der elektrosmose, der strömungsströme und der oberflächenleitfähigkeit. Z. Physik. Chem., 163A(1), 1933.
- J. J. Bikerman. Electrokinetic equations and surface conductance. a survey of the diffuse double layer theory of colloidal solutions. *Trans. Faraday Soc.*, 35: 154–160, 1940.
- F. Booth. The cataphoresis of spherical fluid droplets in electrolytes. *J. Chem. Phys.*, 19(11):1331–1336, 1951.
- R. Chanamai and D. J. McClements. Dependence of creaming and rheology of monodisperse oil-in-water emulsions on droplet size and concentration. *Colloids* Surf., A, 172(1):79 – 86, 2000.
- H. B. de Aguiar, A. G. F. de Beer, M. L. Strader, and S. Roke. The interfacial tension of nanoscopic oil droplets in water is hardly affected by sds surfactant. J. Am. Chem. Soc., 132(7):2122–2123, 2010.
- A. M. Djerdjev, J. K. Beattie, and R. J. Hunter. Stagnant layer conduction in surfactant-stabilized hexadecane emulsion systems measured by electroacoustics. *Aust. J. Chem.*, 56(10):1081–1089, 2003a.
- A. M. Djerdjev, J. K. Beattie, and R. J. Hunter. An electroacoustic and high-frequency dielectric response study of stagnant layer conduction in emulsion systems. *J. Colloid Interface Sci.*, 265(1):56–64, 2003b.
- M. R. Gittings and D. A. Saville. Electrophoretic mobility and dielectric response measurements on electrokinetically ideal polystyrene latex particles. *Langmuir*, 11(3):798–800, 1995.
- R. J. Hill. Electrokinetic spectra of dilute surfactant-stabilized nano-emulsions. *J. Fluid Mech.*, 902(A15), 2020.
- R. J. Hill and G. A. Afuwape. Dynamic mobility of surfactant stabilized nanodroplets: unifying equilibrium thermodynamics, electro-kinetics and Marangoni effects. *J. Fluid Mech.*, 895(A14), 2020.

- S. Hollingshead, G. A. Johnson, and B. A. Pethica. Electrophoretic properties of an octadecanol dispersion. *Trans. Faraday Soc.*, 61:577–582, 1965.
- R. J. Hunter. More reliable zeta potentials using electroacoustics. In *Surface and Colloid Science*, pages 1–10, Berlin, Heidelberg, 2004. Springer Berlin Heidelberg.
- M. L. Jiménez, F. J. Arroyo, F. Carrique, and A. V. Delgado. Surface conductivity of colloidal particles: experimental assessment of its contributions. *J. Colloid Interface Sci.*, 316(2):836–843, 2007.
- L. Kong, J. K. Beattie, and R. J. Hunter. Electroacoustic study of concentrated oil-in-water emulsions. *J. Colloid Interface Sci.*, 238(1):70 79, 2001.
- L. Kong, J. K. Beattie, and R. J. Hunter. Electroacoustic study of hexadecane/water emulsions. *Aust. J. Chem.*, 54(8):503–511, 2002.
- J. Lyklema. Fundamentals of Interface and Colloid Science, volume 2. Elservier Academic press, 1995.
- C. S. Mangelsdorf and L. R. White. Effects of stern-layer conductance on electrokinetic transport properties of colloidal particles. J. Chem. Soc., Faraday Trans., 86:2859–2870, 1990.
- S. C. Mangelsdorf and L. R. White. The dynamic double layer part 1: Theory of a mobile stern layer. *J. Chem. Soc.*, Faraday Trans., 94:2441–2452, 1998.
- T. Mason. New fundamental concepts in emulsion rheology. Curr. Opin. Colloid Interface Sci., 4:231–238, 1999.
- T. G. Mason, J. Bibette, and D. A. Weitz. Yielding and flow of monodisperse emulsions. *J. Colloid Interface Sci.*, 179(2):439 448, 1996.
- R. W. O'Brien. Electro-acoustic effects in a dilute suspension of spherical particles. J. Fluid Mech., 190:71–86, 1988.
- R. W. O'Brien and R. J. Hunter. The electrophoretic mobility of large colloidal particles. *Can. J. Chem.*, 59(13):1878–1887, 1981.
- R. W. O'Brien and L. R. White. Electrophoretic mobility of a spherical colloidal particle. J. Chem. Soc., Faraday Trans. 2, 74:1607–1626, 1978.

- R. W. O'Brien, D. W. Cannon, and W. N. Rowlands. Electroacoustic determination of particle size and zeta potential. *J. Colloid Interface Sci.*, 173(2):406–418, 1995.
- H. Ohshima. A simple expression for henry's function for the retardation effect in electrophoresis of spherical colloidal particles. J. Colloid Interface Sci., 168(1): 269 – 271, 1994.
- H. Ohshima, T. W. Healy, and L. R. White. Electrokinetic phenomena in a dilute suspension of charged mercury drops. J. Chem. Soc., Faraday Trans. 2, 80: 1643–1667, 1984.
- V. E. Shubin, R. J. Hunter, and R. W. O'Brien. Electroacoustic and dielectric study of surface conduction. *J. Colloid Interface Sci.*, 159(1):174 183, 1993.
- D. Stigter and K. J. Mysels. Tracer electrophoresis. ii. the mobility of the micelle of sodium lauryl sulfate and its interpretation in terms of zeta potential and charge. J. Phys. Chem., 59(1):45–51, 1955.
- Y. Takata, T. Miyayama, T. Nagahashi, A. Hyono, and H. Ohshima. Micelle formation effect on electroacoustics in an aqueous surfactant solution: Colloid vibration current and ion vibration current. *J. Oleo Sci.*, 58(11):557–563, 2009.
- A. G. van der Put and B. H. Bijsterbosch. Electrokinetic measurements on concentrated polystyrene dispersions and their theoretical interpretation. J. Colloid Interface Sci., 92(2):499 507, 1983.
- F. Yang, W. Wu, S. Chen, and W. Gan. The ionic strength dependent zeta potential at the surface of hexadecane droplets in water and the corresponding interfacial adsorption of surfactants. *Soft Matter*, 13:638–646, 2017.
- E. Zdrali, Y. Chen, H. I. Okur, D. M. Wilkins, and S. Roke. The molecular mechanism of nanodroplet stability. *ACS Nano*, 11(12):12111–12120, 2017.
- E. Zdrali, G. Etienne, N. Smolentsev, E. Amstad, and S. Roke. The interfacial structure of nano- and micron-sized oil and water droplets stabilized with sds and span80. *J. Chem. Phys.*, 150(20):204704, 2019.

Chapter 7

Dynamic mobility of nanodrops in hydrogels

7.1 Preface

The incorporation of nanoemulsions in hydrogels has been suggested as a means of cargo for lipophilic entities for different applications. Short time stability is achieved using surface active agents in the nanoemulsion formation, and long term stability or modifiable delivery techniques are weaved in by incorporating the drops in polymer networks. Electroacoustic spectroscopy is used to investigate the interaction of nanoemulsion-doped polyacrylamide hydrogel composites to highlight the potential change in particle size, composite properties, and furnish the potential influence of volume fraction and monomer concentration on these properties. Data are interpreted by modifying the theory of Hill and Afuwape (2020) with a complex viscosity for a hydrogel skeleton.

7.2 Abstract

The electrokinetic-sonic-amplitude of SDS-stabilized hexadecane in water nanoemulsions dispersed in polyacrylamide hydrogels is used to ascertain their dynamic mobility spectra. The dynamic mobility is theoretically interpreted using a recent model for highly charged drops with thin double layers for which we replaced the electrolyte viscosity with complex-valued shear modulus obtainable from linear-viscoelastic rheology. The drop size is found to be invariant to the formation of a cross-linked polymer network, suggesting that the hydrogel immobilizes the drops. The theoretical interpretation also furnishes a shear viscosity for the composite (at megahertz frequencies) that increases with the oil volume fraction. The experimental and theoretical analysis undertaken here provides a new non-invasive means of studying the microstructure of these novel viscoelastic nanocomposites.

7.3 Introduction

The concept of incorporating colloidal particles, such as nanoparticles (Nazli et al., 2014, Thoniyot et al., 2015), vesicles (Carafa et al., 2011, López Mora et al., 2014, Grijalvo et al., 2016, Zhou et al., 2019), micelles (Wei et al., 2009, Gong et al., 2013), nanoemulsions (Mou et al., 2008, An et al., 2012, Lei et al., 2017, Cong et al., 2017, Wu et al., 2017, Hashemnejad et al., 2019, Kass et al., 2019), has been used to develop advanced materials, with the defined hydrophobic compartments useful in various applications such as in food, cosmetics, pharmaceutics, imaging, sensors, and other biomedical applications.

The study of nanoemulsion-doped polyacrylamide hydrogels is increasingly coming into the limelight because of the need to encapsulate, and deliver lipophilic entities. The composite combines the merits of nanoemulsions (*i.e.* solubility of entities in the oil phase, increased surface area *etc.*) (Jaiswal et al., 2014, Gupta et al., 2016), with the tuneable possibilities of various stimulus responsive hydrogels for controlled and localized delivery (Chen et al., 1999, Peppas et al., 2000, Alexander, 2001, Urban and Weiss, 2009, Barbucci, 2010, Geckil et al., 2010).

Another merit of the composite stems from the ability to preload by producing nanoemulsions at high volume fraction and preselection of the hydrogel properties to allow for controlled barrier for release (An et al., 2012). However, studies about the nanodrop-hydrogel interactions in a composite are limited to investigating the changes in bulk properties of the composites (Sala et al., 2007, 2009a,b, Zeeb et al., 2015, Hashemnejad et al., 2019) without an understanding of the nanodrop-hydrogel interactions in the composite.

Electroacoustic spectroscopy has been proposed as a non-invasive technique for the investigation of heterogenous nanocomposites. It has been used to explore the effect of ionic concentration and nanoparticle size on the frequency dependent dynamics of particles in Newtonian solvents (O'Brien et al., 1995, Djerdjev et al., 2003), and to elucidate the nanoparticle interaction in polymer networks, and furnish the effect of different polyner mesh sizes, nanoparticle aspect ratio, and shear moduli on nanoparticle-doped hydrogels (Bhosale et al., 2011, Adibnia and Hill, 2014).

Theoretical analysis of nanoparticle dynamics in complex fluids has also been undertaken to provide a background for interpreting electroacoustic experiments at megahertz frequencies available. In this regime, as long as $\kappa a \gg 1$, fluid stresses are dominant over elastic stresses, which makes electroacoustic responses independent of the polymer shear modulus, and fluid and polymer can be assumed to be tightly coupled. At lower frequencies, electro-osmotic flow and particle polarization become apparent (Wang and Hill, 2009).

In this study, we follow the theory of Wang and Hill (2009) and apply a modified form of the dynamic mobility theory of Hill and Afuwape (2020) to help understand the nanodrop hydrogel interaction, and determine the effective particle size as a function of the oil volume fraction, and drop and hydrogel properties. We systematically explore how the oil volume fraction and hydrogel shear modulus influence drop mobility at the megahertz frequencies of sound-wave attenuation and electrokinetic sonic amplitude instrumentation.

7.4 Materials and methods

Materials used for preparing nanoemulsions are outlined in Afuwape and Hill (2020, Ch. 5). Polyacrylamide gels were synthesized from acrylamide (monomer) (40 w/v % aqueous solution, Fisher Scientific U.S.A.), bisacrylamide (cross-linker) (2 w/v % aqueous solution, Fisher Scientific U.S.A.), ammonium persulfate (APS) (powder, Fisher Scientific U.S.A.), and N,N,N',N'-tetramethylethylenediamine (TEMED, GE Healthcare Life Science, Germany) as initiator and catalyst for the free radical polymerization. All materials were used as procured from the manufacturers.

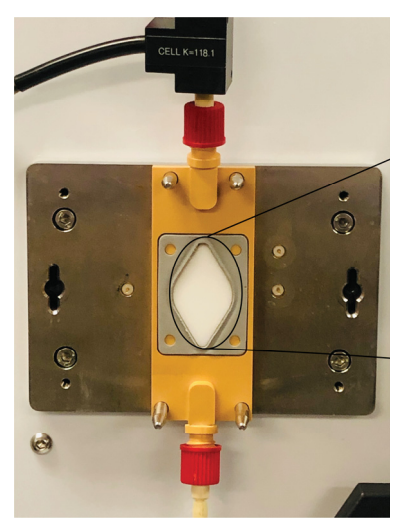




FIGURE 7.1: Nanoemulsion-doped hydrogel in the ESA polysphenylenesulphide (PPS) spacer of the ESA sensor (left) and attached to the ESA electrode (right).

7.4.1 Synthesis of nanoemulsion-doped polyacrylamide hydrogel composites

Nanoemulsions were prepared as outlined in Afuwape and Hill (2020, Ch. 5). Composite were synthesized by adding prescribed volume of nanoemulsion, monomer and cross-linker to form a pre-gel mixture. 10 μ l of ammonium persulfate (0.44 mol l⁻¹) per ml of total gel volume was added to the solution as initiator, nitrogen gas was passed through the sample for ≈ 5 min to remove dissolved oxygen that could inhibit the polymerization process 3 μ l TEMED per ml total gel solution was added as catalyst. The sample is loaded to the Acoustosizer II cell with a syringe. An image of the fully-formed composite is shown below in figure 7.1.

7.4.2 Electroacoustic spectroscopy

Nanoemulsions are pre-characterized in the same approach detailed in Afuwape and Hill (2020, Ch. 5). A batch setup is designed for composites as polymerization makes a continuous run impossible. Following an instrument calibration (according to the manufacturer instructions) gel precursor solution was siphoned into a syringe and loaded into the ESA cell to fill about 2–3 cm of the (top) overflow tube. Using the instrument software, ≈ 30 ESA spectra were measured in succession, each run taking approximately 4.5 min.

7.4.3 Rheology

Oscillatory shear measurements were undertaken using an ARES-G2 (TA Instruments) rheometer. A 1.3 ml sample of gel precursor solution was deposited between parallel plates surrounded by a rubber ring and the gap adjusted to achieve a 1 mm separation. Oscillatory shear was applied at 2% strain with angular frequencies in the range 0.1–100 rad s⁻¹, and at an angular frequency of 10 rad s⁻¹ with strains in the range 0.1–100%. Following an initial incubation period, incipient gelation was identified by a crossing of the storage and loss moduli, with further changes in the storage and loss moduli plateauing over a period of 100 min.

7.5 Results and discussion

Polyacrylamide was selected as an uncharged hydrogel because its gelation kinetics allows for the injection of pre-gel solution into the ESA cell. A nomenclature $P_xG_yS_z$ is adopted to highlight the different composition of the nanoemulsion-doped polyacrylamide hydrogels, P_x is the initial volume fraction of oil in the nanoemulsion, G_y the monomer concentration in wt%, and the S_z the initial added salt concentration for the synthesis of nano-emulsion. The monomer to cross-linker concentration are maintained throughout in all samples (AAm:Bis = 19:1), and the aqueous-phase surfactant concentration in the nanoemulsion $c_{\infty,0}/(1-\phi)=5$ mM, where $c_{\infty,0}$ is the total bulk surfactant concentration.

7.5.1 Rheology

Rheological time series during polymerization and gelation are shown in figure 7.2(a). The storage modulus plateaus at $t \approx 2000$ s Steady state G'_{∞} values were obtained by extrapolation using the Hill relationship

$$G'(t) = \frac{G'_{\infty}t^{\alpha}}{t^{\alpha} + \theta^{\alpha}},\tag{7.1}$$

where t is the time, θ is the gelation half time, G'_{∞} steady state modulus and α is an exponent relative to the slope $P = \alpha G'/(4\theta)$ at half the gelation time (Calvet et al., 2004).

Sample	ϕ^*	c_{AAm}^*	$I_{s,0}^*$	ϕ	$c_{\infty,0}$	$c_{ m AAm}$	$I_{s,0}$	G_{∞}'
	-	(mM)	(mM)	-	(mM)	%	(mM)	(kPa)
$P_0G_4S_0$	0	4	0	0	_	4	0	1.10
$P_2G_4S_0$	0.02	4	0	0.016	4.01	4.06	0	1.41
$P_5G_4S_0$	0.05	4	0	0.039	3.89	4.16	0	1.27
$P_{10}G_4S_0$	0.1	4	0	0.078	3.68	4.34	0	1.30
$P_{20}G_4S_0$	0.2	4	0	0.156	3.27	4.74	0	2.31
$P_2G_4S_5$	0.02	4	5	0.016	4.01	4.06	4.08	1.51
$P_5G_4S_5$	0.05	4	5	0.039	3.89	4.16	4.05	1.65
$P_{10}G_4S_5$	0.1	4	5	0.078	3.68	4.34	4.01	1.55
$P_0G_{5.5}S_0$	0	5.5	0	0	_	5.5	0	4.28
$P_5G_{5.5}S_0$	0.05	5.5	0	0.035	3.56	5.70	0	_
$P_0G_8S_0$	0	8	0	0	_	8	0	13.12
$P_5G_8S_0$	0.05	8	0	0.029	2.99	8.24	0	_

Table 7.1: Nanoemulsion-doped polyacrylamide hydrogel compositions and steady-state storage moduli G'_{∞} as furnished by Eqn. (7.1) from bulk rheology.

A post-polymerization strain amplitude sweep is shown in figure 7.2(b) to emphasize that the rheological characterization was performed in the linear viscoelastic regime. The frequency independence of the storage modulus with and shear thinning viscosity for the three samples in the range $\omega = 0.1$ –100 rad s⁻¹ are demonstrated in figure 7.2(c) and (d).

7.5.2 Dynamic mobility spectra

The effect of polymerization on the dynamic mobility of rigid particles over a range of frequencies has been reported (Adibnia and Hill, 2014), and the experimental results analyzed using the theoretical framework of Wang and Hill (2009), which is valid when the Debye length is smaller than the hydrogel skeleton mesh size, and the hydrogel network behaves as an incompressible fluid. Figure 7.3 shows the attenuation of the dynamic mobility of drops due to the polymerization when an oscillatory electric field is applied across a nanoemulsion-doped hydrogel. The frequency dependence of the dynamic mobility is qualitatively similar to nanoemulsions, albeit with a notable offset in both magnitude, and phase angle, possibly due to the effect of polymer adhesion to the drop. The addition of cross-linked acrylamide has been reported to reduce the mobility and conductivity due to a displacement of the shear plane, thus reducing the ζ -potential (Adibnia and Hill, 2014).

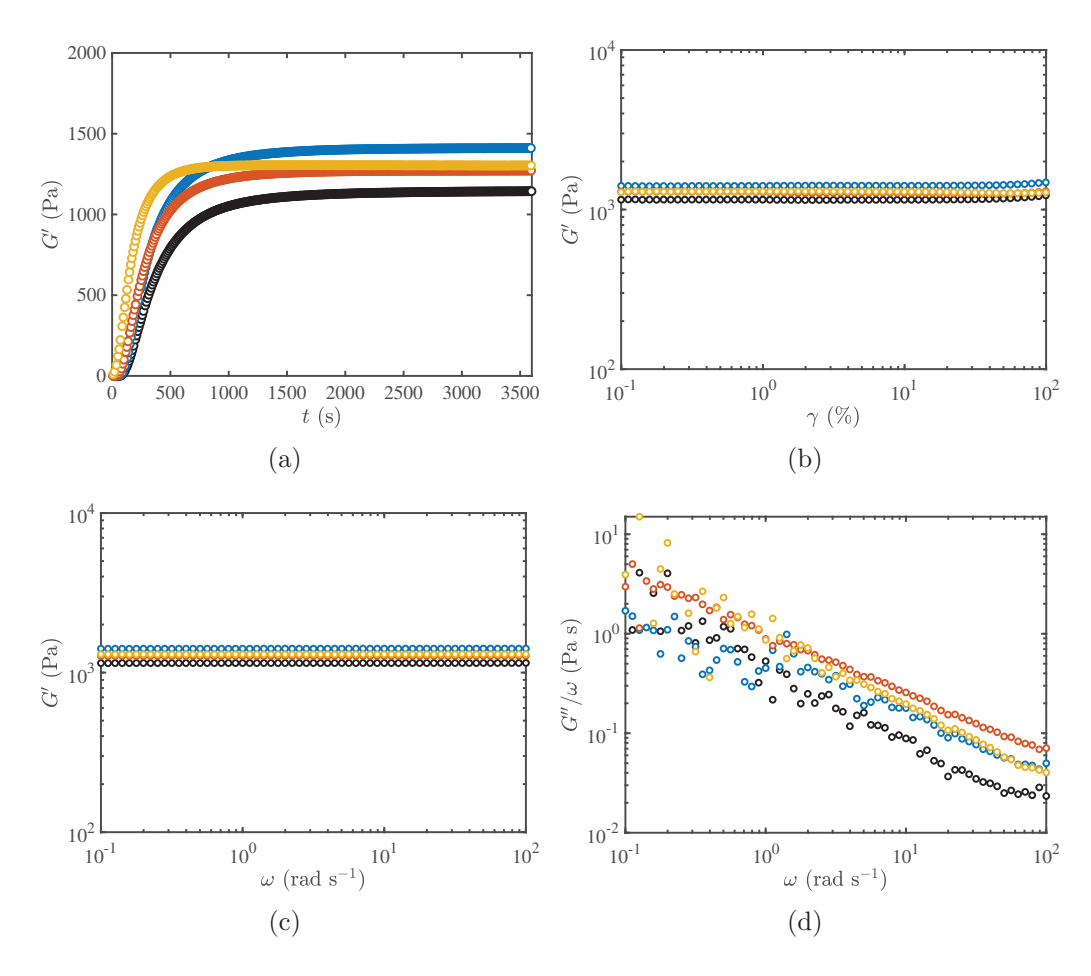


FIGURE 7.2: Rheological characterization of polyacrylamide hydrogels and nanoemulsion-doped hydrogels: $P_0G_4S_0$ (black), $P_2G_4S_0$ (blue), $P_5G_4S_0$ (red) and $P_{10}G_4S_0$ (yellow). (a) Storage modulus time series with $\omega=1$ rad s⁻¹, $\gamma=2$ % (b) Storage modulus strain sweep with $\omega=1$ rad s⁻¹. (c) Storage and (d) loss moduli (shear viscosity $\eta'=G''/\omega$) frequency sweeps with $\gamma=2$ %.

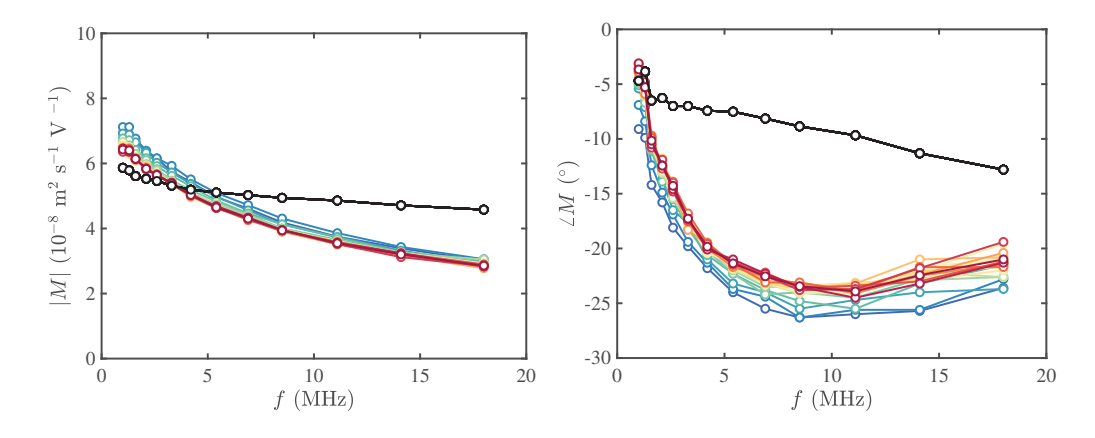


FIGURE 7.3: Dynamic mobility spectra for nanoemulsions with volume fraction $\phi = 0.02$ (black), and for nanoemulsion-doped hydrogels $P_2G_4S_0$ during gelation (with time increasing from $t \sim 4.5$ (blue) to 135 (red) min at time intervals $\Delta t \sim 4.5$ min. Both samples have no added NaCl.

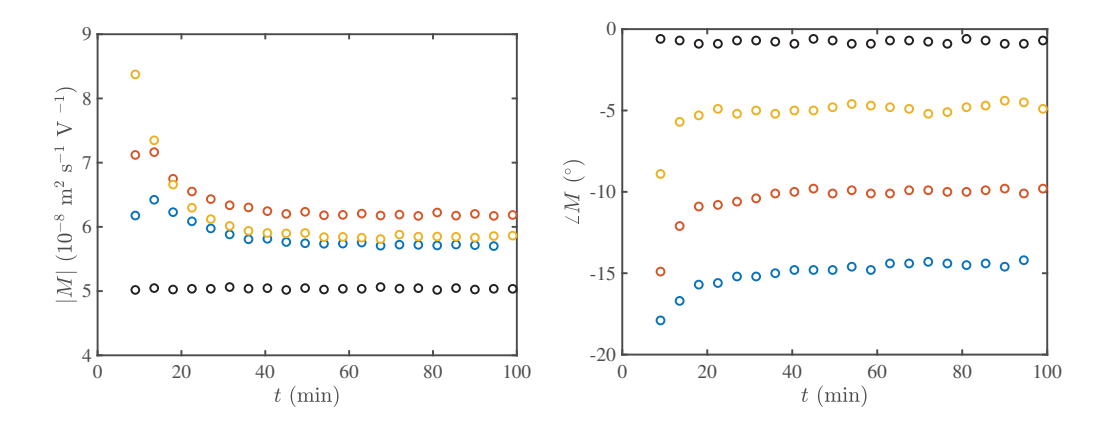


FIGURE 7.4: Dynamic mobility time series ($\omega/(2\pi) = 2.1$ MHz, no added NaCl) for nanoemulsions with oil volume fraction $\phi = 0.05$ (black) and nanoemulsion-doped hydrogels: $P_5G_4S_0$ (blue), $P_5G_{5.5}S_0$ (red) and $P_5G_8S_0$ (yellow).

Figure 7.4 shows the potential effect of monomer concentration on the dynamic mobility spectra of embedded fluid drops as a function of time at a single frequency (f = 2.1 MHz). An increase in the monomer concentration $(c_{AAm}/c_{bis} \approx \text{const.})$ has no appreciable impact on the magnitude of the dynamic mobility spectra, but is observed as a corresponding decrease in phase lag. The increase in phase lag with polymerization suggests an elastic coupling of the particle to the network.

7.5.3 Theoretical interpretation

A theoretical analysis was undertaken by incorporating a complex-valued network viscosity in the fluid-sphere model which furnishes the dynamic mobility of non-rigid particles discussed in Afuwape and Hill (2020, Ch. 5) and Hill and Afuwape (2020). Here, following Wang and Hill (2009), a complex viscosity that fits our data is defined with the form

$$\eta^* = \eta_o + i\mu^*/\omega = \eta_o + \eta' + i\mu'/\omega, \tag{7.2}$$

where η_o is the solvent viscosity and

$$\mu^* = \mu' - i\eta'\omega$$

is a complex shear modulus for the gel. Note that η' is the polymer contribution to the gel shear viscosity, ω is the angular frequency, and μ' is the shear modulus.

The theory of Wang and Hill (2009) defines a shear modulus as the only independent hydrogel parameter that affects particle dynamics for large particles at high (megahertz) frequencies, valid when the Debye length is small compared to the mesh size. Dynamic effects arising from hydrodynamic permeability and skeleton compressibility (Poisson ratio $\nu < 0.5$) are only significant at lower frequencies.

The incorporation of nanodrops in polymer was achieved by adding monomer solution to nanoemulsions, this could result in change in equilibrium concentration of surfactants (which can be estimated from material balance), drop size, ζ -potential and structural properties of the hydrogel. The nanodrop mobility in a polymer network will be dependent on the drop size and structural properties of the hydrogel since ζ -potential or surface charge can be estimated from adsorption isotherms.

The hydrogel background electrolyte was modelled as a simple electrolyte based on the final gel conductivity measured using dielectric relaxation spectroscopy (figure 7.5) as described in Afuwape and Hill (2020, Ch. 5). It should be noted that ion mobilities (hence conductivity) are limited in hydrogels, probably due to the increased viscosity, surfactant molecule binding to the monomer chains etc., as shown in figure 7.6 for salt and surfactant in aqueous solutions and polymer. The conductivity isotherm suggests a lower c.m.c. (~ 6.15 mM) as compared to the c.m.c. for aqueous SDS solutions with no added salt (~ 8.18 mM) (Afuwape and Hill, 2020, Ch. 3).

Note that the conductivities of the salt and surfactant loaded polymers in figure 7.6 are reported after subtracting the conductivity of the gel without emulsion and added salt; these gels contain ions from the polymerization and cross-linking reaction, which impart a conductivity $\sigma_{gel} \approx 0.140 \text{ S m}^{-1}$ that is comparable to that of an $\approx 11 \text{ mM}$ NaCl solution.

The nanodrop mobility was modelled by adjusting the drop diameter d, hydrogel complex shear modulus μ^* as fitting parameters. Equilibrium adsorption isotherm parameters were prescribed $\delta = 0.665$ Å, $a_s = 3.34$ Å, and $\Delta \epsilon = -18.9$, as detailed in Afuwape and Hill (2020, Ch. 5).

Results of non-linear least-squares fitting of the modified theory of Hill and Afuwape (2020) to the terminal dynamic mobility of nanoemulsion-doped polyacrylamide hydrogels with volume fractions ϕ , prescribed NaCl concentration, and monomer concentration c_{AAm} are presented in table 7.2, and shown in figure 7.7.

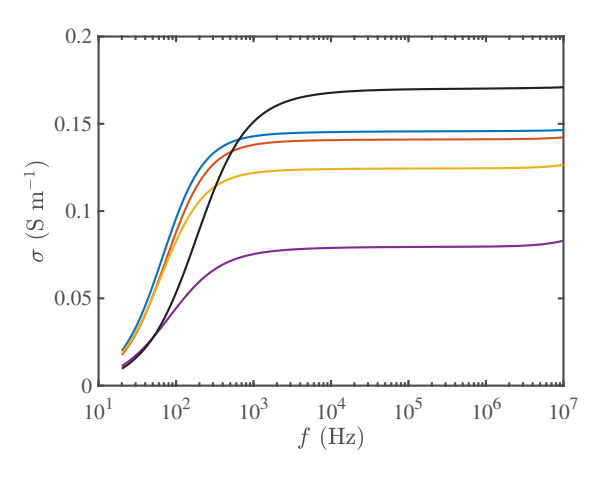


FIGURE 7.5: Conductivity spectra for polyacrylamide hydrogels with 2 (blue), 4 (red), 8 (yellow) and 16 % wt monomer (violet) and no added salt. Black line is for a solution containing ammonium persulfate and TEMED at the same concentrations used to synthesize gels.

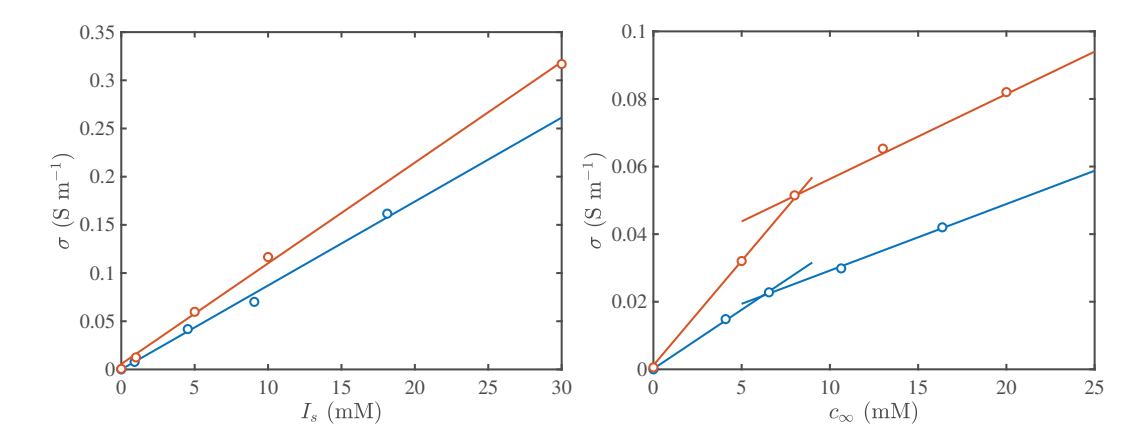


FIGURE 7.6: Conductivity of NaCl (right) and SDS (right) in solutions (red) and polyacrylamide hydrogel (4 wt%, blue) as a function of NaCl and SDS concentration, respectively. For the hydrogels, the conductivity of the gels without added NaCl and SDS has been subtracted ($\sigma_{gel} \approx 0.140 \text{ S m}^{-1}$). Lines are best fits, identifying c.m.c.s of SDS $\approx 6.15 \text{ mM}$ (polymer, blue), and $\approx 8.18 \text{ mM}$ (aqueous solution, red) with no added NaCl.

The model fitting parameters are reported in table 7.2. These show an increase in the composite shear viscosity when increasing the oil volume fraction. This is consistent with rheological characterization in figure 7.2(d). Drop diameters from the fitting are comparable to those from sound-wave attenuation and from the dynamic mobility of the same drops in aqueous electrolytes (no gel). This suggests that immobilizing nanodrops in hydrogels maintains the as-prepared drop size, potentially maintaining this state over much longer time periods. Targeted release might be achieved by leveraging the swelling or degradation abilities of the polymer network.

TABLE 7.2: Parameters for the fluid-sphere model of Hill and Afuwape (2020) with a complex shear viscosity $\eta^*(\omega)$ (see Eqn. (7.2)). Data and the model are plotted in figure 7.7. The accompanying aqueous phase SDS concentration c_{∞} and ζ -potential, are furnished by the isotherm and SDS material balance.

Sample	ϕ	$c_{\infty,0}$	c_{∞}	$-\zeta e/kT$	d	μ'	$\overline{\eta'}$
-	-	(mM)	(mM)	-	(μm)	(kPa)	(mPa s)
$P_2G_4S_0$	0.016	4.01	3.62	7.80	0.789	0.980	0.401
$P_5G_4S_0$	0.039	3.89	2.96	7.77	0.805	0.996	0.452
$P_{10}G_4S_0$	0.078	3.68	2.54	7.73	1.209	0.826	0.668
$\overline{P_2G_4S_5}$	0.016	4.01	3.52	7.63	0.659	1.025	0.378
$P_5G_4S_5$	0.039	3.89	2.69	7.59	0.660	1.117	0.457
$P_{10}G_4S_5$	0.078	3.68	1.85	7.49	1.107	0.375	0.846
$P_5G_{5.5}S_0$	0.035	3.56	2.64	7.77	0.706	1.062	0.287
$P_5G_8S_0$	0.029	2.99	2.06	7.74	0.559	1.275	0.256

The change in shear modulus with acrylamide monomer concentration is not the same as measured (at much lower frequencies) from bulk rheology. This difference has been previously highlighted for rigid nanoparticle doped hydrogels (Adibnia and Hill, 2014). It may be that nanoparticle mobilities reflect heterogeneity for which the local nanoparticle environments are different from the bulk. Note also that nanoparticle dynamics are dominated by the elastic stresses at low frequencies.

7.6 Conclusions

Nanoemulsion-doped polyacrylamide hydrogel composites were probed using electroacoustic spectroscopy to highlight polymer-particle interactions. The effect of the polymer environment on the dynamic mobility of nanodrops is shown to decrease the dynamic mobility due to network structure formation vis-a-vis a Newtonian fluid. The fluid-sphere dynamic mobility model of (Hill and Afuwape, 2020) was modified according to Wang and Hill (2009) to fit experiments, thus furnishing the drop size and complex shear modulus for the hydrogel at megahertz frequencies. Results show that nanodrop size is invariant to polymer network formation, and that the effective hydrogel shear viscosity increases with the oil volume fraction, consistent with bulk loss modulus data. The polymer network increased the effective viscosity (at megahertz frequencies) with respect to the solvent by an amount η' that is much less than the viscosity of the solvent (water), increasing with the oil volume fraction ϕ . The shear modulus μ' (at megahertz frequencies),

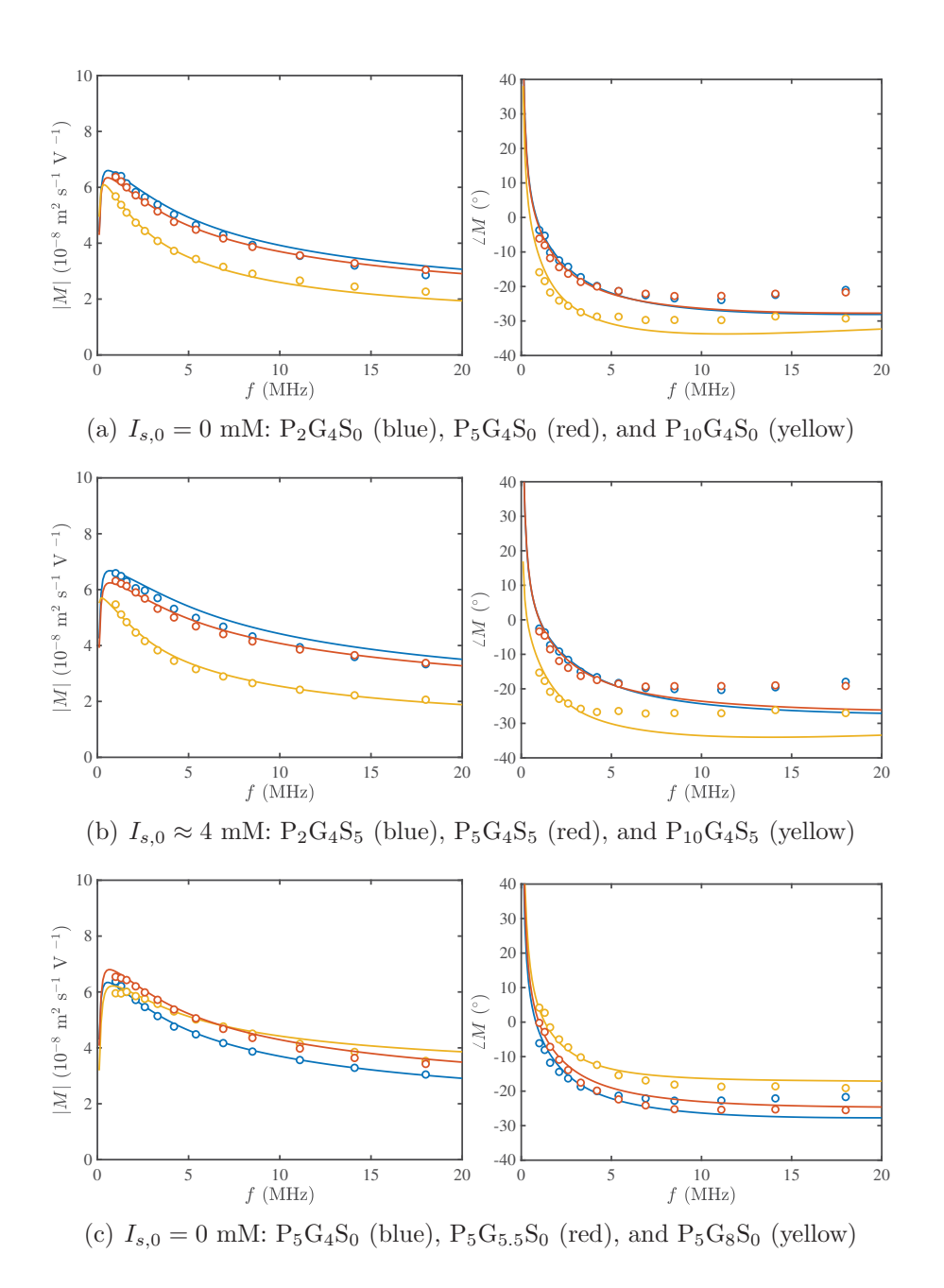


FIGURE 7.7: Steady-state dynamic mobility magnitude (left) and phase (right) spectra of composites after polymerization. Solid lines are fits of the fluid-sphere model of Hill and Afuwape (2020) with a complex shear viscosity. Fitting parameters are in table 7.2 with prescribed parameters: $I_g = 11.2$ mM (from the final hydrogel conductivity), $\eta_o = 0.89$ mPa s, $\eta_i = 3.4$ mPa s, T = 298 K, $\rho_o = 997$ kg m⁻³, and $\rho_i = 771$ kg m⁻³.

however, exhibited no systematic variation with ϕ , but was comparable to the values inferred by bulk rheology (at much lower frequencies.

7.7 Acknowledgements

This work was supported by NSERC Discovery and Research Tools and Instruments grants to R.J.H. G.A. was supported by a PRESSID/PTDF scholarship (Nigeria).

7.8 Author contributions

G.A. and R.J.H. designed the experiments. G.A. performed the experiments and analyzed the data. G.A. and R.J.H. interpreted the results and wrote the paper.

Bibliography

- V. Adibnia and R. J. Hill. Electroacoustic spectroscopy of nanoparticle-doped hydrogels. *Macromolecules*, 47(22):8064–8071, 2014.
- G. A. Afuwape and R. J. Hill. Nanoemulsion-hydrogel composites: Electro-kinetic dynamics, viscoelastic and swelling responses. PhD thesis, McGill University, 2020.
- C. Alexander. Synthetic polymer systems in drug delivery. Expert Opin. Emerg. Drugs, 6(2):345–363, 2001.
- H. Z. An, M. E. Helgeson, and P. S. Doyle. Nanoemulsion composite microgels for orthogonal encapsulation and release. *Adv. Mater.*, 24(28, SI):3838–3844, 2012.
- R. Barbucci. *Hydrogels: Biological properties and applications*. Springer Science & Business Media, 2010.
- P. Bhosale, J. Chun, and J. Berg. Electroacoustics of particles dispersed in polymer gel. *Langmuir*, 27(12):7376–7379, 2011.

- D. Calvet, J. Wong, and S. Giasson. Rheological monitoring of polyacrylamide gelation importance of cross-link density and temperature. *Macromolecules*, 37 (20):7762–7771, 2004.
- M. Carafa, C. Marianecci, L. Di Marzio, F. Rinaldi, C. Meo, P. Matricardi, F. Alhaique, and T. Coviello. A new vesicle-loaded hydrogel system suitable for topical applications: preparation and characterization. *J. Pharm. Pharm. Sci.*, 14(3):336–346, 2011.
- J. Chen, H. Park, and K. Park. Synthesis of superporous hydrogels: Hydrogels with fast swelling and superabsorbent properties. J. Biomed. Mater. Res., 44 (1):53–62, 1999.
- Z. Cong, Y. Shi, X. Peng, B. Wei, Y. Wang, J. Li, J. Li, and J. Li. Design and optimization of thermosensitive nanoemulsion hydrogel for sustained-release of praziquantel. *Drug Dev. Ind. Pharm.*, 43(4):558–573, 2017.
- A. M. Djerdjev, J. K. Beattie, and R. J. Hunter. An electroacoustic and high-frequency dielectric response study of stagnant layer conduction in emulsion systems. *J. Colloid Interface Sci.*, 265(1):56–64, 2003.
- H. Geckil, F. Xu, X. Zhang, S. Moon, and U. Demirci. Engineering hydrogels as extracellular matrix mimics. *Nanomedicine*, 5(3):469–484, 2010.
- C. Gong, Q. Wu, Y. Wang, D. Zhang, F. Luo, X. Zhao, Y. Wei, and Z. Qian. A biodegradable hydrogel system containing curcumin encapsulated in micelles for cutaneous wound healing. *Biomaterials*, 34(27):6377 – 6387, 2013.
- S. Grijalvo, J. Mayr, R. Eritja, and D. D. Díaz. Biodegradable liposome-encapsulated hydrogels for biomedical applications: a marriage of convenience. *Biomater. Sci.*, 4:555–574, 2016.
- A. Gupta, H. B. Eral, T. A. Hatton, and P. S. Doyle. Nanoemulsions: formation, properties and applications. *Soft Matter*, 12:2826–2841, 2016.
- S. M. Hashemnejad, A. Z. M. Badruddoza, B. Zarket, C. Ricardo Castaneda, and P. S. Doyle. Thermoresponsive nanoemulsion-based gel synthesized through a low-energy process. *Nat. Commun.*, 10(1):2749, 2019.
- R. J. Hill and G. A. Afuwape. Dynamic mobility of surfactant stabilized nanodroplets: unifying equilibrium thermodynamics, electro-kinetics and Marangoni effects. *J. Fluid Mech.*, 895(A14), 2020.

- M. Jaiswal, R. Dudhe, and P. K. Sharma. Nanoemulsion: an advanced mode of drug delivery system. *Biotech.*, 5(2):123–127, 2014.
- L. Kass, E. D. Cardenas-Vasquez, and L. C. Hsiao. Composite double network hydrogels with thermoresponsive colloidal nanoemulsions. *AIChE J.*, 65(12), 2019.
- L. Lei, Y. Zhang, L. He, S. Wu, B. Li, and Y. Li. Fabrication of nanoemulsion-filled alginate hydrogel to control the digestion behavior of hydrophobic nobiletin. LWT-Food Sci. Technol., 82:260–267, 2017.
- N. López Mora, J. S. Hansen, Y. Gao, A. A. Ronald, R. Kieltyka, N. Malmstadt, and A. Kros. Preparation of size tunable giant vesicles from cross-linked dextran(ethylene glycol) hydrogels. *Chem. Commun.*, 50(16):1953–1955, 2014.
- D. Mou, H. Chen, D. Du, C. Mao, J. Wan, H. Xu, and X. Yang. Hydrogel-thickened nanoemulsion system for topical delivery of lipophilic drugs. *Int. J. Pharm.*, 353(1):270 276, 2008.
- C. Nazli, G. S. Demirer, Y. Yar, H. Y. Acar, and S. Kizilel. Targeted delivery of doxorubicin into tumor cells via mmp-sensitive peg hydrogel-coated magnetic iron oxide nanoparticles (mionps). *Colloids Surf.*, B, 122:674 – 683, 2014.
- R. W. O'Brien, D. W. Cannon, and W. N. Rowlands. Electroacoustic determination of particle size and zeta potential. *J. Colloid Interface Sci.*, 173(2):406–418, 1995.
- N. Peppas, P. Bures, W. Leobandung, and H. Ichikawa. Hydrogels in pharmaceutical formulations. *Eur. J. Pharm. Biopharm.*, 50(1):27–46, 2000.
- G. Sala, G. Van Aken, M. Stuart, and F. Van De Velde. Effect of droplet-matrix interactions on large deformation properties of emulsion-filled gels. *J. Texture* Stud., 38(4):511–535, 2007.
- G. Sala, T. van Vliet, M. Cohen Stuart, F. van de Velde, and G. van Aken. Deformation and fracture of emulsion-filled gels: Effect of gelling agent concentration and oil droplet size. *Food Hydrocoll.*, 23(7):1853–1863, 2009a.
- G. b. Sala, T. van Vliet, M. Cohen Stuart, G. Aken, and F. van de Velde. Deformation and fracture of emulsion-filled gels: Effect of oil content and deformation speed. *Food Hydrocoll.*, 23(5):1381–1393, 2009b.

- P. Thoniyot, M. J. Tan, A. A. Karim, D. J. Young, and X. J. Loh. Nanoparticle—hydrogel composites: Concept, design, and applications of these promising, multi-functional materials. *Adv. Sci.*, 2(1-2):1400010, 2015.
- G. A. Urban and T. Weiss. Hydrogels for Biosensors. Springer, 2009.
- M. Wang and R. J. Hill. Dynamic electric-field-induced response of charged spherical colloids in uncharged hydrogels. *J. Fluid Mech.*, 640:357–400, 2009.
- L. Wei, C. Cai, J. Lin, and T. Chen. Dual-drug delivery system based on hydrogel/micelle composites. *Biomaterials*, 30(13):2606 2613, 2009.
- H. Wu, L. Song, L. Chen, Y. Huang, Y. Wu, F. Zang, Y. An, H. Lyu, M. Ma, J. Chen, N. Gu, and Y. Zhang. Injectable thermosensitive magnetic nanoemulsion hydrogel for multimodal-imaging-guided accurate thermoablative cancer therapy. *Nanoscale*, 9(42):16175–16182, 2017.
- B. Zeeb, A. H. Saberi, J. Weiss, and D. J. McClements. Formation and characterization of filled hydrogel beads based on calcium alginate: Factors influencing nanoemulsion retention and release. Food Hydrocoll., 50:27–36, 2015.
- Y. Zhou, S. Liu, M. Zhao, C. Wang, L. Li, Y. Yuan, L. Li, G. Liao, W. Bresette, J. Zhang, Y. Chen, J. Cheng, Y. Lu, and J. Liu. Injectable extracellular vesicle-released self-assembling peptide nanofiber hydrogel as an enhanced cell-free therapy for tissue regeneration. *J. Controlled Release*, 316:93 104, 2019.

7.A Particle size characterization

Table 7.3 compares the sound-wave-attenuation diameters for nanoemulsions and nanoemulsion-hydrogels. Note that attenuation techniques for particle sizing are dependent on the thermal properties of both phases, therefore it might not be appropriate for particle size characterization of hydrogels as evidenced in the particle size moments obtained with varying monomer concentration for the same nanoemulsion composition.

Table 7.3: Sound-wave-attenuation diameters for nanoemulsions ($c_{AAm} = 0$) and nanoemulsion-hydrogels at varying monomer concentrations.

Sample	d_{15}	d_{50}	d_{85}	c_{AAm}
-	$(\mu \mathrm{m})$	$(\mu \mathrm{m})$	$(\mu \mathrm{m})$	%
$P_2G_0S_0$	0.338	0.437	0.543	-
$P_5G_0S_0$	0.326	0.41	0.507	-
$P_{10}G_0S_0$	0.476	0.625	0.785	-
$P_2G_0S_5$	0.257	0.431	0.723	-
$P_5G_0S_5$	0.257	0.431	0.724	-
$P_{10}G_0S_5$	0.353	0.528	2.201	-
$P_2G_4S_0$	0.263	0.329	0.406	4.06
$P_5G_4S_0$	0.308	0.433	0.542	4.16
$P_5G_{5.5}S_0$	0.301	0.357	0.424	5.70
$P_5G_8S_0$	0.261	0.290	0.321	8.24
$P_{10}G_4S_0$	0.558	0.780	0.976	4.34
$P_2G_4S_5$	0.239	0.295	0.362	4.06
$P_5G_4S_5$	0.281	0.375	0.471	4.16
$P_{10}G_4S_5$	0.489	0.858	1.503	4.34

7.B Dynamic mobility spectra

Figures in the main text are extended in figure 7.8 to show the model over a wider (logrithmically scaled) frequency range (0.1–100 MHz) than the Acoustosizer II.

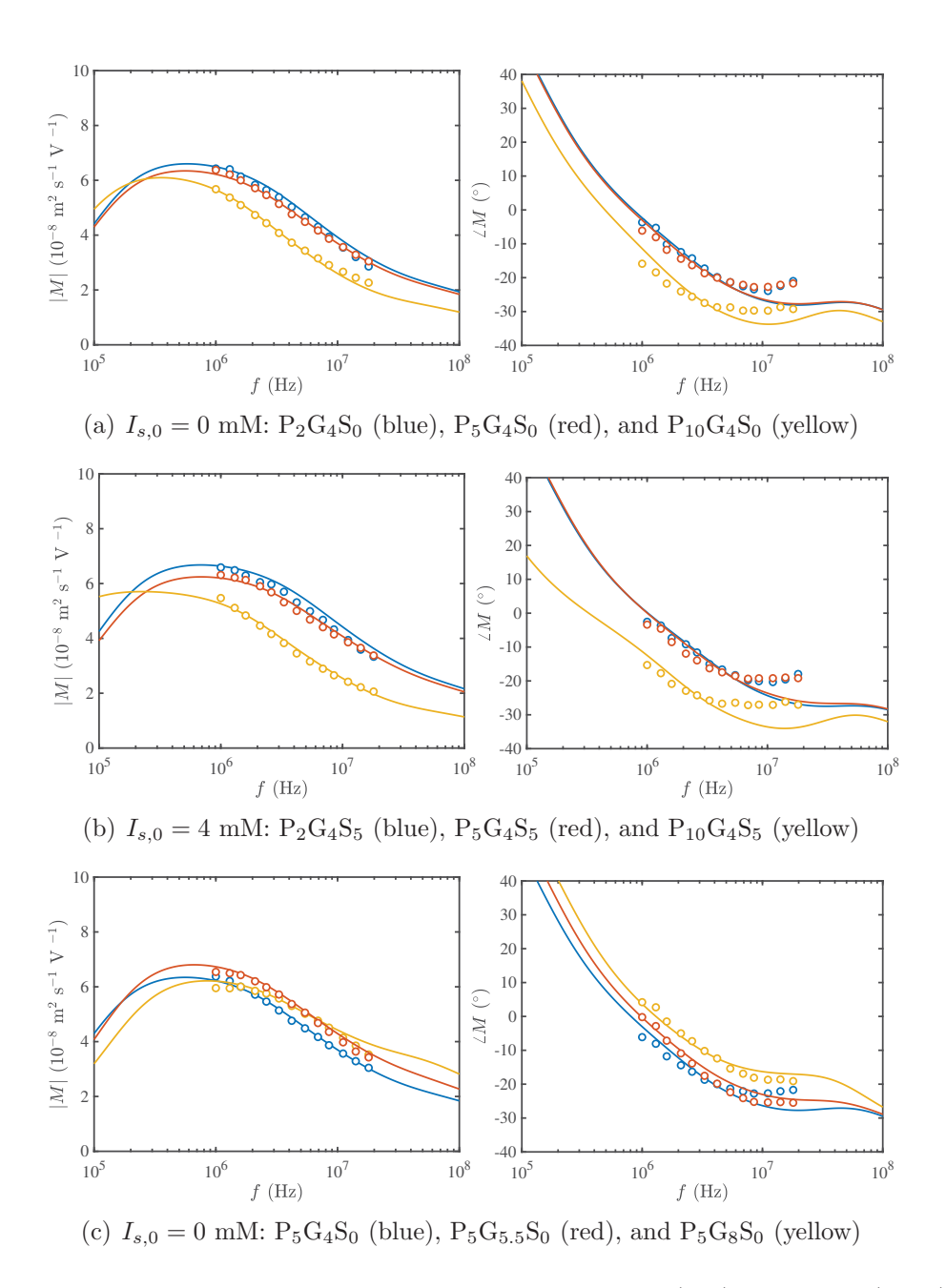


FIGURE 7.8: Steady-state dynamic mobility magnitude (left) and phase (right) spectra of composites after polymerization. Solid lines are fits of the fluid-sphere model of Hill and Afuwape (2020) with a complex shear viscosity. Fitting parameters are in table 7.2 with prescribed parameters: $I_s = 11.2$ mM (from the final hydrogel conductivity), $\eta_o = 0.89$ mPa s, $\eta_i = 3.4$ mPa s, T = 298 K, $\rho_o = 997$ kg m⁻³, and $\rho_i = 771$ kg m⁻³.

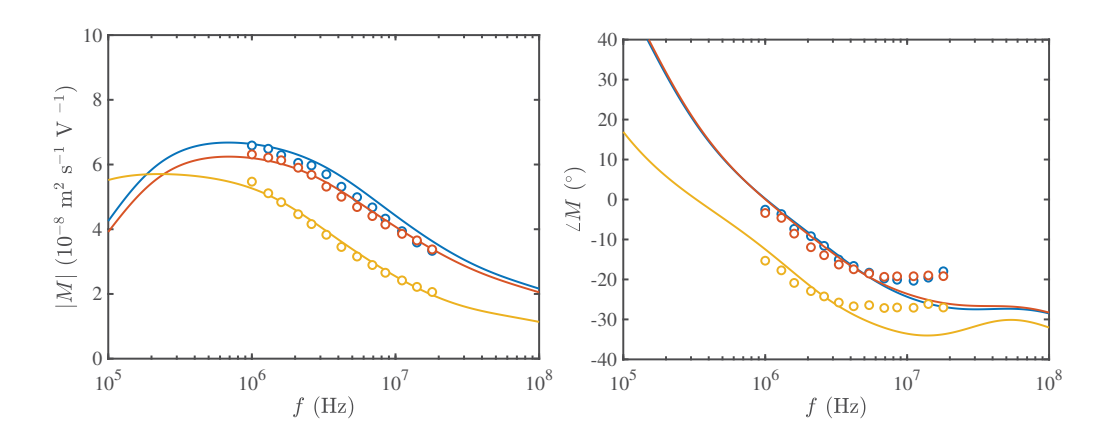


FIGURE 7.9: The same as figure 7.8, but with added NaCl concentration $I_{s,0} = 4$ mM: $P_2G_4S_5$ (blue), $P_5G_4S_5$ (red), and $P_{10}G_4S_5$ (yellow).

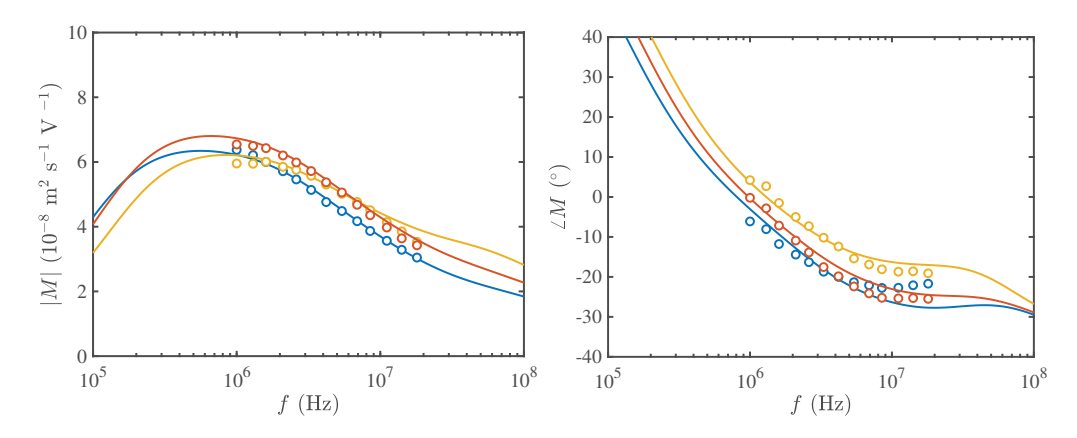


FIGURE 7.10: The same as Figure 7.8 for samples with no added NaCl salt: $P_5G_4S_0$ (blue), $P_5G_{5.5}S_0$ (red), and $P_5G_8S_0$ (yellow).

Chapter 8

Nanoemulsion-doped hydrogels

8.1 Preface

In Afuwape and Hill (2020, Ch.7), electroacoustic spectroscopy was used to non-invasively probe the microstructure of nanoemulsion-hydrogels. This investigation suggested that drops are immobilized in the polymer network with sizes and surface charges comparable to those in their nano-emulsion counterparts. Here, composites prepared from SDS-stabilized hexadecane drops in cross-linked polyacrylamide are studied using confocal microscopy, bulk rheology, swelling, and thermogravimetric analysis. The objective is to understand in greater detail how the oil droplets affect the micro-structure and macroscopic properties. These insights will provide further insight for the design nanoemulsion-hydrogel delivery systems.

8.2 Abstract

Nano-emulsion-hydrogels present new opportunities for designing novel drug delivery vehicles for lipophilic active pharmaceutical ingredients. The gel provides a mechanical barrier to coalescence, thus providing a route toward stable surfactantfree nanoemulsions. Here, changes in a polyacrylamide hydrogel doped with hexadecane nanodrops are investigated. Confocal microscopy reveals a dense, immobilized packing of micrometer sized drops, which sound-wave attenuation suggests must be embedded among a population of much smaller droplets, below optical resolution. The swelling ratio decreases with increasing oil volume fraction, and drying the as-prepared nanocomposites (in air at room temperature) was found to the oil content. Interestingly, drying the nonocomposites enabled the gels to uptake approximately twice the volume of water as their non-dried counterparts. Rheological analysis suggests that the imbedded drops behave as rigid inclusions, either due to the interfacial surface tension resisting shear-induced deformation or the interface promoting a solid-like coating during the polymerization and gelation. These results provide new insights for designing nano-emulsion loaded gels for drug delivery and other biomedical applications.

8.3 Introduction

Hydrogels have been embraced as advanced materials for the design of controlledrelease matrices for biomedical applications. The monomer chemistry produces defined physicochemical properties that can be exploited for encapsulation and controlled temporal and spatial release of bioactive materials (Lin and Metters, 2006, Li and Mooney, 2016). Material selection for the fabrication of hydrogel delivery systems must fulfill basic needs, such as maintaining drug bioactivity, and ensuring chemical and physical stability (Peppas et al., 2000).

Hydrogels provide a platform for release using their modifiable physical properties, controlled degradability to protect denaturing of bioactive materials. Novel delivery systems have been developed in tadem with biodegradable, smart, and biomimetic hydrogels; with mathematical models to understand and predict the bioactive material release (Lin and Metters, 2006, Amsden, 1998, Siepmann and Peppas, 2001). Release models include diffusion (Amsden, 1998, Masaro and Zhu, 1999), swelling (Yoshida et al., 1993, Siepmann and Peppas, 2001), and chemical (Sakiyama-Elbert and Hubbell, 2000) mechanisms.

Diffusion-controlled release is observed when the network mesh size is larger than the drug, so diffusion times are $\sim L^2/D$, where L is the characteristic length and D is the drug diffusivity. Steric hinderance become significant when the mesh size is smaller than the drug, leading to complete immobilization. For drug-immobilized systems, controlled release occurs by network degradation, swelling, or mechanical deformation (Li and Mooney, 2016).

Reviews documenting design considerations and material selection for the fabrication of hydrogel delivery systems are abundant (Peppas et al., 2000, Kanjickal and Lopina, 2004, Lin and Metters, 2006, Li and Mooney, 2016), but a major challenge is delivering hydrophobic bioactive ingredients (Josef et al., 2010, An et al., 2012). Active pharmaceutical ingredients (APIs) produced in the last three decades have been considered hydrophobic (Josef et al., 2010, Eral et al., 2014). Hydrophobic copolymers could provide binding sites for hydrophobic drugs (Li and Mooney, 2016). Moreover, crystals of hydrophobic APIs have been loaded into hydrogels by pre-dissolution into hydrophobic droplets (nanoemulsions), which then act as crystallization reactors. Controlled composite evaporation and and elastic network then act to control the size and degree API loading (Eral et al., 2014, Gupta et al., 2017).

In occlusive dressings for dermal wound treatments, hydrogels have been employed to prevent wound desiccation, and to increase the rate of wound epithelialization during healing (Helfman et al., 1994). Moreover, dispersed lipophilic phases can concurrently serve to release antimicrobial agents while providing improved moisturization (Francesko et al., 2018).

Generally, pre-dissolved hydrophobic APIs can be delivered using nanoemulsion-hydrogel composites. The solubility mismatch between dispersed lipophilic phase and hydrogels is overcome by nanoemulsions in mesoscale domains (Kass et al., 2019). These composites combine the merits of nanoemulsions (*i.e.*, oil solubility, high surface area, *etc.*), with the tailored possibilities enabled by stimuli responsive hydrogels for controlled and localized delivery.

The dispersed phase in nanoemulsions is typically an essential oil, such as from olives, (Lupi et al., 2015), almonds (Bonacucina et al., 2009), peanuts and linseeds (Komarova et al., 2013). These are able to serve as vehicles for the hydrophobic APIs used topically as analgesics and rubefacients (e.g., ibuprofen, menthol, methyl salicylate) in the therapeutic treatment of arthritis and muscle pain (Mou et al., 2008). The polymer is chosen to meet specific physicochemical functional property needs, such as release stimuli, stability, and rheology (Kim et al., 2001, Shingel et al., 2009, Wei et al., 2009, Hashemnejad et al., 2019).

Another merit of hydrogel-composites stems from an ability to produce nanoemulsions with high volume fraction and pre-selection of the hydrogel properties for controlled release (An et al., 2012). However, the mode of release of API-carrying droplets and their influence on the physical properties of the hydrogels have remained largely untested. Komarova et al. (2013) reported the absence of oil (tetradecane, olive, and linseed) release from poly(N-isopropylacrylamide) with increasing temperature, despite the PNIPAM hydrogels deswelling at temperatures above 34°C. The authors expected the release of oil, as observed in cryogels whose deswelling was accompanied by oil release.

Few studies have been undertaken to understand the nanoemulsion-hydrogel combination on rheology and emulsion stability. For example, the release of curcumin encapsulated in a nanoemulsion-hydrogel composite (lipid-calcium alginate) has been hypothesized to depend on hydrogel pore size and surfactant concentration, as micelles are also capable of serving as cargo carriers for diffusion controlled release (Zeeb et al., 2015). The improved mechanical strength and energy dissipation of double-network hydrogels and nanoemulsions have demonstrated potential for use in high-shear-rate manufacturing processes (Kass et al., 2019). Release mechanisms of polymer-network encapsulated entities can be achieved by the dissolution of cross-linker chains in physical hydrogels or swelling due to the hydrophilic groups in chemical and physical hydrogels (Milimouk et al., 2001, Yu and Zheng, 2011, Bicak et al., 2004).

Understanding how changes in hydrogel properties arising from nanodrop loading are essential for designing these materials for specific applications. For example, swelling has been proposed as a strategy for controlled release of entrapped materials (Ohmine and Tanaka, 1982, Brannon-Peppas and Peppas, 1991, Murdan, 2003), but it is not clear if this approach transfers to hydrophobic inclusions, such as nanodrops. Also, while hydrogels are useful for wound exudate absorption, the absorption capacity, and how the mesh size changes with lipophilic load are unknown. In this study, we use a model nanoemulsion-hydrogel composite to examine how hydrogel properties respond to systematic changes in the oil volume fraction, drawing on confocal microscopy, swelling, thermogravimetric analysis, and bulk rheology.

8.4 Materials and methods

8.4.1 Nanoemulsions

Surfactant solutions were prepared with a prescribed mass of sodium dodecyl sulphate (SDS) (98.5%, Sigma-Aldrich Canada) added to a known volume of reverse osmosis (RO) water (Type 1, $\sigma \approx 5.6~\mu \mathrm{S~m^{-1}}$), and agitated using a vortex mixer for 1 min to ensure dissolution. A prescribed volume of hexadecane oil (99%, Sigma-Aldrich Canada) was added to the solution to obtain a coarse emulsion of known volume fraction ϕ . High-energy emulsification was undertaken using a probe sonicator (QSonica Q500 model) at 20 kHz (2 runs, 15 min each, separated by ≈ 2 min). Sonication is widely used to produce nanoemulsions, but the procedure is not standardized, as the sonication time depends on the power intensity. By trail-and-error, the sample temperature could be maintained less than $\sim 35^{\circ}\mathrm{C}$ for each 15 min run.

8.4.2 Polyacrylamide gels

Polyacrylamide gels were synthesized from acrylamide (monomer) (40 w/v % aqueous solution, Fisher Scientific U.S.A.), bisacrylamide (cross-linker) (2 w/v % aqueous solution, Fisher Scientific U.S.A.), ammonium persulfate (APS) (powder, Fisher Scientific U.S.A.), and N,N,N',N'-tetramethylethylenediamine (TEMED, GE Healthcare Life Science, Germany) as initiator and catalyst for the free radical polymerization. 1,2-dioleoyl-sn-glycero-3-phosphoethanolamine-N-(carboxyfluorescein)(ammonisalt) (18:1 PE CF) (Avanti Polar lipids, Inc.) was added as a fluorescent lipid for confocal microscopy. All materials were used as provided by the manufacturer.

8.4.3 Nanoemulsion-hydrogel composites

To prepare a known volume (e.g., 20 ml) of pre-gel mixture, a prescribed volume of acrylamide solution (to achieve a desired monomer concentration, e.g., 4 wt% requires 2 ml) was pipetted into a prescribed volume of nanoemulsion (e.g., 15.635 ml), and a prescribed volume of cross-linker solution (2.105 ml) was added to maintain the monomer-cross-linker ratio (19:1). This pre-gel mixture was agitated using a vortex mixer for ~ 1 min, and 10 μ l per ml of ammonium persulfate

(0.44 mol l⁻¹) was added to the solution as initiator before the pre-gel solution was degassed by bubbling nitrogen for ≈ 5 min to remove dissolved oxygen. Finally, 3 μ l TEMED per ml of pre-gel solution was added as catalyst, and the sample immediately syringed into the Acoustosizer II sample cell.

8.4.4 Confocal microscopy

To image the composites, samples were prepared as detailed above. However, before passing nitrogen through the pre-gel mixture, 2 μ L mL⁻¹ of 18:1 PE CF was added and mixed for \approx 1 min with a vortex mixer. The suspension was mixed in an aluminium wrapped glass vial (to avoid lipid photo-bleaching), and TEMED was added to accelerate the polymerization. Samples were pipetted into a coverslip channel and sealed using another coverslip with taped edges.

8.4.5 Rheology

Oscillatory shear measurements were undertaken using an ARES-G2 (TA Instruments) rheometer. A 1.3 ml sample of gel precursor solution was deposited between parallel plates surrounded by a rubber ring and the gap adjusted to achieve a 1 mm separation. Oscillatory shear was applied at strain $\gamma = 2\%$ with angular frequencies $\omega = 0.1$ –100 rad s⁻¹, and $\omega = 1$ rad s⁻¹ with $\gamma = 0.1$ –100%. Following an initial incubation period, incipient gelation was identified by a crossing of the storage and loss moduli, with further changes in the storage and loss moduli plateauing in ≈ 60 min.

8.4.6 Swelling

To investigate the swelling of nanoemulsion-hydrogel composites, 650 μ L of pregel solution containing 0, 10 and 20% dispersed oil phase volume fraction were pipetted into cuvettes to polymerize, forming cubic shaped composite gels with cubic length $l \approx 8$ mm. These were briefly rinsed in reverse-osmosis (RO) water in a petri dish for ≈ 1 min (3 times), and the excess water removed by placing on filter paper. Some samples were placed in an oven at $T=40^{\circ}$ C for 3 hr, and further dried at room temperature $T\approx 22^{\circ}$ C for 12 hr. Samples treated in this

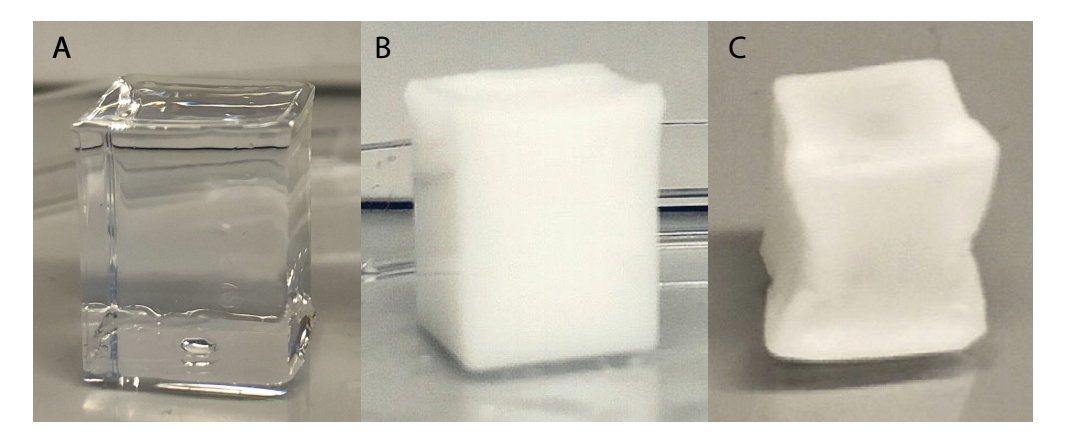


FIGURE 8.1: Representative gels: (A) PA gel in as-prepared state; (B) Nano-emulsion-doped gel in as-prepared state; (C) Nano-emulsion-doped gel in "dried" state (following ~ 12 hr in air).

manner are designated "dried", whereas those used without drying are designated "wet".

The samples were weighed before being placed in a petri dish containing 10 mL of RO water to monitor swelling uptake. The average mass of as-prepared "wet" samples were $m_{w,0} \approx 0.615$, $m_{w,10} \approx 0.571$, $m_{w,20} \approx 0.514$ g, whereas the average mass of the dried samples were $m_{d,0} \approx 0.160$, $m_{d,10} \approx 0.224$, $m_{d,20} \approx 0.223$ g, respectively. Upon swelling, the equilibrium masses of the as-prepared "wet" samples were $m_{w,0,\infty} \approx 0.759$, $m_{w,10,\infty} \approx 0.724$, $m_{w,20,\infty} \approx 0.635$ g, whereas those of the initially dried samples were $m_{d,0,\infty} \approx 1.688$, $m_{d,10,\infty} \approx 1.565$, $m_{d,20,\infty} \approx 1.330$ g, respectively. Representative images are shown in figure 8.1.

8.4.7 Thermogravimetric analysis

Thermogravimetric experiments were undertaken using a TGA-Q50 (TA Instruments), with samples prepared as detailed in section 8.4.3. Following instrument calibration, a sample was placed in a balance pan, were the initial weight is measured (manufacturer's recommendation 3–10 mg). Gravimetric analysis was performed by heating the sample in a nitrogen atmosphere at a flow rate 40 ml min⁻¹ for T < 500°C, followed by air. Sample degradation with temperature change (20°C per min) is reported by the instrument software.

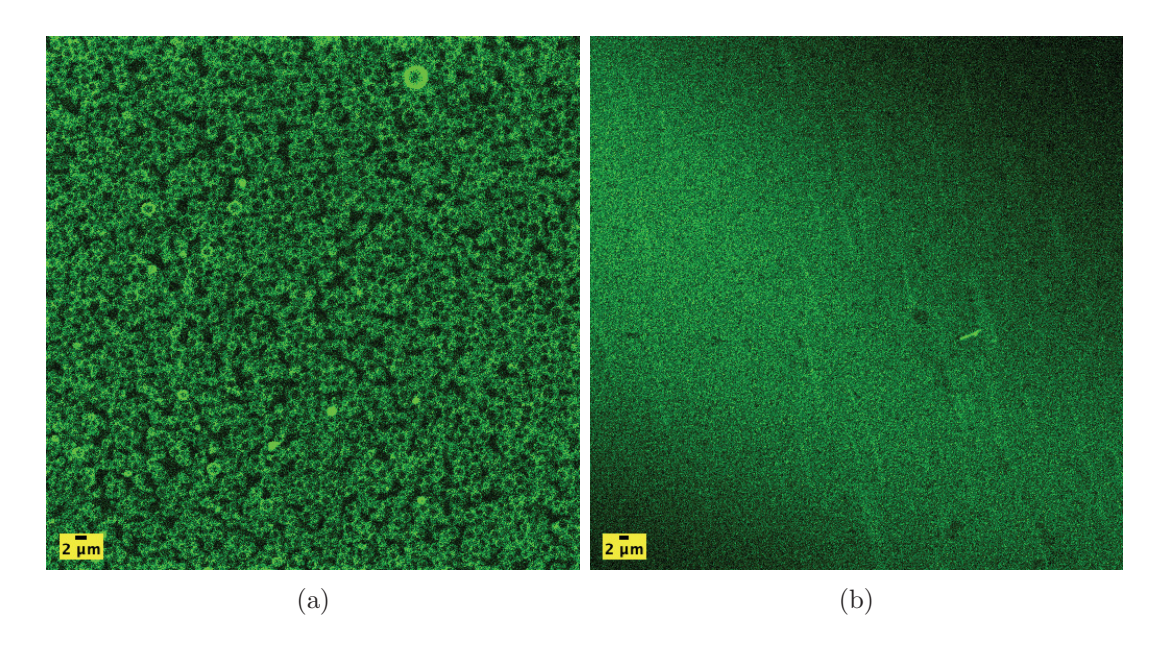


FIGURE 8.2: Confocal microscopy of a nanoemulsion-hydrogel composite (a) prepared from nanoemulsion with oil volume fraction $\phi = 0.1$, aqueous phase SDS concentration $c_{\infty,0}/(1-\phi) = 5$ mM and diameter $d_{85} = 785$ nm (from sound-wave attenuation) compared with a pure AAm hydrogel (b). Both gels have a monomer concentration ≈ 4 wt % and monomer to cross-linker ratio 19:1.

8.5 Results and discussion

Confocal sections of a nanoemulsion-hydrogel composite ($\phi = 0.08$) and a pure gel (both with monomer concentration ≈ 4 wt %) are shown in figure 8.2. Figure 8.2(a) is with an oil volume fraction $\phi \sim 0.08$, whereas figure 8.2(b) shows an hydrogel with no oil. The drops are immobilized in the polymer network, and the densely populated image of nanodrops reflects the increased interfacial surface area created by emulsification. Note that the confocal imaging resolves a dense packing of drops with diameter $\sim 1-2~\mu\text{m}$, whereas sound-wave attenuation suggests a significant population (number density) of drops that are too small to resolve in an optical micrograph.

8.5.1 Swelling

Water retention and swelling give insights to the polymer-oil interaction. Figure 8.3 shows the swelling time series of nanoemulsion-hydrogel samples. The

Table 8.1: Model parameters according to fits of Eqn. (8.2) to swelling time series for initially as-prepared (top) and dried (bottom) nanoemulsion-hydrogel composites (figure 8.3). The mesh size $\xi = (k_B T/G_{\infty}')^{1/3}$, and the characteristic length L calculated for dried samples from their mass, accounting for the change in oil volume fraction, e.g., $L_d^3 = m_d/[\phi_d \rho_o + (1 - \phi_d) \rho_w]$.

$\overline{\phi}$	S_m	$ au_s$	L_0	L	D_c	ℓ	ξ
		(hr)	(mm)	(mm)	$(10^{-7} \text{ m}^2 \text{ s}^{-1})$	(nm)	(nm)
0	0.24	8.13	8.5	9.1	1.87	362	14.7
0.1	0.26	9.64	8.4	9.0	2.16	343	13.6
0.2	0.26	10.28	8.1	8.7	2.16	288	12.1
0	9.03	20.42	5.4	11.9	8.03	750	14.7
0.1	5.73	17.70	6.2	11.6	6.61	600	13.6
0.2	5.32	19.92	6.3	11.1	6.82	512	12.1

(mass) swelling ratio

$$S(t) = \frac{m(t) - m_0}{m_0},\tag{8.1}$$

where m and m_0 are the sample mass at time t, and initial mass, respectively. The change in mass was after removing excess surface water with filter paper. Equilibrium swelling ratios are furnished by fitting Eqn. (8.2) to the swelling-ratio time series:

$$S(t) = S_m (1 - e^{-t/\tau_s}), (8.2)$$

where S_m is the equilibrium swelling ratio and τ_s is the time constant (Tanaka and Fillmore, 1979).

Note that the cooperative diffusion coefficient

$$D_c \sim L^2/\tau_s$$

furnishing the network permeability

$$\ell^2 \sim \eta D_c/\mu$$
,

where ℓ is the Brinkman screening length. With $\eta=0.89$ mPa s, $\mu=1,270$ $(\phi=0),\,1,632$ $(\phi=0.1),\,$ and 2,311 Pa $(\phi=0.2)$ from plateau moduli $(G'_{\infty}),\,$ D_c and ℓ are are listed in table 8.1 for measured sample characteristic length L. Note that these are somewhat larger than the mesh size $\xi=(k_BT/G'_{\infty})^{1/3}$.

Whereas the initially as-prepared samples attain an equilibrium swelling ratio $S_m \approx 25\%$ that is independent of the oil volume fraction, the swelling of initially

dried samples is notably hindered by the oil, but independent of the oil volume fractions 0.1 and 0.2. This suggests that drops in the initially as-prepared gels do not interact with the network. Thus, upon swelling, the drop-templated voids are expected to increase in size, forming solvent-filled gaps between the drops and network. On the other hand, upon drying, the oil seems to irreversibly wet the polymer, thus hindering its subsequent rehydration.

From the dried and as-prepared masses, their ratios are $0.16/0.615 \approx 0.26$, $0.224/0.571 \approx 0.39$, and $0.223/0.514 \approx 0.43$ for $\phi = 0$, 0.08 and 0.16, respectively. Thus, if the mass lost upon drying is attributed only to the loss of water, then the ratios for the oil-containing gels would be $\approx 1 - (1 - 0.26)(1 - \phi) \approx 0.32$ and 0.38 for $\phi = 0.08$ and 0.16, respectively. On the other hand, if, in addition, all the oil evaporated, then the ratios would be $\approx 1 - \phi 0.77/0.98 - (1 - 0.26)(1 - \phi) \approx 0.26$ and 0.25 (approximating the initial composite density as that of water $\sim \rho_w$ with the ratio of the oil and water densities $\rho_o/\rho_w = 0.77/0.98$). Comparing these estimates with the measured ratios suggests that the gels retain the oil upon drying.

It is therefore pertinent to consider the extent to which the dried samples swell with respect to their as-prepared counterparts. Accordingly, the ratio of the final masses for the initially dried and as-prepared samples is

$$R = \frac{m_d(1 + S_{m,d})}{m_0(1 + S_{m,w})},$$

where m_d and m_0 are the dried and as-prepared masses (section 8.4), with $S_{m,d}$ and $S_{m,w}$ their respective equilibrium swelling ratios. From the measured masses, and the equilibrium swelling ratios in table 8.1, we find R = 0.16(1 + 8.13)/[0.615(1 + 0.24)] = 1.92, 0.224(1+5.73)/[0.571(1+0.26)] = 2.10, and 0.223(1+5.32)/[0.514(1+0.26)] = 2.18 for $\phi = 0$, 0.08 and 0.16, respectively. Thus, perhaps surprising—in view of the swelling ratios in figure 8.3(b)—drying approximately doubles the equilibrium water uptake, irrespective of ϕ . This suggests that drying reduces the effective degree of cross-linking, perhaps breaking covalent bonds.

The composites were subjected to thermogravimetric analysis at temperatures T=0–500°C under nitrogen, followed by T=500–700°C in air. The foregoing hypothesis that oil remains in the gels after 24 hr at $T\lesssim 40$ °C is strengthened by peaks in figure corresponding to the decomposition of hexadecane when $T\approx 200$ –280°C. Polyacrylamide has been reported to degrade when $T\approx 200$ –400°C (Leung et al., 1987).

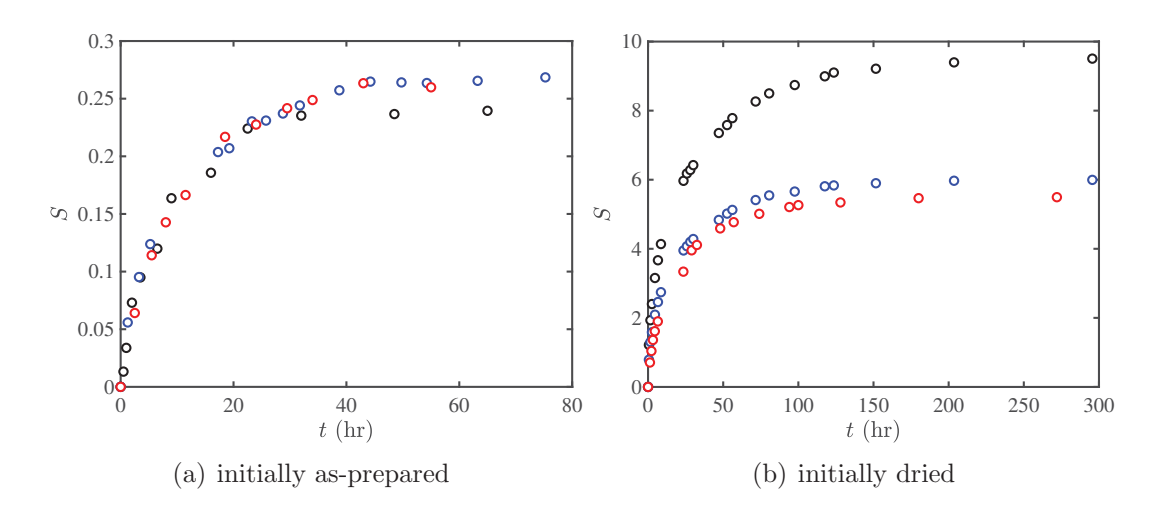


FIGURE 8.3: Swelling-ratio time series of initially as-prepared (a) and dried (b) hydrogels and nanoemulsion-hydrogel composites. Hydrogels are from ≈ 4 wt % monomer with oil volume fractions $\phi = 0$ (black), 0.08 (blue) and 0.16 (red), and aqueous-phase SDS concentration $c_{\infty,0}/(1-\phi) = 13$ mM.

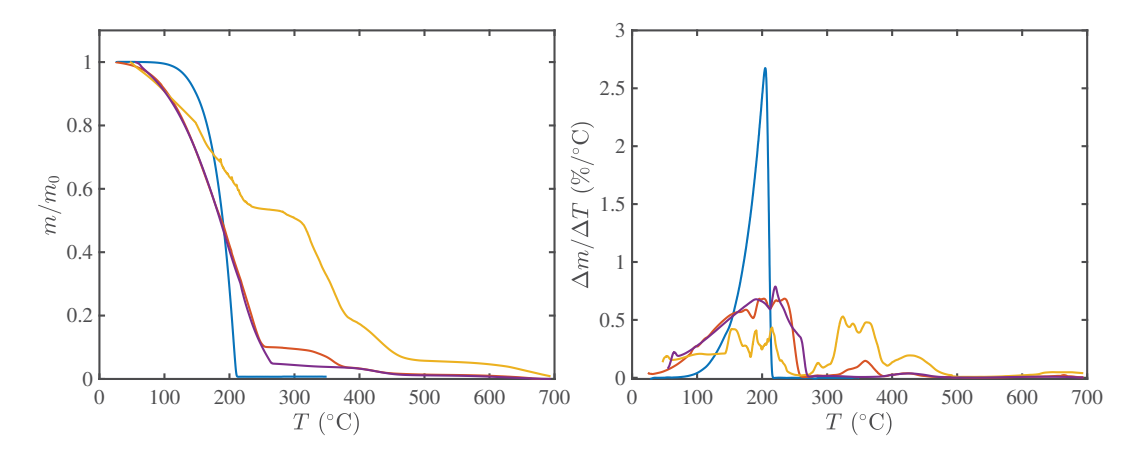


FIGURE 8.4: Gravimetric analysis of hexadecane (blue), an as-prepared nanoemulsion-hydrogel composite ($\phi=0.16$, red), dried nanoemulsion-hydrogel composite ($\phi=0.16$, yellow), and as-prepared or dried hydrogel ($\phi=0$, violet) versus temperature.

8.5.2 Rheology

Viscoelasticity of the nanoemulsion-hydrogel composites is summarized in figure 8.5. At aqueous-phase SDS concentration $c_{\infty,0}/(1-\phi)=5$ mM (below the c.m.c. in water without added salt) the oil volume fraction that was dispersible using sonication during nanoemulsion preparation without coalescence was limited to $\phi \approx 0.1$. With $\phi \approx 0.2$, however, the aqueous-phase SDS concentration was $c_{\infty,0}/(1-\phi)=13$ mM (above the c.m.c. in water without added salt). Amplitude and frequency sweeps demonstrate a linear viscoelastic response.

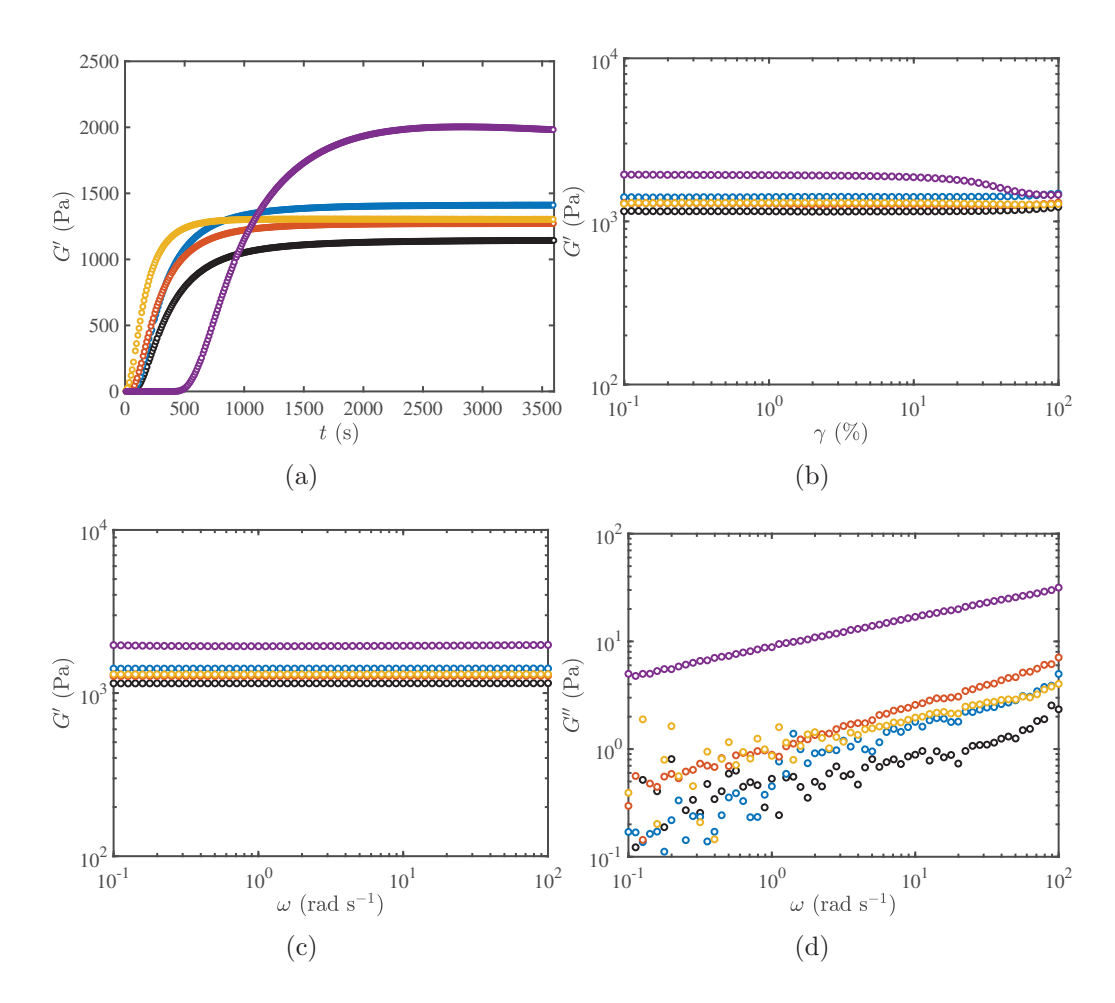


FIGURE 8.5: Rheological characterization of polyacrylamide and nanoemulsion composites with 4 wt % monomer concentration and oil volume factions $\phi = 0$ (black), 0.02 (blue), 0.05 (red), 0.1 (yellow), and 0.2 (violet). (a) Storage modulus time series with $\omega = 1$ rad s⁻¹, $\gamma = 2\%$ (b) Storage modulus sweep with $\omega = 1$ rad s⁻¹. (c) Storage and (d) loss modulus frequency sweep with $\gamma = 2\%$.

Time series of the storage moduli in figure 8.5(a) were fit to

$$G'(t) = \frac{G'_{\infty}t^{\alpha}}{t^{\alpha} + \theta^{\alpha}},\tag{8.3}$$

where G'_{∞} is the steady state storage modulus, t is the time, θ is the gelation half time, and α is a fitting exponent (Calvet et al., 2004).

As shown in figure 8.6, the plateau storage modulus increases with the oil volume fraction. This is surprising given that the drops have no intrinsic elasticity. However, they do bear a surface-tension that acts to maintain a spherical shape, and this seems to explain them behaving as rigid spheres, as demonstrated by the comparison to the elastic anologue of Einstein's viscosity. Similar behavior

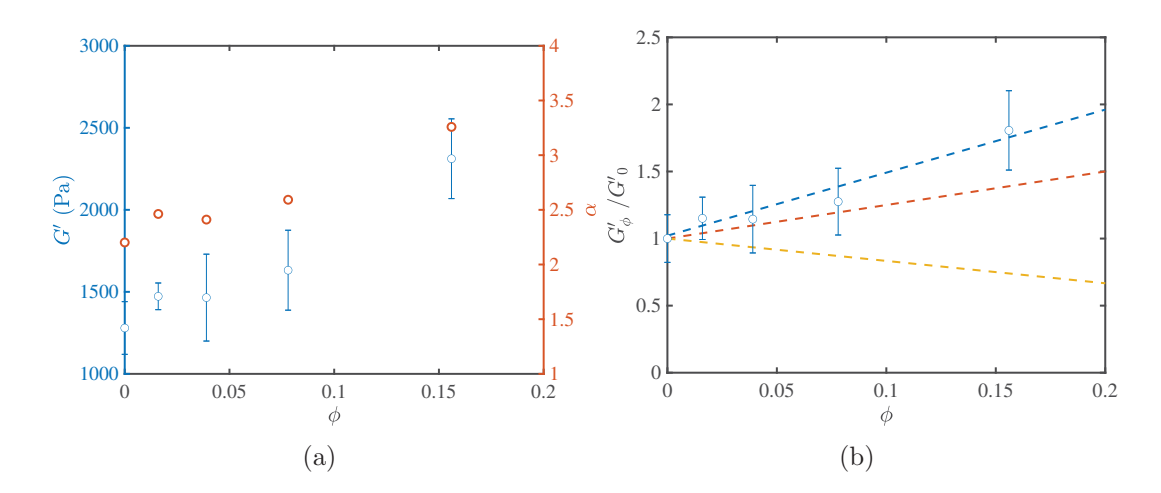


FIGURE 8.6: (a) Steady-state storage modulus (blue) and exponent α (Eqn.(8.3), red) for cross-linked nanoemulsion composites versus oil volume fraction ϕ ($\gamma \approx 2\%$, $\omega \approx 1$ rad s⁻¹). Error bars are the standard deviation from three samples. (b) The storage modulus scaled with the value for gels with $\phi = 0$. Solid line is a linear fit that weights residuals according to the errors: $G'/G'_0 = (4.7 \pm 1.9)\phi + (1.00 \pm 0.1)$ (Browaeys, 2020). This is compared to the Einstein viscosity formula (Einstein, 1906) (red) and its counterpart for inviscid, but penetrable spheres (Wang and Hill, 2009) (yellow, dashed line).

has been reported for polyacrylamide-chitosan composites (Martinez-Ruvalcaba, 2008). and rheological studies of monodisperse emulsions have reported the dependence of the emulsion storage modulus on the interfacial tension γ and drop radius a. These furnish $G' = A\gamma/a$, where A depends on the oil volume fraction (Mason et al., 1995, 1996).

Analogs of shear-viscosity enhancement relationships (Einstein, 1906, Wang and Hill, 2009) are shown for the shear modulus of our nanoemulsion-hydrogel composites in figure 8.6. The Einstein formula $\mu = \mu_0(1 + [\mu]\phi)$ furnishes $[\mu] = 5/2$ for rigid spheres in Newtonian fluids, whereas Wang and Hill (2009) calculated $[\mu] \approx (5\chi - 5)/(2\chi + 3) \rightarrow -5/3$ as $\chi = \mu_i/\mu_o \rightarrow 0$ for penetrable inviscid drops in creeping flow with χ the ratio of the internal and external shear moduli (shear viscosities in their paper). For impenetrable drops, Taylor (1932) showed that $[\mu] \approx (5\chi/2 + 1)/(\chi + 1) \rightarrow 1$ as $\chi \rightarrow 0$. Our rheological data show that oil drops enhance the hydrogel shear modulus with $[\mu] \approx 4.7$, thus behaving more like rigid spheres that occupy a volume that is larger than that of the oil. Similar enhancements have been reported for oil-filled gels (Sala et al., 2007, Vliet, 1988).

According to Vliet (1988), the effective shear modulus of drops—based on the Laplace pressure—is $2\gamma/a$, where γ is the interfacial tension. Thus, with $\gamma \approx 7 \text{ mN m}^{-1}$ and $a \approx 1 \mu\text{m}$, we find $2\gamma/a \approx 3.5 \text{ kPa}$, whereas the gel shear modulus

 $\mu_0 \approx 1.27$ kPa. Thus, with a ratio $\chi = 3.5/1.27 = 2.8$, the theory of Wang and Hill (2009) furnishes $[\mu] \approx (5\chi - 5)/(2\chi + 3) = 1.3$, and the theory of Taylor (1932) gives $[\mu] \approx (5\chi/2 + 1)/(\chi + 1) = 2.1$.

Again, these are all somewhat lower than measured, suggesting that (i) the interfacial tension is much higher than estimated and/or (ii) the average drop radius is smaller than estimated. Indeed, given that the shear-induced energy of the drops arises from interfacial energy, a small area-averaged drop radius may be justified. In addition, Vliet (1988) has proposed that the gel may be locally modified by the oil. According to this hypothesis, the theory of Wang and Hill (2009) may be applied for spherical drops with a perfect-slip boundary condition between the oil and elastic coating with a thickness that is δ/a times the drop radius, and a shear modulus that is a factor χ times that of the bulk gel. For example, with $\delta/a = 0.25$ and $\chi = 10$, their theory furnishes $[\mu] = 3.8$, which is close to the measured value. It is not clear, however, which such layers having $\delta \sim 200$ nm and $\mu \sim 10$ kPa actually exist. Dynamic mobility measurements suggest that this is not the case (Afuwape and Hill, 2020, Ch. 6).

8.6 Conclusions

Bulk properties of nanoemulsion composites were investigated to understand the dispersed (oil) and continuous (hydrogel) phase interactions using confocal microscopy, swelling, rheology, and thermogravimetric analysis. Confocal microscopy resolved a microstructure of densely packed micrometer sized drops immobilized in the polymer network, whereas sound-wave attenuation identifies a significant number density of much smaller drops. Swelling experiments quantify the degree to which water uptake is hindered by an increasing oil volume fraction. Moreover, we showed that oil is retained within the cross-linked polymer network upon drying, and that drying increases subsequent water uptake capacity. Rheological analysis reveals a distinct increase in the composite shear moduli with oil volume fraction, somewhat larger than expected for rigid inclusions. For applications,

 $^{^1\}mathrm{For}$ SDS solutions at the hexadecane-water interface with SDS concentration $c_\infty=5$ mM and added NaCl ionic strength $I_s=20$ mM, we have measured $\gamma=6.89$ mN m $^{-1}$; and with $I_s=5$ mM, we measured $\gamma=7.6$ mN m $^{-1}$. Here, we have taken the bulk aqueous-phase SDS concentration $c_\infty^*=5$ mM with an effective NaCl concentration (based on the measured hydrogel conductivity) $I_g=11$ mM (Afuwape and Hill, 2020, Ch. 5). Our estimate of the SDS concentration in the pre-gel solution is $c_{\infty,0}\approx3.6$ –5.0 mM, depending on the monomer concentration.

such as wound dressing, our swelling studies quantify how oil loading may decrease exudate retention capacity, showing also that network degradation would be necessary to release oil droplets.

8.7 Acknowledgements

This work was supported by NSERC Discovery and Research Tools and Instruments grants to R.J.H. G.A. was supported by a PRESSID/PTDF scholarship (Nigeria). The authors thank O. Odunola for assisting with TGA, and A. Al-Amodi for assisting with confocal microscopy.

8.8 Author contributions

G.A. designed and performed the experiments, and analyzed the data. G.A. and R.J.H. interpreted the results and wrote the paper.

Bibliography

- G. A. Afuwape and R. J. Hill. Nanoemulsion-hydrogel composites: Electro-kinetic dynamics, viscoelastic and swelling responses. PhD thesis, McGill University, 2020.
- B. Amsden. Solute diffusion within hydrogels. mechanisms and models. *Macro-molecules*, 31(23):8382–8395, 1998.
- H. Z. An, M. E. Helgeson, and P. S. Doyle. Nanoemulsion composite microgels for orthogonal encapsulation and release. *Adv. Mater.*, 24(28, SI):3838–3844, 2012.
- N. Bicak, B. Senkal, and M. Gazi. Hydrogels prepared by crosslinking copolymerization of n-allyl maleamic acid with acrylamide and acrylic acid. Des. Monomers Polym., 7(3):261–267, 2004.
- G. Bonacucina, M. Cespi, and G. F. Palmieri. Characterization and stability of emulsion gels based on acrylamide/sodium acryloyldimethyl taurate copolymer. *AAPS PharmSciTech*, 10(2):368–375, 2009.

- L. Brannon-Peppas and N. A. Peppas. Equilibrium swelling behavior of phsensitive hydrogels. *Chem. Eng. Sci.*, 46(3):715 722, 1991.
- J. Browaeys. Linear fit with both uncertainties in x and in y. MATLAB Central File Exchange., 2020.
- D. Calvet, J. Wong, and S. Giasson. Rheological monitoring of polyacrylamide gelation importance of cross-link density and temperature. *Macromolecules*, 37 (20):7762–7771, 2004.
- A. Einstein. Zur theorie der brownschen bewegung. Ann. Phys., 324(2):371–381, 1906.
- H. B. Eral, M. O'Mahony, R. Shaw, B. L. Trout, A. S. Myerson, and P. S. Doyle. Composite hydrogels laden with crystalline active pharmaceutical ingredients of controlled size and loading. *Chem. Mater.*, 26(21):6213–6220, 2014.
- A. Francesko, P. Petkova, and T. Tzanov. Hydrogel dressings for advanced wound management. *Curr. Med. Chem.*, 25(41):5782–5797, 2018.
- A. Gupta, A. Z. M. Badruddoza, and P. S. Doyle. A general route for nanoemulsion synthesis using low-energy methods at constant temperature. *Langmuir*, 33(28): 7118–7123, 2017.
- S. M. Hashemnejad, A. Z. M. Badruddoza, B. Zarket, C. Ricardo Castaneda, and P. S. Doyle. Thermoresponsive nanoemulsion-based gel synthesized through a low-energy process. *Nat. Commun.*, 10(1):2749, 2019.
- T. Helfman, L. Ovington, and V. Falanga. Occlusive dressings and wound healing. Clin. Dermatol., 12(1):121 – 127, 1994.
- E. Josef, M. Zilberman, and H. Bianco-Peled. Composite alginate hydrogels: An innovative approach for the controlled release of hydrophobic drugs. *Acta Biomater.*, 6(12):4642 4649, 2010.
- D. G. Kanjickal and S. T. Lopina. Modeling of drug release from polymeric delivery systems—a review. *Crit. Rev. Ther. Drug Carrier Syst.*, 21(5):345–386, 2004.
- L. Kass, E. D. Cardenas-Vasquez, and L. C. Hsiao. Composite double network hydrogels with thermoresponsive colloidal nanoemulsions. *AIChE J.*, 65(12), 2019.

- K. Kim, J. Renkema, and T. Van Vliet. Rheological properties of soybean protein isolate gels containing emulsion droplets. *Food Hydrocoll.*, 15(3):295–302, 2001.
- G. Komarova, S. Starodubtsev, V. Lozinsky, I. Nasimova, and A. Khokhlov. Intelligent gels and cryogels with embedded emulsions of various oils. *J. Appl. Polym. Sci.*, 127(4):2703 2709, 2013.
- W. M. Leung, D. E. Axelson, and J. D. Van Dyke. Thermal degradation of poly-acrylamide and poly(acrylamide-co-acrylate). J. Polym. Sci., Part A: Polym. Chem., 25(7):1825–1846, 1987.
- J. Li and D. J. Mooney. Designing hydrogels for controlled drug delivery. *Nat. Rev. Mater.*, 1(12), 2016.
- C.-C. Lin and A. T. Metters. Hydrogels in controlled release formulations: network design and mathematical modeling. Adv. Drug Deliv. Rev., 58(12-13):1379–1408, 2006.
- F. Lupi, L. Gentile, D. Gabriele, S. Mazzulla, N. Baldino, and B. de Cindio. Olive oil and hyperthermal water bigels for cosmetic uses. J. Colloid Interface Sci., 459:70–78, 2015.
- A. Martinez-Ruvalcaba. Swelling characterization and drug delivery kinetics of polyacrylamide-co-itaconic acid/chitosan hydrogels. Express Polym. Lett., 3: 25–32, 2008.
- L. Masaro and X. Zhu. Physical models of diffusion for polymer solutions, gels and solids. *Prog. Polym. Sci.*, 24(5):731 775, 1999.
- T. G. Mason, J. Bibette, and D. A. Weitz. Elasticity of compressed emulsions. *Phys. Rev. Lett.*, 75:2051–2054, 1995.
- T. G. Mason, J. Bibette, and D. A. Weitz. Yielding and flow of monodisperse emulsions. *J. Colloid Interface Sci.*, 179(2):439 448, 1996.
- I. Milimouk, A. Hecht, D. Beysens, and E. Geissler. Swelling of neutralized polyelectrolyte gels. *Polymer*, 42(2):487–494, 2001.
- D. Mou, H. Chen, D. Du, C. Mao, J. Wan, H. Xu, and X. Yang. Hydrogel-thickened nanoemulsion system for topical delivery of lipophilic drugs. *Int. J. Pharm.*, 353(1):270 276, 2008.

- S. Murdan. Electro-responsive drug delivery from hydrogels. J. Controlled Release, 92(1):1-17, 2003.
- I. Ohmine and T. Tanaka. Salt effects on the phase transition of ionic gels. *J. Chem. Phys.*, 77(11):5725–5729, 1982.
- N. Peppas, P. Bures, W. Leobandung, and H. Ichikawa. Hydrogels in pharmaceutical formulations. *Eur. J. Pharm. Biopharm.*, 50(1):27–46, 2000.
- S. E. Sakiyama-Elbert and J. A. Hubbell. Development of fibrin derivatives for controlled release of heparin-binding growth factors. *J. Control. Release*, 65(3): 389 402, 2000.
- G. Sala, G. Van Aken, M. Stuart, and F. Van De Velde. Effect of droplet-matrix interactions on large deformation properties of emulsion-filled gels. *J. Texture* Stud., 38(4):511–535, 2007.
- K. Shingel, C. Roberge, O. Zabeida, M. Robert, and J. Klemberg-Sapieha. Solid emulsion gel as a novel construct for topical applications: Synthesis, morphology and mechanical properties. *J. Mater. Sci. Mater. Med.*, 20(3):681–689, 2009.
- J. Siepmann and N. A. Peppas. Modeling of drug release from delivery systems based on hydroxypropyl methylcellulose (hpmc). *Adv. Drug Deliv. Rev.*, 48(2): 139 157, 2001. =.
- T. Tanaka and D. J. Fillmore. Kinetics of swelling of gels. J. Chem. Phys., 70(3): 1214–1218, 1979.
- G. I. Taylor. The viscosity of a fluid containing small drops of another fluid. Proc. R. Soc. London, Ser. A, 138(834):41–48, 1932.
- T. Vliet. Rheological properties of filled gels. influence of filler matrix interaction. *Colloid Polym. Sci.*, 266(6):518–524, 1988.
- M. Wang and R. J. Hill. Anomalous bulk viscosity of polymer-nanocomposite melts. *Soft Matter*, 5:3940–3953, 2009.
- L. Wei, C. Cai, J. Lin, and T. Chen. Dual-drug delivery system based on hydrogel/micelle composites. *Biomaterials*, 30(13):2606 2613, 2009.
- R. Yoshida, K. Sakai, T. Okano, and Y. Sakurai. Pulsatile drug delivery systems using hydrogels. *Adv. Drug Deliv. Rev.*, 11(1):85 108, 1993.

- R. Yu and S. Zheng. Poly(acrylic acid)-grafted poly(n-isopropyl acrylamide) networks: Preparation, characterization and hydrogel behavior. *J. Biomater. Sci.*, *Polym. Ed.*, 22(17):2305–2324, 2011.
- B. Zeeb, A. H. Saberi, J. Weiss, and D. J. McClements. Formation and characterization of filled hydrogel beads based on calcium alginate: Factors influencing nanoemulsion retention and release. *Food Hydrocoll.*, 50:27–36, 2015.

Chapter 9

Conclusions and future work

9.1 Summary of conclusions

The goal of this thesis was to understand the dynamics of surfactant stabilized oil droplets in polymer networks, and relate experimental observations to standard electrokinetic theories to furnish the colloidal properties. Also, to elucidate macroscopic property changes with oil inclusions in nanoemulsion-hydrogels.

In chapter 3, dielectric relaxation spectra of aqueous SDS micelle solutions with different added NaCl concentration were measured and interpreted with the standard electrokinetic model (accounting for the contribution of added counterions and non specific adsorption) using a variety of definitions of fractional ionization. Though micelle fractional degree of ionization have been reported ~ 0.3 , values obtained using SEKM are ~ 1 , indicating that previous values deduced from mobility measurements are probably due to nonlinear electrostatics.

Chapter 4 reported the electrical dynamics of polystyrene latex beads investigation via dielectric relaxation spectroscopy. Theoretical interpretations were undertaken using a standard electrokinetic model of Hill et al. (2003) to furnish the electrokinetic surface charge, and the possibility of modelling these polystyrene latices as colloidal particles with charged coatings was also reported.

Hexadecane-in-water interfacial dynamics in the presence of SDS and NaCl were investigated using pendant drop tensiometry, before interfacial tension data interpreted with a thermodynamic model that furnishes the adsorption isotherm parameters in chapter 5. Adsorption isotherms were used to prescribe ζ -potentials

and surface charge for oil droplets in nanoemulsions. Nanoemulsion dielectric relaxation spectra were interpreted with rigid-particle electrokinetic theory, which suggested apparent particle polarizability being dominated by larger droplets due to the polydisperse nature of the suspension.

In chapter 6, electro-kinetic-sonic amplitude measurements were used to report the dynamic mobility spectra of SDS-stabilized hexadecane nanodrops in aqueous NaCl electrolytes. The spectra were interpreted using a recently proposed theory for highly charged drops with thin double layers, and fluid-dynamics due to interfacial Maxwell and Marangoni stresses were highlighted in megahertz frequencies.

Chapter 7 reported the electro-kinetic-sonic amplitude measurements of hexadecane in water nanoemulsions dispersed in polyacrylamide hydrogels. Measured dynamic mobility spectra were interpreted using the fluid sphere theory by Hill and Afuwape (2020) with the electrolyte viscosity substituted for a complex-shear modulus to account for the viscoelastic environment. The reported invariant droplet size in the polymer network suggested droplet immobilization, while the theoretical interpretation furnished a shear viscosity for the composite that increases with oil volume fraction.

In chapter 8, the influence of droplet inclusion on hydrogel properties was probed. Swelling experiments were performed on hydrogels, and nanocomposites of different dispersed oil volume fractions. The successful entrapment of the oil phase in the polymer network is emphasized by the decrease in water retention capacity of the nanocomposites with increasing oil volume fraction, while the composite heterogeneity were ascertained from confocal images.

9.2 Contributions to knowledge

Original contributions of this thesis to knowledge include:

Frequency dependent conductivity spectra provided insights on the influence
of NaCl concentration on SDS micelle dynamics. Standard electrokinetic interpretation of these spectra, while accounting for the contribution of added
counterions and non specific adsorption influenced the ζ-potential and accompanying micelle charge. It was observed that the customary fractional

degree of ionization might be misconstrued due to non-linear electrostatics, such as counterion condensation, arising from the high surface charge density.

- A robust experimental approach that unifies equilibrium adsorption thermodynamics with electrokinetic measurements to understand nanoemulsions, and captures the effect of added NaCl on colloidal properties.
- Electrokinetic interpretation of the dynamic mobility spectra for highly charged nanodroplets highlighted the increased influence of Marangoni and viscous stresses at megahertz frequencies, perhaps suggesting fluid-like dynamics are plausible reasons for the limitations of rigid-particle theory.
- The study of nanodroplet-hydrogels provided new insights on nanodroplet dynamics in a viscoelastic environment. The role of monomer concentration, and oil phase volume fraction were reported. These provide fundamental insights that could be exploited in developing applications.
- Swelling experiments highlighted the influence of oil volume fraction on the water retention capacity of oil bearing hydrogels.

9.3 Suggestions for future work

- In chapter 4, quantitative agreement between data and SEKM calculations was elusive, despite accounting for all contributions to the conductivity of colloidal suspension. A different cleaning protocol, or precise technique to account for the constituent ions in the colloidal suspension might improve data and theoretical interpretation.
- In chapter 5 and 6, the polydisperse nature of nanoemulsions required fitting electrokinetic models to data by prescribing an effective diameter. A robust approach would be to fit data to a particle size distribution.
- In chapter 5, non-rigid particles were fitted to SEKM calculations for rigid particles, an assumption that is valid in the frequency range. It is noteworthy to mention a non-rigid particle theory might be appropriate to interpret the electrokinetic spectra of nanoemulsions at megahertz frequencies.

- R. J. Hill and G. A. Afuwape. Dynamic mobility of surfactant stabilized nanodroplets: unifying equilibrium thermodynamics, electro-kinetics and Marangoni effects. *J. Fluid Mech.*, 895(A14), 2020.
- R. J. Hill, D. Saville, and W. Russel. Polarizability and complex conductivity of dilute suspensions of spherical colloidal particles with charged (polyelectrolyte) coatings. *J. Colloid Interface Sci.*, 263(2):478 497, 2003.

Appendix A

Dielectric relaxation spectroscopy of polyacrylamide hydrogels

A.1 Preface

Adibnia et al. (2020) measured the conductivity of charged hydrogels, showing that this decreases with polymerization due to ion mobility being hindered by network formation. This is contrary to uncharged polyacrylamide gels, which exhibited no distinct change in conductivity with polymerization and cross-linking. Here, dielectric relaxation is used to probe the polymerization and cross-linking of polyacrylamide, with bisacrylamide as cross-linker, adding known concentrations of NaCl and SDS to the pre-gel solution. Monomer concentrations were varied to elucidate the correlation between gel stiffness and conductivity.

A.2 Materials and methods

Polyacrylamide gels were synthesized from acrylamide (monomer) (40 w/v % aqueous solution, Fisher Scientific U.S.A.), bisacrylamide (crosslinker) (2 w/v % aqueous solution, Fisher Scientific U.S.A.), ammonium persulfate (APS) (powder, Fisher Scientific U.S.A.), and N,N,N',N'-tetramethylethylenediamine (TEMED, GE Healthcare Life Science, Germany) as initiator and catalyst for the free radical polymerization. Different ionic strengths were obtained by pre-dissolving prescribed mass of NaCl (Sigma Aldrich) and sodium dodecyl sulphate (SDS) (98.5 %,

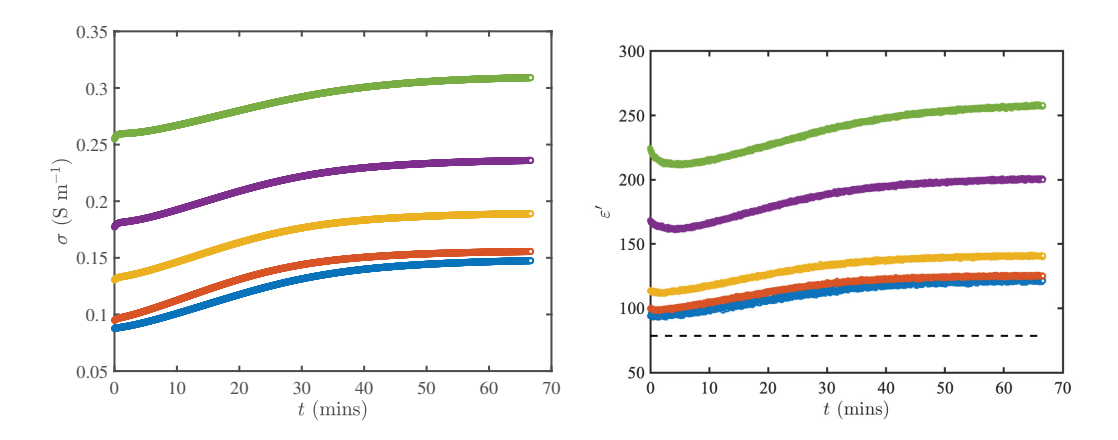


FIGURE A.1: Conductivity (left) and dielectric constant (right) time series for polyacrylamide hydrogels (2 wt %) with added NaCl concentrations $I_s = 0$ (blue), 1 (red), 5 (yellow), 10 (violet), 20 mM (green) measured at f = 100 kHz.

Sigma-Aldrich Canada), and reverse-osmosis (RO) water (Type 1, $\sigma \approx 5.6 \,\mu\text{S m}^{-1}$, $\Omega \approx 18$ MOhm cm). All materials were used as procured from the manufacturers.

A.3 Results

The change in dielectric relaxation properties of polyacrylamide gels with time is shown in figure A.1. The conductivity and dielectric constant spectra increase with polymerization and cross-linking. This is counter intuitive, as ion mobility should be hindered by the network formation. However, since acrylamide junctions are formed by free radical polymerization, the increase in conductivity may be due to unreacted monomer radicals.

The addition of NaCl produces an additive effect on the hydrogel conductivity. This is highlighted in figure A.2, where hydrogel spectra are compared to those of aqueous NaCl solutions with the same NaCl concentration.

A similar trend is seen in figures A.3 and A.4 for polyacrylamide gels with varying SDS concentration.

From the conductivity plots in figure A.5, the point of inflexion for gels changes with respect to their aqueous SDS solution counterpart, suggesting that the polymer and/or the reagents in the pre-gel solution decrease the critical micelle concentration.

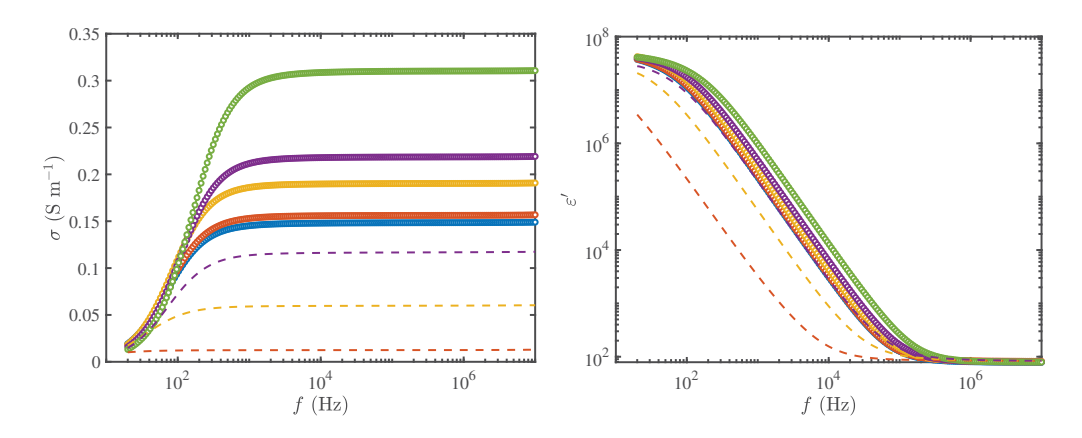


FIGURE A.2: Conductivity (left) and dielectric constant (right) spectra of polyacrylamide hydrogels (2 wt %), with added NaCl concentrations $I_s = 0$ (blue), 1 (red), 5 (yellow), 10 (violet), 20 mM (green). Dashed lines are spectra for NaCl solutions with NaCl concentrations $I_s = 1$ (red), 5 (yellow), 10 (violet) mM.

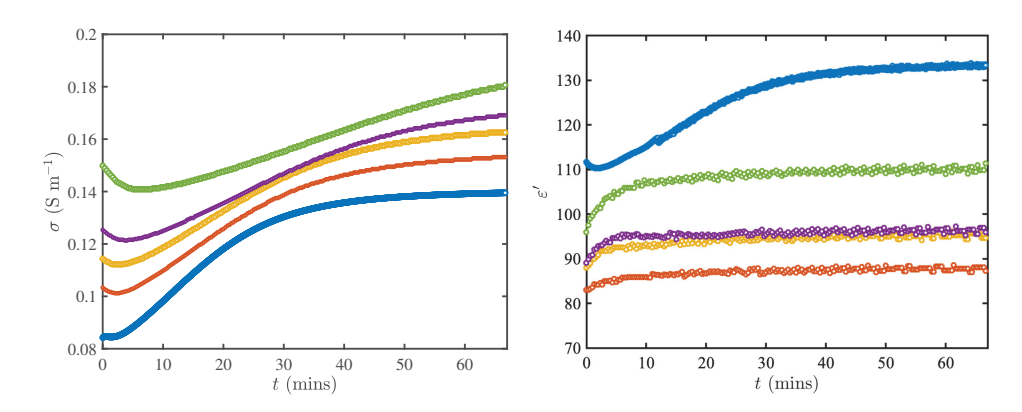


FIGURE A.3: Conductivity (left) and dielectric constant (right) time series for polyacrylamide hydrogels (4 wt%) with SDS concentrations $c_{\infty} = 0$ (blue), 5 (red), 8 (yellow), 13 (violet), 20 (green) mM measured at f = 1 MHz.

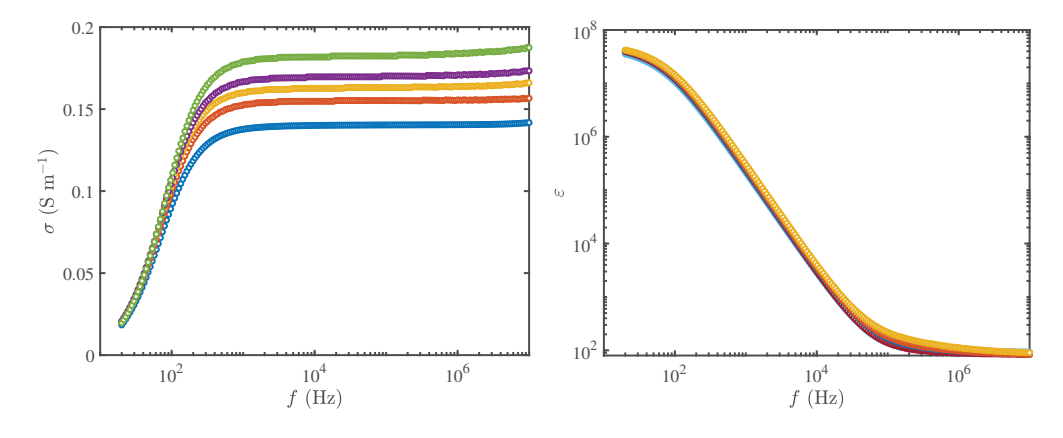


FIGURE A.4: Conductivity (left) and dielectric constant (right) spectra of polyacrylamide hydrogels (4 wt%) with SDS concentrations $c_{\infty} = 0$ (blue), 5 (red), 8 (yellow), 13 (violet), 20 mM (green).

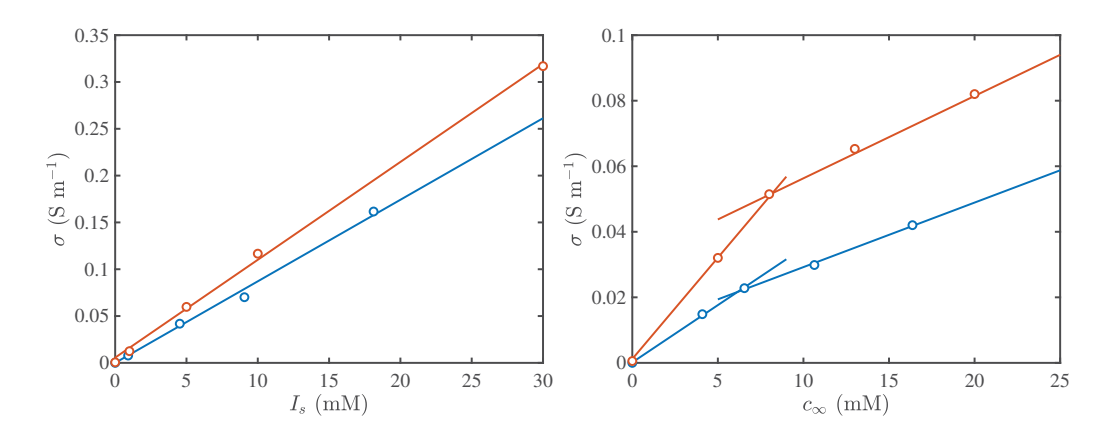


FIGURE A.5: Conductivity of NaCl (right) and SDS (right) aqueous solutions (red) and gels (blue) versus NaCl and SDS concentration, respectively. For the hydrogels, the conductivity without added NaCl and SDS has been subtracted ($\sigma_{gel} \approx 0.140~\mathrm{S~m^{-1}}$). Lines are best fits, identifying the c.m.c. of SDS $\approx 6.5~\mathrm{mM}$ (gel, blue) and $\approx 8.18~\mathrm{mM}$ (aqueous solution, red) with no added NaCl.

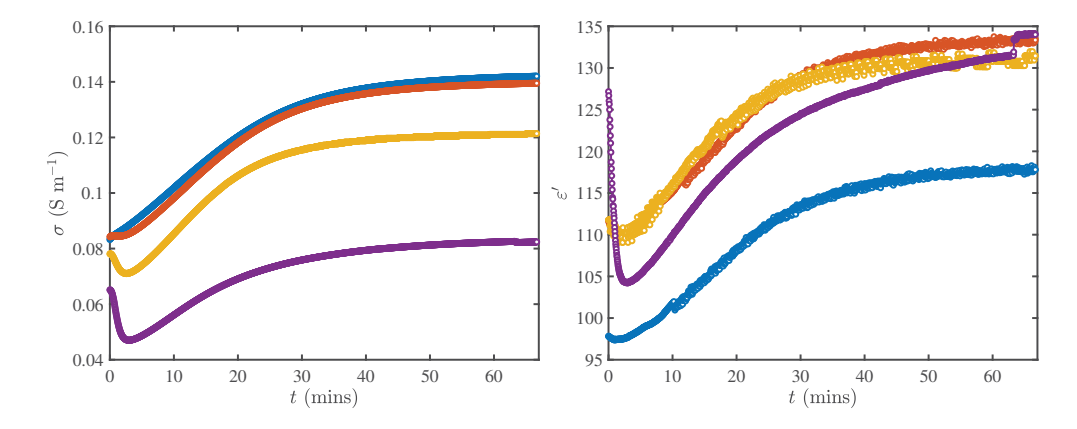


FIGURE A.6: Conductivity (left) and dielectric constant (right) time series for 2 (blue), 4 (red), 8 (yellow), and 16 (violet) wt% polyacrylamide hydrogels with no added salt.

A decrease in gel conductivity with increasing monomer concentration is demonstrated in figures A.6 and A.7. This can be attributed to the denser networks (higher storage modulus, smaller mesh sizes). The conductivity of aqueous solutions of initiator and catalyst are included in figure A.7.

A.4 Conclusions

Radical formation increases the conductivity and permittivity of uncharged polymers as polymerization and cross-linking proceeds. Added salt (or other ionic species, such as surfactants) contribute to the dielectric relaxation in an additive

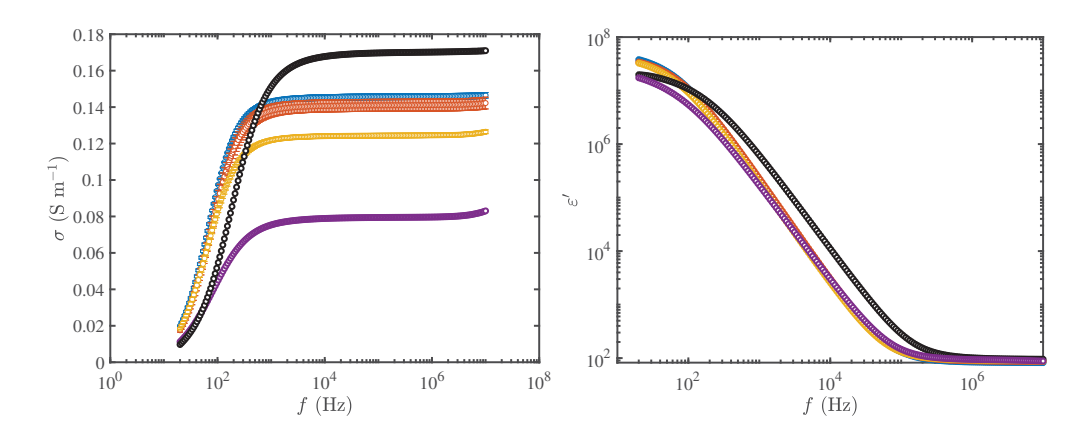


FIGURE A.7: Conductivity (left) and dielectric constant (right) spectra for 2 (blue), 4 (red), 8 (yellow), and 16 (violet) wt% polyacrylamide hydrogels with no added salt. Black circles are for a solution of ammonium persulfate and TEMED at the same concentrations as used to synthesize the gels.

manner, and are effective for modifying the background solvent in a polymer network. Micelle formation might be promoted in a polymer network with respect to aqueous solutions, because of the higher ionic strength (from radical formation). Increasing the monomer concentration reduces the hydrogel conductivity, because denser networks hinder ion mobility.

Bibliography

V. Adibnia, G. Afuwape, and R. J. Hill. Electrokinetic sonic amplitude of polyelectrolyte solutions and networks. *Macromolecules*, 53(17):7460–7468, 2020.

Appendix B

Detailed experimental protocols

B.1 Electroacoustic spectroscopy

This check-list comprises 7 sections addressing:

- Pre-experimental cleanup
- Post-experiment cleanup
- Conductivity probe calibration
- pH probe calibration
- ESA cell calibration
- ESA measurements on emulsions and gels

The following procedures are adapted from the manufacturer's instruction manual for the Acoustosizer II flow-through system. The procedure for measuring the ESA of gels was adapted from Adibnia (2015). Note that reverse-osmosis (RO) water was used instead of deionized water (DI) for all calibrations and measurements (RO water measured conductivity $\sigma_{\rm RO~water} \approx 5.6~\mu~{\rm S~m^{-1}}$). All parts must be completed to ensure accurate results and maintain instrument operation:

B.1.1 Pre-experimental cleanup

- Always remove the ESA attenuation sensor head by simultaneously lifting both handles to ensure the electrodes stay parallel for a long time.
- Clean the sensor electrodes with deionised water and designated soft damp non-abrasive tissue.
- Air dry the electrodes, taking precautions to avoid scratching.
- Clean the plastic spacer between the electrodes with deionised water and air dry.
- Ensure all removable parts are completely dry before reassembling.
- Carefully fit the ESA sensor back to the frame.
- Power up the AcoustoSizer II and laptop.

B.1.2 Post-experimental cleanup

- After every experimental run, use distilled water as feed into the complete flow circuit as wash fluid into the ESA setup.
- Change the feed until the conductivity of the flowing fluid reaches the detection limit ($\approx 0.001-0.002 \text{ mS cm}^{-1}$).
- Rinse tubes with deionised water, air dry, and replace into the designated bags.
- Clean the ESA sensor, plastic spacer and conductivity probe with the designated cloth and air dry.

B.1.3 Conductivity probe calibration

- Conduct the cleanup procedure as stated in section A.
- Rinse designated KCl flow tubes with deionised water and air dry.
- Connect flow tubes to the ESA sensor and pump.
- Connect 30 ml of standard KCl solution as feed to the flow circuit.

- Launch the Acoustosizer II software.
- Select the solvent type as POLAR.
- When the flow circuit is complete, switch on the pump in the FWD mode with speed 4.
- Shut-off the pump and switch on the pump in REV mode.
- Repeat steps 7 and 8 to ensure that all air bubbles ere eliminated.
- Switch on the pump in FWD mode, and the reduce pump speed to about 1 to achieve a steady temperature.
- Observe conductivity and temperature measurements on the MAIN Acoustosizer II panel window.
- When a steady temperature is reached, estimate the conductivity from the standard chart on the conductivity standard bottle.
- Click CALIBRATE on the main panel.
- Select the SUPPORT SENSOR calibration option.
- Select CONDUCTIVITY PROBE.
- Select SET CELL CONSTANT(K).
- Select USE CONDUCTIVITY STANDARD.
- Input calculated value into the conductivity of standard (mS cm⁻¹).
- Click CALIBRATE so the system outputs the corresponding cell constant.
- Record the cell constant in the appropriate log book with your name and calibration date.
- Click CLOSE.
- Recover the solution to its bottle. The standard should be replaced monthly or when the conductivity measurement from the ESA cell deviates ($\approx 5\%$ was taken to be significant) from the values reported in the conductivity/temperature table supplied by the standard's manufacturer.

B.1.4 pH probe calibration

- Rinse pH probe with deionised water.
- Click the CALIBRATE button on the tool bar.
- Select the SUPPORT SENSOR calibration option.
- Select pH PROBE.
- Select the buffer to be used in calibrating (preferably in the order NEU-TRAL, ACID, BASE).
- Dip the pH probe tip in the neutral buffer solution, and monitor until the pH is steady (do not let more than ≈ 0.5 cm of the probe be in the solution).
- Click CALIBRATE.
- Record the value of the pH probe potential (mV).
- Press NEXT.
- Repeat same procedure for ACID and BASE calibration, rinsing the pH probe with DI (or RO) water after every measurement.

B.1.5 ESA cell calibration

- Conduct the cleanup procedure as stated in section B.
- Rinse designated KSiW tubes with deionised water and air dry.
- Connect the tube to make a complete flow loop.
- Connect 30 ml of Standard KSiW as feed to the complete flow loop.
- Pump the KSiW solution through the sensor flow loop in FWD mode, shut it off, and switch on to the REV mode.
- Repeat step above to ensure trapped air bubbles in the system are eliminated.
- Compare KSiW conductivity value to that on the bottle to ensure calibration process is reliable.
- Click on the ESA SENSOR.

- Click on CALIBRATE on the main software panel.
- Select MEASURE to commence calibration measurement and ensure a message prompting successful operation is seen before proceeding.
- Click TOOLS DIAGONISTICS [FILL THE FORM] [NOTE FILE SAVE EXTENSION]. This would help with comparing our diagnostic data should we need to validate experiments. Do not forget to check the box to see the result at the end of the measurement.
- Recover KSiW solution after the calibration process by re-routing the piping back into the initial bottle.

B.1.6 ESA for nanoemulsions

- Conduct the cleanup procedure as stated in section B.
- Rinse designated nanoemulsion tubes with DI water and air dry.
- Prepare 30 ml of nanoemulsion via high-energy sonication.
- Use nanoemeulsion as feed to the flow loop.
- Make initial forward and reverse runs to ensure all trapped air bubbles are eliminated.
- Select Data logging on the main panel.
- Specify Measurement Settings (Particle 1D: hexadecane; Sizing method: Attenuation; Size distribution: lognormal; Total Number of Measurements: 9)
- Click MEASURE.
- Conduct the cleanup procedure as stated in section B.
- Check spreadsheets for result on C:\AZR2X\ [filename].

B.1.7 ESA for gels

- Conduct the cleanup procedure as stated in section B.
- Rinse and air dry designated tubes for gel.

- Connect tube to the ESA cell.
- Take in about 20 ml of the prepared gel solution to a syringe.
- Tap to ensure trapped air bubbles are eliminated.
- Connect syringe to the lower tube to form a batch flow.
- Pump fluid into the ESA cell slowly until about 2–3 cm of the top tube is filled.
- Secure the syringe position.
- Select Data logging on the main panel.
- Specify Measurement Settings (Particle 1D: Silica amorphous typical; Sizing method: Attenuation; Size distribution: Nanoparticle, High frequency; Total Number of Measurements: 40)
- Click MEASURE.
- Abort measurement when steady readings are observed (at least 25 measurements are required).
- Convert Attenuation measurements to ESA by opening $Get_raw_ESA2.exe$ on the laptop desktop folder.
- Select RAW data of the saved file name.
- Click OK.
- Cleanup gel from ESA cell with designated cloth, DI water, and air dry.
- Check spreadsheets for result on $C : AZR2X \setminus [filename]$.

B.2 Dielectric relaxation spectroscopy

The procedures below were adapted from Hollingsworth and Saville (2003). The single-spacer correction for electrode polarization as adapted from Beltramo and Furst (2012).

B.2.1 Open/short compensation

- Stainless steel electrodes are cleaned with a damp soft cloth and RO water before air drying.
- The cell is assembled by placing the electrodes in contact to measure the short due to residual impedances in the cell. The inductance spectrum is measured.
- Open-compensation measurements are performed with the acrylic spacer between both electrodes to account for stray admittance.
- The sample impedance Z^* can be calculated from the measured impedance Z_M , the residual impedance from short compensation, and the stray admittance Y_O from open compensation as

$$Z^* = \frac{Z_M - Z_S}{1 - (Z_M - Z_S)Y_O}$$
 (B.1)

- Cell constant can be extrapolated by measuring the complex impedance of solvent of known dielectric constant (e.g. water).
- The cell constant is estimated from the high frequency-fit of the dielectric constant spectrum.

B.2.2 Single-spacer correction for electrode polarization

The limitation of the single-spacer technique to correcting for electrode polarization at higher ionic strength is emphasized in figure B.1. The technique approximates low-frequency dielectric constants to that of pure water, unlike infinite spacer separation methods.

Bibliography

V. Adibnia. Electroacoustic and rheological characterization of hydrogel nanocomposites. PhD thesis, McGill University, 2015.

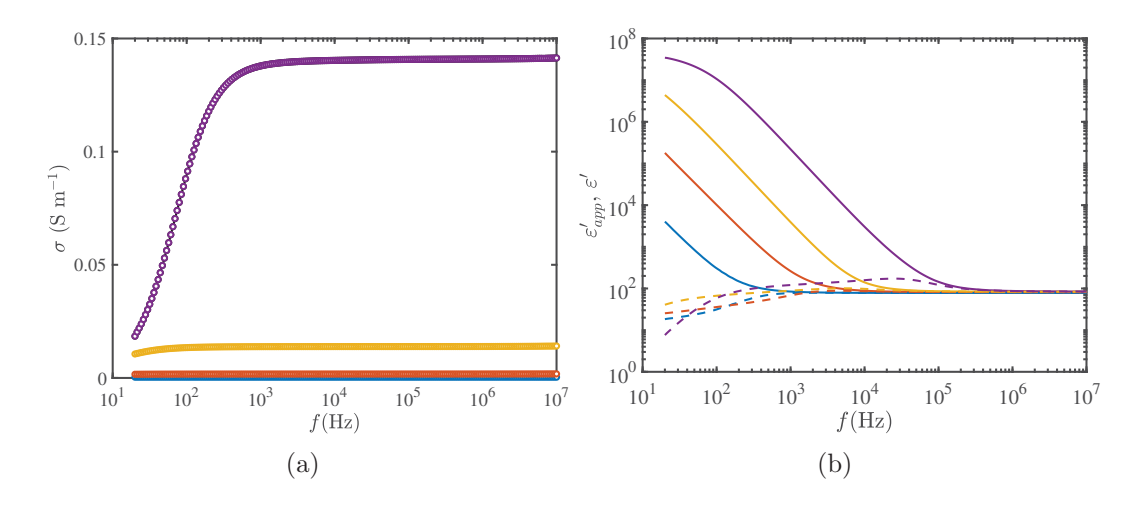


FIGURE B.1: Conductivity (right) and dielectric constant (left) spectra of aqueous KCl solutions with ionic strength $I_s = 0.01$ (blue), 0.1 (red), 1 (yellow), and 10 (violet) mM. Dashed lines are dielectric constant spectra corrected for electrode polarization using the single-spacer technique.

- P. Beltramo and E. Furst. A simple, single-measurement methodology to account for electrode polarization in the dielectric spectra of colloidal dispersions. *Chem. Lett.*, 41(10):1116–1118, 2012.
- A. Hollingsworth and D. Saville. A broad frequency range dielectric spectrometer for colloidal suspensions: cell design, calibration, and validation. *J. Colloid Interface Sci.*, 257(1):65 – 76, 2003.

Bibliography

C. Aaij and P. Borst. The gel electrophoresis of dna. *Biochim. Biophys. Acta, Nucleic Acids Protein Synth.*, 269(2):192 – 200, 1972.

- B. Abismal, J. Canselier, A. Wilhelm, H. Delmas, and C. Gourdon. Emulsification by ultrasound: drop size distribution and stability. *Ultrason. Sonochem.*, 6(1–2): 75–83, 1999.
- V. Adibnia. Electroacoustic and rheological characterization of hydrogel nanocomposites. PhD thesis, McGill University, 2015.
- V. Adibnia and R. J. Hill. Electroacoustic spectroscopy of nanoparticle-doped hydrogels. *Macromolecules*, 47(22):8064–8071, 2014.
- V. Adibnia, G. Afuwape, and R. J. Hill. Electrokinetic sonic amplitude of polyelectrolyte solutions and networks. *Macromolecules*, 53(17):7460–7468, 2020.
- G. A. Afuwape and R. J. Hill. Nanoemulsion-hydrogel composites: Electro-kinetic dynamics, viscoelastic and swelling responses. PhD thesis, McGill University, 2020.
- G. S. Aleiner and O. G. Us'yarov. Conductivity of micellar solutions of ionic surfactants and surface conductivity of micelles. *Colloid J.*, 72(5):588–594, 2010.
- C. Alexander. Synthetic polymer systems in drug delivery. Expert Opin. Emerg. Drugs, 6(2):345–363, 2001.
- B. Amsden. Solute diffusion within hydrogels. mechanisms and models. *Macro-molecules*, 31(23):8382–8395, 1998.
- H. Z. An, M. E. Helgeson, and P. S. Doyle. Nanoemulsion composite microgels for orthogonal encapsulation and release. *Adv. Mater.*, 24(28, SI):3838–3844, 2012.
- N. Annabi, Š. Selimović, J. P. Acevedo Cox, J. Ribas, M. Afshar Bakooshli, D. Heintze, A. S. Weiss, D. Cropek, A. Khademhosseini, and A. Khademhosseini. Hydrogel-coated microfluidic channels for cardiomyocyte culture. *Lab Chip*, 13(18):3569—3577, 2013.
- K. Asami. Characterization of heterogeneous systems by dielectric spectroscopy. *Prog. Polym. Sci.*, 27(8):1617–1659, 2002.

J. M. Asua. Miniemulsion polymerization. *Prog. Polym. Sci.*, 27(7):1283 – 1346, 2002.

- R. Barbucci. *Hydrogels: Biological properties and applications*. Springer Science & Business Media, 2010.
- R. Barchini and D. A. Saville. Electrokinetic properties of surfactant-stabilized oil droplets. *Langmuir*, 12(6):1442–1445, 1996.
- J. C. Baygents and D. A. Saville. Electrophoresis of drops and bubbles. *J. Chem. Soc.*, Faraday Trans., 87:1883–1898, 1991.
- R. Beckett, G. Nicholson, D. M. Hotchin, and B. T. Hart. The use of sedimentation field-flow fractionation to study suspended particulate matter. *Hydrobiologia*, 235(1):697–710, 1992.
- P. Beltramo and E. Furst. A simple, single-measurement methodology to account for electrode polarization in the dielectric spectra of colloidal dispersions. *Chem. Lett.*, 41(10):1116–1118, 2012a.
- P. J. Beltramo. *Polarization and self-assembly of colloidal suspensions*. PhD thesis, University of Delaware, 2013.
- P. J. Beltramo and E. M. Furst. Transition from dilute to concentrated electrokinetic behavior in the dielectric spectra of a colloidal suspension. *Langmuir*, 28 (29):10703–10712, 2012b.
- J. D. Berry, M. J. Neeson, R. R. Dagastine, D. Y. Chan, and R. F. Tabor. Measurement of surface and interfacial tension using pendant drop tensiometry. J. Colloid Interface Sci., 454:226 237, 2015.
- P. Bhosale, J. Chun, and J. Berg. Electroacoustics of particles dispersed in polymer gel. *Langmuir*, 27(12):7376–7379, 2011.
- N. Bicak, B. Senkal, and M. Gazi. Hydrogels prepared by crosslinking copolymerization of n-allyl maleamic acid with acrylamide and acrylic acid. *Des. Monomers Polym.*, 7(3):261–267, 2004.
- J. J. Bikerman. Ionentheorie der elektrosmose, der strömungsströme und der oberflächenleitfähigkeit. Z. Physik. Chem., 163A(1), 1933.

J. J. Bikerman. Electrokinetic equations and surface conductance. a survey of the diffuse double layer theory of colloidal solutions. *Trans. Faraday Soc.*, 35: 154–160, 1940.

- G. Bonacucina, M. Cespi, and G. F. Palmieri. Characterization and stability of emulsion gels based on acrylamide/sodium acryloyldimethyl taurate copolymer. AAPS PharmSciTech, 10(2):368–375, 2009.
- F. Booth. The cataphoresis of spherical fluid droplets in electrolytes. *J. Chem. Phys.*, 19(11):1331–1336, 1951.
- F. Booth and N. F. Mott. The cataphoresis of spherical, solid non-conducting particles in a symmetrical electrolyte. *Proc. R. Soc. London, Ser. A*, 203(1075): 514–533, 1950.
- F. Bordi, C. Cametti, and R. H. Colby. Dielectric spectroscopy and conductivity of polyelectrolyte solutions. *J. Phys.: Condens. Matter*, 16(49):R1423, 2004.
- R. Borwankar and D. Wasan. Equilibrium and dynamics of adsorption of surfactants at fluid-fluid interfaces. *Chem. Eng. Sci.*, 43(6):1323 1337, 1988.
- K. Bouchemal, S. Briançon, E. Perrier, and H. Fessi. Nano-emulsion formulation using spontaneous emulsification: solvent, oil and surfactant optimisation. *Int.* J. Pharm., 280(1–2):241–251, 2004.
- L. Brannon-Peppas and N. A. Peppas. Equilibrium swelling behavior of phsensitive hydrogels. *Chem. Eng. Sci.*, 46(3):715 722, 1991.
- J. Browaeys. Linear fit with both uncertainties in x and in y. MATLAB Central File Exchange., 2020.
- D. Calvet, J. Wong, and S. Giasson. Rheological monitoring of polyacrylamide gelation importance of cross-link density and temperature. *Macromolecules*, 37 (20):7762–7771, 2004.
- M. Carafa, C. Marianecci, L. Di Marzio, F. Rinaldi, C. Meo, P. Matricardi, F. Alhaique, and T. Coviello. A new vesicle-loaded hydrogel system suitable for topical applications: preparation and characterization. *J. Pharm. Pharm. Sci.*, 14(3):336–346, 2011.
- G. Castellan. Physical Chemistry. The Benjamin/Cummings Publishing Co, 1982.

R. Chanamai and D. J. McClements. Dependence of creaming and rheology of monodisperse oil-in-water emulsions on droplet size and concentration. *Colloids* Surf., A, 172(1):79 – 86, 2000.

- Y. Chao, Q. Chen, and Z. Liu. Smart injectable hydrogels for cancer immunotherapy. Adv. Funct. Mater., 30(2):1902785, 2020.
- H. Chen, D. Mou, D. Du, X. Chang, D. Zhu, J. Liu, H. Xu, and X. Yang. Hydrogel-thickened microemulsion for topical administration of drug molecule at an extremely low concentration. *Int. J. Pharm.*, 341(1–2):78–84, 2007.
- J. Chen, H. Park, and K. Park. Synthesis of superporous hydrogels: Hydrogels with fast swelling and superabsorbent properties. J. Biomed. Mater. Res., 44 (1):53–62, 1999.
- A. Chojnicka, G. Sala, C. G. de Kruif, and F. van de Velde. The interactions between oil droplets and gel matrix affect the lubrication properties of sheared emulsion-filled gels. *Food Hydrocoll.*, 23(3):1038–1046, 2009.
- B. G. Chung, K.-H. Lee, A. Khademhosseini, and S.-H. Lee. Microfluidic fabrication of microengineered hydrogels and their application in tissue engineering. *Lab Chip*, 12:45–59, 2012.
- Y.-I. Chung, K.-M. Ahn, S.-H. Jeon, S.-Y. Lee, J.-H. Lee, and G. Tae. Enhanced bone regeneration with bmp-2 loaded functional nanoparticle—hydrogel complex. J. Controlled Release, 121(1):91 – 99, 2007.
- E. Commission. Types and uses of nanomaterials, including safety aspects accompanying the communication from the commission to the european parliament, the council and the european economic and social committee on the second regulatory review on nanomaterials. Technical Report 572 Final, European Commission, 2012.
- Z. Cong, Y. Shi, X. Peng, B. Wei, Y. Wang, J. Li, J. Li, and J. Li. Design and optimization of thermosensitive nanoemulsion hydrogel for sustained-release of praziquantel. *Drug Dev. Ind. Pharm.*, 43(4):558–573, 2017.
- C. Dannert, B. T. Stokke, and R. S. Dias. Nanoparticle-hydrogel composites: From molecular interactions to macroscopic behavior. *Polymers*, 11(2):275, 02 2019.

H. B. de Aguiar, A. G. F. de Beer, M. L. Strader, and S. Roke. The interfacial tension of nanoscopic oil droplets in water is hardly affected by sds surfactant. J. Am. Chem. Soc., 132(7):2122–2123, 2010.

- P. Debye. A method for the determination of the mass of electrolytic ions. *J. Chem. Phys.*, 1(1):13–16, 1933.
- E. H. B. DeLacey and L. R. White. Dielectric response and conductivity of dilute suspensions of colloidal particles. *J. Chem. Soc., Faraday Trans.* 2, 77:2007–2039, 1981.
- A. Delgado, F. González-Caballero, R. Hunter, L. Koopal, and J. Lyklema. Measurement and interpretation of electrokinetic phenomena. J. Colloid Interface Sci., 309(2):194 224, 2007.
- T. Delmas, H. Piraux, A. Couffin, I. Texier, F. Vinet, P. Poulin, M. Cates, and J. Bibette. How to prepare and stabilize very small nanoemulsions. *Langmuir*, 27(5):1683–1692, 2011.
- A. M. Djerdjev, J. K. Beattie, and R. J. Hunter. Stagnant layer conduction in surfactant-stabilized hexadecane emulsion systems measured by electroacoustics. *Aust. J. Chem.*, 56(10):1081–1089, 2003a.
- A. M. Djerdjev, J. K. Beattie, and R. J. Hunter. An electroacoustic and high-frequency dielectric response study of stagnant layer conduction in emulsion systems. *J. Colloid Interface Sci.*, 265(1):56–64, 2003b.
- D. E. Dunstan and L. R. White. An electrokinetic study of micellar solutions. J. Colloid Interface Sci., 134(1):147-151, 1990.
- D. E. Dunstan and L. R. White. The dielectric response of dilute polystyrene latex dispersions. *J. Colloid Interface Sci.*, 152(2):308 313, 1992.
- A. Einstein. Zur theorie der brownschen bewegung. Ann. Phys., 324(2):371–381, 1906.
- H. B. Eral, M. O'Mahony, R. Shaw, B. L. Trout, A. S. Myerson, and P. S. Doyle. Composite hydrogels laden with crystalline active pharmaceutical ingredients of controlled size and loading. *Chem. Mater.*, 26(21):6213–6220, 2014.
- H. Feil, Y. H. Bae, J. Feijen, and S. W. Kim. Molecular separation by thermosensitive hydrogel membranes. *J. Membr. Sci.*, 64(3):283 294, 1991.

A. Francesko, P. Petkova, and T. Tzanov. Hydrogel dressings for advanced wound management. *Curr. Med. Chem.*, 25(41):5782–5797, 2018.

- H. Geckil, F. Xu, X. Zhang, S. Moon, and U. Demirci. Engineering hydrogels as extracellular matrix mimics. *Nanomedicine*, 5(3):469–484, 2010.
- L. Gilbert, C. Picard, G. Savary, and M. Grisel. Rheological and textural characterization of cosmetic emulsions containing natural and synthetic polymers: Relationships between both data. *Colloids Surf.*, A, 421:150–163, 2013.
- M. R. Gittings and D. A. Saville. Electrophoretic mobility and dielectric response measurements on electrokinetically ideal polystyrene latex particles. *Langmuir*, 11(3):798–800, 1995.
- C. Gong, Q. Wu, Y. Wang, D. Zhang, F. Luo, X. Zhao, Y. Wei, and Z. Qian. A biodegradable hydrogel system containing curcumin encapsulated in micelles for cutaneous wound healing. *Biomaterials*, 34(27):6377 6387, 2013.
- M. Grazia-Cascone, Z. Zhu, F. Borselli, and L. Lazzeri. Poly(vinyl alcohol) hydrogels as hydrophilic matrices for the release of lipophilic drugs loaded in plga nanoparticles. *J. Mater. Sci. Mater. Med.*, 13(1):29–32, 2002.
- S. Grijalvo, J. Mayr, R. Eritja, and D. D. Díaz. Biodegradable liposome-encapsulated hydrogels for biomedical applications: a marriage of convenience. *Biomater. Sci.*, 4:555–574, 2016.
- C. Grosse and A. Delgado. Dielectric dispersion in aqueous colloidal systems. Curr. Opin. Colloid Interface Sci., 15(3):145 – 159, 2010.
- D. Gulsen and A. Chauhan. Dispersion of microemulsion drops in {HEMA} hydrogel: a potential ophthalmic drug delivery vehicle. *Int. J. Pharm.*, 292(1–2): 95–117, 2005.
- A. Gupta, H. B. Eral, T. A. Hatton, and P. S. Doyle. Nanoemulsions: formation, properties and applications. *Soft Matter*, 12:2826–2841, 2016.
- A. Gupta, A. Z. M. Badruddoza, and P. S. Doyle. A general route for nanoemulsion synthesis using low-energy methods at constant temperature. *Langmuir*, 33(28): 7118–7123, 2017.

J. Gutièrrez, C. Gonzélez, A. Maestro, I. Solé, C. Pey, and J. Nolla. Nano-emulsions: New applications and optimization of their preparation. *Curr. Opin. Colloid Interface Sci.*, 13(4):245–251, 2008.

- M. Hamidi, A. Azadi, and P. Rafiei. Hydrogel nanoparticles in drug delivery. *Adv. Drug Deliv. Rev.*, 60(15):1638–1649, 2008.
- G. V. Hartland, F. Grieser, and L. R. White. Surface potential measurements in pentanol—sodium dodecyl sulphate micelles. *J. Chem. Soc.*, Faraday Trans. 1, 83:591–613, 1987.
- S. M. Hashemnejad, A. Z. M. Badruddoza, B. Zarket, C. Ricardo Castaneda, and P. S. Doyle. Thermoresponsive nanoemulsion-based gel synthesized through a low-energy process. *Nat. Commun.*, 10(1):2749, 2019.
- J. B. Hayter and J. Penfold. Determination of micelle structure and charge by neutron small-angle scattering. *Colloid Polym. Sci.*, 261(12):1022–1030, 1983.
- T. Helfman, L. Ovington, and V. Falanga. Occlusive dressings and wound healing. Clin. Dermatol., 12(1):121 127, 1994.
- M. E. Helgeson. Colloidal behavior of nanoemulsions: Interactions, structure, and rheology. Curr. Opin. Colloid Interface Sci., 25:39 50, 2016.
- D. C. Henry and A. Lapworth. The cataphoresis of suspended particles. part i. *Proc. R. Soc. London, Ser. A*, 133(821):106–129, 1931.
- R. J. Hill. Electrokinetic spectra of dilute surfactant-stabilized nano-emulsions. *J. Fluid Mech.*, 902(A15), 2020.
- R. J. Hill and G. A. Afuwape. Dynamic mobility of surfactant stabilized nanodroplets: unifying equilibrium thermodynamics, electro-kinetics and Marangoni effects. *J. Fluid Mech.*, 895(A14), 2020.
- R. J. Hill, D. Saville, and W. Russel. Polarizability and complex conductivity of dilute suspensions of spherical colloidal particles with charged (polyelectrolyte) coatings. J. Colloid Interface Sci., 263(2):478 497, 2003a.
- R. J. Hill, D. Saville, and W. Russel. Electrophoresis of spherical polymer-coated colloidal particles. *J. Colloid Interface Sci.*, 258(1):56 74, 2003b.
- R. J. Hill, D. A. Saville, and W. B. Russel. High-frequency dielectric relaxation of spherical colloidal particles. *Phys. Chem. Chem. Phys.*, 5:911–915, 2003c.

R. M. Hill and J. Cooper. Characterization of water-in-oil emulsions by means of dielectric spectroscopy. J. Mater. Sci., 27(17):4818–4827, 1992.

- S. Hollingshead, G. A. Johnson, and B. A. Pethica. Electrophoretic properties of an octadecanol dispersion. *Trans. Faraday Soc.*, 61:577–582, 1965.
- A. Hollingsworth and D. Saville. A broad frequency range dielectric spectrometer for colloidal suspensions: cell design, calibration, and validation. *J. Colloid Interface Sci.*, 257(1):65 – 76, 2003.
- A. D. Hollingsworth and D. A. Saville. Dielectric spectroscopy and electrophoretic mobility measurements interpreted with the standard electrokinetic model. J. Colloid Interface Sci., 272(1):235 – 245, 2004.
- R. J. Hunter. The calculation of ζ -potential from mobility measurements. J. Phys. Chem., 66(7):1367–1368, 1962.
- R. J. Hunter. Zeta Potential in Colloid Science. Academic Press, 1981. ISBN 978-0-12-361961-7.
- R. J. Hunter. More reliable zeta potentials using electroacoustics. In *Surface and Colloid Science*, pages 1–10, Berlin, Heidelberg, 2004. Springer Berlin Heidelberg.
- R. J. Hunter and R. W. O'Brien. Electroacoustic characterization of colloids with unusual particle properties. *Colloids Surf.*, A, 126(2):123 128, 1997.
- M. Jaiswal, R. Dudhe, and P. K. Sharma. Nanoemulsion: an advanced mode of drug delivery system. *Biotech.*, 5(2):123–127, 2014.
- J. Jiao and D. J. Burgess. Ostwald ripening of water-in-hydrocarbon emulsions. J. Colloid Interface Sci., 264(2):509–516, 2003.
- M. Jiménez, F. Arroyo, A. Delgado, F. Mantegazza, T. Bellini, and R. Rica. Electrokinetics in extremely bimodal suspensions. *J. Colloid Interface Sci.*, 309 (2):296 – 302, 2007a. Elkin 06, International Electrokinetics Conference, June 25-29, Nancy, France.
- M. L. Jiménez, F. J. Arroyo, F. Carrique, and A. V. Delgado. Surface conductivity of colloidal particles: experimental assessment of its contributions. *J. Colloid Interface Sci.*, 316(2):836–843, 2007b.

P. H. Johnson and L. I. Grossman. Electrophoresis of dna in agarose gels. optimizing separations of conformational isomers of double- and single-stranded dnas. *Biochemistry*, 16(19):4217–4225, 1977.

- E. Josef, M. Zilberman, and H. Bianco-Peled. Composite alginate hydrogels: An innovative approach for the controlled release of hydrophobic drugs. *Acta Biomater.*, 6(12):4642 4649, 2010.
- D. G. Kanjickal and S. T. Lopina. Modeling of drug release from polymeric delivery systems—a review. *Crit. Rev. Ther. Drug Carrier Syst.*, 21(5):345—386, 2004.
- L. Kass, E. D. Cardenas-Vasquez, and L. C. Hsiao. Composite double network hydrogels with thermoresponsive colloidal nanoemulsions. *AIChE J.*, 65(12), 2019.
- I. Katime, L. Guerrero, and E. Mendizabal. Size matters: Smart copolymeric nanohydrogels: Synthesis and applications. *Front. Biosci. Elite*, 4 E(4):1314–1334, 2012.
- M. Khademi and D. P. J. Barz. Dielectric relaxation spectroscopy of aqueous micellar electrolyte solutions: A novel application to infer dukhin number and zeta potential of a micelle. *Electrophoresis*, 40(5):710–719, 2019.
- K. Kim, J. Renkema, and T. Van Vliet. Rheological properties of soybean protein isolate gels containing emulsion droplets. *Food Hydrocoll.*, 15(3):295–302, 2001.
- J. Koehler, F. P. Brandl, and A. M. Goepferich. Hydrogel wound dressings for bioactive treatment of acute and chronic wounds. *Eur. Polym. J.*, 100:1 11, 2018.
- G. Komarova, S. Starodubtsev, V. Lozinsky, I. Nasimova, and A. Khokhlov. Intelligent gels and cryogels with embedded emulsions of various oils. *J. Appl. Polym. Sci.*, 127(4):2703 2709, 2013.
- L. Kong, J. K. Beattie, and R. J. Hunter. Electroacoustic study of concentrated oil-in-water emulsions. *J. Colloid Interface Sci.*, 238(1):70 79, 2001.
- L. Kong, J. K. Beattie, and R. J. Hunter. Electroacoustic study of hexadecane/water emulsions. *Aust. J. Chem.*, 54(8):503–511, 2002.

L. Lanzi, M. Carlà, L. Lanzi, and C. M. Gambi. A new insight on the dynamics of sodium dodecyl sulfate aqueous micellar solutions by dielectric spectroscopy. J. Colloid Interface Sci., 330(1):156 – 162, 2009.

- L. Lei, Y. Zhang, L. He, S. Wu, B. Li, and Y. Li. Fabrication of nanoemulsion-filled alginate hydrogel to control the digestion behavior of hydrophobic nobiletin. LWT-Food Sci. Technol., 82:260–267, 2017.
- T. Leong, T. Wooster, S. Kentish, and M. Ashokkumar. Minimising oil droplet size using ultrasonic emulsification. *Ultrason. Sonochem.*, 16(6):721–727, 2009.
- W. M. Leung, D. E. Axelson, and J. D. Van Dyke. Thermal degradation of polyacrylamide and poly(acrylamide-co-acrylate). *J. Polym. Sci., Part A: Polym. Chem.*, 25(7):1825–1846, 1987.
- J. Li and D. J. Mooney. Designing hydrogels for controlled drug delivery. *Nat. Rev. Mater.*, 1(12), 2016.
- Y. Li, E. Wong, A. Volodine, C. Van Haesendonck, K. Zhang, and B. Van der Bruggen. Nanofibrous hydrogel composite membranes with ultrafast transport performance for molecular separation in organic solvents. *J. Mater. Chem. A*, 7:19269–19279, 2019.
- I. Lifshitz. The kinetics of precipitation from supersaturated solid solutions. *J. Phys. Chem. Solids*, 19:35–50, 1961.
- C.-C. Lin and A. T. Metters. Hydrogels in controlled release formulations: network design and mathematical modeling. *Adv. Drug Deliv. Rev.*, 58(12-13):1379–1408, 2006.
- A. L. Loeb, J. T. G. Overbeek, P. H. Wiersema, and C. V. King. The electrical double layer around a spherical colloid particle. *J. Electrochem. Soc.*, 108(12): 269C, 1961.
- N. López Mora, J. S. Hansen, Y. Gao, A. A. Ronald, R. Kieltyka, N. Malmstadt, and A. Kros. Preparation of size tunable giant vesicles from cross-linked dextran(ethylene glycol) hydrogels. *Chem. Commun.*, 50(16):1953–1955, 2014.
- F. Lupi, L. Gentile, D. Gabriele, S. Mazzulla, N. Baldino, and B. de Cindio. Olive oil and hyperthermal water bigels for cosmetic uses. J. Colloid Interface Sci., 459:70–78, 2015.

J. Lyklema. Fundamentals of Interface and Colloid Science, volume 2. Elservier Academic press, 1995.

- C. S. Mangelsdorf and L. R. White. Effects of stern-layer conductance on electrokinetic transport properties of colloidal particles. J. Chem. Soc., Faraday Trans., 86:2859–2870, 1990.
- C. S. Mangelsdorf and L. R. White. Electrophoretic mobility of a spherical colloidal particle in an oscillating electric field. J. Chem. Soc., Faraday Trans., 88:3567– 3581, 1992.
- S. C. Mangelsdorf and L. R. White. Dielectric response of a dilute suspension of spherical colloidal particles to an oscillating electric field. *J. Chem. Soc.*, Faraday Trans., 93:3145–3154, 1997.
- S. C. Mangelsdorf and L. R. White. The dynamic double layer part 1: Theory of a mobile stern layer. *J. Chem. Soc.*, Faraday Trans., 94:2441–2452, 1998.
- J. P. Marcolongo and M. Mirenda. Thermodynamics of sodium dodecyl sulfate (sds) micellization: An undergraduate laboratory experiment. J. Chem. Educ., 88(5):629–633, 2011.
- Y. Marcus. Ionic radii in aqueous solutions. Chem. Rev., 88(8):1475–1498, 1988.
- A. Martinez-Ruvalcaba. Swelling characterization and drug delivery kinetics of polyacrylamide-co-itaconic acid/chitosan hydrogels. *Express Polym. Lett.*, 3: 25–32, 2008.
- L. Masaro and X. Zhu. Physical models of diffusion for polymer solutions, gels and solids. *Prog. Polym. Sci.*, 24(5):731 775, 1999.
- T. Mason. New fundamental concepts in emulsion rheology. Curr. Opin. Colloid Interface Sci., 4:231–238, 1999.
- T. G. Mason, J. Bibette, and D. A. Weitz. Elasticity of compressed emulsions. *Phys. Rev. Lett.*, 75:2051–2054, 1995.
- T. G. Mason, J. Bibette, and D. A. Weitz. Yielding and flow of monodisperse emulsions. *J. Colloid Interface Sci.*, 179(2):439 448, 1996.
- D. J. McClements and J. Rao. Food-grade nanoemulsions: formulation, fabrication, properties, performance, biological fate, and potential toxicity. *Crit. Rev. Food Sci. Nutr.*, 51(4):285–330, 2011.

I. Milimouk, A. Hecht, D. Beysens, and E. Geissler. Swelling of neutralized polyelectrolyte gels. *Polymer*, 42(2):487–494, 2001.

- S. Mitragotri, D. G. Anderson, X. Chen, E. K. Chow, D. Ho, A. V. Kabanov, J. M. Karp, K. Kataoka, C. A. Mirkin, S. H. Petrosko, J. Shi, M. M. Stevens, S. Sun, S. Teoh, S. S. Venkatraman, Y. Xia, S. Wang, Z. Gu, and C. Xu. Accelerating the translation of nanomaterials in biomedicine. ACS Nano, 9(7):6644–6654, 2015.
- Y. Moroi and N. Yoshida. A new approach to micellization parameters: Its application to sodium dodecyl sulfate micelle. *Langmuir*, 13(15):3909–3912, 1997.
- D. Mou, H. Chen, D. Du, C. Mao, J. Wan, H. Xu, and X. Yang. Hydrogel-thickened nanoemulsion system for topical delivery of lipophilic drugs. *Int. J. Pharm.*, 353(1):270 276, 2008.
- S. Murdan. Electro-responsive drug delivery from hydrogels. J. Controlled Release, 92(1):1-17, 2003.
- Nature. Nanomaterials definition matters. Nat. Nanotechnol., 14(3):193–193, 2019.
- C. Nazli, G. S. Demirer, Y. Yar, H. Y. Acar, and S. Kizilel. Targeted delivery of doxorubicin into tumor cells via mmp-sensitive peg hydrogel-coated magnetic iron oxide nanoparticles (mionps). *Colloids Surf.*, B, 122:674 – 683, 2014.
- S. A. Nespolo, M. A. Bevan, D. Y. C. Chan, F. Grieser, and G. W. Stevens. Hydrodynamic and electrokinetic properties of decane droplets in aqueous sodium dodecyl sulfate solutions. *Langmuir*, 17(23):7210–7218, 2001.
- R. W. O'Brien. The electrical conductivity of a dilute suspension of charged particles. J. Colloid Interface Sci., 81(1):234 248, 1981.
- R. W. O'Brien. Electro-acoustic effects in a dilute suspension of spherical particles. J. Fluid Mech., 190:71–86, 1988.
- R. W. O'Brien and R. J. Hunter. The electrophoretic mobility of large colloidal particles. *Can. J. Chem.*, 59(13):1878–1887, 1981.
- R. W. O'Brien and L. R. White. Electrophoretic mobility of a spherical colloidal particle. J. Chem. Soc., Faraday Trans. 2, 74:1607–1626, 1978.

R. W. O'Brien, D. W. Cannon, and W. N. Rowlands. Electroacoustic determination of particle size and zeta potential. *J. Colloid Interface Sci.*, 173(2):406–418, 1995.

- S. G. Oh and D. O. Shah. The effect of micellar lifetime on the rate of solubilization and detergency in sodium dodecyl sulfate solutions. *J. Am. Oil Chem. Soc.*, 70 (7):673–678, 1993.
- I. Ohmine and T. Tanaka. Salt effects on the phase transition of ionic gels. *J. Chem. Phys.*, 77(11):5725–5729, 1982.
- H. Ohshima. A simple expression for henry's function for the retardation effect in electrophoresis of spherical colloidal particles. J. Colloid Interface Sci., 168(1): 269 – 271, 1994.
- H. Ohshima. Dynamic electrophoretic mobility of spherical colloidal particles in concentrated suspensions. J. Colloid Interface Sci., 195(1):137 148, 1997.
- H. Ohshima. Electrokinetic phenomena of soft particles. Curr. Opin. Colloid Interface Sci., 18(2):73 – 82, 2013. ISSN 1359-0294.
- H. Ohshima, T. W. Healy, and L. R. White. Electrokinetic phenomena in a dilute suspension of charged mercury drops. J. Chem. Soc., Faraday Trans. 2, 80: 1643–1667, 1984.
- J. Overbeek. Theorie der electrophorese. Kolloid B, 1(54):287–364, 1943.
- K. Pal, A. K. Banthia, and D. K. Majumdar. Biomedical evaluation of polyvinyl alcohol–gelatin esterified hydrogel for wound dressing. J. Mater. Sci. - Mater. Med., 18(9):1889–1894, 2007.
- A. Patist, S. Oh, R. Leung, and D. Shah. Kinetics of micellization: its significance to technological processes. *Colloids Surf.*, A, 176(1):3 16, 2001.
- K. A. Payne, L. J. Magid, and D. F. Evans. Structural changes in anionic micelles induced by counterion complexation with a macrocyclic ligand: A neutron scattering study. In H. Hoffmann, editor, New Trends in Colloid Science, pages 10–17, Darmstadt, 1987. Steinkopff.
- N. Peppas, P. Bures, W. Leobandung, and H. Ichikawa. Hydrogels in pharmaceutical formulations. *Eur. J. Pharm. Biopharm.*, 50(1):27–46, 2000.

C. Persson, A. Jonsson, M. Bergström, and J. C. Eriksson. Testing the gouy-chapman theory by means of surface tension measurements for sds-nacl-h2o mixtures. *J. Colloid Interface Sci.*, 267(1):151 – 154, 2003.

- K. Rehman, M. Amin, and M. Zulfakar. Development and physical characterization of polymer-fish oil bigel (hydrogel/oleogel) system as a transdermal drug delivery vehicle. J. Oleo Sci., 63(10):961–970, 2014.
- L. A. Rosen and D. A. Saville. Dielectric spectroscopy of colloidal dispersions: Comparisons between experiment and theory. *Langmuir*, 7(1):36–42, 1991.
- M. J. Rosen. Surfactants and interfacial phenomena, volume 27. John Wiley & Sons, Inc., 2 edition, 1989.
- W. B. Russel, D. A. Saville, and W. R. Schowalter. *Colloidal Dispersions*. Cambridge University Press, Cambridge, UK, 1989.
- S. E. Sakiyama-Elbert and J. A. Hubbell. Development of fibrin derivatives for controlled release of heparin-binding growth factors. *J. Control. Release*, 65(3): 389 402, 2000.
- G. Sala, G. Van Aken, M. Stuart, and F. Van De Velde. Effect of droplet-matrix interactions on large deformation properties of emulsion-filled gels. *J. Texture* Stud., 38(4):511–535, 2007a.
- G. Sala, F. van de Velde, M. Cohen Stuart, and G. van Aken. Oil droplet release from emulsion-filled gels in relation to sensory perception. *Food Hydrocoll.*, 21 (5–6):977–985, 2007b.
- G. Sala, T. van Vliet, M. Cohen Stuart, F. van de Velde, and G. van Aken. Deformation and fracture of emulsion-filled gels: Effect of gelling agent concentration and oil droplet size. *Food Hydrocoll.*, 23(7):1853–1863, 2009a.
- G. b. Sala, T. van Vliet, M. Cohen Stuart, G. Aken, and F. van de Velde. Deformation and fracture of emulsion-filled gels: Effect of oil content and deformation speed. *Food Hydrocoll.*, 23(5):1381–1393, 2009b.
- R. A. SAS. Conductivity: Theory and Practice. Radiometer analytical SAS, 2003.
- D. A. Saville. Electrical conductivity of suspensions of charged particles in ionic solutions. *J. Colloid Interface Sci.*, 71(3):477 490, 1979.

D. A. Saville. The electrical conductivity of suspensions of charged particles in ionic solutions: the roles of added counterions and nonspecific adsorption. J. Colloid Interface Sci., 91(1):34 – 50, 1983.

- J. E. Seebergh and J. C. Berg. Evidence of a hairy layer at the surface of polystyrene latex particles. *Colloids Surf.*, A, 100:139 153, 1995.
- P. C. Shanks and E. I. Franses. Estimation of micellization parameters of aqueous sodium dodecyl sulfate from conductivity data. *J. Phys. Chem.*, 96(4):1794–1805, 1992.
- M. Shao, Z. Hussain, H. E. Thu, S. Khan, H. Katas, T. A. Ahmed, M. Tripathy, J. Leng, H.-L. Qin, and S. N. A. Bukhari. Drug nanocarrier, the future of atopic diseases: Advanced drug delivery systems and smart management of disease. Colloid Surf. B, 147:475–491, 2016.
- S. Sharma, A. Verma, B. V. Teja, G. Pandey, N. Mittapelly, R. Trivedi, and P. Mishra. An insight into functionalized calcium based inorganic nanomaterials in biomedicine: Trends and transitions. *Colloids Surf.*, B, 133:120 – 139, 2015.
- K. Shingel, C. Roberge, O. Zabeida, M. Robert, and J. Klemberg-Sapieha. Solid emulsion gel as a novel construct for topical applications: Synthesis, morphology and mechanical properties. *J. Mater. Sci. Mater. Med.*, 20(3):681–689, 2009.
- V. E. Shubin, R. J. Hunter, and R. W. O'Brien. Electroacoustic and dielectric study of surface conduction. *J. Colloid Interface Sci.*, 159(1):174 183, 1993.
- J. Siepmann and N. A. Peppas. Modeling of drug release from delivery systems based on hydroxypropyl methylcellulose (hpmc). *Adv. Drug Deliv. Rev.*, 48(2): 139 157, 2001. =.
- C. Solans, P. Izquierdo, J. Nolla, N. Azemar, and M. Garcia-Celma. Nano-emulsions. *Curr. Opin. Colloid Interface Sci.*, 10(3–4):102–110, 2005.
- C. D. Spicer. Hydrogel scaffolds for tissue engineering: the importance of polymer choice. *Polym. Chem.*, 11:184–219, 2020.
- D. Stigter. On density, hydration, shape, and charge of micelles of sodium dodecyl sulfate and dodecyl ammonium chloride. *J. Colloid Interface Sci.*, 23(3):379 388, 1967.

D. Stigter. Theory of conductance of colloidal electrolytes in univalent salt solutions. *J. Phys. Chem.*, 83(12):1663–1670, 1979.

- D. Stigter and K. J. Mysels. Tracer electrophoresis. ii. the mobility of the micelle of sodium lauryl sulfate and its interpretation in terms of zeta potential and charge. J. Phys. Chem., 59(1):45–51, 1955.
- H. T. Ta, C. R. Dass, and D. E. Dunstan. Injectable chitosan hydrogels for localised cancer therapy. *J. Controlled Release*, 126(3):205 216, 2008.
- T. Tadros, P. Izquierdob, J. Esquenab, and C. Solansb. Formation and stability of nano-emulsions. *Adv. Colloid Interface Sci.*, 108–109:303–318, 2004.
- Y. Takata, T. Miyayama, T. Nagahashi, A. Hyono, and H. Ohshima. Micelle formation effect on electroacoustics in an aqueous surfactant solution: Colloid vibration current and ion vibration current. J. Oleo Sci., 58(11):557–563, 2009.
- T. Tanaka and D. J. Fillmore. Kinetics of swelling of gels. J. Chem. Phys., 70(3): 1214–1218, 1979.
- C. Tanford. Micelle shape and size. *J. Phys. Chem.*, 76(21):3020–3024, 1972.
- G. I. Taylor. The viscosity of a fluid containing small drops of another fluid. *Proc. R. Soc. London, Ser. A*, 138(834):41–48, 1932.
- P. Taylor. Ostwald ripening in emulsions. *Colloids Surf.*, A, 99(2–3):175–185, 1995.
- P. Thoniyot, M. J. Tan, A. A. Karim, D. J. Young, and X. J. Loh. Nanoparticle—hydrogel composites: Concept, design, and applications of these promising, multi-functional materials. *Adv. Sci.*, 2(1-2):1400010, 2015.
- V. Tjong, J. Zhang, A. Chilkoti, and S. Zauscher. Stimulus-Responsive Polymers as Intelligent Coatings for Biosensors: Architectures, Response Mechanisms, and Applications, pages 1–30. John Wiley & Sons, Inc., 2012.
- G. A. Urban and T. Weiss. Hydrogels for Biosensors. Springer, 2009.
- O. G. Us'yarov. The electrical double layer of micelles in ionic surfactant solutions in the presence of a background electrolyte: 1. diluted micellar solutions of sodium dodecyl sulfate. *Colloid J.*, 69(1):95–102, 2007.

A. G. van der Put and B. H. Bijsterbosch. Electrokinetic measurements on concentrated polystyrene dispersions and their theoretical interpretation. *J. Colloid Interface Sci.*, 92(2):499 – 507, 1983.

- T. Vliet. Rheological properties of filled gels. influence of filler matrix interaction. Colloid Polym. Sci., 266(6):518–524, 1988.
- S. Wall. The history of electrokinetic phenomena. Curr. Opin. Colloid Interface Sci., 15(3):119 124, 2010.
- M. Wang and R. J. Hill. Dynamic electric-field-induced response of charged spherical colloids in uncharged hydrogels. *J. Fluid Mech.*, 640:357–400, 2009a.
- M. Wang and R. J. Hill. Anomalous bulk viscosity of polymer-nanocomposite melts. *Soft Matter*, 5:3940–3953, 2009b.
- X. Wang, C. Cheng, S. Wang, and S. Liu. Electroosmotic pumps and their applications in microfluidic systems. *Microfluid Nanofluidics*, 6(2):145, Feb 2009. ISSN 1613-4982 (Print); 1613-4982 (Linking).
- Y. Wang, D. W. Malcolm, and D. S. Benoit. Controlled and sustained delivery of sirna/nps from hydrogels expedites bone fracture healing. *Biomaterials*, 139: 127 138, 2017.
- L. Wei, C. Cai, J. Lin, and T. Chen. Dual-drug delivery system based on hydrogel/micelle composites. *Biomaterials*, 30(13):2606 2613, 2009.
- P. Wiersema, A. Loeb, and J. Overbeek. Calculation of the electrophoretic mobility of a spherical colloid particle. *J. Colloid Interface Sci.*, 22(1):78 99, 1966.
- H. Wu, L. Song, L. Chen, Y. Huang, Y. Wu, F. Zang, Y. An, H. Lyu, M. Ma, J. Chen, N. Gu, and Y. Zhang. Injectable thermosensitive magnetic nanoemulsion hydrogel for multimodal-imaging-guided accurate thermoablative cancer therapy. *Nanoscale*, 9(42):16175–16182, 2017.
- S. Xianquan, J. Shi, Y. Kakuda, and J. Yueming. Stability of lycopene during food processing and storage. *J. Med. Food*, 8(4):413–422, 2005.
- F. Yang, W. Wu, S. Chen, and W. Gan. The ionic strength dependent zeta potential at the surface of hexadecane droplets in water and the corresponding interfacial adsorption of surfactants. *Soft Matter*, 13:638–646, 2017.

X. Yang, M. Yang, B. Pang, M. Vara, and Y. Xia. Gold nanomaterials at work in biomedicine. *Chem. Rev.*, 115(19):10410–10488, 2015.

- R. Yoshida, K. Sakai, T. Okano, and Y. Sakurai. Pulsatile drug delivery systems using hydrogels. *Adv. Drug Deliv. Rev.*, 11(1):85 108, 1993.
- R. Yu and S. Zheng. Poly(acrylic acid)-grafted poly(n-isopropyl acrylamide) networks: Preparation, characterization and hydrogel behavior. J. Biomater. Sci., Polym. Ed., 22(17):2305–2324, 2011.
- E. Zdrali, Y. Chen, H. I. Okur, D. M. Wilkins, and S. Roke. The molecular mechanism of nanodroplet stability. *ACS Nano*, 11(12):12111–12120, 2017.
- E. Zdrali, G. Etienne, N. Smolentsev, E. Amstad, and S. Roke. The interfacial structure of nano- and micron-sized oil and water droplets stabilized with sds and span80. *J. Chem. Phys.*, 150(20):204704, 2019.
- B. Zeeb, A. H. Saberi, J. Weiss, and D. J. McClements. Formation and characterization of filled hydrogel beads based on calcium alginate: Factors influencing nanoemulsion retention and release. *Food Hydrocoll.*, 50:27–36, 2015.
- K. Zhao and K. He. Dielectric relaxation of suspensions of nanoscale particles surrounded by a thick electric double layer. *Phys. Rev. B*, 74(20):205319, 2006.
- Y. Zhou, S. Liu, M. Zhao, C. Wang, L. Li, Y. Yuan, L. Li, G. Liao, W. Bresette, J. Zhang, Y. Chen, J. Cheng, Y. Lu, and J. Liu. Injectable extracellular vesicle-released self-assembling peptide nanofiber hydrogel as an enhanced cell-free therapy for tissue regeneration. *J. Controlled Release*, 316:93 104, 2019.
- C. F. Zukoski and D. A. Saville. An experimental test of electrokinetic theory using measurements of electrophoretic mobility and electrical conductivity. J. Colloid Interface Sci., 107(2):322 – 333, 1985.